UNIVERSITY OF SOUTHAMPTON

FACULTY OF NATURAL AND ENVIRONMENTAL SCIENCES

School of Chemistry

Volume 1 of 3

A novel high-speed AC impedance method for monitoring transient cavitation

by

Hannah Louise Martin

Thesis for the degree of Doctor of Philosophy

July 2018

UNIVERSITY OF SOUTHAMPTON

ABSTRACT

FACULTY OF NATURAL AND ENVIRONMENTAL SCIENCES
Doctor of Philosophy

A NOVEL HIGH-SPEED AC IMPEDANCE METHOD FOR MONITORING TRANSIENT CAVITATION

By Hannah Louise Martin

This thesis details an investigation of bubble dynamics using a set of novel electrochemical impedance measurements with the ability to monitor the motion of bubbles during cavitation. This method was able to report dynamic information about the motion of bubbles over an electrode surface with a time resolution of 2 μs. The results produced from these impedance studies are supported by other techniques used to characterise cavitation, such as acoustic output measurements and high-speed imaging. Cavitation was generated inside a suitable electrochemical cell using a variety of sound sources. The different acoustic environments were chosen so that different types of bubble activity could be investigated.

Initial investigations were carried out inside a cylindrical resonance chamber, chosen for its high symmetry and good resonance properties. A solid reflector (aluminium or steel) inserted inside the cylinder formed a mobile solid/liquid interface. We were able to show that acoustic cavitation occurred at the reflector surface when regions of high acoustic pressure were formed at the electrode surface. Electrochemical data was recorded by an electrode embedded into the reflector surface. The data recorded was used to quantify the amount of cavitation activity as a function of reflector position and also to indicate mechanistic detail of the bubble growth and collapse under cavitation. Complementary studies were carried out using acoustic measurements as the bubbles acted as secondary sound sources. It was also shown that changing the reflector material changed the acoustic properties of the chamber.

Further investigations were performed using an ultrasonic horn as a piston-like emitter (PLE) to generate acoustic cavitation. The PLE was positioned over the surface of a highly polished electrode. This electrode was used to monitor the motion of cavitation bubbles electrochemically using the novel high-speed AC impedance technique. These investigations were able to interrogate different types of cavitation bubble motion to that seen inside the cylindrical cell. The electrochemical studies revealed details of the oscillatory motion of the bubbles under the influence of the PLE. Complementary evidence for the bubble activity observed by the impedance results was provided by high-speed imaging of the electrode surface.

Contents

Academic Thesis: Declaration Of Authorship

I, Hannah Louise Martin

declare that this thesis and the work presented in it are my own and has been generated by me as the result of my own original research.

A Novel High-Speed AC Impedance Method for Monitoring Transient Cavitation

I confirm that:

1. This work was done wholly or mainly while in candidature for a research degree at this University;
2. Where any part of this thesis has previously been submitted for a degree or any other qualification at this University or any other institution, this has been clearly stated;
3. Where I have consulted the published work of others, this is always clearly attributed;
4. Where I have quoted from the work of others, the source is always given. With the exception of such quotations, this thesis is entirely my own work;
5. I have acknowledged all main sources of help;
6. Where the thesis is based on work done by myself jointly with others, I have made clear exactly what was done by others and what I have contributed myself;
7. None of this work has been published before submission:

Signed: .....

Date: .....

Acknowledgements

Would like to thank the following people for their help and guidance through my PhD.

First, to Pete thank you for your insight and guidance both through the project and during the writing of this thesis. Your catchphrases of ‘job’s a good’un’, ‘the plot thinnens!’ and ‘good group meeting’ (when I was the only person working in the lab) made the lab based work all the more joyful to complete. I shall be reusing some of these catchphrases in future to boost others’ moral.

I also wish to thank the rest of the Birkin group, to Tom for his early help with writing visual basic code and to Laura and Jack for their moral support. My vocabulary has been greatly expanded by our three-a-day crossword habit.

To everyone who has played with me in the university orchestra, the end of my PhD also concludes my eight years with SUSO. I have gained some great friends and have thoroughly enjoyed every concert. I hope to come back to watch you play in the future.

I would like to thank my friends, in particular to Eleonore and Fiona. Our swimming trips and evening skype dates to watch TV together have brightened my weekends and given me the motivation to continue writing.

Last, but certainly not least, I would like to thank my Mum and Dad for their constant love and support.

Abbreviations and Definitions

A	Electrode Area (cm2)
C	Capacitance (F)
c	Speed of Sound (m s^{-1})
C_{dl}	Double Layer Capacitance (F)
dE/dt	Change in Potential with Respect to Time
dn/dt	Mass Transfer Rate to Electrode Surface
dq/dt	Change in Charge with Respect to Time
E	Electrode Potential (V)
E_{Cdl}	Potential Across a Capacitor (V)
E_R	Potential Across a Resistor (V)
E_{we}	Working Electrode Potential
f	Drive Frequency (Hz)
f_{mnp}, f_{mnq}, f_{mnz}	Mode Frequency (Hz)
f_o	Fundamental Frequency (Hz)
G	Gain Amplification (V A^{-1})
I	Mean DC Current (A)
i	Current (A)
i_C	AC Current Response Across a Capacitor (A)
i_{dc}	Faradaic Current (A)
$\mathrm{Im}(Z_{cell})$	Imaginary Component of Cell Impedance (Ω)
i_{out}	Measured AC Current Response of the Electrochemical System (A)
i_R	AC Current Response Across a Resistor (A)
I_w	Incident Wave
j_{mn}	Solutions to the Bessel Function
k	Wavenumber (cm^{-1})
k_r	Transverse Wavenumber (cm^{-1})
k_z	Axial Wavenumber (cm^{-1})
L	Height of the Cylindrical Chamber (cm)
l	Recess Length (cm)
p	Acoustic Pressure in Liquid (Pa)
p_∞	Bulk Liquid Pressure (Pa)
P_B	Blake Pressure (Pa)
p_L	Pressure at Bubble Wall (Pa)
p_o	Hydrostatic Liquid Pressure (Pa)
q	Charge (C)
Q_1	Constant Phase Element (F s^{a-1})
r	Bubble Radius (cm)

R	Resistance (Ω)
r, θ, z	Cylindrical Polar Coordinate System
r_B	Blake Radius (cm)
R_{ch}	Chanel Resistance (Ω)
R_{ct}	Charge Transfer Resistance (Ω)
$\mathrm{Re}(Z_{cell})$	Real Component of Cell Impedance (Ω)
R_h	Hemispherical Electrode Resistance (Ω)
r_o	Equilibrium Bubble Radius (cm)
R_o	Fixed External Resistor (Ω)
R_u	Uncompensated Resistance (Ω)
R_w	Wave Reflection Factor
s_C	Standard Deviation for Capacitance
s_{Ru}	Standard Deviation for Uncompensated Resistance
s_{Xc}	Standard Deviation for Capacitive Resistance
s_y	Standard Deviation
t	Time (s)
T_w	Wave Transmission Factor
V	Potential Across Working and Reference Electrodes (V)
V_{app}	Applied AC Potential (V)
V_{out}	i_{out} x Amplifier Gain (V)
x, y, z	Cartesian Coordinate System
X_c	Capacitive Resistance (=$1/\omega C_{dl}$, Ω)
Z	Impedance (Ω)
Z'	Real Component of Cell Impedance (Ω)
Z''	Imaginary Component of Cell Impedance (Ω)
Z_a	Acoustic Impedance of Aluminium (kg cm^{-2} s^{-1})
Z_{cell}	Cell Impedance (Ω)
Z_w	Acoustic Impedance of Water (kg cm^{-2} s^{-1})
α	Void Fraction
ΔE	Zero-to-Peak AC Potential Amplitude
$\Delta E(t)$	Fluctuation in Potential as a Function of Time (V)
$\Delta i_{100}(t)$	AC Current Perturbation (A)
$\Delta R(t)$	Fluctuation in Resistance as a Function of Time (Ω)
ΔR_u	Change in Uncompensated Resistance (Ω)
$\Delta V(t)$	Fluctuation in Voltage as a Function of Time (V)
η	Shear Viscosity of the Liquid (Pa s)
θ	Phase Shift between Applied AC Potential and AC Current Response
κ	Solution Conductivity (mS cm^{-2})
λ	Wavelength (cm)

ρ_o	Liquid Density (g cm^{-3})
σ	Surface Tension on Bubble (N m^{-1})
ϕ	Electrode Diameter (cm)
ω	Angular Frequency (Hz)

ABS	Acrylonitrile Butadiene Styrene
AC	Alternating Current
CE	Counter Electrode
CPE	Constant Phase Element
DC	Direct Current
DSP	Data Signal Processing
FFT	Fast Fourier Transform
HS-CF	High-Speed Current Follower
ID	Inner Diameter
MME	Micromosaic Electrode
MMS	Mercury/Mercury Sulphate Reference Electrode
OD	Outer Diameter
PEEK	Polyether Ether Ketone
PET	Polyethylene Terephthalate
PLE	Piston-Like Emitter
RE	Reference Electrode
SEM	Scanning Electron Microscope
SR	Sample Rate
WE	Working Electrode

Chapter 1 Introduction

1.1 Cavitation

The phenomenon of cavitation can be described as the formation of bubbles in a liquid by the application of suitable stimuli to the liquid. Sources of suitable stimuli for cavitation include light (laser beams)[1], sound waves[2] and mechanical disruption of fluid flow such as a propeller[3]. In fact it is the observation of these effects which was partially responsible for the discovery of cavitation in the early part of the 20th century[3]. In particular the observation of erosion on ship propellers brought cavitation to the attention of researchers[3,1].

The type of cavitation which occurs during the pressure cycle of a sound wave is termed acoustic cavitation[4]. For this to occur in the absence of a suitable nuclei, the tension setup applied to the system must be greater than the tensile strength of the liquid[5]. In practice however, the initiation of cavitation in a liquid almost always relies on the presence of impurities in the liquid, such as pre-existing microscopic bubbles[6]. This reduces the liquid strength and provides nucleation points for cavitation[7]. Under these conditions, when a cavitation bubble is driven periodically by an acoustic wave, an oscillatory bubble response is observed[2]. The standard model used to describe these bubble oscillations resembles a periodic damped linear response[5]. Further details of the bubble oscillations will be discussed in Chapter 1.2. This bubble response is described as 'non-inertial' or 'stable'[5]. Oscillatory bubble activity such as this will be referred to in this thesis as stable cavitation.

In the presence of applied acoustic wave pressure fluctuations with an amplitude larger than the Blake threshold[*], microscopic bubbles within the liquid can expand rapidly in the rarefaction portion of the wave[6]. If this bubble expansion is sufficiently large, inertial forces dominate and subsequently the bubble collapses[6,8]. This type of cavitation has been termed 'inertial' owing to the fact that inertial forces are dominant on the bubble. It is also commonly referred to as 'transient' cavitation, the term which will be used to describe this phenomenon in this thesis[6,8].

[*] typically around atmospheric pressure for bubbles with a radius larger than 3 μm at driving frequencies of 20-30 kHz in water

There are many examples of apparatus which will produce transient cavitation[9-11]. For example, an ultrasonic horn (generating continuous wave fields at driving frequencies of 20 – 30 kHz) can be used to generate these transient cavitation events in liquids which have not undergone any kind of pre-treatment such as degassing or deionizing[12,13]. Under these conditions the threshold acoustic pressure required to generate transient cavitation is around ~100-120 kPa (zero-to-peak amplitude)[6]. In the collapsing bubble, extreme transient conditions have been measured with temperatures of almost 5000 K and several hundred atmospheres[14]. Many effects are associated with this transient cavitation. Observed effects include radical generation[15-17], light emission[18,19], shock waves[20,21] and material erosion[22]. Owing to these various observed cavitation effects, this phenomenon can be exploited in a wide variety of laboratory and industrial situations. These include enhancement of chemical kinetics[23,24], and in a number of industrial cleaning applications such as the food industry[25], and dentistry[26,27] and also in a number of laboratory cleaning applications[28,29]. The use of cavitation has also been observed in nature as an attack or defence mechanism by animals such as the mantis shrimp[30,31].

The work presented in this thesis will focus on the potential of cavitation bubbles to clean objects and surfaces. This will be achieved by characterising the motion of cavitation bubbles generated using ultrasonic sources. The aim was to develop an -'*in situ*'- electrochemical technique which was able to describe the motion of the bubbles and also give us dynamic information about the electrode surface. Impedance was chosen as the most suitable experimental method for this purpose as it is an extremely powerful technique, capable of providing us with the dynamic information about the electrode surface required. In the following sections of this introduction a brief summary of existing cavitation techniques found in the literature is given. These studies include other electrochemical investigations[24,32], as well as other methods of characterisation such as high-speed imagery[1] and acoustic measurements[33,34]. In addition, information is also provided on other time-dependent impedance techniques developed and the situations in which these techniques have been employed[35,36].

In the generation and monitoring of this type of cavitation and its associated effects, it is also important to consider how the individual gas bubbles would respond to the driving sound field[37]. Therefore, the next section briefly discusses a theoretical model which describes the response of a gas bubble in a liquid under different conditions and then relates the conclusions to the work detailed in the rest of this thesis.

1.2 The Rayleigh-Plesset equation

The theoretical model most commonly used to describe the non-linear response of a gas bubble in a liquid during cavitation is the Rayleigh-Plesset equation (1.1)[38]. This is usually expressed in terms of the bubble radius, *r*

$$r\ddot{r} + \frac{3\dot{r}^2}{2} = \frac{1}{\rho_0}\left(p_L - \frac{4\eta\dot{r}}{r} - p_\infty\right) \quad (1.1)$$

where ρ_0 is the unperturbed liquid density, η is the shear viscosity of the liquid, p_L the pressure at the bubble wall and p_∞ is the liquid pressure far from the bubble. Solutions to this equation show that the bubble response is similar to a linear damped oscillator for low amplitude bubbles. This response becomes more non-linear as the driving amplitude is increased[5].

Using the numerical solutions to the Rayleigh-Plesset equation, the behaviour of a cavitation bubble can be categorized as either ‘stable’ or ‘transient’ (as defined in Chapter 1.1)[5].

Models employing the Rayleigh-Plesset equation showing the potential variation in bubble radius and bubble wall velocity in the case of stable and transient cavitation are given in Figures 1.1 and 1.2[38]. Many approximations are made about the initial state of the bubble and the ambient conditions in these calculations. For these calculations, the media surrounding the bubble was assumed to be water and so values of liquid viscosity, density, surface tension and static pressure were chosen to be characteristic of this liquid.

Figure 1.1 shows the radius time profile for stable cavitation. The bubble expands and contracts in a periodic fashion. In this simulation the initial bubble radius was set to 10 µm with an applied zero-to-peak pressure amplitude of 80 kPa and the drive frequency, *f*, was 22.8 kHz. A zero-to-peak pressure amplitude of 80 kPa was deployed as this value was below the threshold value for observing transient cavitation.

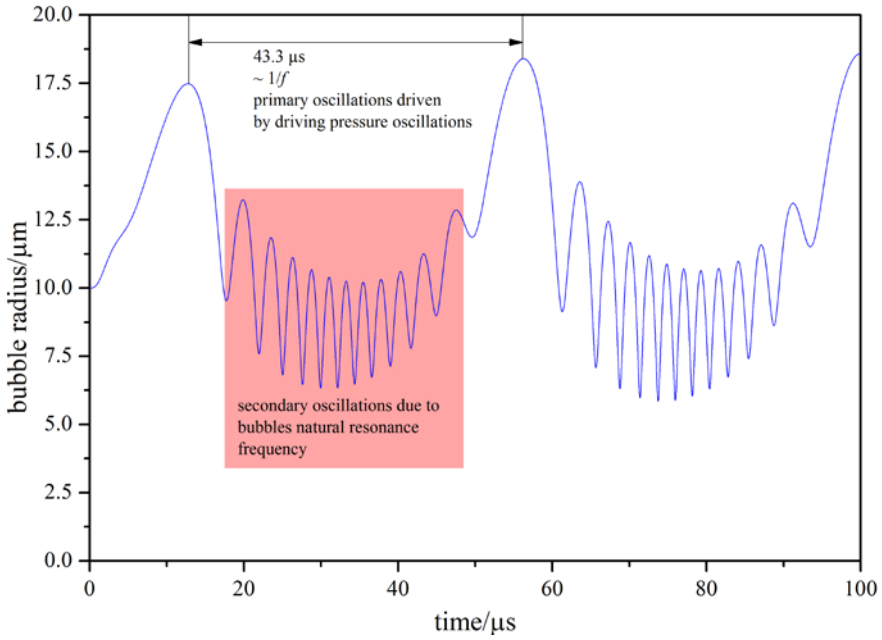

Figure 1.1 Plot showing the radius time profile for an initial 10 µm radius bubble (—), during stable cavitation. The applied zero-to-peak pressure amplitude was 80 kPa and the drive frequency was 22.8 kHz. The viscosity of the liquid was 0.000891 kg m^{-1} s^{-2}, the density was 990 kg m^{-3} and the surface tension 0.073 N m^{-1}. The static pressure was 101 kPa and vapour pressure 3.5 kPa.

Two periods of oscillation can be seen in this radius time profile. First, the peaks of maximum bubble radius indicated in Figure 1.1 have a peak separation of 43.3 µs. This is equal to the time period for oscillations at 23 kHz. This is approximately equal to the drive frequency of 22.8 kHz, hence showing that the frequency of bubble oscillations are driven by the external drive frequency. Second, the smaller oscillations in bubble radius (highlighted by the red box in Figure 1.1) have an average peak separation of 2.5 µs equivalent to a frequency of oscillation of 400 kHz. This higher frequency oscillation is the bubble oscillating at its resonance frequency. The resonance frequency of the bubble will depend of the bubble radius with the resonance frequency increasing with decreasing initial bubble radius[5].

In transient cavitation, the bubbles expand to a maximum size then rapidly collapse[5]. This occurs when a higher amplitude pressure field is applied to the bubble[5]. During the tension phase of the acoustic wave, the application of the pressure field on the gas bubble causes the bubble to expand. The bubble then has a large amount of ‘elastic’ energy stored in the expanded bubble and collapses violently[5]. The high energy collapse of the bubble is able to generate a range of observable effects such as erosion and sonoluminescence[5, 39].

Figure 1.2 shows the radius time profile for the case where transient cavitation is generated. In order to move across the threshold level for observation of transient bubble

behaviour, a greater zero-to-peak amplitude of 200 kPa was deployed. Again the initial bubble radius was set to 10 µm and the drive frequency was maintained at 22.8 kHz.

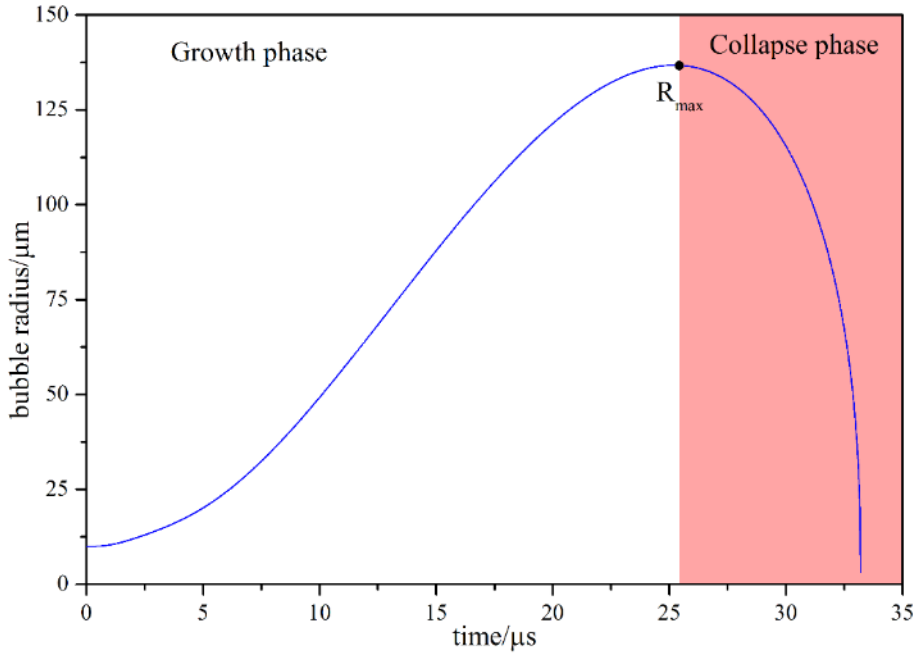

Figure 1.2 Plot showing the radius time profile for an initial 10 µm radius bubble (—), during transient cavitation. The applied zero-to-peak pressure amplitude was 200 kPa and the drive frequency was 22.8 kHz. The viscosity of the liquid was 0.000891 kg m-1 s-2, the density was 990 kg m-3 and the surface tension 0.073 N m-1. The static pressure was 101 kPa and vapour pressure 3.5 kPa.

The radius time profile shown in Figure 1.2 for the transient bubble shows that the bubble grows in size until it reaches a maximum, labelled R_{max}. After reaching this maximum radius the bubble rapidly collapses (collapse phase lasts for ~ 8 µs in Figure 1.2).

There are a number of factors affecting whether a bubble will undergo transient cavitation[40]. Consequently the threshold conditions for transient cavitation have been studied by a number of authors[41,42]. The simplest of these models states that there is a minimum acoustic pressure amplitude, the Blake pressure[5] (P_B), below which transient cavitation will not be observed. The Blake pressure is given by equation 1.2

$$P_B = p_o + \frac{8\sigma}{9}\sqrt{\frac{3\sigma}{2r_B^3\left(p_o + (2\sigma/r_B)\right)}} \qquad (1.2)$$

where r_B is the Blake radius (threshold value of equilibrium bubble radius, r_o, below which the bubble will not grow explosively), p_o is the hydrostatic liquid pressure outside the bubble and σ is the surface tension of the liquid. It should be noted however that this model neglects the inertial and viscous effects on the bubble[43]. As such the model cannot be

applied to all systems and can only be applied to quasi-static processes (where the system changes slowly enough to remain in internal equilibrium)[43]. Cavitation is also often induced by stimuli present in the solution such as particles in solution or microbubbles[44], or surface defects in the vessel in which the liquid is contained[45]. Thus the model used to predict the threshold for transient cavitation must account for such stimuli (e.g. pre-existing microbubbles). One such model is presented by Holland and Apfel[8]. Their model predicts the cavitation threshold assuming that there are suitable gas bubbles in the liquid. The variation in threshold pressure with the radius of the stimuli was predicted using this model. From their calculations it was suggested that for smaller stimuli the threshold pressure is close to that predicted by the Blake pressure as the bubble motion is dominated by surface tension effects for smaller nuclei. As the size of the nuclei increases the predicted threshold deviates more from the Blake threshold as viscous and inertial effects now dominate the bubble motion[8]. Flynn[44] also showed that the cavitation threshold depended not only on the pressure applied to the bubble but also relied on the bubble radius (R) lying within a critical size range 0.063 μm < R < 0.13 μm.

The results of these simulations show the expected bubble radius response in both stable and transient cavitation cases. In attempting to characterise cavitation bubbles and their associated effects it is important to note the short time frame of the bubble wall oscillations. The techniques used in the characterisation of such cavitation activity must therefore take this into account. The following section will discuss the characterisation methods most commonly employed in greater detail.

1.3 Characterisation techniques

The general physical and chemical effects generated by cavitation are well-known and documented. However, analytical quantification of the effects of cavitation produced by ultrasound has proved to be more difficult[20]. There are a number of reasons for this, key among these is that the processes involved generally occur over a very short time period and their effects are extremely localised[46]. Isolating individual events is also a recognised issue, as the events usually occur in clusters, obscuring the field of vision making visual observation difficult[6]. In the case of cavitation driven by tension setup in a liquid, for example with high power ultrasound, techniques used to monitor pressure fields can be difficult to use as the cavitation activity can cause damage to the sensors[47]. Another issue encountered with these measurement techniques is that the bubbles generated can scatter

the acoustic signal produced by the source, which is the object of the investigations[47]. In the following section, some of the key characterisation methods will be highlighted and their advantages and disadvantages as techniques discussed.

1.3.1 High-speed imaging

In order to attempt to create a more complete characterisation of cavitation and its associated effects, a number of experimental approaches have been employed. One such technique is high-speed imaging[4]. Philipp and Lauterborn used a high power laser to produce single cavitation bubbles[4]. The presence of shockwaves in cavitation bubble collapse, due to the strong compression of the bubble contents, have been known about since the first theoretical work performed by Rayleigh[48]. The first experimental evidence for these shockwaves was provided using acoustic measurements by Harrison[49] and by Güth[50] employing a schlieren technique to visualise the shockwave. The schlieren technique is an optical technique which is used to highlight changes in refractive index which occur as a result of heating, pressure changes or concentration changes in a liquid[51].

By employing high-speed imaging as their chosen technique, Philipp and Lauterborn were able to map the whole life cycle of the bubble during growth and collapse[4]. Showing in detail the shape of the bubble as these shockwaves were emitted in the bubble collapse[4]. These shockwaves were particularly prominent when the sound field in which the bubble collapsed in was not spherically symmetrical, for example a bubble collapsing near a solid flat surface[4]. This environment causes a high-speed jet to form as the bubble collapses[4]. A cartoon representation of the mechanism for bubble collapse and high-speed jet can be seen in Figure 1.3.

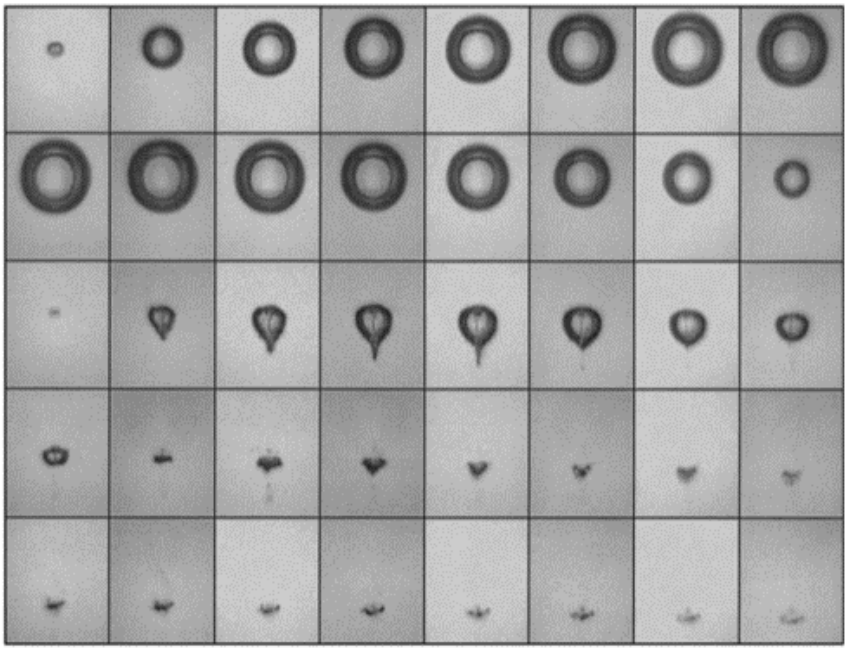

Figure 1.3 A series of high-speed images of a laser-induced cavitation bubble showing the principle stages of bubble collapse close to a fixed wall (located below the bubble in the images shown). Reproduced with permission from ref.[1] Copyright 1998, Journal of Fluid Mechanics.

The images shown in Figure 1.3 show the key stages of cavitation bubble growth and collapse for a single cavitation bubble generated using a high powered laser. The cavitation bubble was produced near a solid surface (below the bubble in the images shown). The sequence of images shown was created by recording multiple individual sequences with different bubbles. For each new sequence recorded the moment at which the recording was triggered was shifted to increase the apparent frame rate of the final image sequence. This was possible as the method for generating cavitation bubbles was reproducible enough that each bubble generated was almost identical in size. The bubble reaches a maximum size (in the second row of images, with a maximum bubble radius of 1.45 mm) and then collapses. In the collapse a micro-jet forms travelling towards the solid surface below the bubble (seen in the third row of images).

These studies have been useful in showing the collapse mechanism of the collapsing bubble. The jet formed by the collapsing bubble releases a number of shock waves which are thought to be responsible for many of the observed effects of cavitation, such as sonoluminescence and erosion/corrosion of a surface. For example, this phenomenon has been employed in microsurgery where laser-produced cavitation acts to selectively remove cell tissue[52]. With proper control of the laser equipment employed to induce the cavitation (pulse energy, location of the focal point of the laser beam) and owing to the localised

nature of the cavitation effects themselves this technique could be very precisely controlled[52]. The process of removing the unwanted skin cells was also very rapid[52].

In other methods for generating cavitation, such as the acoustic source investigated in this thesis, single bubble generation is not possible and bubbles are generated in groups or 'clusters'. Where cavitation is generated in clusters of bubbles, high-speed imaging can be less useful for revealing mechanistic details of the bubbles, as it is difficult to isolate individual bubbles. Therefore, other methods must be considered to monitor the activity of cavitation bubbles.

Other commonly used approaches include using the cavitation to stimulate a chemical reaction and using analysis techniques to detect the formation of the products[53]. Other analysis techniques include taking acoustic measurements[47], studies of surface damage[5] and electrochemical studies[23,24]. Further details of some of these acoustic and electrochemical studies will be discussed in the following sections.

1.3.2 Acoustic measurements

Many studies into cavitation involve acoustic measurement as it has been shown that the bubbles generated in this manner act as secondary acoustic sources[5,54]. Features of the acoustic emissions from cavitation bubbles are correlated with bubble oscillation. Hence, the acoustic emissions of cavitation bubbles are used to elucidate information about bubble dynamics[2]. The oscillation of cavitation bubbles occurs on a microsecond timescale and so an acoustic sensor must have a fast response time to record this dynamic activity.

Acoustic measurement of cavitation generally involves the use of hydrophones made from piezoelectric materials within the cavitation liquid. One issue therefore with such acoustic measurements is that the violent nature of bubble collapse by inertial cavitation bubbles can cause damage to the sensor material. Consideration must therefore be given to the positioning or design of the hydrophone or similar sensor to minimise the amount of damage to the sensor. The design of a sensor suitable for measuring emission from acoustic cavitation must therefore include shielding material to protect the piezoelectric material. Thought must also be given to the acoustic properties of the shield material and of the shape of the sensor itself so as not to impede the acoustic field generated inside the reaction vessel[54]. The size of the sensor also results in a degree of spatial averaging as the sensor itself occupies a relatively large volume (several cm^3).

It is also important to consider the spatial variation of cavitation activity over the cell or vessel in which cavitation is being observed. In most experimental setups used to generate cavitation the energy output cannot be assumed to be homogenous across the entire volume of the vessel. For example, for cavitation generated in a vessel by an ultrasonic sound source, This is because the intensity of the energy at a particular point comprises of both the energy intensity due to the driving ultrasonic field and cavitation energy of the bubbles themselves[55,56]. The distribution of the bubbles within the vessel continuously changes with the propagation of the acoustic wave. Thus the measured acoustic intensity has spatial variation. Therefore rather than a single sensor, multiple sensors may be used in an array to take into account the variation in cavitation energy with spatial position[57].

To elucidate mechanistic information from the hydrophone data collected the acoustic data is often processed to produce a frequency spectrum. The behaviour of a single, stable bubble has been used to model the key features of such a spectrum[58,59]. An example of a typical measured acoustic spectrum, produced by Hodnett *et al.*[33] in an ultrasonic cleaning vessel operating at 40 kHz, is shown in Figure 1.4. This spectrum contains a range of signals of different frequencies. The different frequencies contained within this spectrum indicate the types of oscillation the cavitation bubble is undergoing.

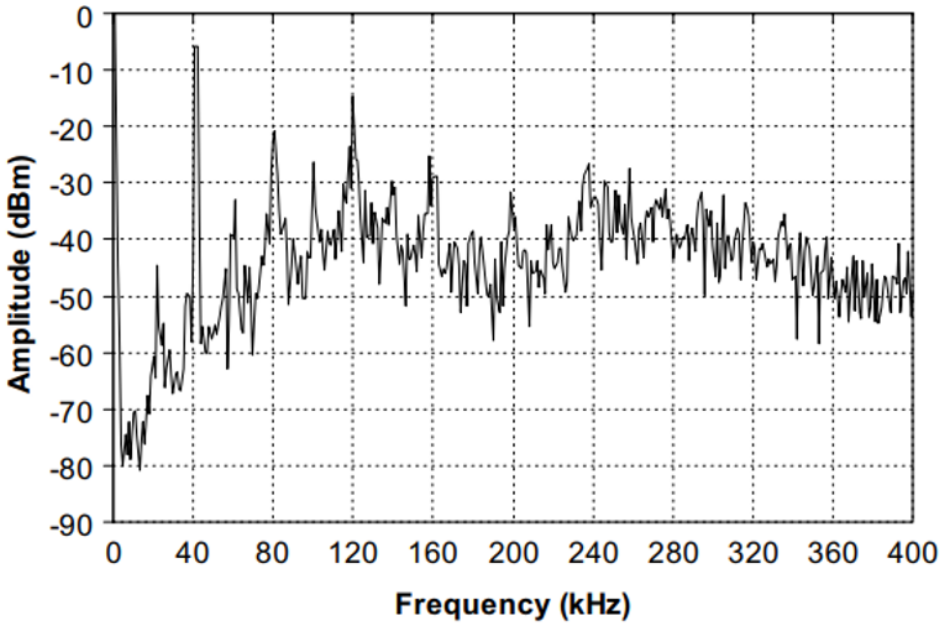

Figure 1.4 An example of a typical emission spectrum from a vessel in which cavitation is generated. The source used to generate the cavitation is an ultrasonic transducer operating at 40 kHz. The output is measured by an underwater acoustics hydrophone. Reproduced with permission from ref.[33] Copyright 2004, Ultrasonics Sonochemistry.

The first signal contained within this spectrum (Figure 1.4) is the fundamental frequency, f_0 at approximately 40 kHz. This frequency is produced by both the driving ultrasonic source and also to a lesser extent by linear oscillations of the cavitation bubbles[5,33]. Second, harmonics of the fundamental frequency are observed (qf_0, where q is a whole integer) resulting from non-linear bubble oscillations[43], and by harmonic signals of the transducer itself[33]. Third, subharmonics of the fundamental frequency (f_0/n, where n is a whole integer). In Figure 1.4 the 20 kHz signal can be clearly observed[33]. This signal is either interpreted as the linear oscillation of a bubble of twice the resonance size of the 40 kHz bubble or as an indication of the onset of inertial cavitation activity[43]. Similar physical interpretations are given to ultraharmonics of the fundamental (mf_o/p, where m and p are both integers, $m > p$ and m/p is not an integer)[5,33]. Finally a broadband (noise) signal is observed, generated by the shockwaves emitted upon bubble collapse.

Other acoustic studies have used a combination of acoustic bubble emission with other measurement techniques to elucidate information about bubble dynamics. One such study was performed by Matula *et al.*[34]. In this study single bubbles were held in an acoustic trap with a driving frequency of 33.8 kHz. The acoustic emissions of the bubble were measured using a transducer focussed at 10 MHz as a hydrophone. The transducer output showed that the acoustic emission occurred in four pulses, the main bubble collapse and three

rebound pulses. The acoustic output is shown in Figure 1.5 (reproduced from paper by Matula *et al.*[34]).

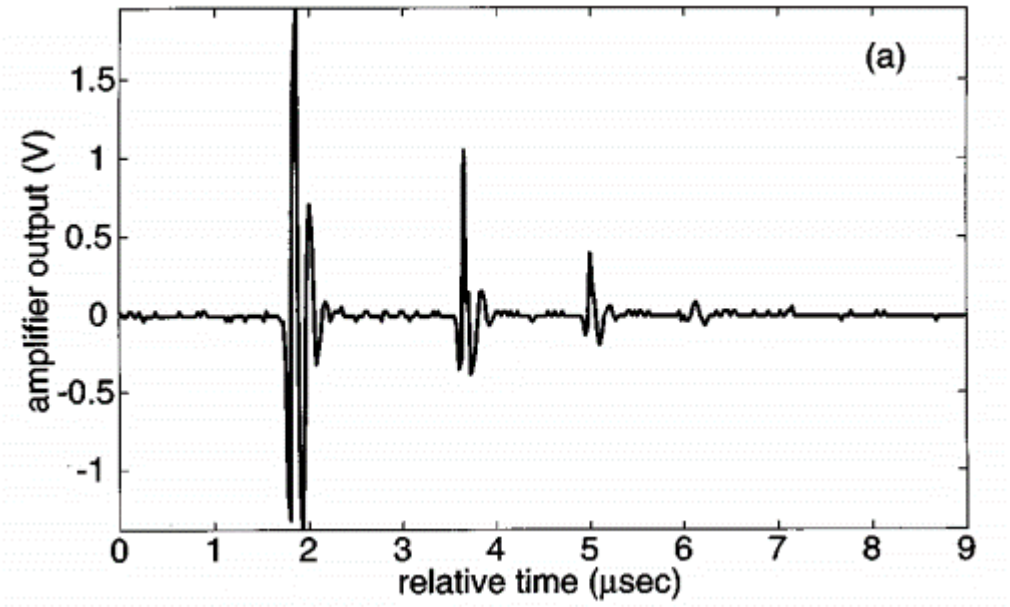

Figure 1.5 Pressure pulses from a single trapped bubble obtained by a hydrophone focussed at 10 MHz acting as a hydrophone. The fast oscillations are due to the ringing of the hydrophone. Reproduced with permission from ref.[34] Copyright 1998, Journal of the Acoustical Society of America.

The acoustic emission of this bubble was directly correlated to the bubble motion by the simultaneous use of a light scattering technique, details of this method are described elsewhere[60,61]. The amplitude of the laser scattering signal can be correlated with the radius of the cavitation bubble. Thus it was shown that the acoustic emission occurs as the bubble reaches a minimum radius. The light-scattering signal and corresponding acoustic data is shown in Figure 1.6.

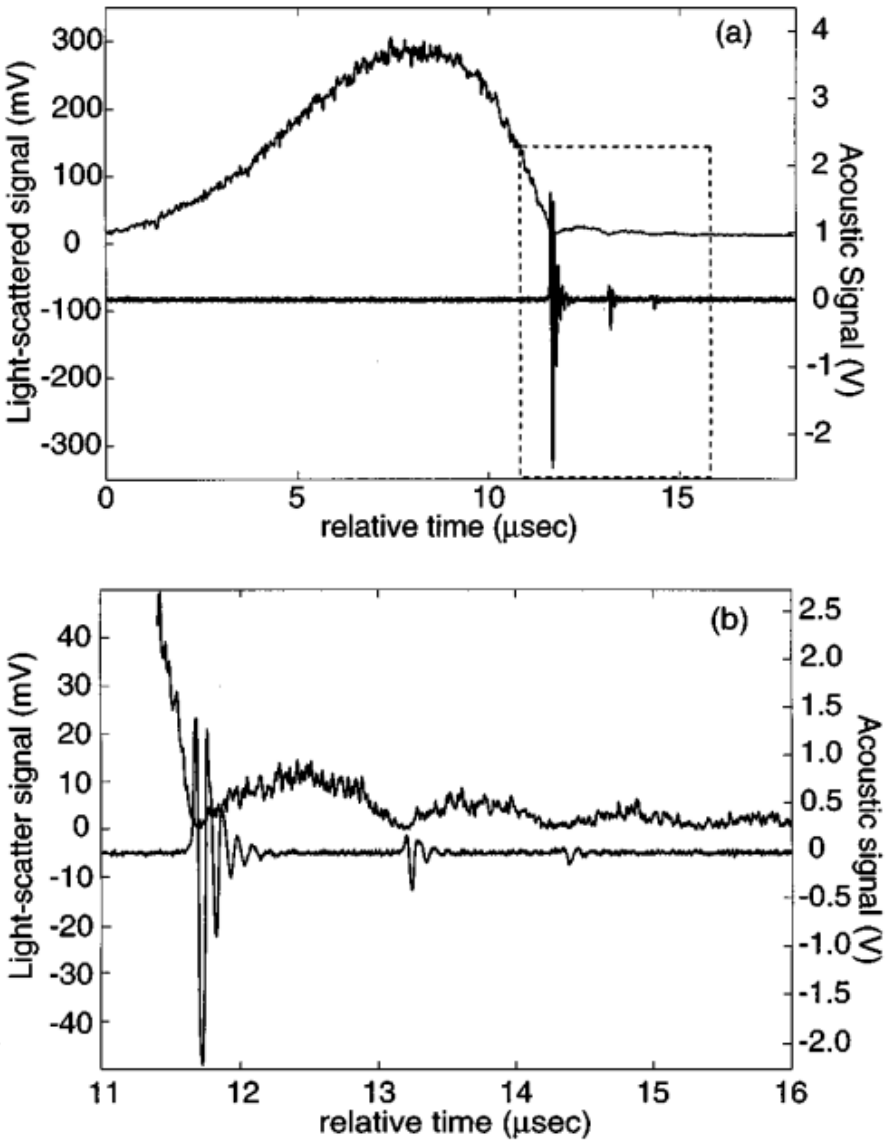

Figure 1.6 Bubble oscillation curve measured by light scattering (upper curve) along with the accompanying acoustic emission measured by the 10 MHz focussed transducer (lower curve). (b) Shows a detailed view of the boxed area in (a). Reproduced with permission from ref.[34] Copyright 1998, Journal of the Acoustical Society of America.

The criteria for a suitable acoustic sensor detailed above makes it challenging to measure cavitation activity using acoustic sensors. In order to be positioned close enough to the source of the activity without impeding the acoustic field the sensors used are often small in size and over time the fragile piezoelectric material is eroded by the cavitation activity. The sensors cannot therefore be used for long periods of time as the sensor itself is eventually destroyed by the cavitation it is recording.

One alternative sensor to acoustic sensors is to use electrodes to measure cavitation activity electrochemically. Electrodes are at an advantage as a sensor as although they too can be eroded by the cavitation activity, this can be minimised by the choice of electrode material.

Also after the surface of an electrode is roughened by cavitation it can still be polished back to a flat surface and used again as a sensor. This means the lifetime of an electrode as a sensor can be longer than the piezoelectric material of an acoustic sensor. The details of a few studies employing electrochemistry to monitor cavitation will be discussed in the following chapter.

1.3.3 Electrochemical studies

Electrochemistry is noteworthy among the techniques currently used to characterise cavitation activity[23,24]. Data from electrochemical techniques can be used in three principal areas of investigation, characterisation of surface damage[13,62], mass transfer of material[24,63,64] and chemical change[65]. Although the experimental techniques developed by a number of authors are powerful, they only provide additional evidence for the effects that are taking place, as the systems at work are complex in nature[66]. Hence it is normal to combine any physical/chemical measurement with complementary studies such as microscopy images of the electrode surface to fully elucidate the effects that are taking place within the system[24]. In the following section, a few different electrochemical approaches to studying cavitation are outlined along with the complementary studies performed.

An example of one such electrochemical investigation involves electrochemically monitoring the cleaning of micropores by an ultrasonic horn acting as a piston-like emitter (PLE)[32]. In this study recessed microelectrodes with diameters between 0.5 mm and 0.05 mm were fabricated. The recesses were filled with an electrochemically inactive contaminant material and the current between the recessed working electrode and platinum gauze counter electrode was monitored as function of time as the pore was cleaned with the piston-like emitter. As a comparison to cleaning using ultrasonic cavitation the pores cleaning using fluid flow from a pump was also investigated. This investigation found that the ultrasonic cavitation was much more effective at removing the contaminant than bulk fluid flow. A figure illustrating the difference in cleaning using ultrasound and fluid flow is shown in Figure 1.7[32].

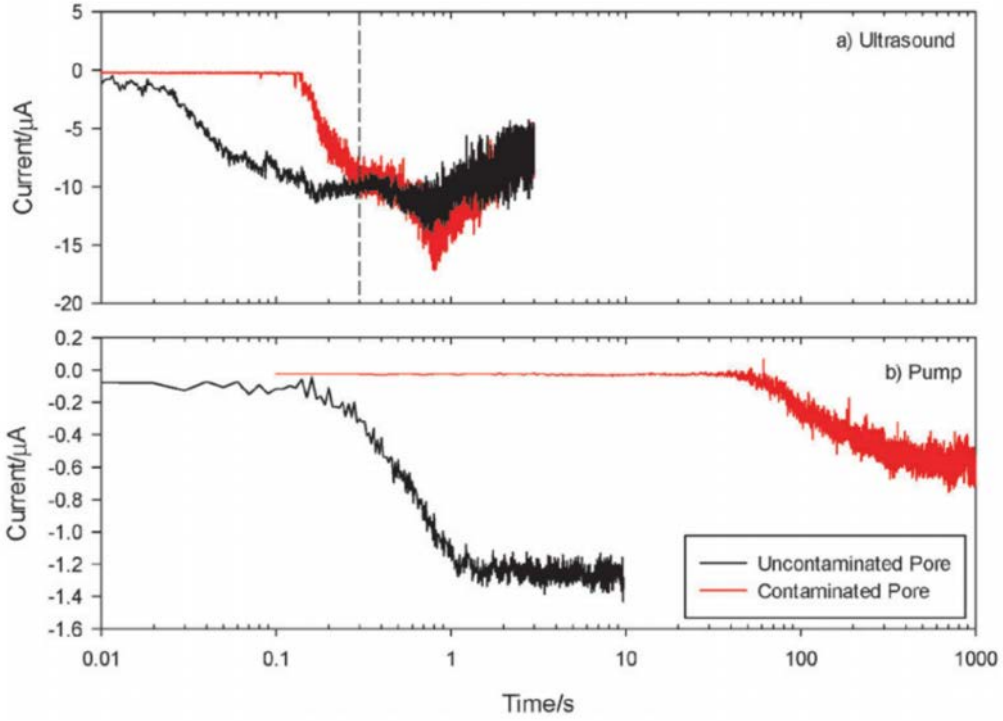

Figure 1.7 Plots of electrode current recorded as a function of time for a platinum electrode at the base of uncontaminated (—) and contaminated pore (—) (500 μm x 400 μm). The pores are exposed to ultrasound (a) and fluid flow from a pump (b). The distance between the pore and PLE or pump nozzle was 5 mm and the experiments were performed in a solution of 5 mM $K_3Fe(CN)_6$ and 0.1 M $Sr(NO_3)_2$ in an emulsion of water and F54 surfactant. Reproduced with permission from ref.[32] Copyright 2014, Physical Chemistry Chemical Physics.

Figure 1.7 shows a comparison in the currents measured at the electrode inside the pore in the presence (—) and absence (—) of contamination inside the pore. In Figure 1.7 (a) the pore is exposed to ultrasound by a PLE and in Figure 1.7 (b) the pore is exposed to fluid flow by a pump. In all cases the PLE tip or pump nozzle was placed at a distance of 5 mm from the pore. For the uncontaminated pore exposed to ultrasound (—, Figure 1.7 (a)) the current is observed to increase between t = 0.02 and 0.03 s (note logarithmic scale employed for time scale). The current at the electrode is then seen to reach a stable value at t = 0.03 s. After t = 0.03 s the current oscillates considerably, an indication of bubble entrapment inside the pore. For the contaminated pore exposed to ultrasound (—, Figure 1.7 (a)) the current remains at 0 until t = 0.15 s when the current increases, reaching the same plateau current value as the uncontaminated pore exposed to ultrasound at t = 0.3 s.

The current response to the flow from the pump (Figure 1.7 (b)) also shows an increase in current with the application of flow. For the uncontaminated pore (—, Figure 1.7 (b)) the current begins to increase at t = 0.2 s, reaching a plateau at t = 1 s. As bubble entrapment is

not a concern with the fluid flow from the pump oscillation the oscillation in current is not observed in Figure 1.7 (b). For the contaminated pore exposed to fluid flow from the pump (—, Figure 1.7 (b)) the current recorded remains essentially 0 until t = 40 to 50 s. The current then increases slowly and by t = 1000 s it has still not reached the plateau current value seen for the uncontaminated pore under the same conditions (—, Figure 1.7 (b)). This is an indication that the pore still contains some contamination material. These results indicate that the ultrasound is more effective at removing the contamination from the pore than bulk fluid flow alone.

Complementary results to the electrochemical experiments here were provided by high-speed imaging of the pores during exposure to ultrasonic cavitation, showing how the material was removed from the pore by the action of the cavitation bubbles generated.

As well as measuring the erosion of electrode material, cavitation can also be employed to enhance chemical kinetics. An example of this is in the use of high-intensity ultrasound to increase electron transfer rates on glassy carbon electrodes[24]. In investigations carried out by Zhang and Coury, the electrochemical activity of glassy carbon electrode surfaces was increased by ultrasonic irradiation of the electrodes in a thermostatically controlled sonication cell[24]. The electrodes were irradiated in different solvents and the rate of heterogeneous electron transfer for various redox reactions recorded before and after the sonication of the electrodes[24]. These investigations found that heterogeneous electron transfer rate at the glassy carbon electrode increased after sonication in dioxane, but did not improve after sonication in water. This was thought to be because sonication with the organic solvent was able to remove powdered carbon and organic binder materials introduced to the electrode surface in the procedure to polish the electrodes[24].

Acoustic cavitation was also used to catalyse the production of hydrogen peroxide in aqueous citric acid solutions in a 5.5 pH citrate/phosphate buffer solution[53]. The reaction itself was carried out inside a cylindrical sonochemical reactor, attached to a flow cell[67,68]. Electrochemical measurement of the products of the reaction was contained within the flow cell. This setup had a number of advantages. First, the mass transfer coefficients within the flow cell are steady state and well characterised[53]. Second, the disturbance of the sound field on the electrodes was kept to a minimum so effectively eliminating the likelihood of high localised rates of mass transfer or erosion of electrodes[13,69]. This system

has been used in a number of other successful studies employing sonochemical reactions[67,68].

The investigation found that production of $OH^{\bullet}$ required a minimum acoustic pressure threshold above this threshold the rate of peroxide generation increased with increasing acoustic pressure and then reached a plateau level. The maximum rate of peroxide generation at this plateau level was around 120 nmol dm^{-3} h^{-1} at an acoustic pressure amplitude of 3.2 bar[53]. This rate was a factor of ~ 5 greater than the maximum rate reported elsewhere in the literature[70].

Electrode arrays have been shown as a useful and effective tool for studying the effects of cavitation. By employing electrode arrays the spatial extent of the bubble activity from the energy source can be investigated[71]. Maisonhaute *et al*. showed how electrode arrays can be employed to characterise the bubbles (size and shape) and interaction between the bubbles and electrode surface[71,72]. In the novel and ground-breaking research performed by Nyborg *et al.*[73,74], an array of band electrodes (down to 200 µm in width) was employed to investigate the mass transfer of material caused by microstreaming from an acoustic source[73]. This was achieved by placing the electrode array beneath an oscillating piston-like sound emitter. It was observed that a large amount of liquid motion occurred when stimulated by the acoustic source if the liquid contained small pockets or bubbles of gas, but not if the gas was excluded from the liquid[74]. Potential *vs.* time curves were recorded in oxygen-saturated solutions both with and without acoustic stimulation to examine the extent to which the acoustic source enhanced the mass transfer. In addition, the spatial extent of microstreaming on mass transfer was also examined. The investigations concluded that mass transport at the surface (dn/dt) was enhanced by the acoustic source and that the enhancement in mass transport was proportional to the oscillation-velocity amplitude A[73].

The effect of bubbles on mass transfer has also been widely reported, notably in a set of studies by Tobias *et al.*[75,76]. An assessment of the effect on mass transfer was carried out using a microelectrode array (micromosaic electrode, MME) developed by Dees and Tobias[77] (Figure 1.8). Using this array the authors were able to assess how electrochemically produced bubbles could be used to enhance the mass transfer coefficient at the electrodes in the array[76,78]. They concluded that the rising stream of gas bubbles enhanced the mass transfer at the electrode surface by renewing the material present at the

electrode surface. Therefore it is the frequency at which the bubbles passed the electrode surface, rather than the velocity or bubble size, which determines the level of mass transfer enhancement[76].

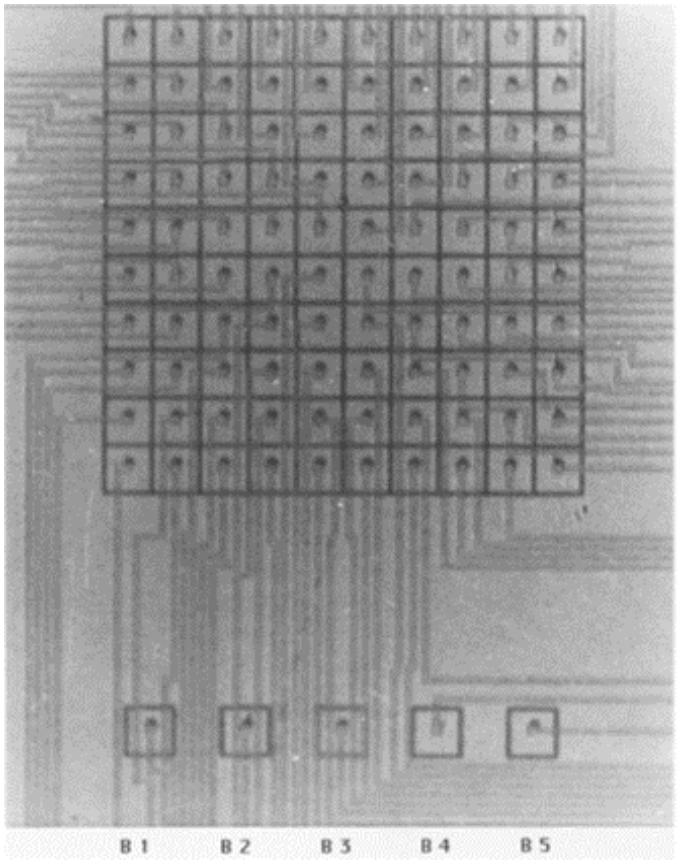

Figure 1.8 Scanned image of a micromosaic electrode used by Tobias *et al.*, to investigate the mass transfer contributions of bubble activity. The five generator 'satellite' electrodes (labelled B1 – B5) were used to electrochemically produce the gas bubbles below the 10 x 10 array of mass-transport sensing electrodes Reproduced with permission from ref.[76] Copyright 1994, The Electrochemical Society.

Through the use of analytical techniques described above, much has been discovered about the mechanisms behind cavitation. However, much like acoustic measurement studies, none of the electrochemical techniques commonly in use are able to provide a full explanation of the mechanisms in isolation.

It became clear that there was a need for an alternative technique, capable of presenting a more complete description of the cavitation bubble dynamics. The analysis techniques employed in this report aim to provide this broader understanding of the cavitation systems. Many of the investigations in this report focus on the use of an AC impedance analysis technique. The advantages of this technique, provided a suitable model for the electrochemical cell can be adopted, are that it allows for simultaneous measurement of uncompensated resistance[79], the surface capacitance and Faradaic current passed at a single

electrode. It has also shown to be able to resolve these parameters on a microsecond timescale. This was important, as the transient events observed in cavitation occur over very short time periods. The details of the technique developed will be discussed further in Chapter 2.3.

1.4 Time-dependent Impedance studies

There have been a small number of studies carried out to develop time-dependent impedance techniques, in other words, impedance techniques which can be used to measure impedance changes as a function of time. This is very useful for measuring dynamic information about the bubble activity over the electrode used as a sensor, giving information about the cavitation bubble position, velocity and size over the data capture period chosen.

The impedance of an electrochemical cell can be measured using a few different experimental methods. One early method developed for measuring cell impedance is to employ a circuit known as a Wheatstone bridge[80]. A typical example of such a circuit setup as used to measure impedance is shown in Figure 1.9[80,81].

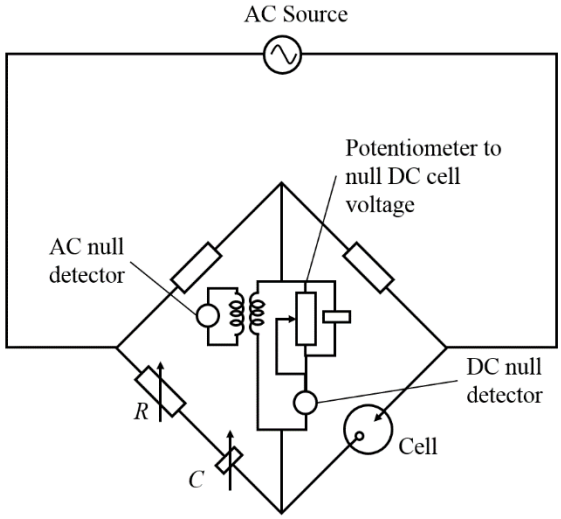

Figure 1.9 A diagram showing a Wheatstone bridge arrangement for measuring electrochemical cell impedances. The dc null detector is a sensitive galvanometer and the ac detector is an oscilloscope or ac microvoltmeter. Adapted from ref.[80].

In this arrangement, the cell is inserted into one arm of a diamond shaped circuit and the resistance and capacitance of the cell is balanced by a variable resistor and capacitor on the opposite arm of the bridge[81]. Both *R* and *C* have to be balanced at the same time as each other. Thus the balancing process is achieved using an iterative process in which *R* and *C* are repeatedly adjusted successively until the ac signal minimum is reached[80]. This is a

slow process, and so this approach is usually applied to static or slow changing systems[80]. There is also a restricted frequency range on this circuit arrangement and cannot be used below approximately 10 kHz[80].

A slightly modified version of this circuit arrangement was used by Case and Nagel to develop a time-dependent AC impedance technique[82,35]. This technique was used to investigate the early stages of coalescence between two drops of a low viscosity liquid[83,84]. An AC potential perturbation of frequency *f*, where *f* was varied between *f* = 10 kHz and *f* = 10 MHz, and magnitude |V| was applied across two electrodes inside the fluid droplets. The lower drop was grown at a slow fixed rate until the two droplets coalesced. The impedance of the cell electrochemical cell, Z_{cell}, was evaluated by the circuit shown in Figure 1.10[35]. The opposite arm of the bridge to the electrochemical cell has a known impedance, Z_t, and this was connected in series with the measurement device. The other two arms of the bridge, Z_0, are the effective input impedance of the measurement device (a high-speed DAQ system). The voltage was measured at two points, between Z_t and Z_0 (V_r) and between Z_{cell} and Z_0 (V_s). The voltages V_r and V_s were sampled at a sample rate of 10 times the frequency of the applied AC potential perturbation (10*f*) except for *f* = 10 MHz where a sample rate of 60 MHz, the maximum allowed by the measurement device, was used[35].

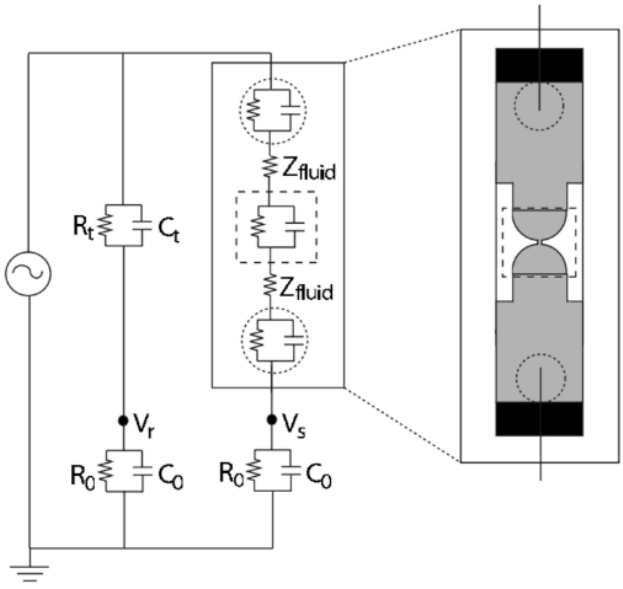

Figure 1.10 The Wheatstone bridge measurement circuit. The upper left branch is composed of known circuit elements (R_t and C_t) and the lower two branches are the input impedance of the measurement device (R_0) in parallel with the capacitance of the coaxial cables connecting the circuit to the measurement device (C_0). The potential is measured between Z_t (R_t and C_t) and Z_0 (R_0 and C_0) at V_r and between Z_{cell} and Z_0 at V_s. Reproduced with permission from ref.[35] Copyright 2009, Physical Review E.

By sampling the voltage at both V_r and V_s the ratio of their amplitudes, $|V_r|/|V_s|$, could be calculated. Both AC signals were also compared to a known sine wave to calculate the relative phase shift of each signal. From this the phase shift between the two voltage signals, $\Delta\phi$ was also calculated. The measured values $|V_r|/|V_s|$ and $\Delta\phi$ and the known quantities Z_t and Z_0 can then be used to calculate the unknown Z_{cell} using the complex equation (1.3)[35],

$$\frac{|V_r|}{|V_s|} e^{-i\Delta\phi} = \frac{|Z_{cell}+Z_0|}{|Z_t+Z_0|} e^{-i\Delta\phi} \qquad (1.3)$$

This equation can be divided into real and imaginary components and solved for Z_{cell} given by equations 1.4 and 1.5[35],

$$\mathrm{Re}(Z_{cell}) = \frac{2|V_r|}{|V_s|}\{[\mathrm{Re}(Z_0)+\mathrm{Re}(Z_t)]\cos\Delta\phi - [\mathrm{Im}(Z_0)+\mathrm{Im}(Z_t)]\sin\Delta\phi\} - \mathrm{Re}(Z_0) \qquad (1.4)$$

$$\mathrm{Im}(Z_{cell}) = \frac{2|V_r|}{|V_s|}\{[\mathrm{Re}(Z_0)+\mathrm{Re}(Z_t)]\sin\Delta\phi - [\mathrm{Im}(Z_0)+\mathrm{Im}(Z_t)]\cos\Delta\phi\} - \mathrm{Im}(Z_0) \qquad (1.5)$$

As Z_t was a fixed impedance, the data capture (i.e. the speed at which the critical values of R_{cell} and C_{cell} could be evaluated) was not limited by the speed at which Z_t could be matched to Z_{cell} (as in the traditional bridge approach – see Figure 1.9). Hence, under these conditions the effective data capture rate was limited by the measurement device employed (i.e. if the data was captured at 60 MHz, the rate would be 16.7 ns). The device employed to capture the data was able to sample at high frequencies it was therefore possible to make high-speed recordings of cell impedance. It should be noted that care must be taken in setting up the circuit in order for this method to work successfully. In the lower two branches of the circuit, Z_0 is matched by choosing two coaxial cables with the same capacitance. Even a slight mismatch in the capacitances of these two cables would result in unequal impedances in the lower two branches of the circuit and the calculation used to evaluate Z_{cell} is no longer accurate.

An alternative method for determining electrode impedance as a function of time was presented by Fransaer *et al.*[36]. In these studies, a time dependant impedance technique was used to measure changes in electrolyte resistance due to insulating spheres approaching a microelectrode[79,36,85]. Measurements were made using a bespoke designed device to measure electrode potential and resistance simultaneously. The technique and device devised to measure changes of resistance as a function of time, devised by Huet *et al.*[86],

relied on separating the Ohmic and Faradaic components of the potential response and comparing the two responses to determine the resistance changes. Using this technique, resistance time data could be recorded as fast as 1 ms (sample rate of 1 kHz)[86]. As a starting point, the potential measured across working and reference electrodes, *V*, was considered for a typical electrochemical setup given by equation 1.6,

$$V = E + RI \tag{1.6}$$

where *E* is the electrode potential, *R* the solution resistance and *I* the mean dc current. Starting from equation 1.4, the potential response when the electrochemical cell is under galvanostatic control was then considered. Under such conditions events such as bubble detachments are often observed, giving rise to fluctuations in the applied and measured potential as well as the effective solution resistance, as described by equation 1.7,

$$\Delta V(t) = \Delta E(t) + \Delta R(t).\mathrm{I} \tag{1.7}$$

where $\Delta V(t)$, $\Delta E(t)$ and $\Delta R(t)$ are fluctuations in voltage, electrode potential and solution resistance as a function of time. To this electrochemical system, an AC current perturbation ($i_{100}(t)$) was then applied. A high frequency current perturbation of 100 kHz was chosen so that the impedance measured, *Z*, was equivalent to *R* under this high-frequency regime (note this will be highly dependent on the choice of electrode and electrolyte as will be shown later in the results chapters of this thesis). The applied current, i_{100}, was equivalent to

$$i_{100}(\mathrm{t}) = I_{100}\sin(\omega t) \tag{1.8}$$

where I_{100} is the amplitude of the perturbation (chosen to be small enough that the potential amplitude v_{100} was ~ 50 mV) and ω is the angular frequency. Hence the voltage measured across the working and reference electrode was

$$V + \Delta V(t) + v_{100}(t) \tag{1.9}$$

where *V* is the mean voltage, $\Delta V(t)$ the voltage electrochemical noise and $v_{100}(t)$ the sine wave component at 100 kHz

$$v_{100}(t) = RI_{100}\sin(\omega t) \tag{1.10}$$

The device devised for recording resistance changes as a function of time made use of the relationship between the potential response recorded at the reference electrode and the current perturbation as described in equations 1.6 – 1.9. The circuit setup for this device is shown in Figure 1.11. In this circuit setup the potential response was divided into two signals by a series of different high and low-pass filters (as seen in Figure 1.11). The first signal channel is described at the 'potential' channel, in which the voltage electrochemical noise, $\Delta V(t)$, is amplified by a gain (G) and 100 kHz frequency component, $v_{100}(t)$, was eliminated by a low pass filter (filters out high-frequency components). The voltage measured therefore at point A (Figure 1.11) is $G\Delta V(t)$. In the second channel, known as the 'electrolyte resistance' channel, the input voltage is amplified and $\Delta V(t)$ eliminated with a high-pass filter (cut-off at 20 kHz). The sine wave component $v_{100}(t)$ was then rectified by a diode and low-pass filter (cut off 10 kHz). The voltage recorded at point B (Figure 1.11) is $v_{Re}(t)$, which is proportional to the instantaneous amplitude of the v_{100} component and hence proportional to R_e,

$$\Delta v_{Re}(t) = a\Delta R_e(t) \tag{1.11}$$

where a is a constant factor.

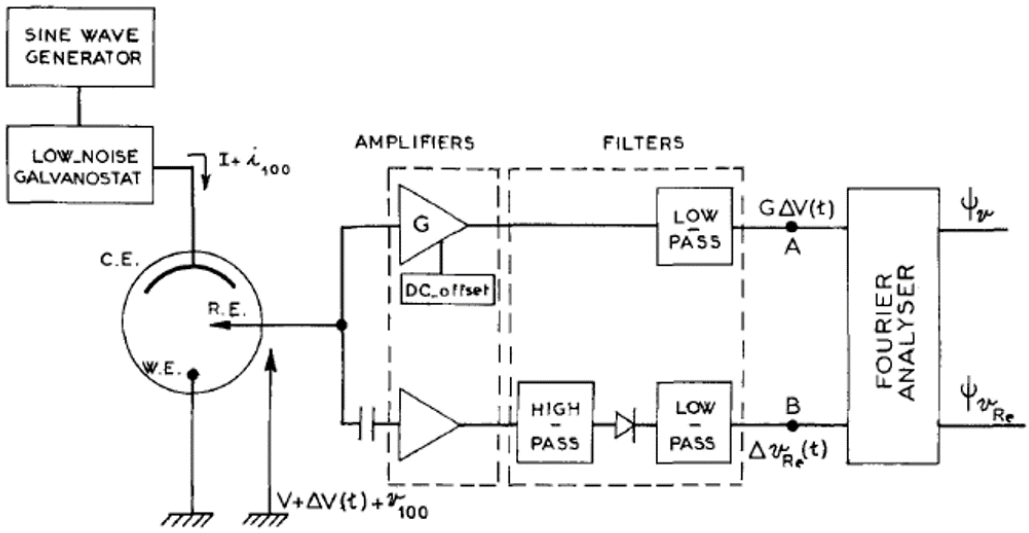

Figure 1.11 Diagram of the circuit arrangement used to measure potential and electrolyte resistance fluctuations. Reproduced with permission from ref.[86] Copyright 1991, Journal of the Electrochemical Society.

The choice of high-pass and low-pass filters and their cut off frequencies was chosen so as to minimise the phase shift between the two voltages, $v(t) = G\Delta V(t)$ and $v_{Re}(t)$ recorded at points A and B (phase shift of less than 1° at 1 kHz). Fourier analysis was also performed on the voltage signals at A and B to calculate the power spectral densities $\Psi_v(f)$ and $\Psi_{vRe}(f)$

of $v(t)$ and $v_{Re}(t)$ respectively in the frequency bandwidth dc to 5 kHz. Using this method the 'real-time' resistance fluctuations could be recorded at a millisecond timescale to an impressive precision of ± 1 mΩ.

These are two rather elegant methods by which the impedance of an electrochemical cell can be determined as a function of time by combining appropriate circuitry and mathematical modelling to interpret the results. Approaches similar to those presented here could be employed to monitor the processes involved in acoustic cavitation, as the bubbles generated will act like insulating particles. Thus perturbations to the electrode potential would be recorded at an electrode similar to those reported for insulated particles.[79,36] The findings of the studies of electrode potential/current perturbation by insulating spheres will be explored further in the next section.

1.5 Current perturbation of an electrode by an insulating particle

The following section describes how an insulating sphere impinging on an electrode surface causes a perturbation of the current passed at the working electrode surface. From the size of this perturbation information about the particle size or particle to electrode distance could be deduced. Treating our own cavitation bubbles as insulating particles, this technique is able to provide us with this same information about the size or spatial position of the bubbles being investigated.

Using the technique developed by Huet *et al.*[86] a series of experimental studies were performed by Fransaer *et al.*[36]. These experimental studies were combined with mathematical simulations to show how resistance changes as a particle approaches the electrode surface during composite plating[36]. The simulations were used as confirmation of the experimental results seen from the time dependant impedance technique developed. The simulations performed showed that the measured resistance at an electrode with the approach of an insulating particle changes as a function of particle size and position, size of electrode and solution conductivity.

$$R_e = \frac{f(r_e, r_p, x, y, z)}{\kappa} \tag{1.12}$$

where R_e is the electrode resistance, r_e the electrode radius, r_p the particle radius, (x, y, z) describes the relative position of the centre of particle to the centre of the electrode in Cartesian coordinates and κ is the solution conductivity. The equations derived for the

simulations were calculated from solutions to the Laplace equation. From the solution it was found that for a particle over the centre of an electrode,

$$\Delta R_e = 0.055\kappa^{-1} r_p^2 r_e^{-3} \quad (1.13)$$

where ΔR_e is the change in electrode resistance[79]. The results of these simulations found that resistance increases as the insulating sphere approaches the surface of the electrode and the greatest change in resistance (ΔR_e) was observed when the particle was close to the edge of the disc electrode ('volcano' shape). This was shown to be the case as this is where the insulating particle interacts with the greatest number of primary current lines, so causing the greatest perturbation to the current flow (hence greatest effect on measured resistance)[79]. This model presented could possibly be applied to a system of cavitation bubbles approaching an electrode surface, treating the bubbles as small insulating spheres. However, assumptions had to be made about electrode potential boundary conditions. Thus the model presented is only accurate assuming the electrode potential distribution is the same as for the setup presented in the work by Fransaer *et al.*[36] rather than being universally applicable to all electrode systems.

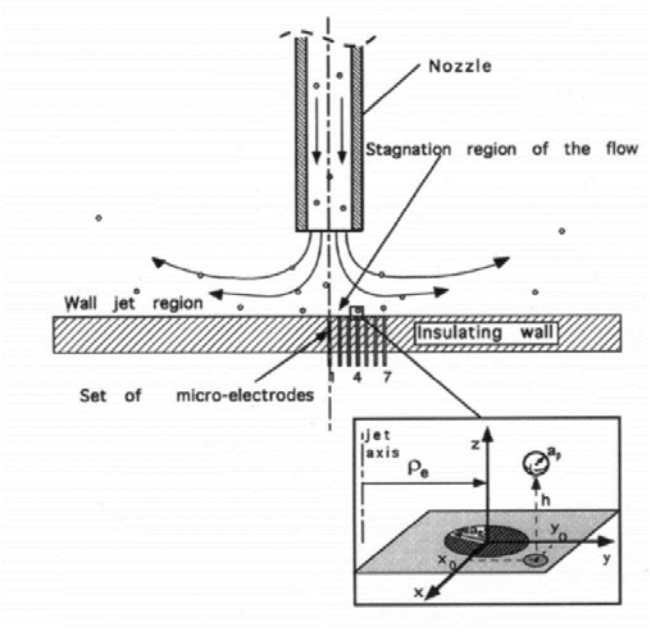

Figure 1.12 Schematic showing flow of particles from jet onto electrode surfaces. Reproduced with permission from ref.[36] Copyright 1998, The Electrochemical Society.

In addition to the simulation results, in-situ experiments were also reported on with particles impinging on electrode surfaces from a jet (Figure 1.12). In these experiments a row of seven microelectrodes (ϕ = 250 μm) spaced at 1 mm intervals from centre of a flow controlled jet containing a known concentration of insulating spheres (ϕ = 25 μm). A

schematic illustrating the experimental setup used can be seen in Figure 1.12. The resistance at each microelectrode was measured as a function of time using device developed by Huet *et al.*[86]. The resistance recorded as a function of time showed transient peaks in resistance as insulating particles passed near the electrode surface. The shape of the recorded resistance transients showed a good agreement with simulation results with 'volcano' shaped transients. An example of the modelled resistance of a particle close to an electrode surface and real transients recorded is shown in Figure 1.13 (a) and (b) respectively.

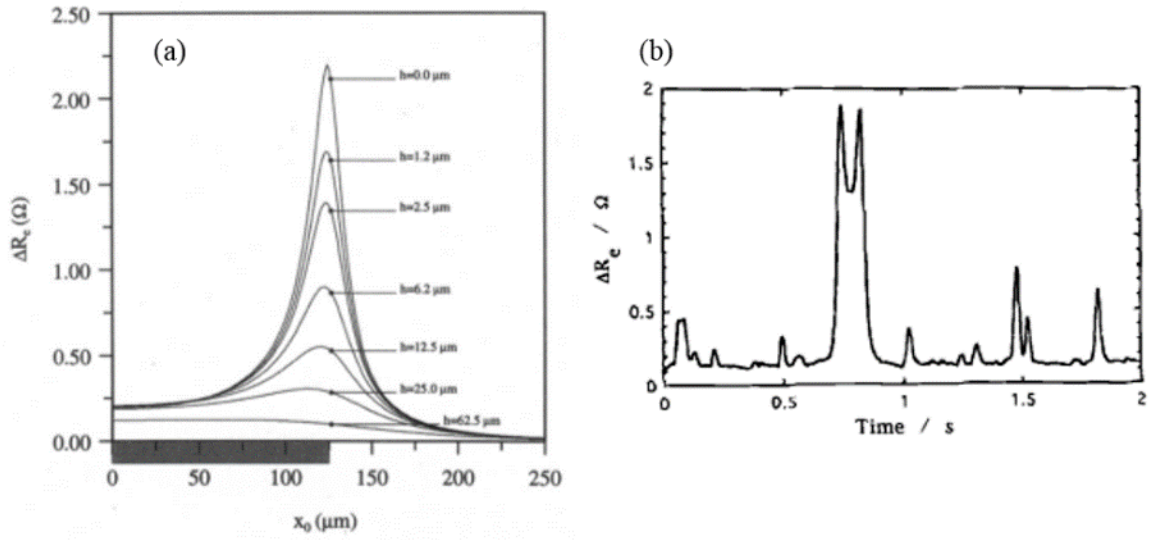

Figure 1.13 (a) Resistance change for the flow of current to a 250 μm electrode by a 25 μm spherical particle as a function of position x_0 from the centre of the electrode and distance h between the particle and the plane of the electrode ($y_0 = 0$). **(b)** Experimental resistance for a 250 μm diameter Pt disc electrode recorded as a function of time in the presence of a low concentration of non-adsorbing PS capsules with a mean diameter between 6 and 30 μm. The fluid flow of the jet containing these capsules was $q_n = 1.76$ cm^3 s^{-1}. Reproduced with permission from ref.[36] Copyright 1998, The Electrochemical Society.

For each electrode, the number of resistance transients per second was also recorded. In these investigations, a region slightly larger than the diameter of the jet nozzle ($\phi = 7$ mm) was described as the 'stagnant' zone. The frequency of transients (particle encounters) was observed to increase with increasing radial distance from the centre of the jet nozzle up to the edge of this stagnant zone (electrodes 1 – 4) and then to decrease past the edge of the stagnant zone (electrodes 5 – 7). Although a large number of the particles were observed moving past the electrode surface, some particles were adsorbed onto electrode surface and in these cases step changes in resistance were recorded.

The technique developed by Huet *et al.*[86] is sensitive enough to record very small changes in resistance (± 1 mΩ). However, the timescale to which this information can be processed

(milliseconds) is slower than the time period in which bubble dynamics are observed (microsecond). Therefore, for the measurement of bubble dynamics the technique used has to be able to resolve this information to a microsecond timescale. The technique presented by Case and Nagel[82,35] provides this smaller time resolution, as the time resolution is only limited by the frequency of the applied AC perturbation and the sample frequencies allowed by the data acquisition card. This technique still presents many challenges for recording cavitation bubble activity, as the circuit setup must be very precisely controlled (e.g. having cables with the same impedance to keep the circuit balance) to produce meaningful results. Therefore, it is challenging to make reliable and reproducible results from this system. An alternative method for recording the cavitation bubble activity to those presented here is required for our systems. The methods developed will be described in Chapter 2.3 and Chapter 6.1. As well as finding a reliable method for recording cavitation bubble activity, the method in which the cavitation is generated must also be considered.

For the generation of such transient cavitation events to be reproducible, it is important to consider the sound field employed. In the work presented in Chapter 3 of this thesis, this sound field was produced inside a cylindrical chamber. The geometry, boundary conditions and materials used in such a cell will now be discussed in detail.

1.6 Sound field in a cylindrical geometry

In the many of the investigations detailed in this thesis, the effect of cavitation on a surface of an electrode was examined. For cavitation to be observed at the electrode surface a stable region of a high acoustic pressure had to be generated in the liquid. One of the pieces of apparatus employed to create the suitable acoustic conditions was a cylindrical resonance chamber. Owing to the high symmetry of the cylindrical chamber it has good resonance properties which make it ideal for this purpose[87]. The spatial distribution of the acoustic pressure fields can be mapped and predicted by considering the cell geometry[39].

As an aid to understanding the modes of resonance setup in this acoustic environment, it is useful to produce a physical model of the resonant structure[39]. To support the assumptions made by this model, the resonant characteristics of the cylindrical cell will be measured (using electrochemical methods and audio emission) and tested against the predictions of the models. To begin with the normal mode frequencies of the acoustic wave inside a

cylindrical chamber can be predicted from solutions to the wave equation. The homogeneous acoustic wave equation is given by equation 1.14

$$\nabla^2 p - \frac{1}{c^2}\frac{\partial^2 p}{\partial t^2} = 0 \qquad (1.14)$$

where p represents the acoustic pressure, c is the speed of sound and t is time[39].

A representation of the cylindrical coordinate system and the boundary positions in the resonance chamber is shown in Figure 1.14.

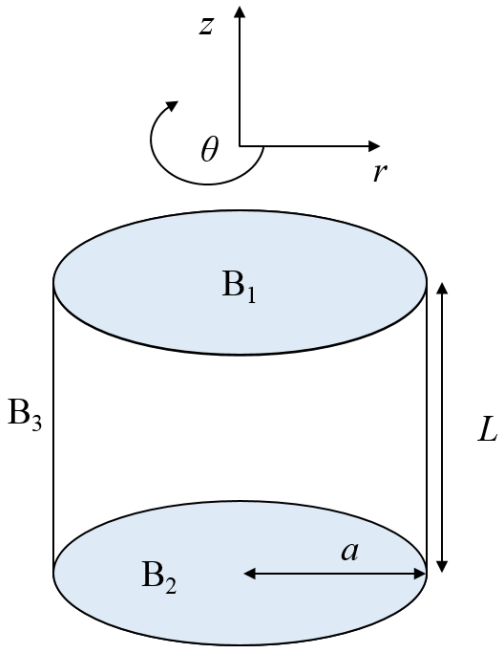

Figure 1.14 A diagrammatic representation of the cylindrical chamber showing how the cylindrical coordinate system relates to the cell geometry. B_1, B_2 and B_3 represent the boundary positions, a is the radius of the cylinder and the height of the cylinder is L.

Here we consider separable harmonic solutions of the wave equation in a cylindrical coordinate system (r,θ,z). These take the form of equation 1.15

$$p(r,\theta,z,t) = \Theta(\theta)R(r)Z(z)e^{i\omega t} \qquad (1.15)$$

where Θ, R and Z are independent functions of θ, r and z respectively and represent the acoustic pressure as a function of θ, r and z[39].

Solutions to each of these functions can be found by making assumptions about the boundary conditions present inside the cylindrical cell. Using the general solution to the wave equation and independent functions of acoustic pressure, Θ, R and Z it can be shown

that the total wavenumber, k, is composed of the transverse and axial wavenumbers k_r and k_z (equation 1.16),

$$k_z^2 + k_r^2 = k^2 \tag{1.16}$$

Expressions for the wavenumbers k_r and k_z can be determined by considering the boundary conditions at the vessel walls. For the chamber used in this thesis it is assumed to a good approximation that the polycarbonate curved walls (B_3) are a pressure release boundary, meaning the overall pressure at the walls is at a minimum. The radial boundary conditions at $r = a$, where a is the radius of the cylinder, are therefore represented by equation 1.17,

$$R(a) = 0 \tag{1.17}$$

where $R(a)$ is the acoustic pressure as a function of radial position, r, evaluated at the wall of the cylinder where $r = a$[39].

This boundary condition restricts possible values of the transverse wavenumber and k_{rmn} is thus given by equation 1.18

$$k_{rmn}=[j_{mn}/a] \tag{1.18}$$

where j_{mn} is a solution to the Bessel differential equation, the Bessel function of order m, m takes integer values (0, 1, 2, 3…) depicts the number of ring divisions when the sound field is viewed from above, n takes integer values (1, 2, 3…) depicts the number of central spots and rings formed and a is the radius of the cylinder (see Appendix 1).

As the cylinder has angular symmetry, therefore the other parameter of interest in calculating the modes of acoustic resonance is the acoustic pressure as a function of the axis, z. In the axial (z) direction, the boundary conditions at the base and top of the cylinder, B_1 ($x = 0$) and B_2 ($x = L$), where L is the height of the cylinder, are considered. Most of the chambers employed in this thesis had a thin polycarbonate base similar to the curved walls of the chamber. The boundary condition for this base was therefore considered a pressure release boundary (equation 1.19).

$$Z(0) = 0 \tag{1.19}$$

where $Z(0)$ is the acoustic pressure as a function of axial position, z, evaluated at the base of the cylinder where $z = 0$.

The upper boundary (B_2) of the cylindrical chambers employed in this thesis was provided by a disc which could be moved thus changing the vertical height L of the chamber. Two different boundary conditions were employed for this boundary. First a solid metal disc at which the pressure field can be expected to have a pressure maximum. Second a polystyrene disc of 2 mm thick, which is assumed to be a pressure release boundary at which the pressure is at a minimum. The equations for these two boundary conditions are given in equations 1.20 and 1.21

For a solid metal boundary: $$\frac{\partial Z(z)}{\partial z}\Big|_{z=L} = 0 \tag{1.20}$$

where $\partial Z(z)/\partial z$ is the differential of acoustic pressure as a function of axial position, z, evaluated at the top of the cylinder where $z = L$.

For a polystyrene (air) boundary: $$Z(L) = 0 \tag{1.21}$$

Considering first the case where the boundary condition at $z = L$ is the solid metal boundary, the solutions for $Z(z)$ must take the form of a sine function. To satisfy the boundary conditions the axial wavenumber k_z takes values

$$k_z = \frac{q\pi}{2L} \tag{1.22}$$

where q can take the integer values (1, 3, 5…) and L is the height of the cylinder[39].

Note that $k_{rmn} = k_r$ in eq. 1.15 hence combining equations 1.16, 1.18 and 1.22 and using the relationship between wavenumber and frequency, $f_{mnq} = \frac{ck}{2\pi}$, the mode frequency, f_{mnq} can be predicted from equation 1.23,

$$f_{mnq} = \left(\frac{c}{2\pi}\right)\sqrt{\left(\frac{j_{mn}}{a}\right)^2 + \left(\frac{q\pi}{2L}\right)^2} \tag{1.23}$$

In the axial (z) direction, at a resonance position, the standing wave set up in the liquid would form a pressure node at the base of the cylinder and antinode at the top of the chamber. The first three of these resonance positions (q = 1, 3 and 5) is shown in

Figure 1.15, the height of the chamber L is shown as a function of the wavelength of the applied sound wave.

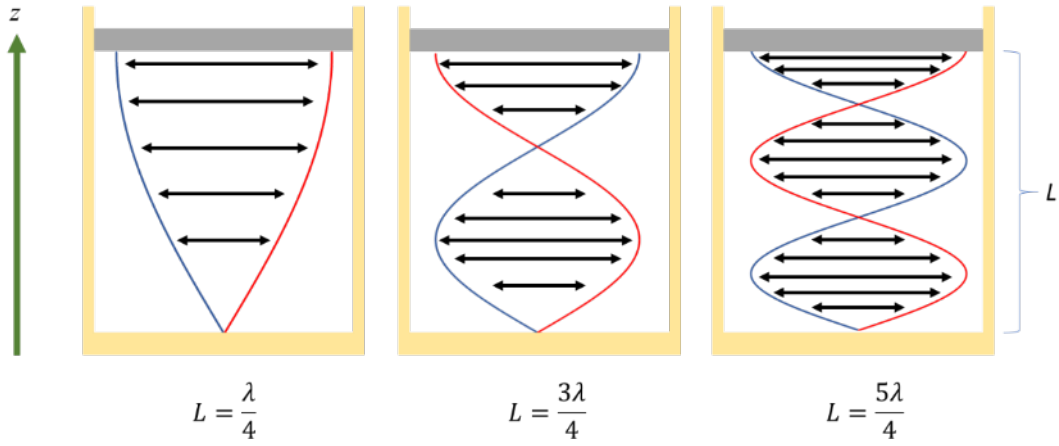

Figure 1.15 Schematic representation of the pressure field in the z direction for the first three resonance positions (q = 1, 3 and 5) where the upper reflector ( ) is a metal/liquid (rigid boundary) and the walls ( ) are pressure release (zero pressure amplitude). The lines (,) represent the pressure fluctuations at the maximum and minimum value (i.e. 180° out of phase) and the arrows ( ) the oscillation of the pressure.

In the case where the boundary condition at $z = L$ is a pressure release boundary (e.g. a polystyrene disc), the solutions for $Z(z)$ must take the form of a cosine function. Therefore to satisfy these boundary conditions the axial wavenumber k_z takes values

$$k_z = \frac{p\pi}{L} \tag{1.24}$$

where p has integer values p = 1, 2, 3…

Combining equations 1.16, 1.18 and 1.24 and using the relationship between wavenumber and frequency, $f_{mnp} = \frac{ck}{2\pi}$, the mode frequency, f_{mnz} can be predicted from equation 1.25,

$$f_{mnp} = \left(\frac{c}{2\pi}\right)\sqrt{\left(\frac{j_{mn}}{a}\right)^2 + \left(\frac{p\pi}{L}\right)^2} \tag{1.25}$$

In the axial (z) direction, at a resonance position, the standing wave set up in the liquid would form a pressure node at both the base of the cylinder the top of the chamber. The first three of these resonance positions (p = 1, 2 and 3) is shown in Figure 1.16, the height of the chamber L is shown as a function of the wavelength of the applied sound wave.

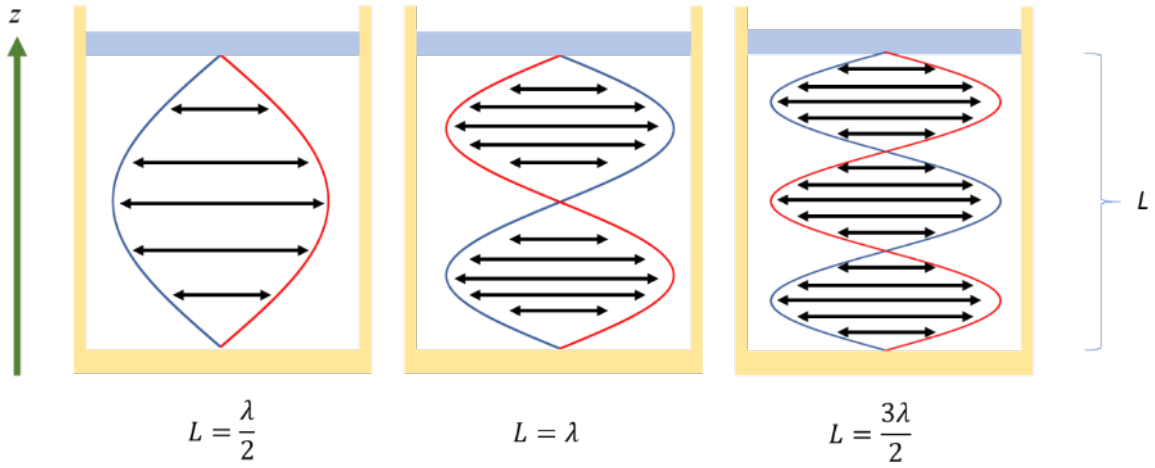

Figure 1.16 Schematic representation of the pressure field in the *z* direction for the first three resonance positions (p = 1, 2 and 3) where the upper reflector (▮) and the walls (▮) are pressure release (zero pressure amplitude). The lines (—, —) represent the pressure fluctuations at the maximum and minimum value (i.e. 180° out of phase) and the arrows (—) the oscillation of the pressure.

The values of m and n in the Bessel function j_{mn} give rise to different mode geometries in the circular plane. The geometry of the sound field when observed from above is analogous to the two dimensional modes of a circular membrane. An illustration of a few possible modes is shown in Figures 1.17 – 1.22. For further information about the mode depicted in each figure, see figure captions. The shaded sections indicate changes of phase between sections.

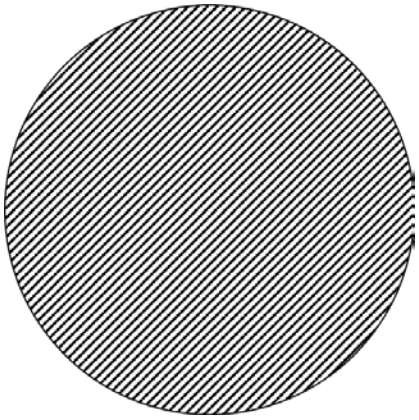

Figure 1.17 Mode $m = 0$, $n = 1$ with $j_{01} = 2.40$

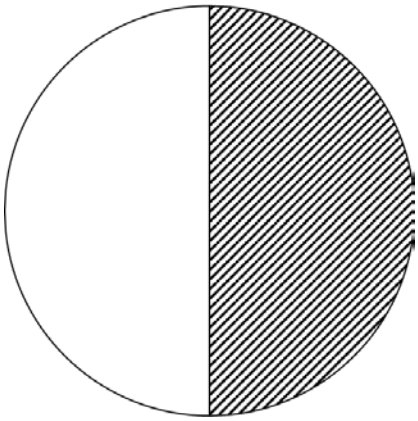

Figure 1.18 Mode $m = 1$, $n = 1$ with $j_{11} = 3.83$

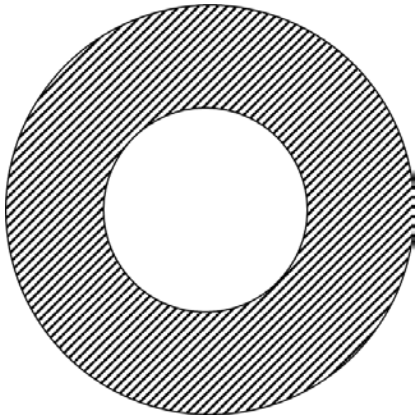

Figure 1.19 Mode $m = 0$, $n = 2$ with $j_{11} = 3.83$

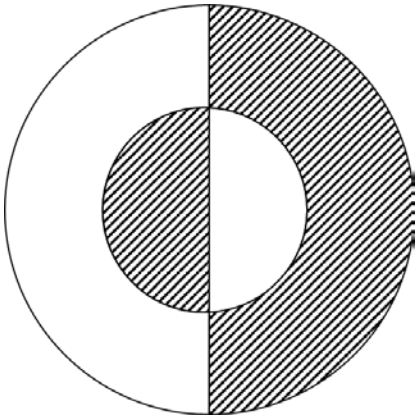

Figure 1.20 Mode $m = 1$, $n = 2$ with $j_{12} = 7.02$

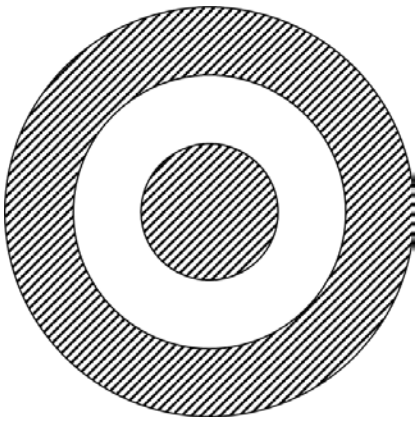

Figure 1.21 Mode $m = 0$, $n = 3$ with $j_{03} = 8.65$

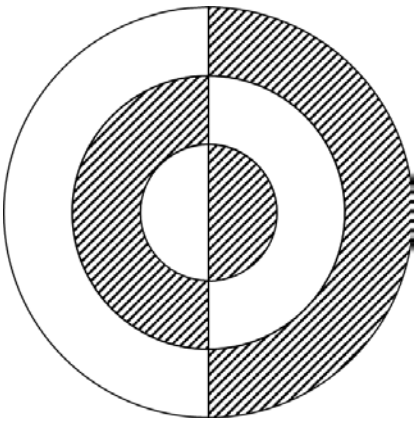

Figure 1.22 Mode $m = 1$, $n = 3$ with $j_{13} = 10.17$

1.7 Thesis outline

The work described in this thesis is on the measurement of acoustic cavitation activity in a number of different acoustic environments. The following chapter (Chapter 2) describes the various experimental studies undertaken to measure cavitation activity along with detailing the construction of custom equipment such as electrodes used as sensors and resonance cells. The majority of the studies undertaken involve electrochemical measurements, primarily our own system for high-speed AC impedance measurement of an electrochemical cell. The details of this method are given in Chapter 2.3. The following four chapters discuss the results of the various experimental studies described in Chapter 2. These results are grouped by the acoustic source employed in these experiments and the measurement techniques used.

In Chapter 3 the use of cylindrical resonance cells will be discussed. The dimensions of the acoustic chamber will be altered by moving the position of the upper boundary. The bubble activity at the reflector surface is characterised by measuring the Faradaic current of a passive electrode at the reflector surface. The impedance technique also used to measure the bubble activity as a function of upper boundary position. The measurement of cavitation activity as a function of boundary position was supported by acoustic measurements of the resonance cell. Investigations were also performed comparing a solid and an air boundary as the upper boundary condition.

Chapter 4 details mechanistic information about bubble motion from bubbles generated by a piston-like emitter called an ultrasonic horn. This includes using high-speed AC impedance measurements to record the motion of a cavitation bubble across a wide flat substrate and show how the bubble activity varies with radial distance from the cavitation source. The observations about bubble motion made by electrochemical measurements are supported by high-speed camera images.

Chapter 5 focusses on the potential applications of the acoustic cavitation bubbles. In particular the potential for the kinetic energy of the bubbles to clean surfaces. The experiments include visual observation of fouled surfaces pre and post exposure to cavitation. The presence of defects in the surface is also explored and a series of high-speed impedance measurements and high-speed camera studies were made with cavitation bubbles being trapped inside pores formed by recessed electrodes.

In Chapter 6 another method for time-dependent impedance measurements is presented. The advantages and disadvantages of this method are compared to the high-speed AC impedance method described in Chapter 2.3. These advantages and disadvantages relate to how easy each technique is to perform, how long it takes to generate meaningful data, the accuracy of the results obtained and the flexibility of each technique.

Chapter 2 Experimental Details

2.1 Reagents and Materials

The materials and reagents used in all experiments performed are presented in Table 2.1. All reagents were used as received from the supplier.

Material/Reagent	Supplier/Additional information
Sodium Sulphate	Fisher, Purity: 99+ %
Sodium Chloride	Fisher Scientific, Purity: 99.9 %
Aluminium wire **ϕ = 100 µm and ϕ = 250 µm**	Advent Purity of 100 µm ϕ wire: 99.5 % Purity of 250 µm ϕ wire: 99.98+ %
Nitric Acid (70 %)	Fisher Scientific
Titanium wire **ϕ = 80 µm and ϕ = 160 µm**	Advent, Purity: 99.8 %
Stainless steel tubing **ϕ = 6 mm, wall thickness 0.5 mm**	Coopers Needle Works Limited
Aluminium disc **ϕ = 75.5 mm, thickness 10 mm**	Made by mechanical workshop at University of Southampton Chemistry department
Stainless steel discs **ϕ = 76 mm, thickness 10 mm**	Made by mechanical workshop at University of Southampton Chemistry department
Silver wire (cylindrical) **ϕ = 500 µm**	Advent, Purity: 99.99 %

Material/Reagent	Supplier/Additional information
Silver wire (cuboid) **500 µm x 500 µm square width**	Palmer materials Sterling silver wire soft condition Code: SS-SW051S
Polycarbonate tube **OD = 80 mm, ID = 76 mm, wall = 2 mm**	The Plastics Shop Tube cut to lengths of 100 mm and 350 mm
Epofix epoxy resin **Part A (resin) and Part B (hardener)**	Struers
Araldite® fast set epoxy resin **2-component resin and hardener**	Huntsman Advanced Materials
Aluminium oxide powder (for polishing) **Particle size 25 µm, 1 µm and 0.3 µm**	25 µm particles: Buehler 1 µm and 0.3 µm particles: Struers
Microfibre cloth (for polishing)	Buehler
Water	Purification and filtration system, Purite Water purified by reverse osmosis purified to > 15 MΩ cm

Table 2.1 A table of materials and chemical reagents used.

2.2 Equipment

Different sized cells and frequencies ultrasonic emitter were used for different purposes. To facilitate identifying each different setup described in this chapter and subsequent chapters the electrochemical cells employed are detailed in Figure 2.1. For ease of future reference the two chambers are labelled as chamber ‘A’ and chamber ‘B’. Further details on how the chambers were constructed is given in Chapter 2.5.2.

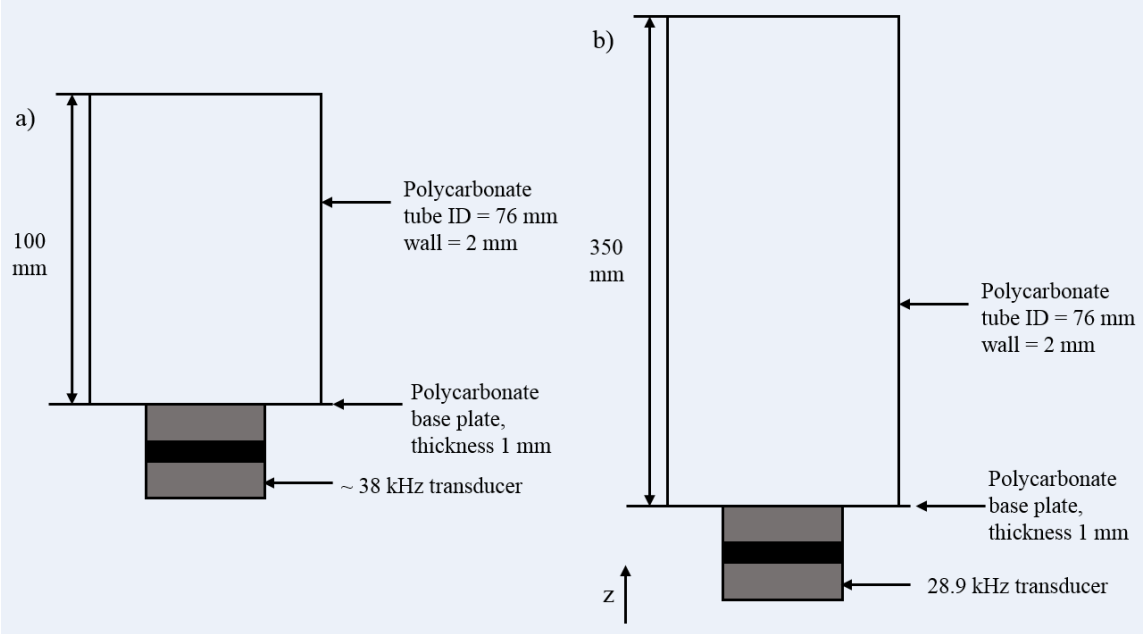

Figure 2.1 a) A cartoon illustration of chamber 'A'. The ultrasonic transducer employed was supplied by Ultrawave and operated at a resonance frequency of ~ 38 kHz. See Table 2.1 for polycarbonate tube supplier. **b)** A cartoon illustration of chamber 'B'. The ultrasonic transducer employed was supplied by MPI Ultrasonics and operated at a resonance frequency of 28.9 kHz. These cartoons are for illustration purposes only and are not to scale.

In the experiments carried out in chambers 'A' and 'B' the acoustic conditions inside the cell were altered using a metal disc as a sound reflector. Owing to the differing heights of the chambers different sound reflectors were made for each chamber. For ease of future reference these are labelled reflector 'A', reflector 'B' and reflector 'C'. Reflector 'A' was made for use with chamber 'A' and reflectors 'B' and 'C' for use with chamber 'B'. Figures 2.2 and 2.3 are schematic illustrations of reflectors 'A', 'B' and 'C' respectively.

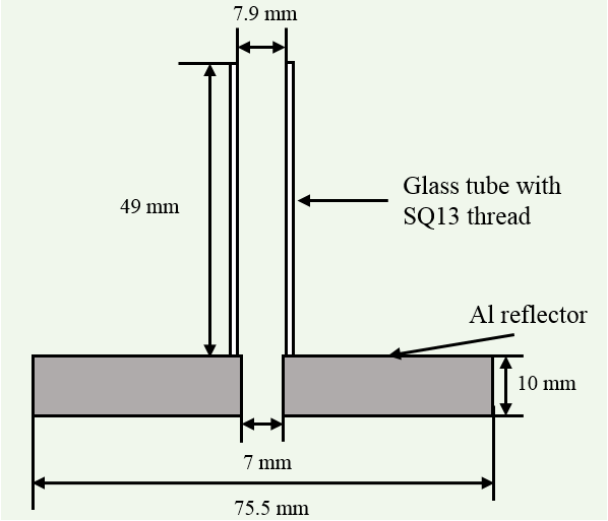

Figure 2.2 A schematic of reflector 'A', made from an aluminium disc (see Table 2.1 for further information) with a glass tube attached to the top surface. The glass tube has an SQ13 thread to facilitate holding an electrode inside the centre of the disc. Further information about the construction of the reflector is given in chapter 2.4. Image not to scale.

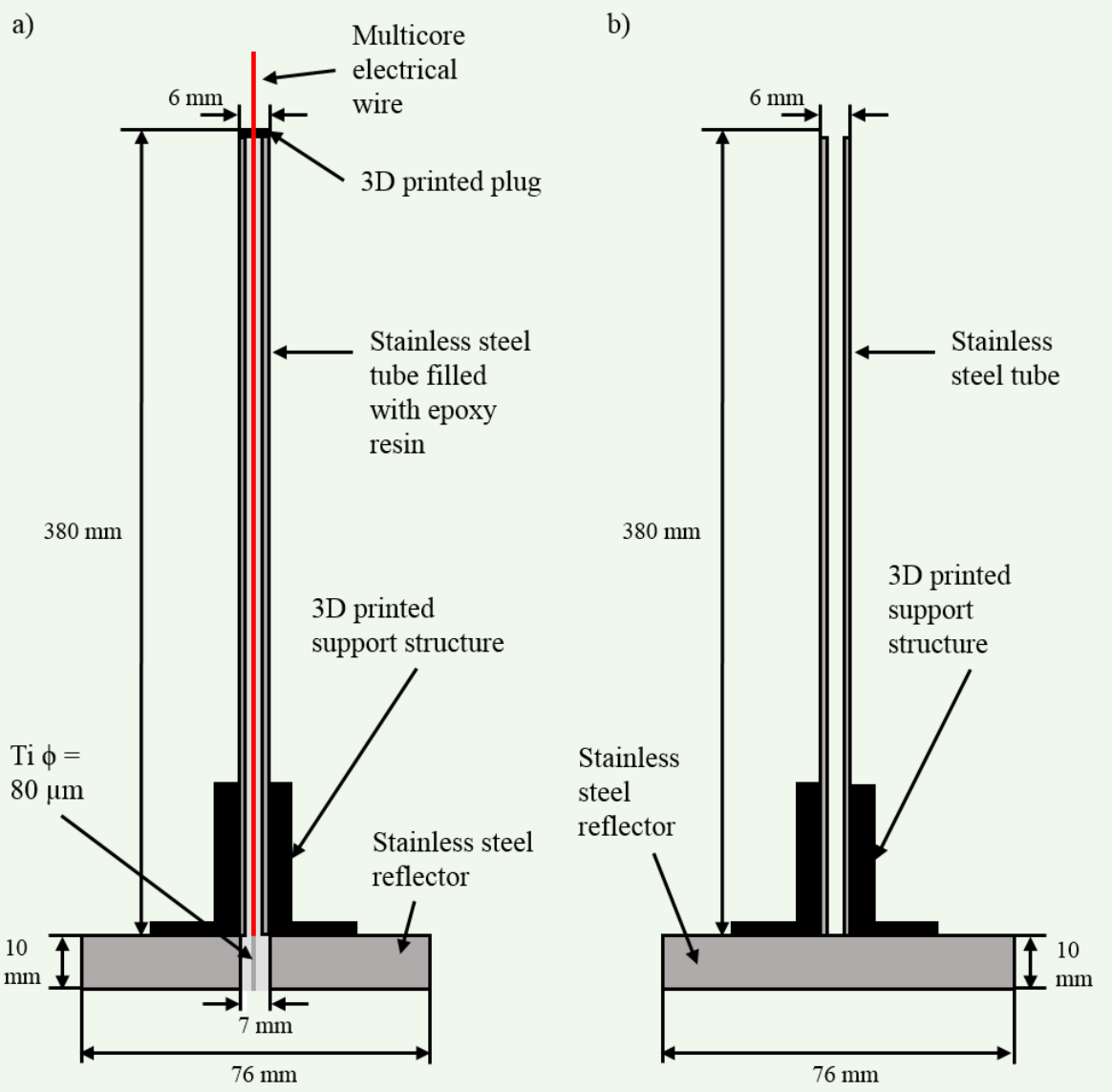

Figure 2.3 a) A schematic of reflector 'B' made from a stainless steel disc and a stainless steel tube handle. The reflector has a titanium wire (ϕ = 80 µm) set into a central hole inside the disc with slow set epoxy resin (see chapter 2.4 for further details of construction). The stainless steel handle is held in position with a 3d printed support structure. **b)** A schematic of reflector 'C' made from a stainless steel disc and a stainless steel tube handle (see chapter 2.4 for further details of construction). The stainless steel handle is held in position with a 3d printed support structure. These schematics are for illustrative purposes only and are not drawn to scale.

Several different pieces of electrical equipment were also required to drive and power the ultrasonic sources and for recording and capture of electrochemical data. For ease of reference all such equipment used, both commercial and custom made, is detailed here is Table 2.2.

Equipment	Purpose	Manufacturer/Additional information
Function generator	Provide drive amplitude for ultrasonic transducer and AC perturbation for impedance technique	Thurlby Thandar instruments TG2512A 25 MHz Dual function/Arb/Pulse generator (AC perturbation for impedance) TG1010A Programmable 10 MHz DDS Function Generator (drive amplitude for ultrasonic transducers)
Power amplifier	Used to amplify the drive amplitude signal for the ultrasonic transducers	Brüel & Kjær Type 2713
Ultrasonic horn and amplifier	Used as a piston-like emitter sound disrupter	Misonix incorporated Amplifier model: XL2007 Maximum output power: 100 W Output frequency: ~ 22 kHz self-tuning Horn tip material: stainless steel Tip diameter: 3 mm Attached to base with 30 % glass filled PEEK thread and washer to provide electrical shielding

Equipment	Purpose	Manufacturer/Additional information
Ultrasonic transducer	Used to propagate ultrasonic waves through a cylindrical chamber	Operating frequency : ~ 38 kHz Manufacturer: Ultrawave
Ultrasonic transducer	Used to propagate ultrasonic waves through a cylindrical chamber	Operating frequency : 28.9 kHz Manufacturer: MPI Ultrasonics
Potentiostat	Used to perform standard electrochemical techniques such as cyclic voltammetry and potential controlled electrochemical impedance spectroscopy	BioLogic Model: SP-150 Controlled using PC software EC-Lab v11.02
Data acquisition card	Acquire data from current follower/demodulator to PC	Measurement Computing PCI-DAS4020/12
Data acquisition card	Used to control pulses with the ultrasonic horn (PLE)	Measurement Computing USB – 204
High-speed camera	Used to capture high-speed images of bubble motion	Photron Fastcam APX RS
Current follower	Convert current signal into a voltage by multiplying by a known gain resistance for data capture by ADC	In-house constructed and battery operated in order to isolate from mains power. See Chapter 3 for further information of operation.

Equipment	Purpose	Manufacturer/Additional information
Demodulator	See Chapter 6 for details of operation	In-house constructed and battery operated in order to isolate from mains power.
Square wave function generator	Battery operated for use with demodulator.	In-house constructed and battery operated in order to isolate from mains power.
Voltage step unit	A variable DC potential supply. See Chapter 2.5.5 for further details of use.	In-house constructed and battery operated in order to isolate from mains power.

Table 2.2 A table of the equipment used.

2.3 AC Impedance Technique

A new technique was developed in order to further investigate electrochemical environment and surface processes at the electrode during cavitation and provide supporting evidence to the initial current follower investigations (see Chapter 3 for further details). AC impedance is a powerful technique which can provide useful information about electrode processes. However, standard AC impedance techniques do not provide the dynamic information required for the bubble processes interrogated here.

The fast nature of bubble kinetics requires the information to be resolved in short time periods. In other words, any -'*in situ*'- information about how the electrode and its local environment changes over time needs to be recorded at a high sample frequency. A high-speed AC impedance technique was therefore developed to characterise the cavitation activity at the surface of an electrode.

The technique devised will be shown to have been successful in achieving the aims set out, however it does have certain limitations. Firstly, the technique employs a single frequency measurement. This limits the interpretation (and the electrochemical equivalent circuit) which can be applied to the data collected. Secondly, in order to get the required high

dynamic range, high-speed apparatus and suitable data processing is required. This approach is outlined in greater detail in the following discussion.

As a starting point, the equivalent circuit of the electrochemical cell should be considered. The first circuit to consider is the Randles circuit.[80] This circuit consists of a solution resistance (uncompensated resistance) and the electrode surface is modelled as a charge transfer resistor and Warburg impedance in series and a double layer charging capacitance in parallel with these two components. The diagram for this circuit is given in Figure 2.4. At high frequencies the effect of the Warburg impedance is negligible in comparison to the charge transfer resistance therefore giving rise to the equivalent circuit shown in Figure 2.5.

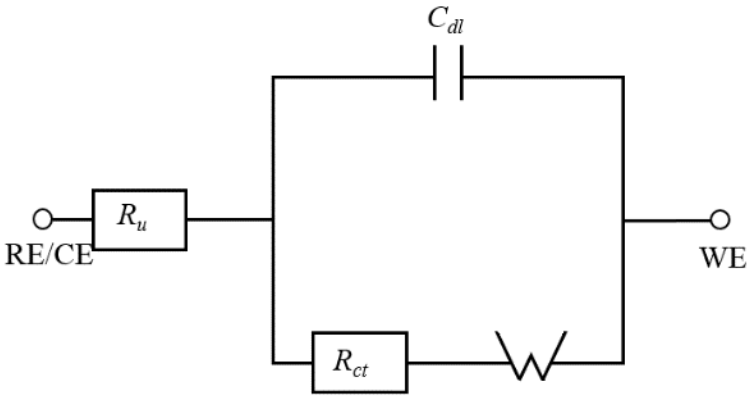

Figure 2.4 A representation of the Randles circuit with uncompensated electrolyte resistance, R_u, between the reference and working electrodes and interface between the electrolyte and working electrode consisting of a double layer capacitance, C_{dl}, charge transfer resistance, R_{ct} and Warburg impedance.

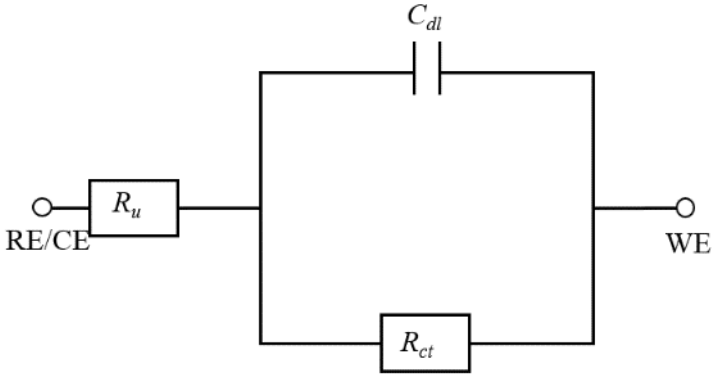

Figure 2.5 A simplification of the Randles circuit where the electrode interface is considered as double layer capacitance, C_{dl}, and charge transfer resistance, R_{ct} and the uncompensated solution resistance, R_u. The effect of the Warburg impedance is negligible compared to R_{ct} at high frequencies and is thus eliminated.

This circuit diagram could be further simplified for the case of an electrode in a simple salt solution, e.g. without the presence of a redox couple. In this case the charge transfer resistance will be much greater than the uncompensated resistance. As resistors in parallel

add reciprocally and the reactance of the capacitive term ($1/\omega C$) will be much smaller in comparison, the effect of the charge transfer resistance will also be negligible in the circuit. As a result the equivalent circuit can now be simplified to that of a resistor (R_u) and capacitor (C_{dl}) in series as seen in Figure 2.6.

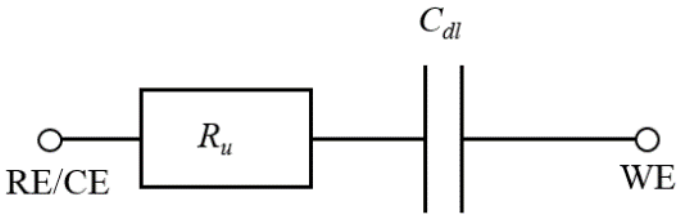

Figure 2.6 A further simplification of the electrochemical cell equivalent circuit consisting of double layer charge capacitance, C_{dl} and uncompensated electrolyte resistance, R_u.

The current response of both of these circuit elements to an applied AC potential (equation 2.1) was considered. The resistor response to an applied potential will follow Ohm's law (equation 2.1) and so will not depend on the frequency of the applied potential (equation 2.3). Thus the resistor current response will be in phase with the applied potential.

$$E = \Delta E \sin \omega t \tag{2.1}$$

with E the applied AC potential, ΔE the zero-to-peak amplitude of the applied AC potential, ω the angular frequency ($2\pi f$, where f is the frequency in Hz) and time, t.

$$E = iR \tag{2.2}$$

with i the current passed and R the resistance of the circuit.

$$i_R = \frac{\Delta E}{R} \sin \omega t \tag{2.3}$$

with i_R the current response of the resistor as a function of time.

A capacitor, however, is defined in terms of the potential difference across two oppositely charged plates (equation 2.4). Current is the movement of charge over time (equation 2.5). As a result the magnitude of the capacitor's current response to an alternating potential will be dependent on the frequency and response will have a $\pi/2$ phase shift from the applied potential (equation 2.6).

$$q = C_{dl}E \tag{2.4}$$

with q the charge on the plates, E the potential difference across the plates and C_{dl} the double layer capacitance. Hence the current passed will be the differential of equation 2.4 with respect to time,

$$i = \frac{\mathrm{d}q}{\mathrm{d}t} = C_{dl}\frac{\mathrm{d}E}{\mathrm{d}t} \tag{2.5}$$

where dq/dt is the change in charge with respect to time and dE/dt the change in potential with respect to time. This leads to the current response of a capacitor (i_C) as a function of time

$$i_{\mathrm{C}} = \frac{\Delta E}{X_{\mathrm{C}}}\sin(\omega t + \frac{\pi}{2}) \tag{2.6}$$

with and X_C the capacitive resistance equivalent to $1/\omega C_{dl}$.

It can then be seen that the overall current response of the approximate equivalent circuit will have a magnitude dependent on both resistance and capacitive elements of the circuit and a phase shift from the applied potential with is dependent on the magnitude of the capacitance and the frequency of the applied potential. This is expressed in phasor notation in equations 2.7 to 2.9.

$$\boldsymbol{E}_{Cdl} = -\mathrm{j}X_{\mathrm{C}}\boldsymbol{i} \tag{2.7}$$

with $\boldsymbol{E}_{Cdl}$ the potential across the capacitor and $\boldsymbol{i}$ the current passed at the capacitor.

$$\boldsymbol{E}_R = R\boldsymbol{i} \tag{2.8}$$

with $\boldsymbol{E}_R$ the potential across the resistor and $\boldsymbol{i}$ the current passed at the resistor. The total circuit response ($\boldsymbol{E}$) is a linear combination of $\boldsymbol{E}_{Cdl}$ and $\boldsymbol{E}_R$,

$$\boldsymbol{E} = \boldsymbol{i}(R - \mathrm{j}X_{\mathrm{C}}) \tag{2.9}$$

A complex plane (argand) diagram of Z = Z’ + Z’’ for such a circuit can be seen in Figure 2.7. As the real part of the impedance does not change as a function of frequency, the plot of real against imaginary resistance results in a straight line. This allows for impedance analysis to be performed using a potential perturbation a just one frequency.

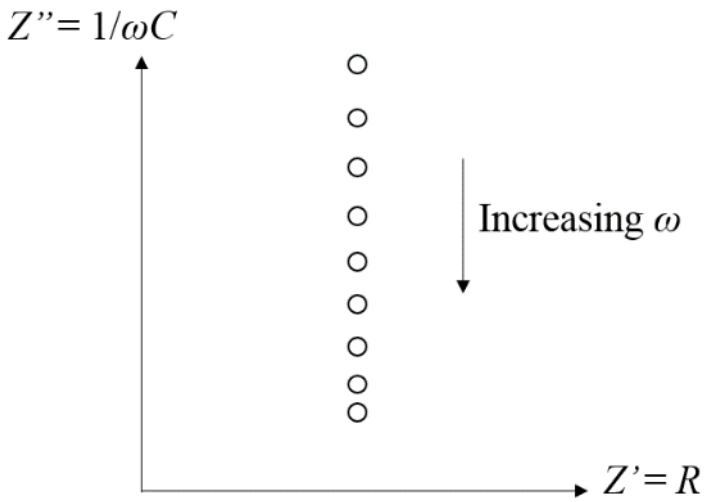

Figure 2.7 A complex plane (argand) diagram showing how the real, *Z'*, and imaginary, *Z''*, components of impedance vary with applied AC potential of varying angular frequencies, ω for an RC circuit.

In the technique devised, an AC perturbation of typically 50 mV zero-to-peak amplitude and frequency of 500 kHz was applied to the electrochemical cell. The current response was passed through a current follower to produce a voltage signal (V_{out}) equal to the output current (i_{out}) multiplied by an appropriate gain value by the amplifier (typically 10^4 V A^{-1}). Both the applied AC potential (V_{app}) and current (V_{out}) were recorded by the data acquisition card. Both of these signals were captured by a program written in visual basic 2010 at a sample rate of 10 MHz. An FFT analysis routine (National Instruments, Measurement studio) was written to determine the Faradaic current, impedance and phase angle between the applied AC signal and working electrode signal. The FFT algorithm allows for the magnitude of the applied potential and current response to be elucidated as a function of frequency. A schematic representation of this process is shown in Figure 2.8.

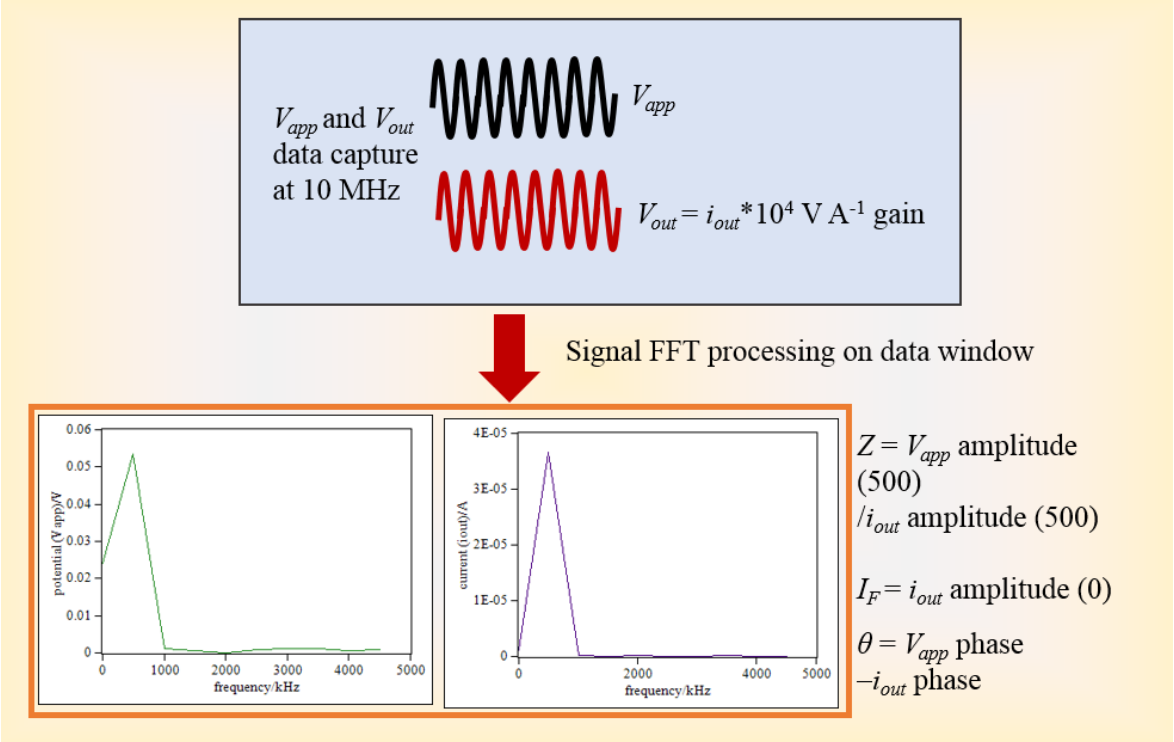

Figure 2.8 A schematic of the data processing routine in the AC impedance technique developed. The two signals captured (applied potential, $V_{app,}$ and current response, $V_{out} = i_{out}$*10^4 V A^{-1} gain) and data processing (FFT) applied to elucidate the amplitude of these two signals as a function of frequency. The impedance, Z, was calculated from ratio of potential and current amplitude at 500 kHz and the Faradaic current (I_F) was calculated from the magnitude of the current response, i_{out}, at 0 Hz. The phase shift, θ, was calculated from the change in phase between V_{app} and i_{out}.

Thus the impedance can be calculated from the ratio of the applied potential and current response at the frequency of the applied potential (here 500 kHz). The Faradaic (direct) current can also be elucidated from this signal processing by recording the amplitude of the AC current response at 0 Hz (see Figure 2.8).

Using a simple RC circuit as an approximate equivalent circuit (see Figure 2.6 and discussion of appropriate models in this chapter) and the uncompensated resistance and electrode capacitance can be determined from the phase shift, θ, and impedance, Z. Figure 2.9 shows the relationship between impedance, Z, phase shift, θ, uncompensated resistance, R_u and electrode capacitance, C.

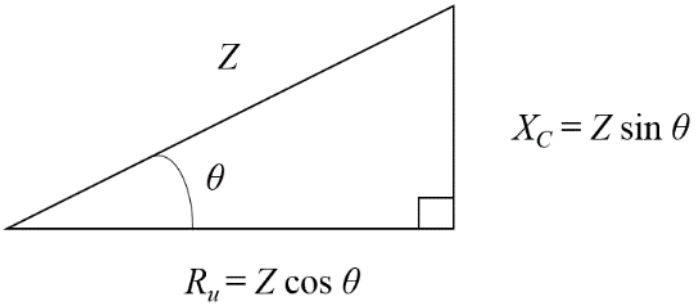

Figure 2.9 Showing the relation between the cell impedance, *Z*, and phase shift, θ, to the uncompensated resistance, R_u, and capacitive resistance, $X_C = 1/\omega C$, where ω is the angular frequency of the applied AC perturbation and *C* the electrode capacitance.

The potential and current data recorded was analysed by this algorithm in sections of 20 data points at a time (equivalent to one complete wave of the applied 500 kHz AC potential). By moving this window through the data set, the impedance, phase shift and Faradaic current could be determined with a resolution of 2 µs. This process from capture of AC potential and AC current response to data post-processing is depicted in the schematic in Figure 2.10.

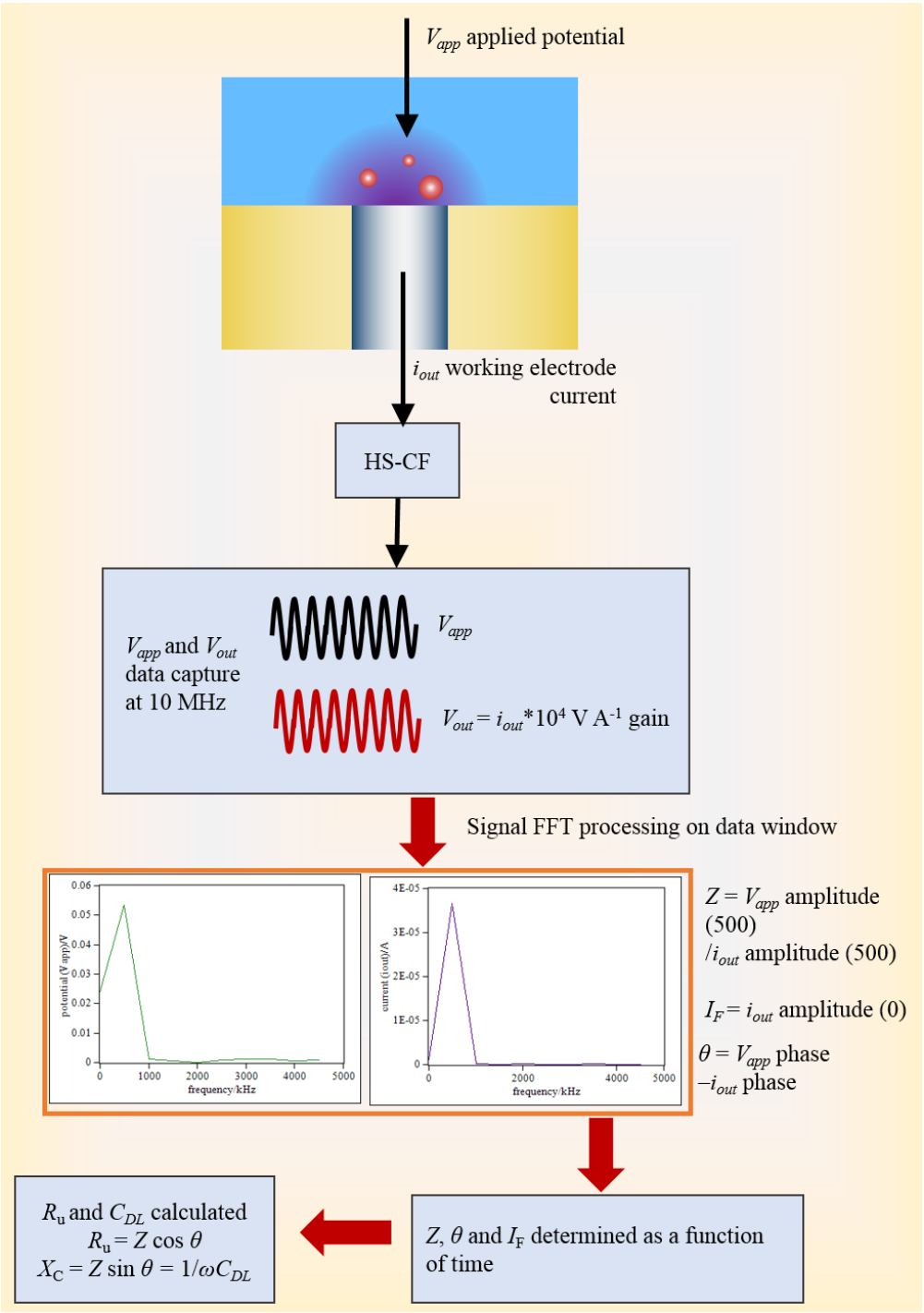

Figure 2.10 A schematic of the data capture and processing routine in the AC impedance technique developed. The two signals captured (applied potential, $V_{app,}$ and current response, $V_{out} = i_{out}*10^4$ V A^{-1} gain) and data processing (FFT) applied to elucidate the amplitude of these two signals as a function of frequency. The impedance, Z, was calculated from ratio of potential and current amplitude at 500 kHz and the Faradaic current (I_F) was calculated from the magnitude of the current response, i_{out}, at 0 Hz. The phase shift, θ, was calculated from the change in phase between V_{app} and i_{out}. The uncompensated resistance, R_u, and double layer capacitance, C_{dl}, were then calculated from the values of Z and θ.

2.4 Selecting the Sample Rate for Data Capture

Much of the work reported on in this thesis is from data collected using 'in-house' programs written in Visual Basic 2010 and using National Instruments Measurement Studio. It was imperative for accurate data collection using this system to select sample rates which could be accurately timed by the data acquisition card (see Table 2.2 for card details). The data acquisition card uses an internal clock (on-card crystal oscillator) running at a frequency of 40 MHz. The card can only accurately record data at the start of a cycle on this internal clock, with the maximum possible sample rate being after two full cycles (20 MHz). In other words, for the greatest accuracy the sample rate (*SR*) used must follow the following equation (2.10),

$$SR = \frac{40\ \text{MHz}}{n} \tag{2.10}$$

where *n* takes integer values *n* = 2, 3, 4, 5, 6, 7, 8 etc. Choosing sample rates which are not full cycles of this 40 MHz clock, for example at a sample rate of 9 MHz the data recorded is less accurate as the card is only able to capture the data at a rate of either 8 MHz (*n* = 5) or 10 MHz (*n* = 4) and oscillates between these two sample frequencies to report data acquisition at 9 MHz. Figure 2.11 is a summary of this information showing the oscillation of the 40 MHz clock and the positions in the clock cycle at which data can be accurately recorded.

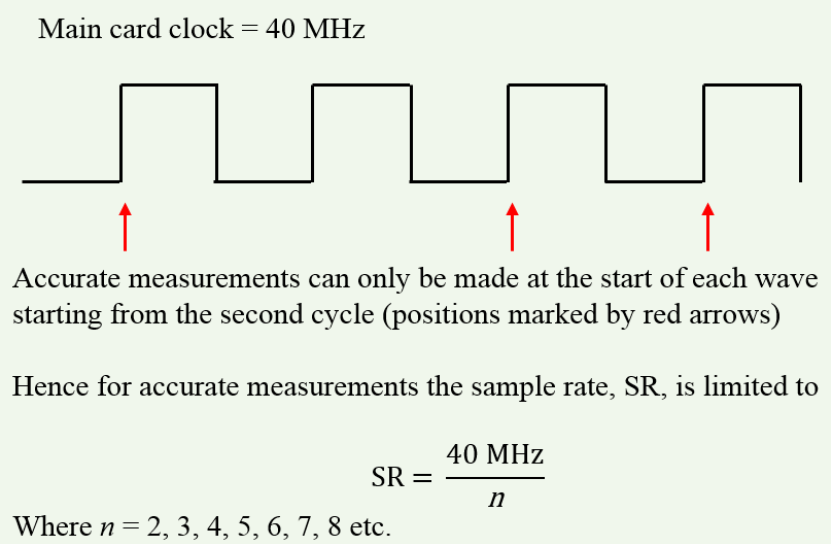

Figure 2.11 A summary of the possible sample rates at which data can be accurately recorded. The square wave shown is the oscillation of the internal card clack, oscillating at a frequency of 40 MHz. Data is sampled at the start point of the wave cycle of this oscillator starting after two complete wave cycles (positions shown by the red arrows).

This was especially important for us to consider in relation to the choice of perturbation frequency for the AC impedance technique developed (see Chapter 2.3 for further details). In this technique the cell impedance was calculated by applying signal FFT processing to the data captured on a data window equal to one complete cycle of the AC potential perturbation. As this needs to be a whole number of data points the limitations in sample rate for data capture also limit the frequency of AC potential perturbation selected. For example, in sampling the data at 10 MHz and choosing an AC potential at 500 kHz (as discussed in Chapter 2.3), the signal processing can be performed on a data window of 20 points (the number of points in one wave cycle). Other perturbation frequencies, and hence target frequencies for impedance data, are possible by selecting different viable sample rates or changing the size of the data window on which the data signal processing was performed. A summary of the combinations of perturbation frequencies and sample rates is given in Table 2.3.

Number of points in data window	**Target frequency for impedance data /MHz**	**Sample rate for recording of V_{app} and i_{out} /MHz**	***n***
20	0.5	10	4
	0.05	1	40
10	0.2	2	20
	0.4	4	10
	0.8	8	5
	1.0	10	4
	2.0	20	2

Table 2.3 A table of the target frequencies chosen (AC potential perturbation frequencies) and the sample frequencies at which V_{app} and i_{out} were recorded in order to achieve the desired target frequencies. Each sample rate used follows the rule $SR = 40\ \text{MHz}/n$ (equation 2.10) and the value of n is given. The number of points in the data window is equal to the number of points recorded for one complete cycle of the chosen AC perturbation at the sample rate at which V_{app} and i_{out} were recorded.

2.5 Cylindrical cell resonance

For the purposes of this research the cavitation bubbles were generated using two different types of ultrasonic sound source, an ultrasonic transducer which could be fixed to the base of the electrochemical cell and an ultrasonic horn which acted as a piston-like emitter inside the cell.

This chapter details the experiments carried out using an ultrasonic transducer with a cylindrical cell. Details of how a resonance mode was set up inside the cell and different methods for measuring and quantifying the activity observed will be discussed further here.

2.5.1 Fabrication of chambers

An investigation was made to determine the positions of standing wave resonance within a cylindrical chamber. The two chambers 'A' and 'B' were fabricated using the same construction process. In this process, an ultrasonic transducer (see Chapter 2.2 for specifications) was fixed centrally to a polycarbonate disc using fast set epoxy resin (see Table 2.1 for full details). The disc was then fixed to the base of a polycarbonate cylinder using fast set resin to form the base plate of a cylindrical chamber. A cartoon image (not to scale) of such a cylindrical cell is shown in Figure 2.12.

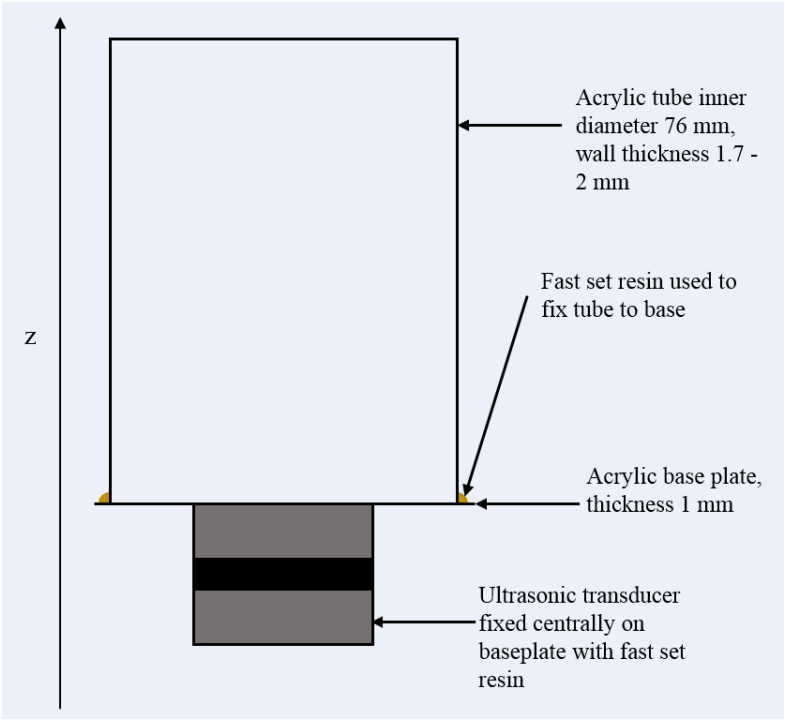

Figure 2.12 A cartoon illustration of the construction of a cylindrical resonance cell.

2.5.2 Fabrication of sound reflectors

A solid upper boundary condition was required for the experiments performed. In order for the resonance properties of the cell to be changed easily the reflector needed to move within the chamber. Reflector ‘A’ was created using an aluminium disc reflector with a thickness of 10 mm. The diameter of the reflector is 75.5 mm, 0.5 mm less than the inner diameter of the chamber to facilitate its movement inside the chamber.

The reflector also has a hole in the centre (diameter 7 mm) to allow for an electrode to be inserted for electrochemical investigations of the reflector surface. The electrode is held in position by a glass tube with an SQ13 end joint secured to the top side of the reflector using fast set resin. This can be seen in the cartoon in Figure 2.13.

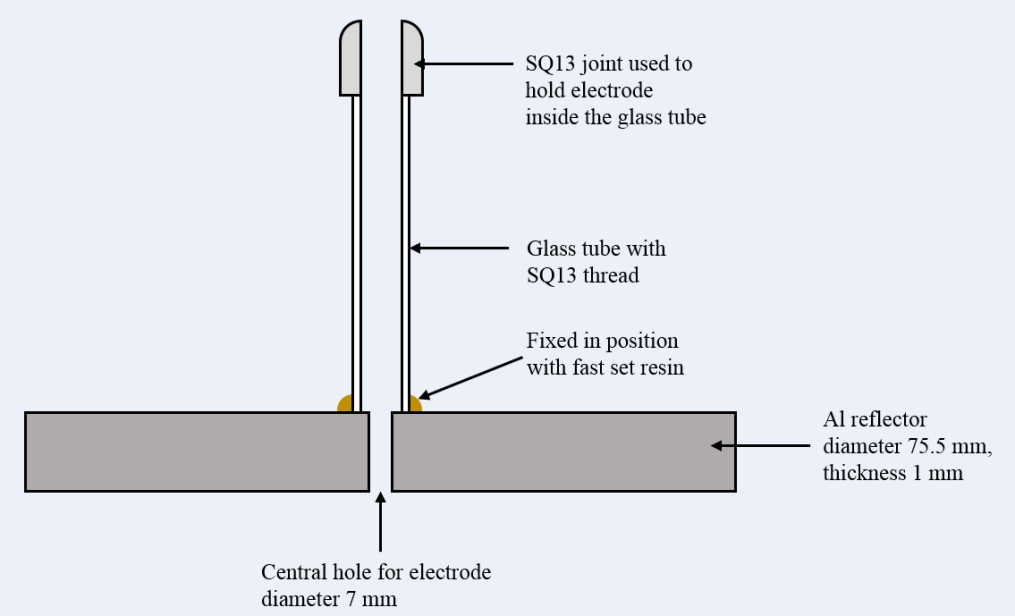

Figure 2.13 A cartoon image of the aluminium disc used as a sound reflector with the SQ13 threaded glass tube secured to the top face of the aluminium reflector using fast set epoxy resin to facilitate the securing of an electrode inside the central hole.

Both reflectors B and C were made using a stainless steel disc with a diameter of 76 mm and a thickness of 1 mm and stainless steel tube as a handle. Stainless steel was chosen to more durable than aluminium (as used in reflector ‘A’). These two reflectors were designed to be used with chamber ‘B’, so the stainless steel tubing made a more stable fixed handle. The adhesion of the tubing was aided by using a 3d printed circular support (as seen in Figure 2.3). The support was wider at the base to give a wider surface area to adhere to the stainless steel discs using fast set epoxy resin. A cartoon image of this 3d printed support is shown in Figure 2.14.

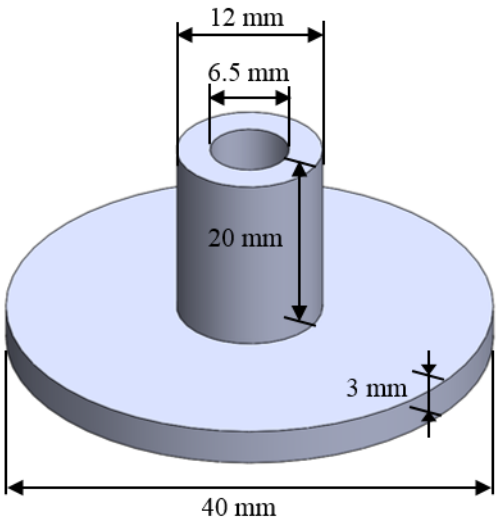

Figure 2.14 A cartoon image of the 3d printed support structure used to help adhere the stainless steel tubes to the stainless steel disc reflectors with dimensions included. The image is an illustration only and is not to scale.

Reflector B also had a titanium disc electrode (ϕ = 80 µm) inset into the centre of the disc. This was achieved by soldering a short length of titanium wire (ϕ = 80 µm, length ~ 30 mm, see Table 2.1 for further information) to a length of multicore electrical wire (length ~ 460 mm). This wire was clamped centrally inside the steel tube and sealed at the end of the rod with a 3d printed plug. The wire was fixed into position by pouring slow set epoxy resin (epofix, see Table 2.1 for full information). The resin was left to cure at room temperature for 24 hours. The excess resin was then removed from the reflector surface using emery paper, then polished using aluminium oxide particle slurries with particle sizes of 25 µm, 1 µm and 0.3 µm (see Table 2.1 for further information). A cartoon image of reflector B in construction during the resin curing stage of production is shown in Figure 2.15.

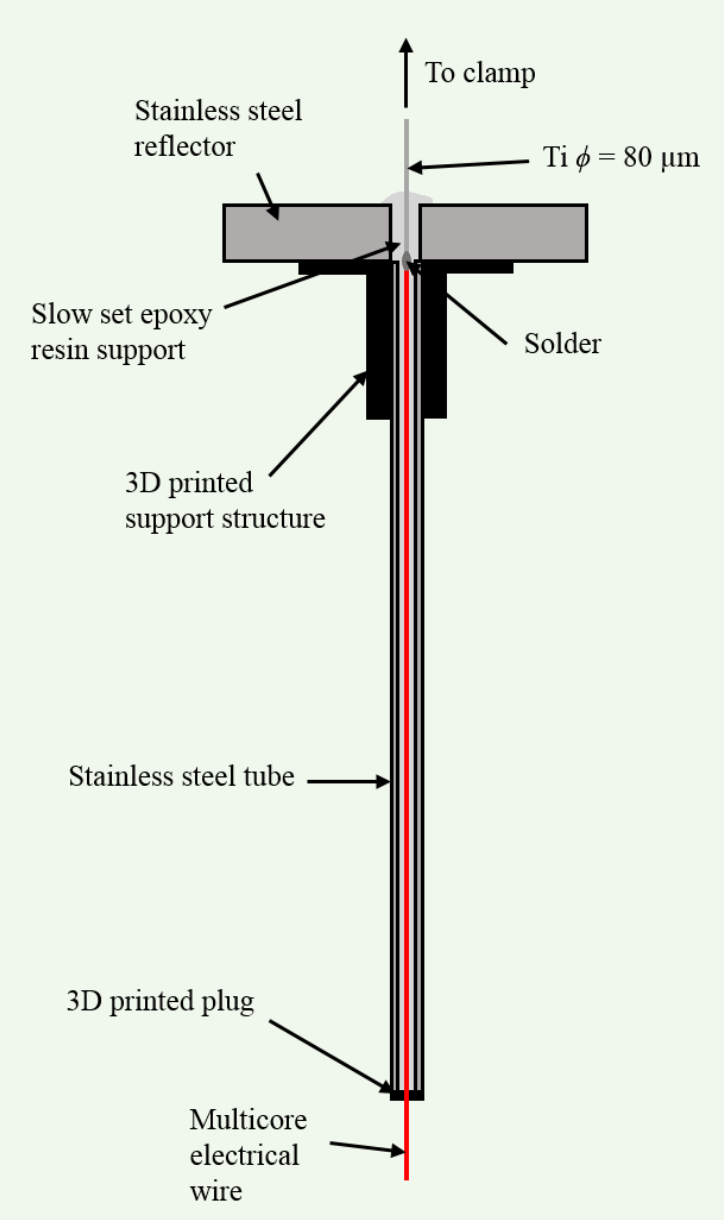

Figure 2.15 A cartoon illustration of reflector B under construction. The electrode wire was held vertically in position using a clamp while the epoxy resin was poured into the stainless steel tube through the hole in the reflector disc. The resin was filled to over the top of the disc so that it could then be sanded down to a flush finish after curing the resin. This cartoon is for illustration purposes only and is not to scale.

In order to achieve fine control of the *z* separation between the base plate and reflector, the movement of the disc is controlled using a stepper motor. The stepper motor was controlled using in-house written program in Visual Basic 2010 (see Appendix 9, 9.9.4). An image of cell A with reflector A and a stepper motor can be seen in Figure 2.16. A 250 µm diameter aluminium electrode inside a stainless steel case can also be seen in this image held inside the SQ13 joint of the glass tube. The length of the electrode was chosen such that the end of the electrode could be used a handle to attach to the stepper motor clamp.

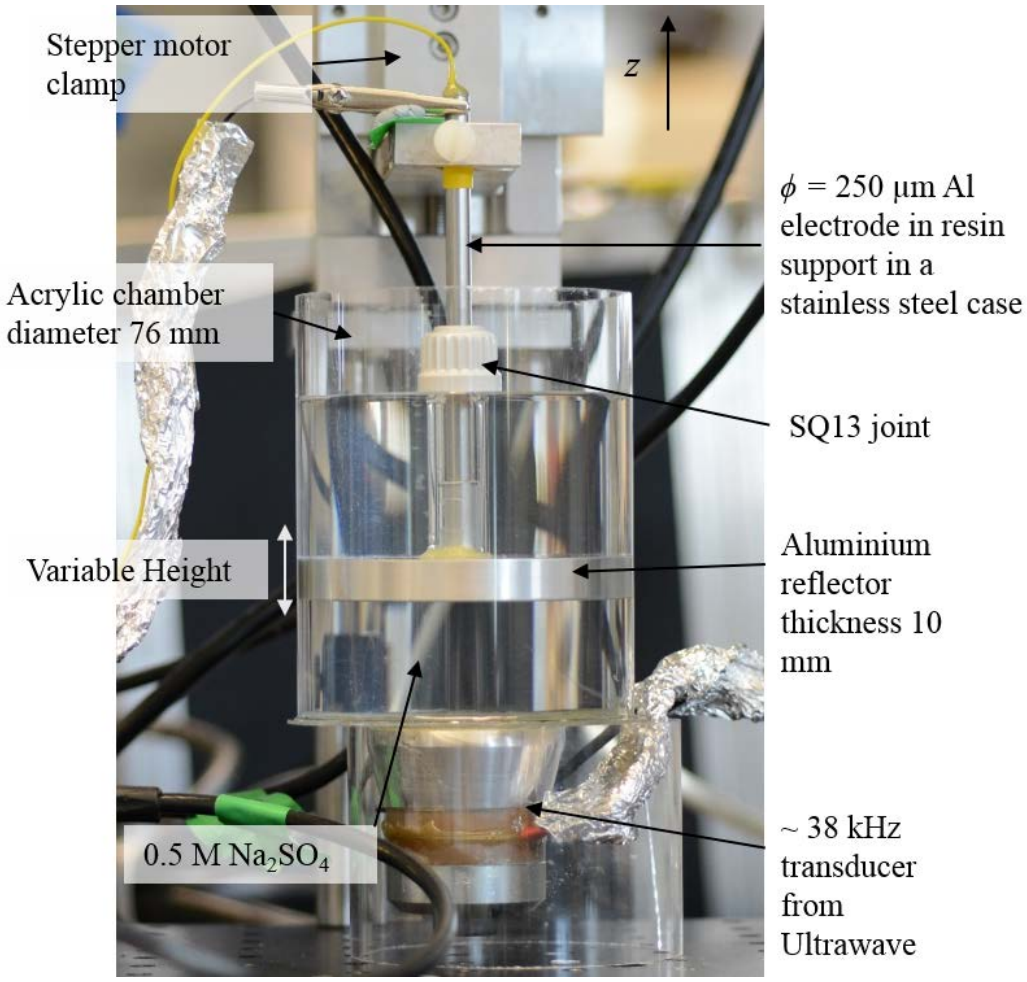

Figure 2.16 A picture showing the resonance chamber. The electrode is an aluminium disc electrode (diameter 250 µm in a resin support) with a stainless steel outer casing (diameter 6 mm) acting as a reference/counter electrode. The electrode is held in the centre of the reflector using an SQ13 joint. The electrolyte solution in the cell is aqueous 0.5 M sodium sulphate at room temperature and aerobic conditions.

2.5.3 Fabrication of electrodes

Electrochemical experiments were performed on the system to monitor the effects occurring at the solid/liquid interface. The electrodes used in this set of experiments performed consisted of a thin aluminium or titanium wire (see Table 2.1 for further details of electrode materials used) set in resin in the centre of a stainless steel tube (diameter 6 mm) to form a disc microelectrode. Once set, the aluminium electrode was exposed by polishing with emery paper followed by alumina slurries (25 µm followed by 1 µm and 0.3 µm) to achieve a mirror like finish. An optical image and cartoon illustration of the electrode construction is shown in Figure 2.17. The stainless steel casing of the electrode was also used in experiments as a reference/counter electrode. The solution used was an aerobic and aqueous solution of 0.5 M Na_2SO_4 prepared using purified water.

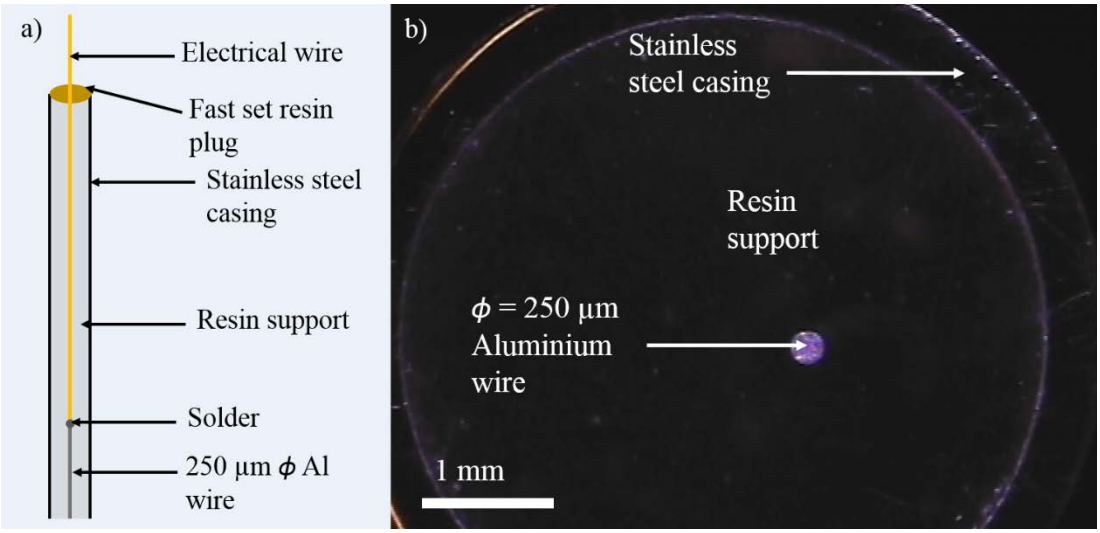

Figure 2.17 A cartoon (not to scale) showing the construction of a 250 µm diameter aluminium electrode **(a)** with an optical image of the polished end of the electrode employed in the experiments **(b)**.

2.5.4 Cavitation activity in a cylindrical cell

2.5.4.1 Current monitoring of surface activity

A range of frequencies (typically in the range of 37.5 kHz to 40.0 kHz for chamber 'A' – see figure legends for exact details) were applied to the ultrasonic transducer using a function generator and amplified by a power amplifier (see Table 2.2 for further details). The *z* separation was altered whilst the ultrasound was being applied to the chamber. The positions at which cavitation was observed were recorded.

The presence of cavitation in the liquid could be observed visually as the formation of bubbles in the liquid and audibly by a characteristic 'hissing' noise. At these positions of cavitation activity, the working electrode current time history at 0 V *vs.* stainless steel (measured as -0.493 V *vs.* MMS) was detected using a current follower (see Table 2.2 for further information) with a fixed gain of 10^4 V A^{-1}. The current follower was required in order to convert the current from the cell (i_{out}) into a potential signal ($V_{out} = i_{out} * 10^4$ V A^{-1} gain) which can be read by the data acquisition card. The output signal (V_{out}) from the current follower was then recorded by the oscilloscope and saved using data acquisition software (TiePie Multi Channel software). Figure 2.18 is a schematic of the experimental setup for these experiments.

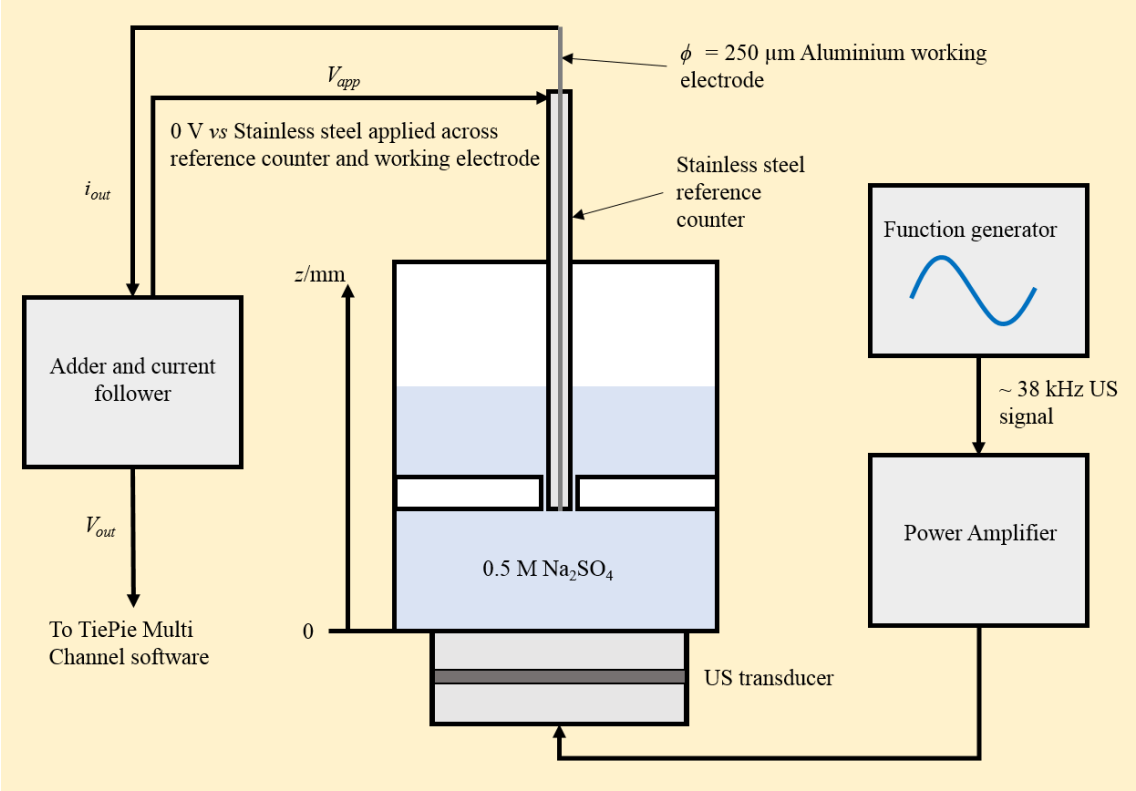

Figure 2.18 A diagram of the experimental setup showing how the ultrasonic signal is amplified using a power amplifier to the transducer and the data collection from the adder and current follower.

Although monitoring the current of the electrode during cavitation yielded some useful information on the surface processes further experimental evidence was required to confirm the proposed mechanisms.

2.5.4.2 AC impedance

Initial impedance investigations were recorded using chamber 'A'. In these experiments the potential of an aluminium or titanium working electrode (see figure captions for exact details) was maintained at 0 V *vs.* stainless steel (-0.493 V *vs.* MMS). The AC perturbation (500 kHz, 50 mV zero-to-peak amplitude) was applied using a function generator to the steel counter reference electrode. A current follower with a fixed gain of 10^4 V A^{-1} was employed. A representation of this setup is shown in Figure 2.19.

Both the applied AC potential (V_{app}) and current passed at the electrode ($V_{out} = i_{out} * 10^4$ V A^{-1} gain) were recorded by a data acquisition card (see Table 2.2 for full details). These signals were captured by a program written in visual basic 2010 at a sample rate of 10 MHz. Using an FFT approach, the uncompensated resistance, R_u, and electrode capacitance, C_{dl}, could also be determined every 2 µs for the total current time data recorded (see Chapter 2.3 for further details on the technique).

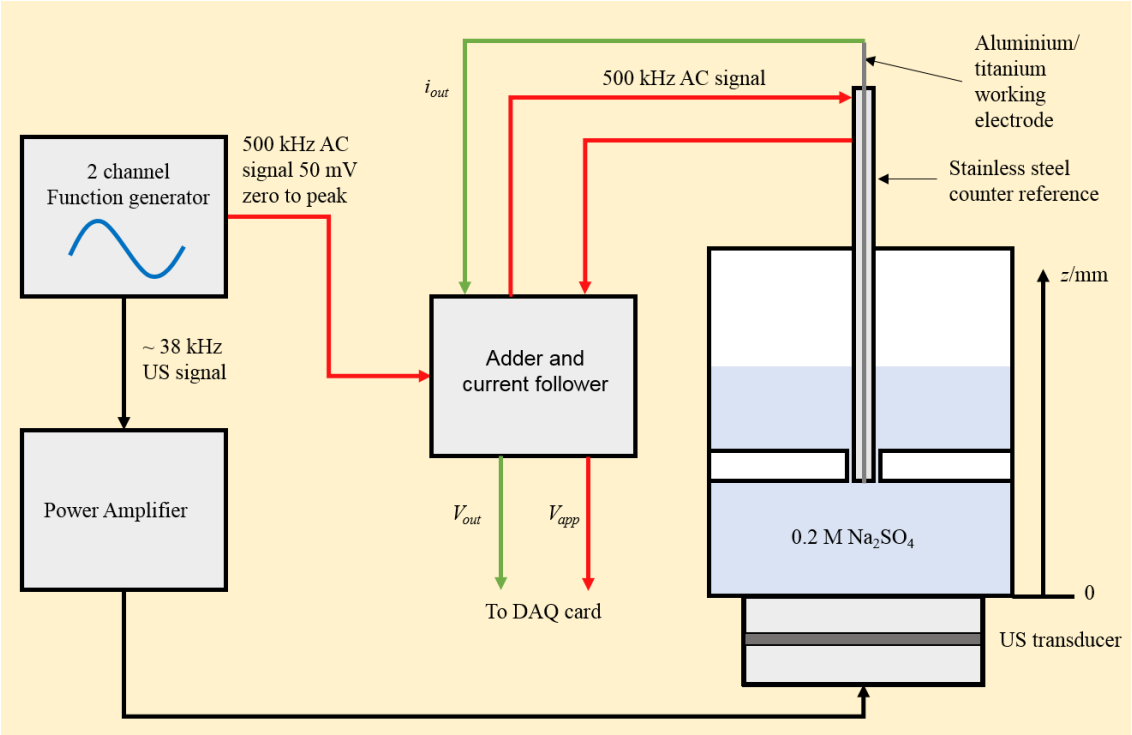

Figure 2.19 A diagram of the setup used to perform the AC impedance experiments showing how the ultrasonic signal was amplified using a power amplifier and then applied to the transducer. An AC signal was added using an adder before application to the cell. The two output voltage signals V_{app} (AC signal) and V_{out} (cell signal) fed to the in-house data collection software.

The solutions used were aerobic and aqueous solutions of typically 0.2 M or 0.5 M Na_2SO_4 (see figure legends for exact details) prepared using purified water (see Table 2.1 for further information). Figure 2.20 is an annotated image of the set up used for these experiments showing the cylindrical cell, the stepper motor used to control the height of the reflector and the current follower. The height of the reflector was changed to identify the positions of resonance. Data was collected at *z* separations between 1 mm and 65 mm in increments of 1 mm.

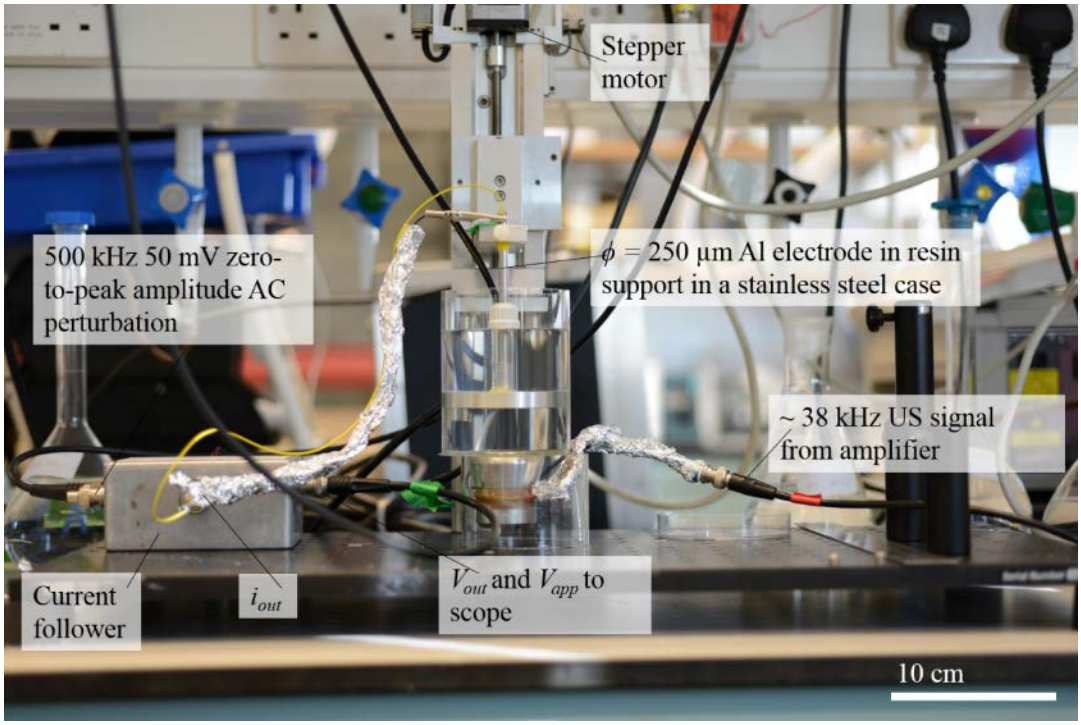

Figure 2.20 Image showing one of the experimental setups used. A 250 µm diameter aluminium electrode was used as the working electrode and stainless steel as the reference/counter electrode. The solution used in the chamber was 0.2 M Na_2SO_4.

This technique provided information on the fine details of the bubble interactions with the surface. The AC impedance technique is also able to give information on the quality of the electrode surface before and after exposure to cavitation.

2.5.4.3 Characterisation of surface damage

An experiment was performed in which the resistance, capacitance and phase shift for a newly polished 100 µm diameter aluminium electrode (polished in a slurry of 0.3 µm Al_2O_3 on microfiber cloth) was calculated using the high speed AC impedance technique without the presence of ultrasound. The data was recorded over 50,000 points and an average value calculated. The measurement was made again after ~3 minutes of exposure to cavitation inside the cylindrical resonance chamber.

As a control experiment the electrode surface was also artificially roughened by polishing in different media. The same experimental method was used with the same 100 µm diameter aluminium electrode first sanded with emery paper and then polished with alumina slurries with particle sizes from 25 µm to 0.3 µm. The average resistance, capacitance and phase shift were reported for each case.

Thus far the high-speed AC impedance technique developed has been able to provide dynamic information of the bubble motion and the electrode surface quality. However, the

technique could not be used to quantify the amount of activity at the surface. Further analysis of the experimental data collected was needed to achieve this.

2.5.5 Quantifying cavitation activity

The previous experiments performed were important in establishing the dynamics of the bubble motion during cavitation and measuring the changes in quality of the electrode surface. These experiments however could not be used to quantify this activity. Thus further experiments and experimental analysis methods were devised to determine the conditions in which the cavitation at the electrode surface was greatest

The cavitation activity was first determined by use of an experimental analysis method on the high-speed AC impedance data. A sub-routine in the Visual Basic data capture and processing programme was used to identify and count all resistance peaks above this threshold value. The total number of these peaks was counted over a time window of 100 ms with an effective sample rate of 500 kHz (50,000 points). The code for this sub-routine program can be found in Appendix 9 (9.9.1).

A voltage step unit was also employed to apply a potential to the working electrode. This was employed to apply a DC bias to the potential across the working electrode and stainless steel reference counter electrode. The applied potential was varied such as to generate H_2 gas evolution at the working electrode and compare the volume of gas activity observed for gas evolution potentials compared to non-gas evolution potentials.

2.5.5.1 Cavitation activity at 0 V *vs.* Reference

Using an 80 µm diameter titanium electrode as the working electrode, a DC potential of 0 V *vs.* stainless steel (-0.493 V *vs.* MMS) was applied across the working electrode and stainless steel reference counter electrode in conjunction with the 50 mV zero-to-peak 500 kHz AC perturbation. The circuit setup is illustrated in Figure 2.21.

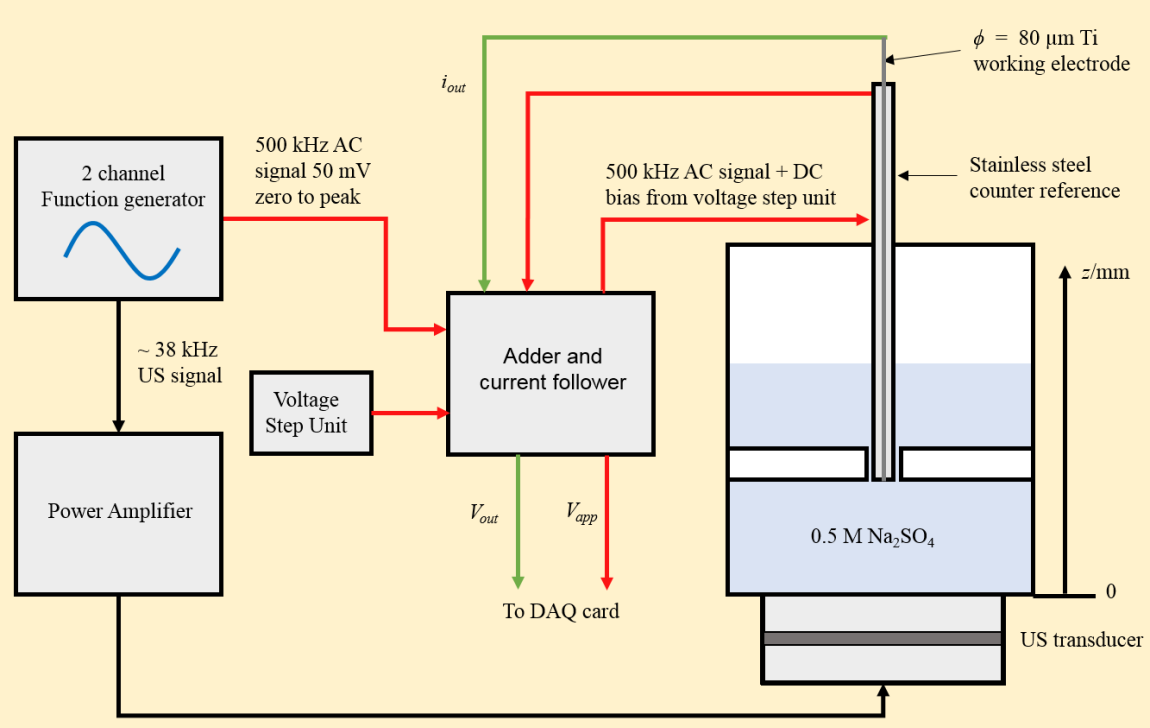

Figure 2.21 A circuit diagram of the setup used to perform the AC impedance experiments showing how the ultrasonic signal was amplified using a power amplifier and then applied to the transducer. Also two signals (a DC bias and an AC signal) were added using an adder before application to the cell. The two output voltage signals V_{app} (AC signal) and V_{out} (cell signal) fed to the in-house data collection software.

Using the peak counting program on the uncompensated resistance data, the number of cavitation events at each height was calculated. The reflector *z* separation was systematically changed in increments of 1 mm for separations of 1 mm to 65 mm and the activity recorded at each separation. Three experiments were performed at each *z* separation and the number of events averaged at each height.

2.5.5.2 Hydrogen evolution at working electrode

These same set experiments were performed at different DC potentials to measure the change in activity observed in the presence of gas evolution at the working electrode. A potential of -2.2 V *vs.* stainless steel (-2.693 V *vs.* MMS) was applied to the working electrode as H_2 gas evolution was observed at this potential. As before three experiments were performed at each disc height and the number of events averaged at each height.

Experiments were also performed in which the disc was kept at a height of 28 mm, chosen as a height at which cavitation events were expected, and the potential of the electrode was varied between non-gas evolution potentials and gas evolution potentials of 0 V *vs.* stainless steel (-0.493 V *vs.* MMS) and -2.2 V *vs.* stainless steel (-2.693 V *vs.* MMS) with measurements taken at 0.1 V intervals. The number of resistance peaks or

‘cavitation/bubble events’ was counted, as described above, and averaged over three experiments at each potential.

2.5.6 Using a microphone to measure acoustic output

To complement the impedance measurements of cell activity due to acoustic resonance a second method was devised using a microphone to measure the acoustic output. This made use of the audible ‘hissing’ noises heard during cavitation to determine the intensity of the cavitation activity.

For these experiments, chamber ‘B’ and reflectors ‘B’ and ‘C’ were employed as the longer chamber and lower frequency transducer meant that a larger number of resonance positions could be found. The software controlling the stepper motor was able to control the height of the disc to a resolution of 100 μm. As the reflector was moved up through the chamber cavitation activity was observed at a number of positions in the form of an audible ‘hissing noise’ characteristic of acoustic cavitation. At the positions at which cavitation was observed a microphone was used to measure the sound output. Figure 2.22 shows the setup of the cylindrical cell with the plunger and microphone next to the cylinder to record the sound output to an oscilloscope.

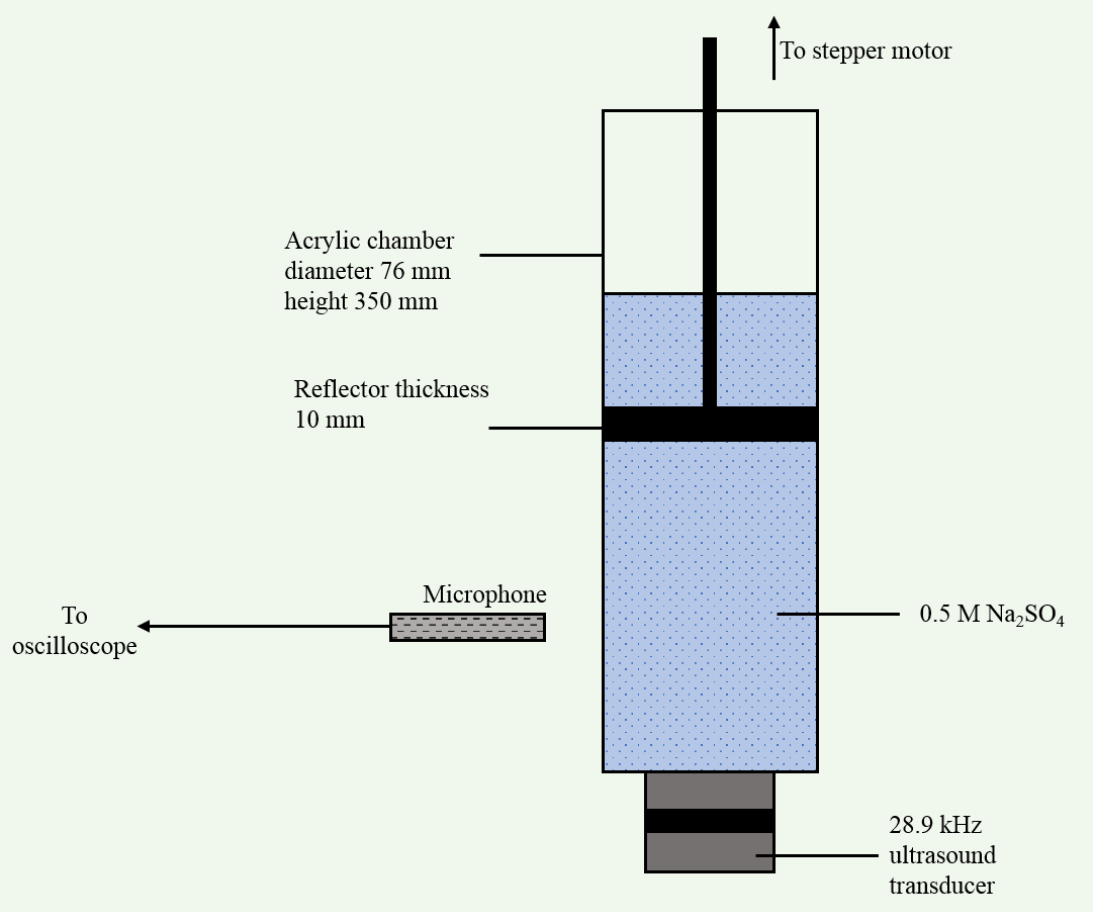

Figure 2.22 An illustration of the cylindrical chamber used in the experiments performed. The height of the steel reflector was controlled by a stepper motor to an accuracy of 100 µm. A clamp stand was used to hold the microphone next to the chamber close to the 'hissing' from the acoustic cavitation. The base of the chamber was also placed in a custom designed stand to suspend the end of the transducer from touching the bench and also to provide stability. The electrolyte solution is aqueous 0.5 Na_2SO_4 at room temperature (22 - 23 °C) and aerobic conditions.

The microphone data was recorded in 1 s sections at a sample rate of 1 MHz, a total of 1,000,000 data points. Data was recorded for a series of plunger heights around the position of each resonance band.

This series of experiments was then repeated for a plunger with a polystyrene disc adhered to the base of the steel disc. The microphone output was recorded at various heights from the base when increases in microphone amplitude were observed.

2.6 Ultrasonic horn as Sound Emitter

The other ultrasound source used to generate cavitation activity within a cell was an ultrasonic horn (see Chapter 2.2 for further details). The following chapter details the electrochemical equipment and experiments performed to measure the cavitation activity under these acoustic conditions.

2.6.1 Fabrication of Silver electrodes

A series of silver electrodes were made for use in experiments involving the ultrasonic horn (see Chapter 2.2 for further details). In order to investigate the lateral motion of the bubbles, a series of silver disc electrodes were made with a wide resin surround approximately 20 mm in diameter. These were made using a 50 ml centrifuge tube (PET, Corning) as a mould. A small piece (25 – 30 mm) of the silver electrode wire (500 µm diameter) was connected to a piece of multicore electrical wire (~ 150 mm) with silver paint. The two connected wire were held vertically in the centre in the centre of the mould and the liquid resin poured around the wire. The resin was left to set at room temperature for 24 – 48 hours. Once set the mould was removed to leave a cylinder of resin with the silver embedded in the centre. The end surface was sanded down with emery paper and polished to a high shine with alumina of particle size 25 µm followed by 1 µm and 0.3 µm. An annotated diagram and image of such an electrode is shown in Figure 2.23.

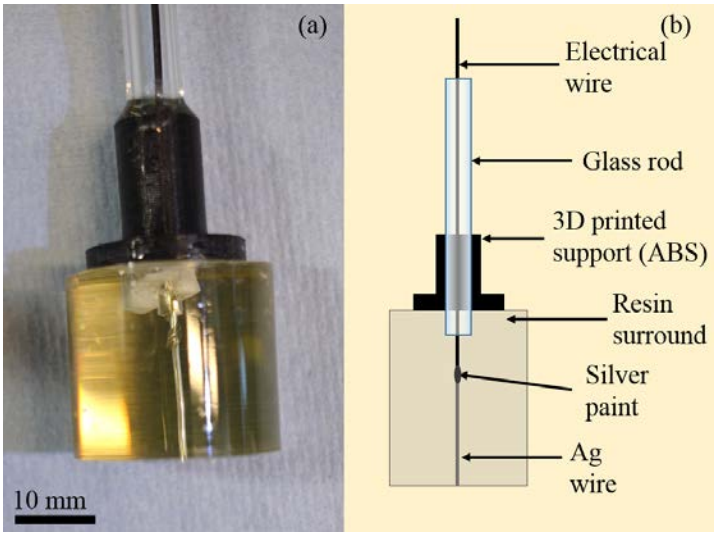

Figure 2.23 (a) An image of a silver electrode with a diameter of 500 µm. **(b)** An annotated diagram of the silver disc electrode.

For a series of experiments involving the motion of bubbles inside a pore, silver electrodes were made using square shaped wire with dimensions of 500 µm by 500 µm. This wire was chosen as it was easier to image the inside of the pore when employing a high-speed

camera (see Table 2.2 for further information) which required the cell to be back lit. For use with the high-speed camera, electrodes were made in which the square wire (~ 15 mm in length) was connected to the multicore electrical wire (~ 120 mm in length) using a metal crimp or silver paint held together with heat shrink plastic. The wire was embedded into resin inside a square cuvette (Fisherbrand, 4 ml). The end of the electrode was sanded with emery paper and then polished with a 25 µm, 1 µm and 0.3 µm alumina slurry to a highly polished finish. A diagram and image of such an electrode is shown in Figure 2.24.

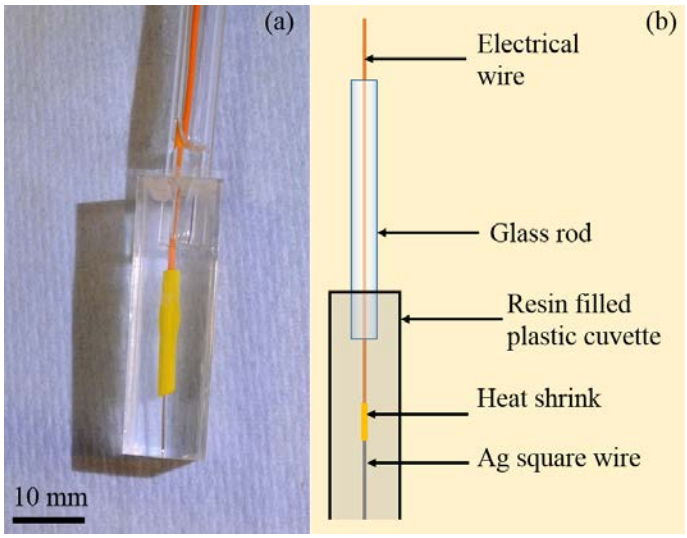

Figure 2.24 (a) An image of a square silver electrode with dimensions of 500 µm x 500 µm. **(b)** An annotated diagram of the square silver electrode.

The polished electrodes were then used to form square shaped pores of varying lengths. This was achieved by electrochemically etching the silver wire in 0.1 M HNO_3. A chronopotentiometric technique was performed in which the working electrode (silver, square) was kept at a constant current using a potentiostat (see Table 2.2 for further information). The reference electrode used in this technique was a saturated calomel electrode and the counter electrode was a ring of steel wire. The working electrode to be etched was held in the centre of the steel wire ring in order to keep the etching of silver uniform in all directions. The electrode was held at a constant current of 0.19 mA and the length of time required was calculated in order to etch out enough material for pores between 500 µm and 2000 µm in depth. An example of such a pore and an annotated diagram of the structure is shown in Figure 2.25.

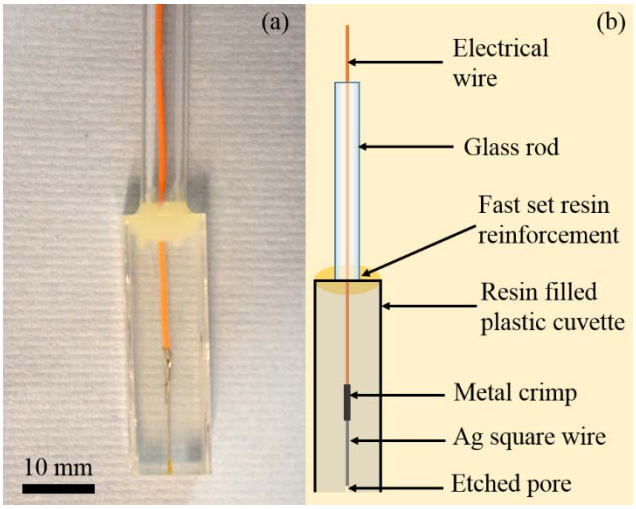

Figure 2.25 (a) An image of a square pore silver electrode with dimensions of 500 µm x 500 µm x 1720 µm made by etching in 0.1 M HNO_3 at a constant applied current of 0.19 mA for 4 hours and 50 minutes and 0.38 mA for 1 hour and 1 minute. **(b)** An annotated diagram of the square pore silver electrode.

An SEM image of one of these channels is shown in Appendix 2.

2.6.2 Lateral motion of cavitation bubbles

The bubble 'activity' on a polished surface was measured under different acoustic conditions. For these investigations a 500 µm silver wire was set in the centre of a 20 mm diameter circular resin block to form a 500 µm diameter silver disc electrode in a large resin surround. This electrode was placed in an electrochemical cell with a stainless steel rod acting as a reference counter electrode in 1 M NaCl. The cavitation bubbles were generated by an ultrasonic horn (see Table 2.2 for further information) placed in the solution above the resin disc. The ultrasonic horn was mounted onto a *z*-*y* stage system, allowing for the lateral and vertical separation between the horn tip and disc electrode to be controlled. This can be seen in a schematic illustration of this setup (Figure 2.26). For ease of future reference the vertical separation between the horn tip and resin surface is referred to as the z separation, with a z separation of 0 mm being when the horn tip is touching the resin surface. The lateral separation between the horn tip and silver disc electrode is referred to as the y separation, with a y separation of 0 mm being the position at which the centre of the horn tip is directly over the centre of the silver disc electrode. The direction of these axes can be seen in Figure 2.26.

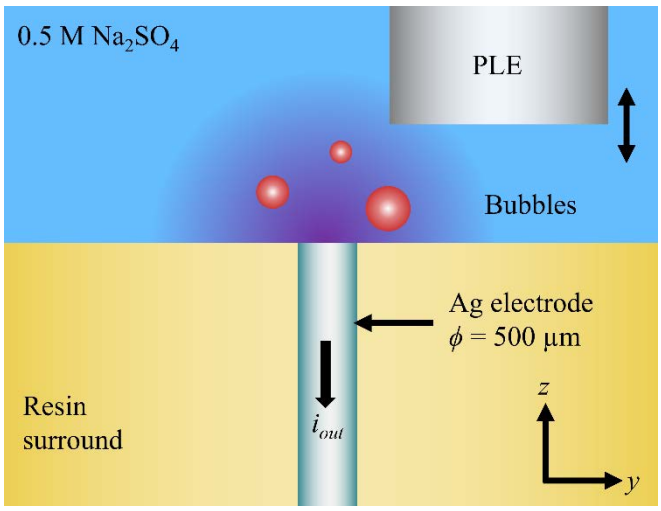

Figure 2.26 A schematic showing the square cell setup used in the ultrasonic horn cavitation experiments. The electrolyte solution is 0.5 M Na_2SO_4 at atmospheric temperature and pressure and under aerobic conditions. The working electrode is an Ag disc (ϕ = 500 µm) in a ϕ = 20 mm resin surround and the reference/counter electrode is a stainless steel rod. The horn (PLE) is mounted on a stage which allows to facilitate change the z and y separation. The *z* and *y* axes are displayed on the schematic for reference. The motion of the PLE is denoted by the double-headed arrow next to the PLE. Cavitation bubbles were observed forming at the tip of the PLE and moving down through the solution onto the electrode surface and its resin surround. The current response (i_{out}) of the electrochemical system was measured at the working electrode. The schematic is an illustration only and not to scale.

In the experiments performed, data captures of an applied AC perturbation of 25 mV zero to peak amplitude at 50 kHz, V_{app}, and current response, i_{out}, were made. The choice to use a smaller amplitude and 50 kHz frequency perturbation will be discussed in Chapter 4.1. The data captured was processed using the AC impedance technique described in Chapter 2.3 to elucidate the uncompensated resistance, R_u, as a function of time.

These measurements were made whilst applying ultrasound to the solution using the PLE at 23.65 kHz. The PLE tip was held at *z* separations of *z* = 2.5 mm, *z* = 5.0 mm and *z* = 7.5 mm. The *y* separation was changed to record the bubble activity seen at the electrode surface as a function of lateral distance from the ultrasonic horn. Data captures were made every 2 mm from a *y* separation of *y* = -10 mm to a *y* separation of *y* = 10 mm. Four separate data captures were recorded at each distance.

2.6.3 Bubble capture inside a square pore

To complement the high-speed impedance investigations carried out using the technique detailed in Chapter 2.3 another method for calculating impedance was developed. This technique used circuitry to generate a ‘demodulated’ current signal from the AC current response and calculate the impedance from the magnitude of the applied potential and magnitude of the ‘demodulated’ current response. Further details of the technique are

given in Chapter 6, and the circuit diagrams for the circuits employed can be found in Appendix 3.

An ultrasonic horn (see Table 2.2 for further information) was used as a 'piston-like' emitter (PLE) to generate cavitation bubbles above the surface of the resin. A square wave potential wave with a frequency of 1 MHz and zero-to-peak amplitude of 100 mV was applied across the square Ag working electrode and a stainless steel reference counter electrode. For further details of the custom made square wave potential function generators used see Table 2.2. Further discussion of the two function wave generators used can also be found in Chapter 6.

An image of a setup used in these experiments shown in Figure 2.27. The working electrode was a square 500 µm x 500 µm flat electrode, set inside a channel made from the resin surround. Further details of the electrode construction can be found in Chapter 2.5.3. The exact length of the channels etched can be found in the figure legends. The distance of the horn tip is measured relative to the pore by measuring the vertical distance from the surface of the resin, *z* separation, and lateral distance from the pore centre, *y* separation. The axes are shown for reference in Figure 2.27.

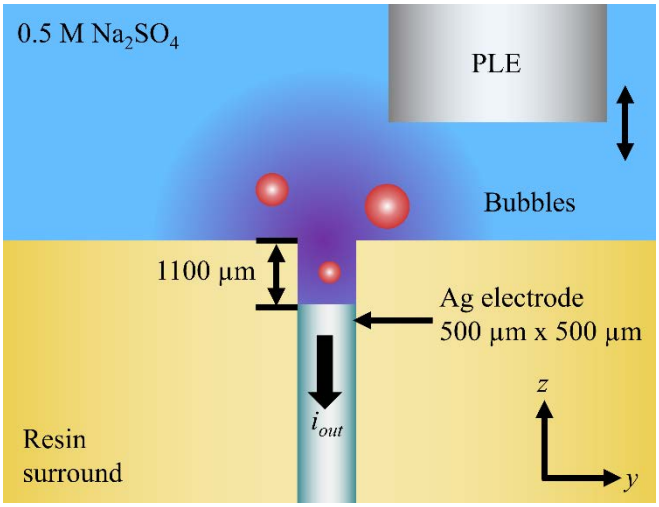

Figure 2.27 A schematic showing the square cell setup used in the ultrasonic horn cavitation experiments. The electrolyte solution is 0.5 M Na_2SO_4 at atmospheric temperature and pressure and under aerobic conditions. The working electrode is an Ag disc (500 µm x 500 µm) in a 500 µm x 500 µm x 1100 µm pore and resin surround. The reference/counter electrode is a stainless steel rod. The horn (PLE) is mounted on a stage which allows to facilitate change the *z* and *y* separation. The *z* and *y* axes are displayed on the schematic for reference. The motion of the PLE is denoted by the double-headed arrow next to the PLE. Cavitation bubbles were observed forming at the tip of the PLE and moving down through the solution onto the resin surround of the electrode and into the etched channel onto the working electrode surface. The current response (i_{out}) of the electrochemical system was measured at the working electrode. The schematic is an illustration only and not to scale.

The ultrasonic horn was turned on in short bursts using a trigger pulse (see Chapter 6 for further information of technique). The current response of the 500 µm x 500 µm Ag electrode was recorded as a function of time during the pulses of ultrasound. A cluster of bubbles formed underneath the PLE during ultrasonic resonance. Some of these bubbles broke away from the cluster and moved down onto the resin surround surface and into the channel (as seen in Figure 2.27).

Chapter 3 Cylindrical Cell Resonance

3.1 Boundary conditions

The cylindrical cell was chosen as a system for studying acoustically driven cavitation as these systems have a number of useful properties. First, the resonant frequencies are well defined, as discussed in Chapter 1, relating to their geometry and physical size. Second, the size of the cylindrical cell can be quite considerable, thus making them a useful analogue to scale up studies. Third, a range of frequencies can be applied to the cell from a single ultrasonic transducer attached to the cell itself. In the study reported here, resonant characteristics of the cell will be investigated using a variety of different physical measurements. In particular, the effect of a moving boundary on the resonance properties of the cell will be investigated.

The aluminium plunger provided a mobile upper boundary condition for the resonance cell. By varying the height of the plunger from the base of the cell, referred to here as the ‘*z* separation’, whilst applying ultrasonic waves of a constant frequency to the chamber it was possible to find the positions of normal modes in the resonance cell. These modes were first observed when the cell emitted a ‘hissing’ noise characteristic of acoustic cavitation.

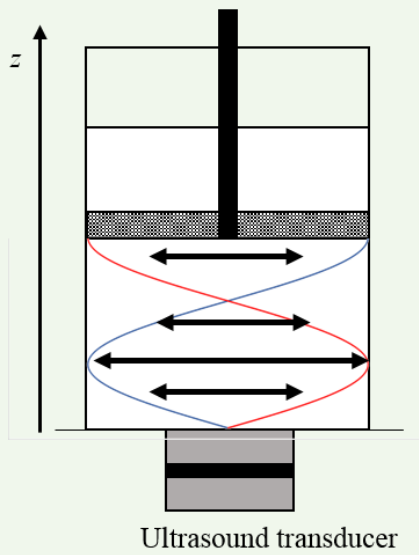

Figure 3.1 A diagram showing the position of a resonance mode inside a cylindrical chamber. The lines (—, —) represent the pressure fluctuations at the maximum and minimum value (i.e. 180° out of phase) and the arrows (—) the oscillation of the pressure. The pressure is at a minimum at the base of the cylinder at a maximum at the solid metal reflector.

The assumption was made that the aluminium disc surface and the transducers surface were pressure antinodes where regions of highest acoustic pressure should be expected. This is illustrated in Figure 3.1. At a boundary, or interface, between materials with different acoustic properties, such as at the aluminium plunger for our acoustic chamber, the incident sound wave can travel in two directions. First, the wave can continue to travel in the same direction as the incident wave (positive *z* direction), called the transmitted wave[88]. Second the wave can travel in the negative *z* direction and this is called the reflected wave[88]. The extent to which the wave is either transmitted or reflected at the boundary between the water in the cylindrical chamber and the aluminium plunger will depend on the value of the reflection factor, R_w, and transmission factor, T_w. These factors can be calculated from an acoustic property of the two materials called the characteristic acoustic impedance, $Z = \rho c$, where ρ is the density of the material and c is the speed of sound in the material[88]. The value of the reflection factor can be calculated by

$$R_w = \frac{Z_w - Z_a}{Z_w + Z_a} \tag{3.1}$$

where Z_w is the acoustic impedance of water, and Z_a is the acoustic impedance of aluminium. The reflection factor can thus take values $-1 \leq R_w \leq 1$[88]. The value of the transmission factor is given by

$$T_w = \frac{2Z_w}{Z_w + Z_a} \tag{3.2}$$

The transmission factor can hence take values $0 \leq T_w \leq 2$[88].

The acoustic impedance of both water and aluminium was calculated at 25°C using literature values for speed of sound and material density[89]. From these literature values the acoustic impedance of water, Z_w, was calculated to be 149.7 kg cm^{-2} s^{-1} and the acoustic impedance of aluminium, Z_a, was calculated to be 1733.4 kg cm^{-2} s^{-1}. From the acoustic impedance values the transmission factor was calculated to be 0.16 and the reflection factor was calculated to be -0.84. Hence at the solid/liquid interface most of the incident wave will be reflected and only a small amplitude wave will propagate through the metal and into the solution above the disc. With the correct chamber dimensions, see discussion in Chapter 1.6, the incident and reflected waves inside the cylindrical chamber will set up a standing wave structure. A schematic representation of the incident (I_w), reflected (R_w) and transmitted (T_w) waves in the chamber is given in Figure 3.2. The wave fronts are represented here by the arrows labelled I_w, R_w and T_w.

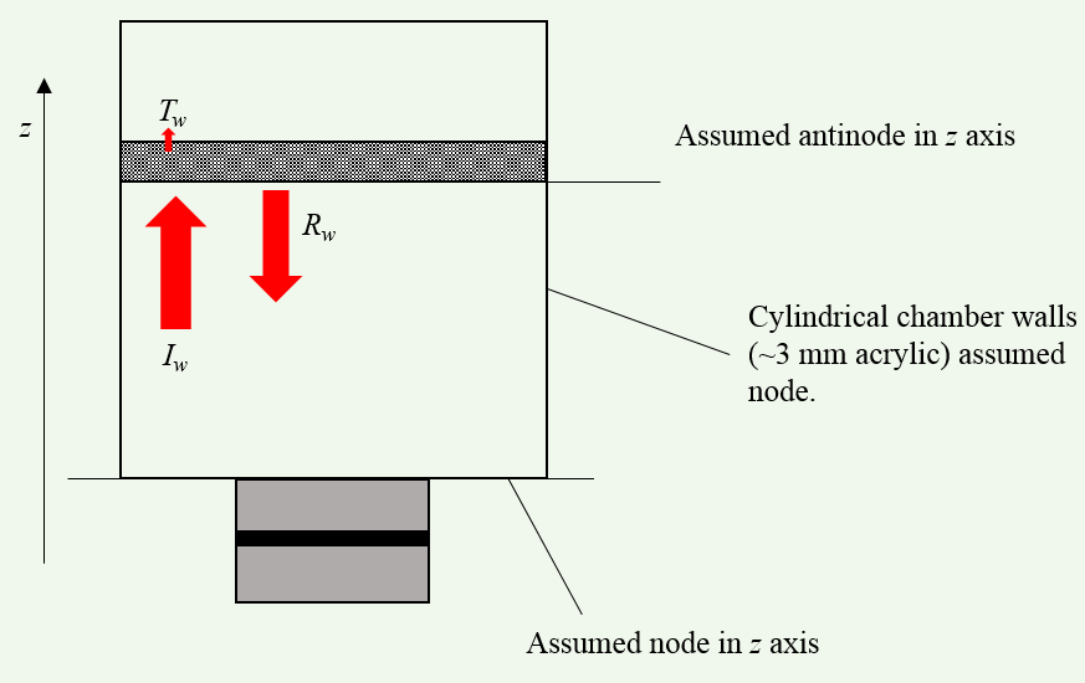

Figure 3.2 A representation of the direction of wave fronts inside the resonance cell. The label 'I_w' indicates the incident wave, 'R_w' the reflected wave and 'T_w' the transmitted wave. The relative size indicates the rough magnitude of the waves, with the reflected wave only slightly smaller than the incident wave as the majority of the energy emitted from the transducer is reflected at the boundary.

3.2 Using a current follower to monitor cavitation

At regions of high acoustic pressure in the cylindrical resonance cell acoustic cavitation was observed. The monitoring of this acoustic cavitation activity was achieved by adopting a number of electrochemical approaches. The first of these approaches was to employ an erosion/corrosion system[6,20,90]. In the first of these sets of experiments an aluminium disc electrode (250 µm diameter), set in epoxy resin within a stainless steel tube (which acted as the reference/counter electrode, as shown in Figure 2.17) was embedded in the aluminium disc reflector (as shown in Figure 2.13). The cylindrical cell used for these experiments was chamber 'A' (see Figure 2.1).

At the *z* separations at which resonance was observed, cavitation bubbles were observed over the surface of the disc and embedded electrode. These bubbles were seen to form a stable semi-circular cluster over the surface of the electrode in the centre of the disc. This is illustrated in Figure 3.3.

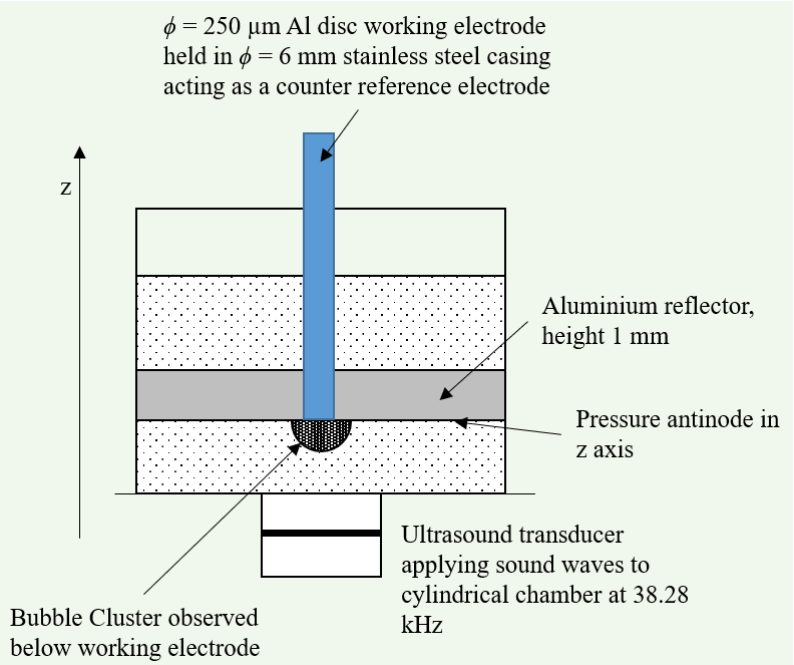

Figure 3.3 An illustration of the bubble cluster formed around the surface of the electrode inset into the disc during acoustic cavitation.

A current follower was employed to record the current passed at the aluminium working electrode as a function of time during acoustic excitation of the cell, as described previously in Chapter 2.5.4.1 and in previous work published by this group[66,91]. It was expected that during acoustic cavitation, spikes in recorded current would be observed. These spikes or transients are henceforth referred to as 'erosion/corrosion events'[91]. These were observed after electrode material had been removed from the surface by cavitation. The collapse of cavitation bubbles commonly causes erosion[1]. It was thus assumed that the surface oxide layer of the aluminium electrode was removed in the cavitation process. As the electrode surface was then reformed, a transient spike in current time profile was then observed a cartoon showing this process is shown in Figure 3.4.

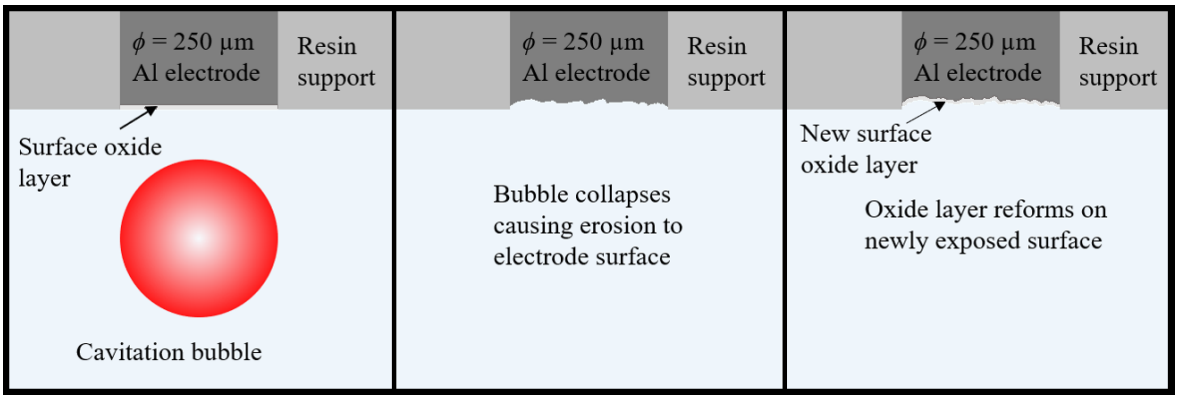

Figure 3.4 A cartoon showing the process by which the electrode is eroded by cavitation collapse and the surface oxide layer reforms on the newly exposed surface.

Ultrasonic cavitation activity was first observed over a short range of *z* separations between 26 mm and 31 mm.The sound intensity observed was seen to increase and diminish in intensity across the narrow *z* separation range in which this cavitation activity was observed. As the sound intensity increased, larger spikes of current were recorded. It was assumed that this indicated a higher pressure at the surface of the reflector therefore greater surface damage to the electrode was incurred. This would result in an increase in the roughness of the surface and so creating a larger surface area electrode. The number of erosion/corrosion events recorded also appeared to increase with increasing cavitation intensity. Figure 3.5 shows the current vs time plots for *z* separations of 26 mm and 31 mm with an applied ultrasound frequency of 38.28 kHz. The small difference in *z* separation has resulted in a decrease in the average peak height at 26 mm *z* separation compared to 31 mm *z* separation. The frequency of erosion/corrosion peaks is also slightly decreased. Changing the position of the reflector has altered the acoustic properties of the chamber and resulted in a decrease in the cavitation activity. This result was observed over a number of experiments.

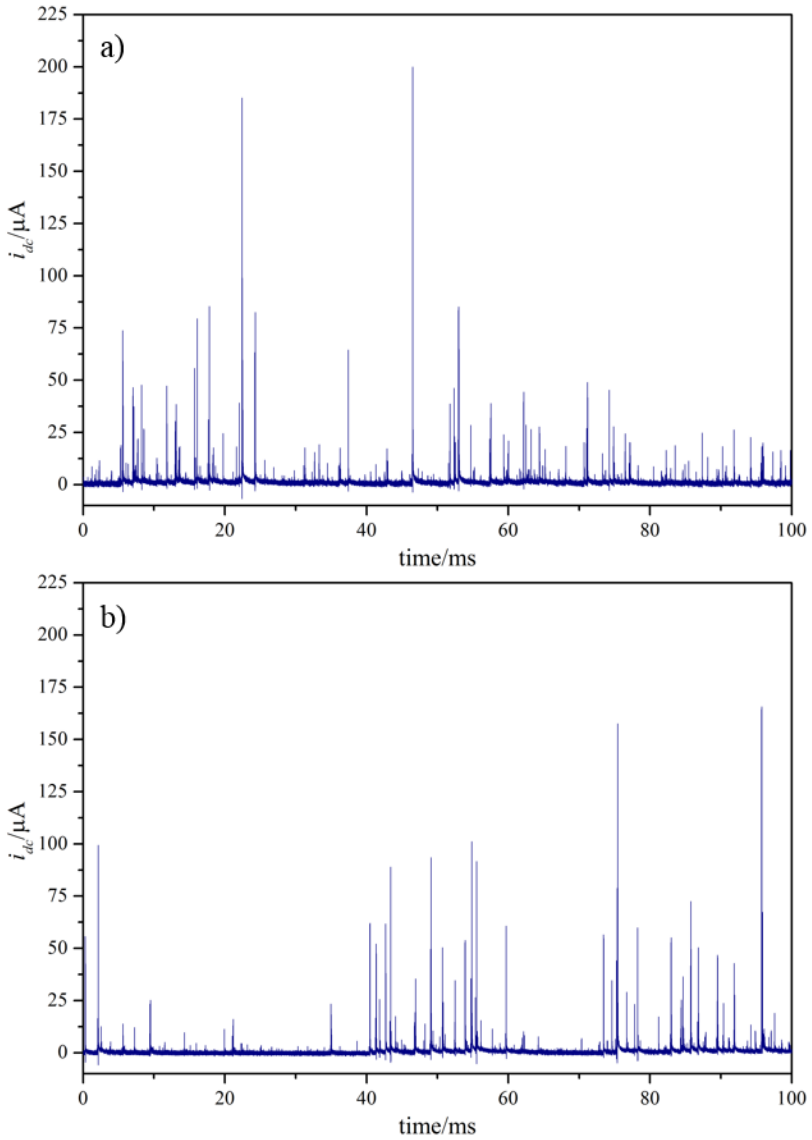

Figure 3.5 a) Plot showing the current, i_{dc}, (—) as a function of time for a 250 µm diameter Al disc within a resin support and a stainless steel outer case acting as a reference counter electrode at a z separation of 26 mm. **b)** Plot showing the current, i_{dc}, (—) as a function of time for a 250 µm diameter Al disc within a resin support and a stainless steel outer case acting as a reference counter electrode at a *z* separation of 31 mm. For both experiments the solution in the resonant chamber was 0.5 M Na_2SO_4. The ultrasonic transducer used is supplied by Ultrawave and operates at ~ 38 kHz. In this experiment the frequency applied to the transducer from the amplifier was 38.28 kHz. The solution temperature was 21 °C and the experiment was performed under aerobic conditions. Data acquired with a 1 MHz sample rate.

The disc was then moved to a *z* separation of 38 mm. No erosion/corrosion events were observed at this height and so it can be inferred that the conditions in the cell are not able to produce inertial cavitation over the surface of the electrode sensor under these conditions.

Acoustic cavitation was also observed to be present within the cell (using appropriate visual and audible observation) for a *z* separation of 53 mm. Despite the observation of

bubbles on the surface of the reflector and the characteristic hissing noise heard during cavitation, recording erosion/corrosion events proved to be challenging under these conditions. This was because the size of the current spikes was much smaller than at the resonance band around 30 mm *z* separation and so the transients were often not clearly visible owing to the drop in signal to noise ratio. An example of the current *vs.* time plot observed at *z* separations of 31 mm, 38 mm and 53 mm is given in Figure 3.6.

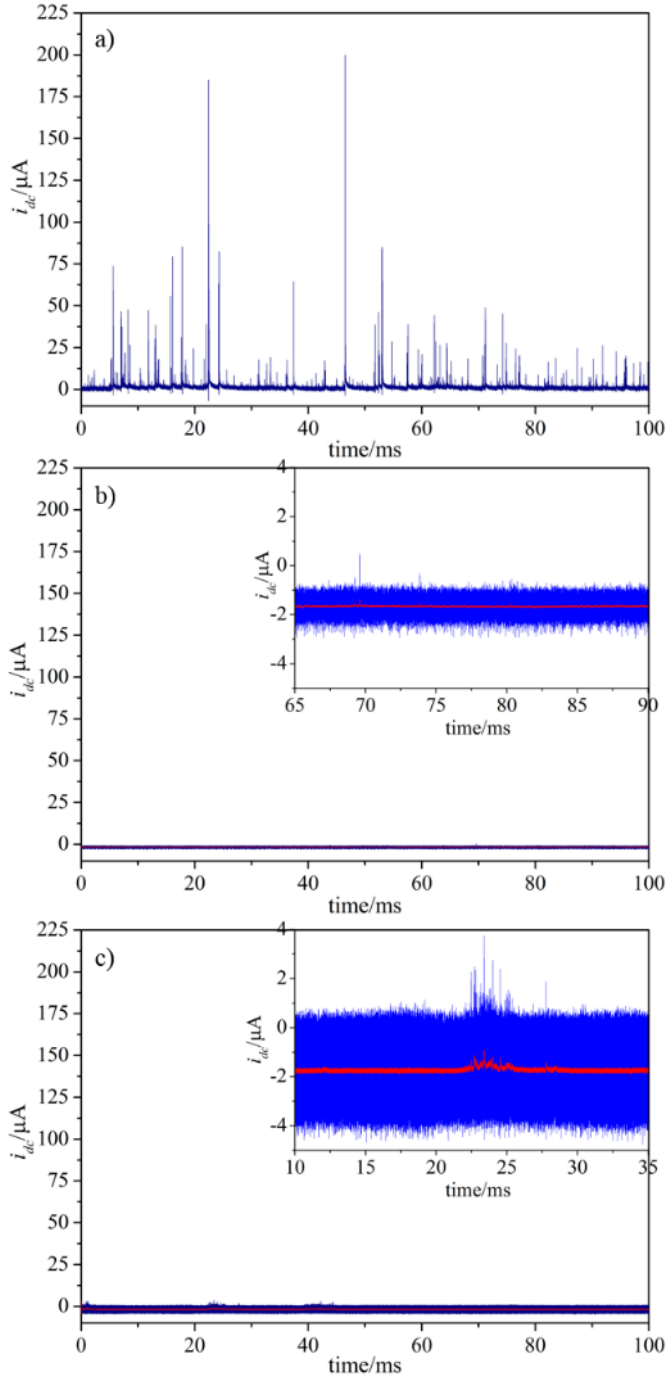

Figure 3.6 a) Plot showing the current, i_{dc}, (—) as a function of time for a 250 µm diameter Al disc within a resin support and a stainless steel outer case acting as a reference counter electrode at a z separation of 31 mm. **b)** Plot showing the current, i_{dc}, (—) and moving average of current (—) as a function of time for a 250 µm diameter Al disc within a resin support and a stainless steel outer case acting as a reference counter electrode at a *z* separation of 38 mm. **c)** Plot showing the current, i_{dc}, (—)and moving average of current (—) as a function of time for a 250 µm diameter Al disc within a resin support and a stainless steel outer case acting as a reference counter electrode at a z separation of 53 mm. For each experiment the solution in the resonant chamber was 0.5 M Na_2SO_4. The ultrasonic transducer used is supplied by Ultrawave and operates at ~ 38 kHz. In this experiment the frequency applied to the transducer from the amplifier was 38.28 kHz. The solution temperature was 21 °C and the experiment was performed under aerobic conditions. Data acquired with a 1 MHz sample rate.

The reduction in amplitude of the current transients at this *z* separation may suggest that the acoustic pressure at the surface was lower at this second pressure antinode or that the position of the cavitation centre was non ideal. There are two possible explanations for this observation. First, this may be due to some absorption of sound in the liquid. Second, it could be as a result of a change in symmetry of the resonance mode excited within the cell. This could change the shape of the acoustic profile in the *x-y* plane. The change in *x-y* plane profile could make it more difficult for a stable cluster to form over the electrode as it did at ~ 30 mm. The absence of a stable cavitation cluster would result in fewer erosion/corrosion events as the surface is not being constantly eroded by gas bubbles directly over the surface. Further experiments were needed to investigate the acoustic properties of the chamber.

Optical images of the aluminium electrode were also taken both before and after exposure to ultrasonic cavitation. From these images the effect on the surface of the electrode, as a result of the conditions employed, can be clearly seen. The freshly polished electrode in Figure 3.7 appears as a flat smooth disc surface. Figure 3.8 shows that exposure to erosion produced through inertial cavitation has damaged the aluminium surface making it much rougher.

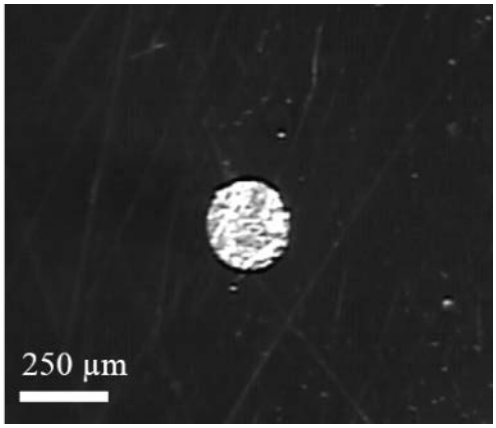

Figure 3.7 An image of a 250 µm aluminium disc electrode. The disc has been polished in a slurry of 0.3 µm aluminium oxide and ultra-pure water. The scale bar shows a length of 250 µm.

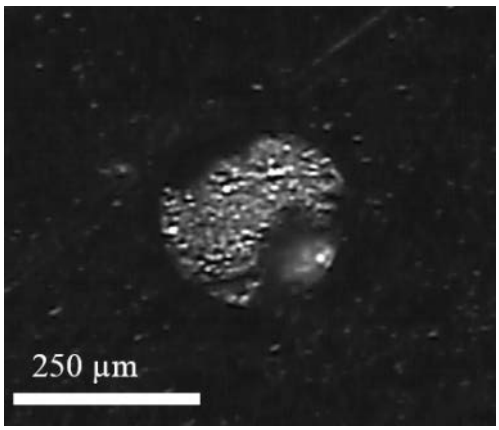

Figure 3.8 An image of a 250 µm aluminium disc electrode after ~ 3 minutes exposure to cavitation in a solution of 0.5 M Na_2SO_4. The solution temperature was ~ 20 °C and the cavitation was carried out in aerobic conditions. The scale bar shows a length of 250 µm.

The data presented shows that erosion/corrosion is generated within this environment. What is missing from this data is any dynamic information relating to the bubbles themselves. The next section will show how a more sophisticated electrochemical approach is able to characterise bubble activity in the absence and presence of inertial

cavitation (i.e. where erosion of the solid liquid interface may not be present, but bubble activity is).

3.3 AC impedance

3.3.1 Cavitation activity in a cylindrical cell

The monitoring of current at the working electrode indicated that inertial cavitation was causing damage to the electrode. However, the transient current changes observed are seen after the bubble collapse has caused erosion to the electrode surface. What is missing is any dynamic information relating directly to the bubble. To explore the cavitation system further, a novel AC impedance technique was developed to elucidate this dynamic bubble information. Further details of the technique devised can be found in Chapter 2.3. The electrochemical technique was employed to characterise the surface of the electrode cavitation and provide mechanistic evidence to support the findings of the erosion/corrosion system discussed in Chapter 3.2.

In the AC impedance technique devised an AC potential perturbation of 500 kHz with a zero-to-peak magnitude of 50 mV was applied across the working electrode and counter reference electrode. Both the input AC potential perturbation and AC current response of the working electrode were recorded as a function of time. The recorded AC potential perturbation and AC current response were then post-processed to elucidate the uncompensated resistance, R_u, working electrode capacitance, C, and Faradaic current, i_{dc} with a 2 µs resolution. Further details of the processing technique is described in Chapter 2.3. It was important for the purposes of calculating R_u and C from the data recorded to select a cell setup such that the measured phase angle between the applied AC potential and AC current (θ) remained somewhere roughly halfway between 0° and 90° (see Figure 2.9). As θ decreases in size the value of capacitive resistance, X_C, becomes smaller and it becomes more difficult to accurately calculate the electrode capacitance from this value. Therefore, to accurately measure the capacitive resistance (and hence capacitance) an electrode with a diameter of 100 µm was chosen. An electrolyte concentration of 0.2 M Na_2SO_4 was also employed. This had the effect of increasing θ compared to a 250 µm diameter electrode in 0.5 M Na_2SO_4 by decreasing the electrode surface capacitance.

An AC potential of 50 mV zero-to-peak amplitude at 500 kHz to the electrochemical system and the AC current response at a 100 µm aluminium disc working electrode was recorded. After the processing described in Chapter 2.3 the uncompensated resistance, electrode capacitance and Faradaic current was elucidated with a time resolution of 2 µs. The initial AC potential perturbation and current response and processed data showing R_u, C and i_{dc} is shown in Figure 3.9.

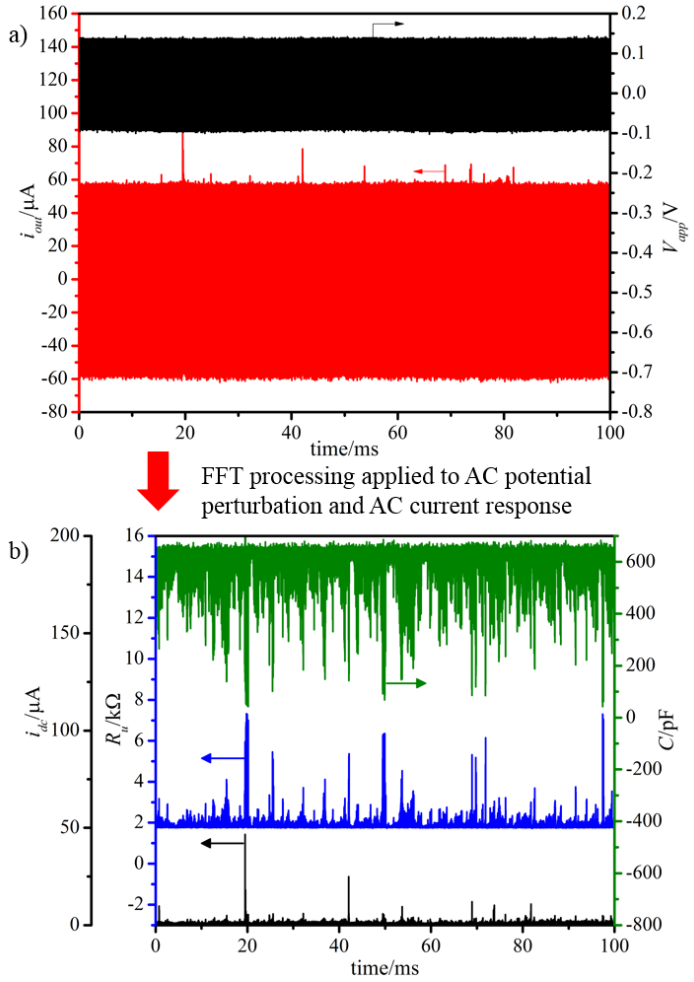

Figure 3.9 a) Plot showing the AC electrode current response, i_{out}, (—) and reference voltage, V_{app}, (—) as a function of time for a 100 µm diameter Al disc within a resin support and a stainless steel outer case acting as a reference counter electrode. The solution in the resonant chamber was 0.2 M Na_2SO_4. The frequency applied to the transducer from the amplifier is 37.97 kHz and the z separation was 32 mm. The solution temperature was 22 °C and the experiment was performed in aerobic conditions. Data acquired with a 10 MHz sample rate. **b)** Plot showing the resistance, R_u, (—) capacitance, C, (—) and Faradaic current, i_{dc}, (—) as a function of time for a 100 µm diameter Al disc within a resin support and a stainless steel outer case acting as a reference counter electrode. The solution in the resonant chamber was 0.2 M Na_2SO_4. The frequency applied to the transducer from the amplifier is 37.97 kHz and the z separation was 32 mm. The solution temperature was 22 °C and the experiment was performed in aerobic conditions. Data acquired with a 500 kHz sample rate.

A section of the AC potential and AC current response from Figure 3.9 a) is shown in Figure 3.10. The AC current response shows a number of changes in amplitude, these

appear as a result of cavitation processes occurring at or near to the solid/liquid interface of the aluminium electrode. The majority of these amplitude changes appear as a reduction in current from the typical current amplitude under these electrode conditions (~50 µA).

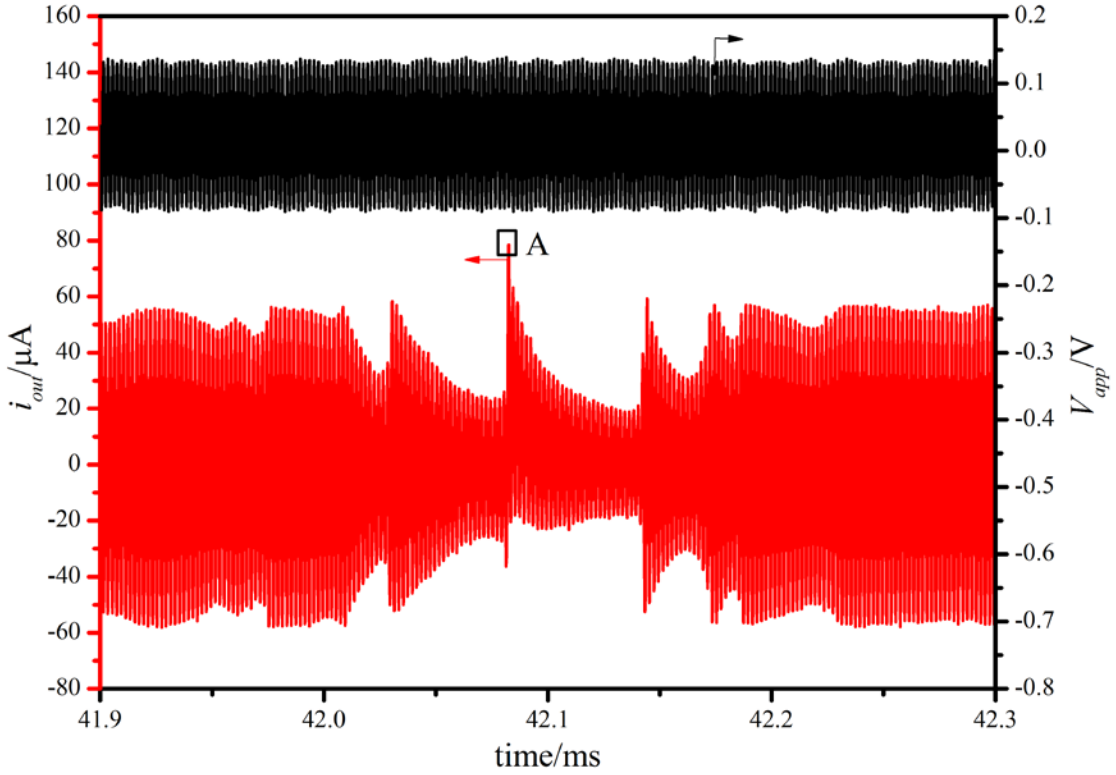

Figure 3.10 Plot showing the AC electrode current response, i_{out}, (—) and reference voltage, V_{app}, (—) as a function of time for a 100 µm diameter Al disc within a resin support and a stainless steel outer case acting as a reference counter electrode. The solution in the resonant chamber was 0.2 M Na_2SO_4. The frequency applied to the transducer from the amplifier is 37.97 kHz and the *z* separation was 32 mm. The solution temperature was 22 °C and the experiment was performed in aerobic conditions. Data acquired with a 10 MHz sample rate.

Increases in current above 50 µA are also observed but these are much less frequent than reductions in amplitude. Such an increase in current is highlighted and labelled A in the Figure 3.10. A trigger threshold level was set at 50 µA, so peaks in current such as point A in Figure 3.10 were needed to trigger the data acquisition. The FFT approach described in Chapter 2.3 was then used to elucidate further information about the system. Using this approach the impedance data was calculated along with the Faradaic current as a function of time with a temporal resolution of 2 µs. The results of this analysis are shown in the plot of resistance, R_u, capacitance, C_{dl}, and Faradaic current, i_{dc}, as a function of time in Figure 3.11.

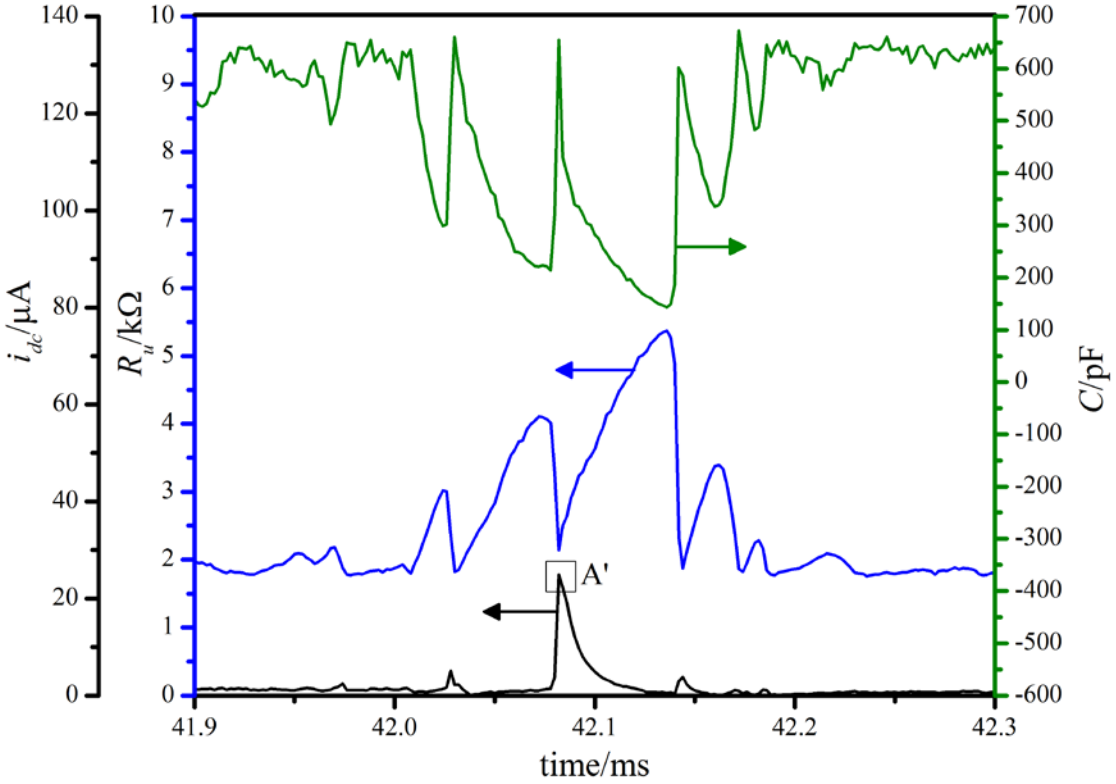

Figure 3.11 Plot showing the resistance, R_u, (—) capacitance, C, (—) and Faradaic current, i_{dc}, (—) as a function of time for a 100 μm diameter Al disc within a resin support and a stainless steel outer case acting as a reference counter electrode. The solution in the resonant chamber was 0.2 M Na_2SO_4. The frequency applied to the transducer from the amplifier is 37.97 kHz and the z separation was 32 mm. The solution temperature was 22 °C and the experiment was performed in aerobic conditions. Data acquired with a 500 kHz sample rate.

The Faradaic current calculated from this analysis technique, Figure 3.11 (—), shows the same trend as that seen in previous current follower investigations. As was previously noted the Faradaic current exhibits transient spikes in current. These are attributed to the erosion of material from the electrode surface and named ‘erosion/corrosion’ events. The largest of these current spikes, labelled A’, in Figure 3.11 corresponds directly to the current peak, labelled A, observed in the alternating current in Figure 3.10. Spikes of increased resistance were also seen in the resistance data. A distinctive asymmetric shape was observed in the resistance time transients. In each case the resistance increases gradually (over ~ 0.05 ms) then sharply decrease back to a base level resistance. The shape of this resistance transient resembles the shape of the radius time profile for a transient cavitation bubble (see Figure 1.2). During bubble growth the electrode surface is partially occluded, thus increasing the measured resistance across the electrodes. When the bubble reaches a maximum size and collapses violently the resistance decreases sharply. The spike in current data was always observed to occur immediately after the decrease in resistance. The new data provided by the AC impedance therefore supports the previous assumption

that the current spikes were caused by the erosion of collapsing transient cavitation bubbles.

The dynamics of bubble growth over the electrode surface can also be seen from the capacitance data. A similar pattern is observed in this capacitance data to the resistance data. The shape of both the resistance and capacitance transients in Figure 3.11 is the same except in the case of the capacitance data the shape is inverted. This inversion is seen as the electrode capacitance is dependent on the active surface area of the working electrode. As a bubble grows over or near the electrode surface the effective active electrode area is decreased and so the capacitance decreases. Similarly when the bubble collapses the effective surface area is increased and so the electrode capacitance rises rapidly back up to a base level. It should be noted here that the cavitation bubble does not necessarily need to be touching the surface of the electrode to cause changes to the measured capacitance of the working electrode and that changes in capacitance can occur when insulating particles (or in this cases, bubbles) approach the electrode surface.

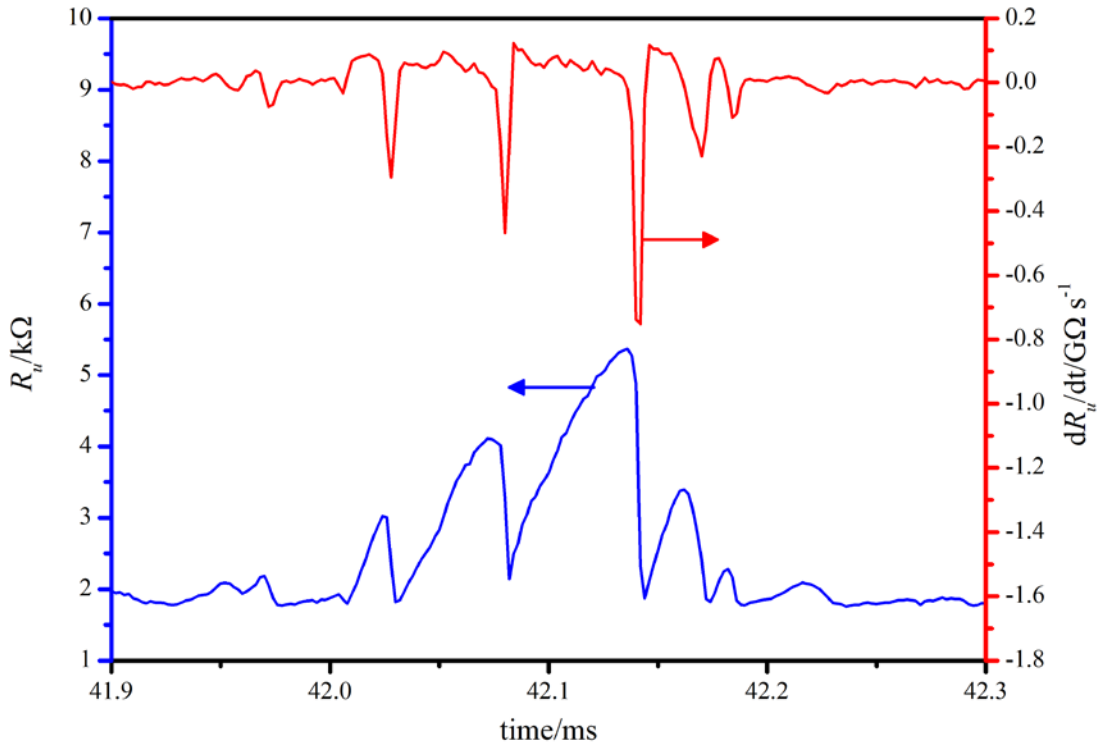

Figure 3.12 Plot showing uncompensated resistance, R_u (—) and first time differential of R_u (—) as a function of time. The solution in the resonant chamber was 0.2 M Na_2SO_4. The frequency applied to the transducer from the amplifier is 37.97 kHz and the *z* separation was 32 mm. The solution temperature was 22 °C and the experiment was performed in aerobic conditions.

The time differential of R_u was calculated from the data recorded and is reported in Figure 3.12 (—). This shows that the rate of change of resistance is very rapid within the resistance changing at a rate approaching 1 GΩ s^{-1} for the largest of the transients. It is the rapidity of this bubble collapse which is seen to cause erosion of material from the electrode surface.

3.3.2 Characterisation of surface damage

In the course of multiple experiments, where the electrode was not re-polished between each experiment, the background capacitance level was observed to rise over time. Aluminium is known to be a soft metal, 2.9 on the Mohs scale[92], therefore making the electrode material relatively easy to erode with exposure to cavitation. The softness of the material is both an advantage and disadvantage for its use as a 'sensor'. The advantage of using aluminium as our 'sensor' material is that the kinetics of the corrosion process are known to be fast, hence we are able to observe transients as the electrode material is eroded. At the same time the softness of the material proves to be a disadvantage for aluminium as being easily eroded means the electrode has a short lifetime as a sensor.

The removal of aluminium from the electrode increased the surface roughness of the electrode. This increase in surface roughness after exposure to ultrasound can be seen in the before and after images in Figures 3.7 and 3.8.

The experiment described in Chapter 2.5.4.3 was used to quantify the change in surface quality before and after exposure to ultrasound. A set of results are tabulated in Table 3.1. The error in phase angle was calculated by excel 'data analysis' and the errors in resistance and capacitance were then calculated by propagation of errors in phase angle and impedance, *Z*. Further details of the error propagation method can be found in Appendix 4.

	Polished electrode	**After ~ 3 minutes exposure to ultrasound**
Resistance, R_u/kΩ	1.047 ± 0.076	0.907 ± 0.085
Capacitance, C/pF	396 ± 39	640 ± 110
Phase angle, θ/deg	37.5 ± 3.7	28.7 ± 4.8

Table 3.1 A tabulation of the calculated resistance, R_u, capacitance, C, and phase angle, θ, for the Al working electrode after polishing in 0.3 μm alumina and after exposure to erosive cavitation. The working electrode is a 100 μm diameter Al disc and the reference/counter is stainless steel. The solution used was 0.2 M Na_2SO_4. The solution temperature was 23 °C and the experiment was performed in aerobic conditions.

As the surface of the electrode becomes roughened with the exposure to cavitation the capacitance of the electrode rose and thus phase shift decreased as the magnitude of the capacitive resistance side of the triangle is decreased (see Figure 2.9). This indicates that the surface area of the electrode has increased. A very small change is also seen in the uncompensated resistance (R_u) value. However, as this change is small, only ~10%, in comparison to the ~85% change observed in the capacitance value, this cannot be considered statistically significant. This change in calculated resistance may arise owing to the simplicity of the RC circuit model used to calculate R_u and C from Z and θ. Changes in the value θ will cause small changes the value of cos θ used to calculate R_u. Thus although there is no real drop in resistance the lower phase angle recorded results in slightly lower values of resistance being calculated.

The results of a control experiment in which the surface was artificially roughened with different polishing media is shown in Table 3.2.

	0.3 µm alumina	**1 µm alumina**	**25 µm alumina**	**Emery paper**
Resistance, R_u/kΩ	1.470 ± 0.071	1.628 ± 0.060	1.621 ± 0.048	1.755 ± 0.058
Capacitance, C/pF	150 ± 5.10	216 ± 8.84	480 ± 34.5	320 ± 18.7
Phase angle, θ/deg	55.3 ± 1.55	42.1 ± 1.55	22.2 ± 1.55	29.5 ± 1.65

Table 3.2 A tabulation of the calculated resistance, R_u, capacitance, C, and phase angle, θ, for the Al working electrode in different polishing media. The working electrode is a 100 µm diameter Al disc and the reference/counter is stainless steel. The solution used was 0.2 M Na_2SO_4. The solution temperature was 23 °C and the experiment was performed in aerobic conditions.

As the surface area increases by polishing with coarser materials, the capacitance of the electrode increases and the phase angle drops as expected. When the electrode was sanded with emery paper however, the recorded capacitance was lower than for the 25 µm alumina polishing. There are explanations for this observation. First, the emery paper creates larger surface defects, rather than a larger number of defects. This would not increase the surface area of the electrode as much as the coarse polish and so the capacitance recorded is lower for the emery paper sanded electrode. Second, the 25 µm alumina particles provide a coarser polish than the fine sandpaper used, so in fact sanding the electrode with the emery paper makes the surface smoother than after the polish in 25 µm alumina. The increase in electrode capacitance is the same as the observation made after exposing the electrode to ultrasound. This control experiment gives further credence to the idea that the cavitation activity is causing the erosion of material away from the electrode surface.

The AC impedance method gave further evidence that the bubbles generated in the cavitation environment have an influence on the erosion/corrosion observed at the electrode. The next step in the observation of this phenomenon was to quantify the amount of cavitation activity observed as a function of z separation within the cylindrical cell.

3.4 Quantifying cavitation activity

The observations of both the current follower and high-speed AC impedance techniques showed that the cavitation bubbles resulted in ‘erosion/corrosion’ activity at the electrode

surface within the cylindrical cell. Further experimental analysis was required to place a value on the level of this activity and discover under what acoustic and geometric conditions the activity at the electrode surface was greatest.

This was first achieved by taking a count of the number of transients in the data recorded from the high-speed AC impedance method. Previous work performed has shown that aluminium electrodes exposed to cavitation for prolonged periods of time have been shown to exhibit considerable surface damage[93]. It was therefore necessary to consider an alternative electrode material for the following experiments to quantify the cavitation activity inside the cell. The material chosen to replace aluminium as the electrode material was titanium[93]. This was chosen as it is a stronger metal than aluminium (4.0 on the Mohs compared to 2.9 for aluminium[92]).

Titanium forms a passive oxide film when held at a potential of 0 V vs. stainless steel, similar to aluminium[93]. Titanium therefore also produces transient current peaks when cavitation events erode the electrode material[93]. However the amplitude of these transient current peaks is significantly reduced compared to those of aluminium (approximately one tenth of the amplitude of the aluminium current transients[93]). The kinetics for the formation of the passive oxide film are also slower for titanium than aluminium, meaning that the peak duration is longer for titanium than for aluminium. In the work performed by Vian[93] a current transient from a titanium electrode took ~ 200 μs to return to 10 % of the peak value compared to ~ 10-40 μs for an aluminium electrode. The small amplitude and longer period of these current transients results in a decrease of signal to noise ratio, making them more difficult to see and record[93].

As less surface damage to the electrode is incurred by using titanium in successive experiments compared to aluminium, the need to dissemble the system to re-polish the working electrode between successive experiments was reduced. In this way the conditions inside the cell could be kept the same for each experiment performed. However the small amplitude current transients and slow electrode kinetics meant that the cavitation activity of the cell could not be measured by monitoring the current and therefore the novel AC impedance method (see Chapter 2.3 for description of technique) proved more reliable to measure the cavitation activity at the titanium electrode.

The cavitation activity experiments were performed using an 80 μm diameter titanium disc working electrode and stainless steel support used as a counter reference electrode. The

measured phase angle for this titanium electrode was smaller than the measured phase angle for the 100 µm aluminium electrode. As the phase angle decreases in size the accuracy of the calculated capacitance values decreases (see Appendix 4 for propagation of error calculations). As a result the capacitance of the titanium electrode could not be accurately calculated for these experiments. Therefore the uncompensated resistance transients were adopted to measure the cavitation activity of the cell.

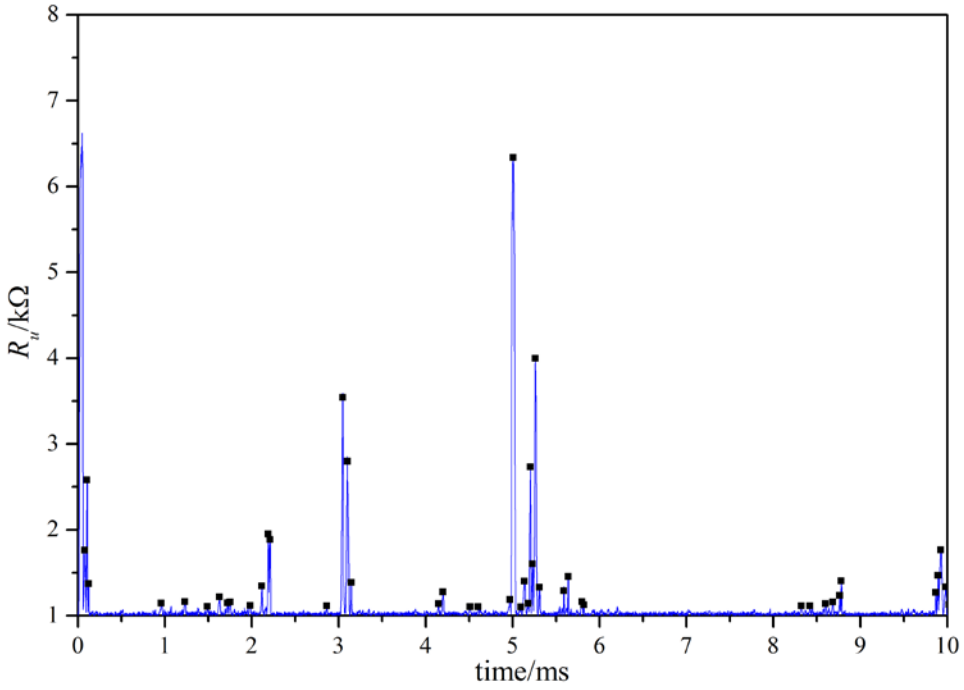

Figure 3.13 Plot showing resistance, R_u, (—) as a function of time for an 80 µm diameter titanium disc electrode within a resin support at open circuit potential and a stainless steel outer case acting as a reference electrode. The assigned peaks for this data section (■) is also shown. The threshold resistance value for the peaks was 1.10 kΩ. The electrolyte solution was 0.5 M Na_2SO_4. The frequency applied to the transducer from the amplifier is 38.8 kHz and the *z* separation was 28 mm. The temperature of the solution was 23 °C and the experiment was carried out in aerobic conditions. The data was acquired with a 500 kHz sample rate.

Experiments were performed to calculate an average number of resistance peaks or 'bubble events' as described in Chapter 2.5.4. Three measurements of each individual experiment were made and so the average number of bubble events recorded represents a mean average of three values. An example of a set of resistance transients with assigned peaks above the threshold level of 1.1 kΩ in Figure 3.13.

3.4.1 Cavitation activity at 0 V *vs.* Reference

It was observed that as the acoustic bubble activity inside the cylindrical resonance cell (chamber 'A') increased the number of resistance transients increased (similar to the current transients observed in Figures 3.5 and 3.6, see Chapter 3.2 for discussion). The number of resistance transient peaks in 100 ms could therefore be used as a measure of

how much bubble activity was occurring inside chamber 'A'. Using the average number of cavitation 'events' recorded at each *z* separation in the cylindrical cell, an activity profile was built of 'events' as a function of *z* separation. The activity profile was produced with the titanium electrode at 0 V *vs.* stainless steel (-0.493 V *vs.* MMS). This potential was chosen so that the electrode was in a passive region with no electrochemical activity (see Figure 3.22 and Chapter 3.4.4 for further discussion of applied potential). The activity profile produced is shown in Figure 3.14. This clearly showed the activity occurring in three bands from 2 mm – 10 mm (labelled band W), from 25 mm to 32 mm (labelled band X) and from 51 mm – 61 mm (labelled band Y). This banding is evidence that cavitation only occurs at the disc surface when a normal mode has been reached in the cell. By using theoretical models of the acoustic waves inside a cylinder it is possible to correspond the observed positions of cavitation activity to positions of high acoustic pressure.

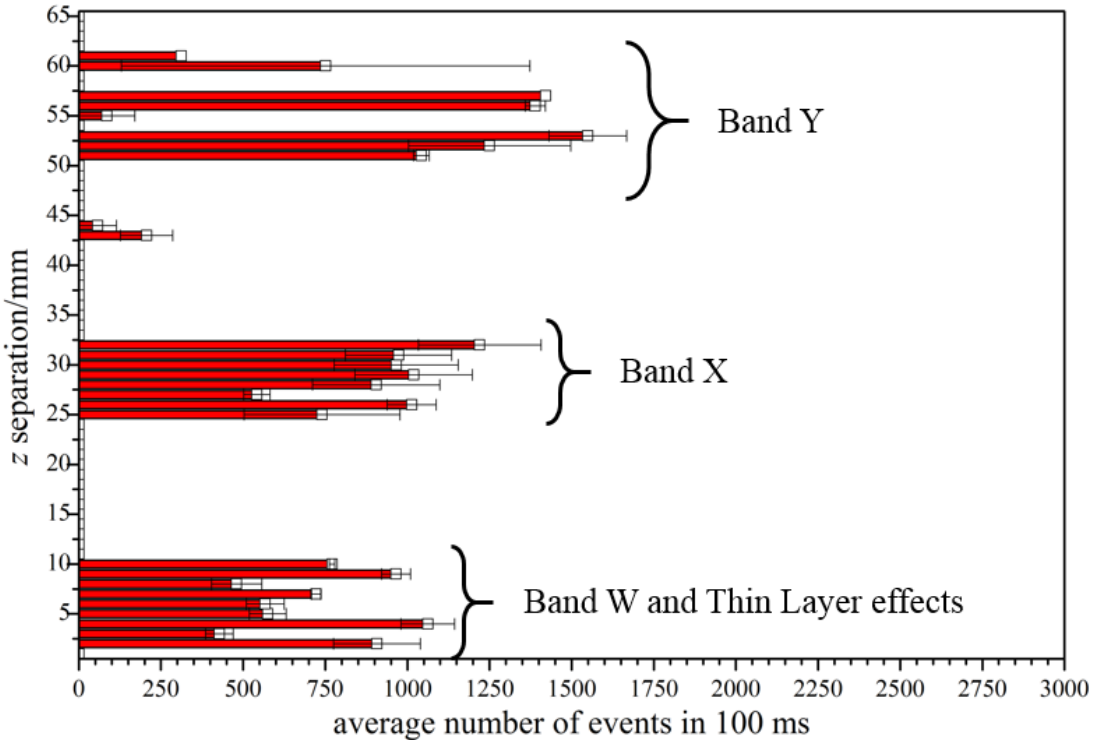

Figure 3.14 Plot of the number of events (■) as a function of *z* separation for an 80 µm diameter titanium disc within a resin support at open circuit potential and a stainless steel case as a reference electrode. Each event number is an average of three separate experiments performed at each height. Experiments were performed over a number of days with an electrolyte solution of 0.5 M Na_2SO_4 at a temperature from 21 – 23 °C in aerobic conditions. Data from individual scans was acquired with a 500 kHz sample rate.

The position of the first resonance band (as will be discussed further in Chapter 3.4.2) is at a *z* separation of 10 mm according to the mathematical model employed. This distance is equal to a quarter of the wavelength of the ultrasound wave applied by the transducer. As

this *z* separation is small this first resonance band is incorporated into what is described as a thin layer effect where the 'bubble activity' recorded at the electrode arises due to the electrode proximity to the ultrasonic transducer rather than cavitation produced at the reflector surface. This has resulted in the first resonance band appearing broader than is predicted.

A significant variability was seen in the average number of 'bubble events' recorded per data run (100 ms). This is likely due to the nature of the cavitation process itself where the position and stability of the bubble cluster formed over the electrode was variable. It was observed that if a stable cluster does not form or the cluster formed is not centred over the titanium working electrode surface, the number of transients counted dropped. It was observed that central stable clusters were more easily formed in resonance bands W and X than band Y. The changes in cavitation cluster stability for band X (Figure 3.15) and band Y (Figure 3.16) are shown diagrammatically.

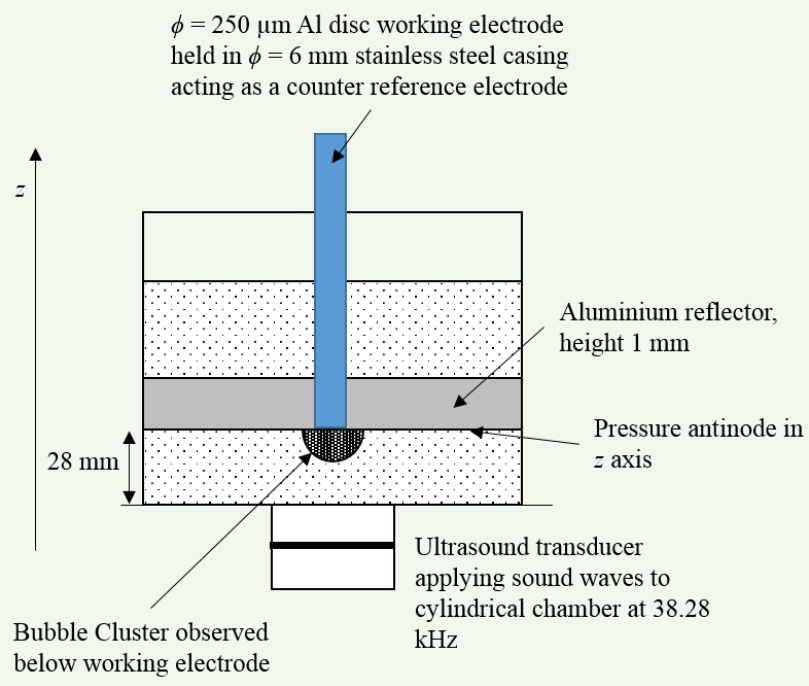

Figure 3.15 A diagram showing chamber 'A' and stable bubble cluster under the working electrode at a *z* separation of 28 mm (in resonance band X).

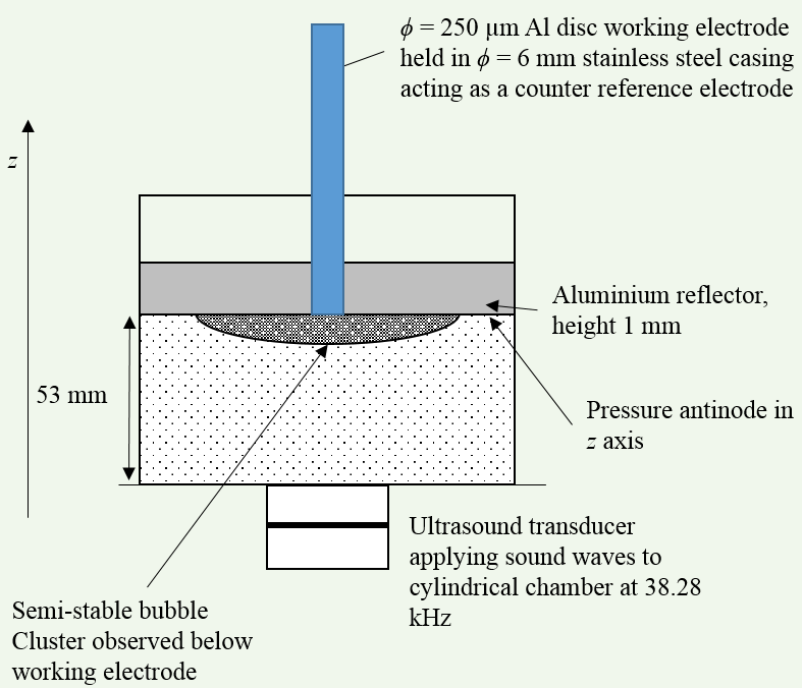

Figure 3.16 A diagram showing chamber 'A' and less stable bubble cluster under the working electrode at a z separation of 53 mm (in resonance band Y).

As a result of the change in cluster stability over the working electrode the error in average number of transients counted at each *z* separation is smaller in band X than band Y. The range in average number of transients through the band is also smaller for band X than for band Y.

In resonance band Y the number of transients counted spanned a larger range than in band X. This lead to the result that for some *z* separations in band Y a larger number of 'bubble events' were recorded than in band X. This was in some ways a surprising result as the intensity of the noise during cavitation was greater in band X. It was intuitively expected therefore that the cavitation 'activity' would be greater in this band. The larger number of 'bubble events' in band Y would indicate the opposite is the case. For example at a *z* separation of 53 mm the average number of 'bubble events' was 1544, which is 324 'bubble events' more than the highest average number of events counted in band X. This result cannot be explained by the stability of the cavitation cluster or intensity of cavitation 'noise'. Another explanation is required to justify this observation.

The reason for this result could possibly be due to the distribution in size of transient resistance peaks. Histograms showing the height of the resistance peak and the number of cavitation events were made. Figures 3.17 and 3.18 show two histograms, one for an experiment performed at a disc height of 30 mm and one at a disc height of 53 mm.

At a *z* separation of 53 mm all of the peaks recorded had resistance values between 1.5 kΩ and 3.1 kΩ with the majority of the peaks being recorded between 1.5 kΩ and 2.7 kΩ. At 30 mm the distribution of peak heights recorded is much broader, from a resistance value of 1.0 kΩ to the largest resistance recoded at 7.7 kΩ. The presence of these larger resistance peaks in the lower resonance band may be masking the smaller events so in total, fewer peaks are counted. In the higher band no very high resistance peaks are seen and so all of the smaller size events can be seen resulting in a larger number of events counted.

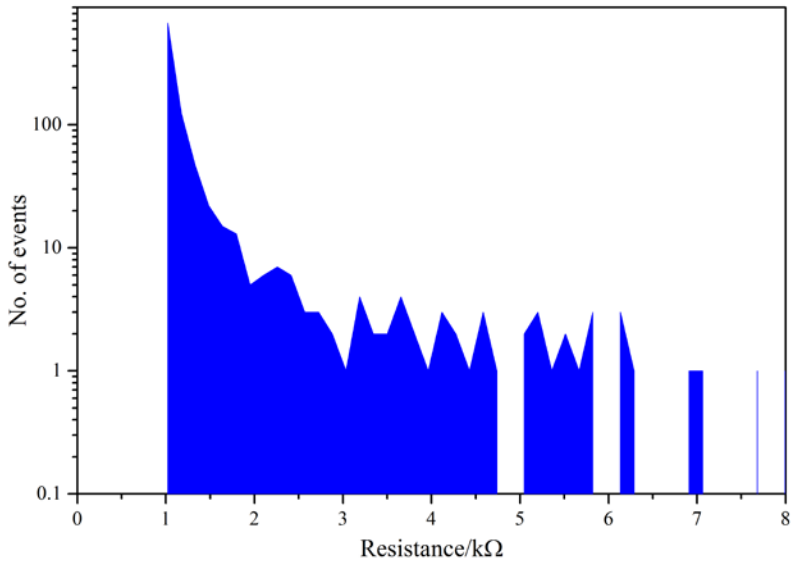

Figure 3.17 Histogram plot showing distribution the magnitude of resistance peaks and number of events recorded at each resistance at a *z* separation of 30 mm. The temperature of the solution was 23 °C and the experiment was carried out in aerobic conditions. The data was acquired with a 500 kHz sample rate.

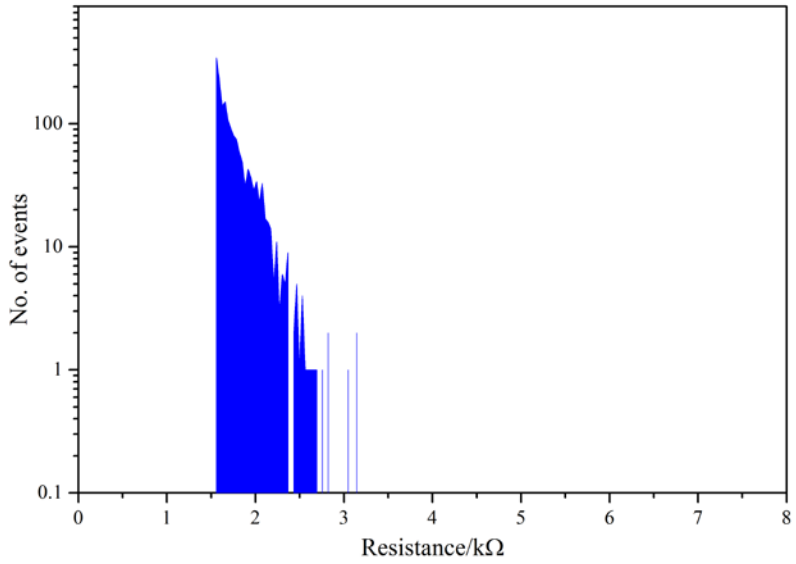

Figure 3.18 Histogram plot showing distribution the magnitude of resistance peaks and number of events recorded at each resistance at a *z* separation of 53 mm. The temperature of the solution was 23 °C and the experiment was carried out in aerobic conditions. The data was acquired with a 500 kHz sample rate.

The other point to note in the data displayed above is the change in lowest resistance peak value between the two data sets. This indicates that between the two experiments the base resistance value had changed. The reaction conditions were kept identical as far as possible, by using the same electrode polished to a glassy finish using 0.3 μm alumina, the same electrolyte solution and the same ultrasound frequency. However, as the series of experiments were performed over several days the experimental conditions could not be kept the same. The difference in conditions, for example the age of the solution used in the cell, could be the cause of this change in baseline recorded resistance.

The number of resonance positions found in the investigations detailed above was limited by the size of the cylindrical chamber. Therefore further experiments were performed to investigate whether by using a larger chamber multiple resonance positions could be found. A second cylindrical chamber (chamber ‘B’, see Figure 2.1) was fabricated for this purpose. The high-speed AC impedance data analysis method used to quantify cell activity in chamber ‘A’ was used on chamber ‘B’. A transducer with a lower driving frequency, 28.9 kHz was also employed. By decreasing the driving frequency, the wavelength was increased, thus eliminating the issue observed with chamber ‘A’ where the first band (band W) was incorporated into thin layer effects. Nine bands of activity were observed between 0 mm and 270 mm using chamber ‘B’. Figure 3.19 shows the average number of events as a function of reflector height.

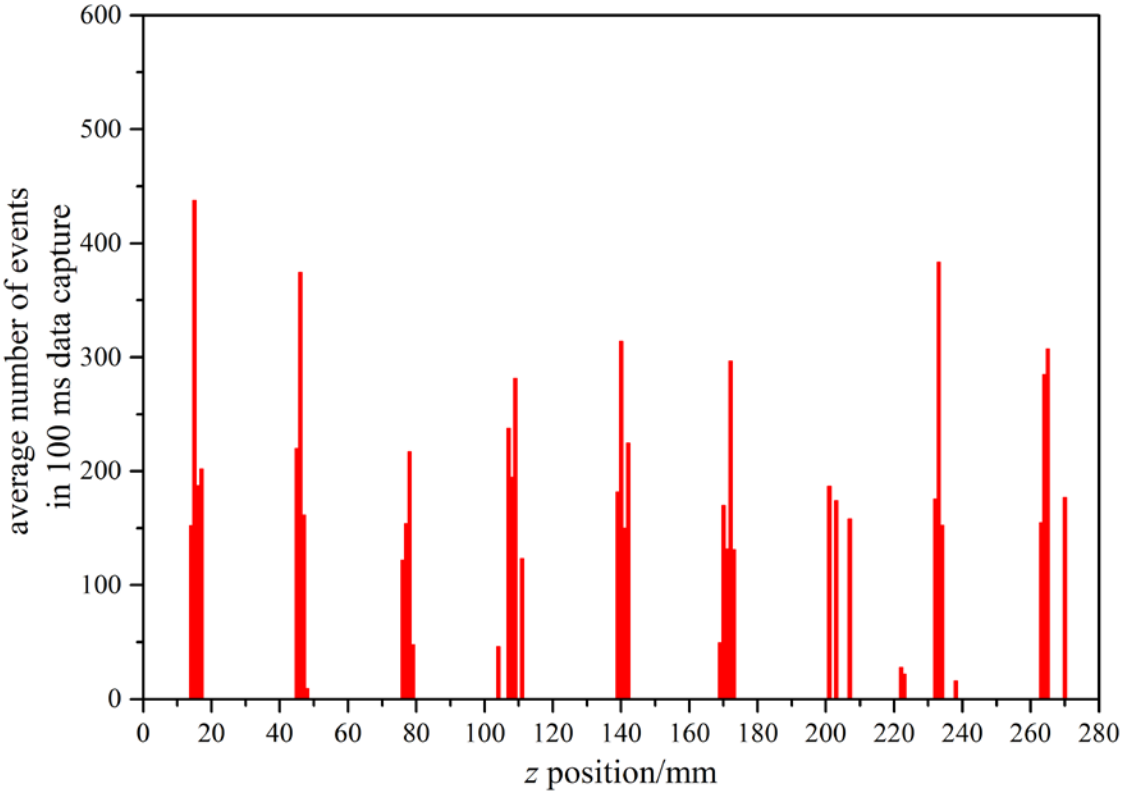

Figure 3.19 A graph showing the average number of 'bubble events' (■) in 100 ms data captures as a function of the reflector height from the base of chamber 'B' (*z* position). Four separate data captures were made at the heights at which cavitation was observed. An 80 µm diameter titanium disc was the working electrode and the steel reflector and rod acted as the reference counter electrode. The ultrasound transducer frequency was 28.9 kHz with an amplitude of 1.5 V peak to peak. This signal was amplified by 39 dB. The electrolyte solution was 0.5 M Na_2SO_4 in aerobic conditions and at atmospheric pressure. The ambient temperature varied between 20 – 27 °C across the experiments.

The 'bubble activity' in Figure 3.19 is seen in narrow bands (3-4 mm in width) and the bands are spaced at regular intervals of approximately 31-32 mm. Within individual experiment runs the range of the resonance band was in fact only observed to be around 1 mm in width. However, changes to the ambient temperature meant the position of the resonance band shifted over successive scans. This is because the changing temperature of the solution is altering the speed of sound through the liquid[89].

3.4.2 Modelling the pressure field inside the cylindrical cell

A mathematical model was developed to map and predict the resonance positions inside the cell. Details of this mathematical model and the boundary conditions applied can be found in Chapter 1.6. This model was compared against the electrochemical measurements of cell activity made using chambers 'A' and 'B' to support these assumptions. There are however other assumptions which have to be made in this model. Some of these

assumptions are supported by the physical characteristics of the system while others are supported through the experimental observations. Table 3.3 shows the assumptions made.

Parameter	**Value assumed**	**Comment**
c	1530 – 730 m s^{-1}	The experiments are performed in a cavitating liquid. These are known to have a significantly different speed of sound (~2500-500 m s^{-1}) depending on the bubble population. The presence of bubbles within the liquid changes the parameters of the medium (inertia and stiffness) on which the speed of sound depends[5]. Previous experiment showed that in these environments this range of values were possible.
$\rho c'$ (wall)	Air like	Previous experiment showed that in these environments this value was observed. Hence, pressure release and zero pressure at this point.
$\rho c'$ (base)	Air like	Unknown for this cylinder design, however, the experimental results (particularly the position of the resonant points in the Z direction) will show what this is. If supported, pressure release and zero pressure at this point.
$\rho c''$ (top)	Metal	Known to be rigid (metal, aluminium or steel)
j_{mn}	2.5, 5.5, 8.65	This parameter is difficult to measure with the current cell design. However, imaging experiments have shown these to be sensible.

Table 3.3 List of parameters and their values assumed in the accompanying model.

For these parameters with a solid reflector upper boundary the mode frequency (f_{mnq}) is described by equation 3.3

$$f_{mnq} = \left(\frac{c}{2\pi}\right)\sqrt{\left(\frac{j_{mn}}{a}\right)^2 + \left(\frac{q\pi}{2L}\right)^2} \qquad (3.3)$$

where j_{mn} is the Bessel function which here takes values $j_{01} = 2.5$, $j_{02} = 5.5$ and $j_{03} = 8.65$, a is the radius of the cylindrical chamber, L is the z separation between the base of the chamber and the reflector and q is an integer which can take values 1, 3, 5 etc.

The mode frequencies can be tested against the observed resonance for chambers 'A' and 'B'. The excitation frequency (38 kHz for chamber 'A' and 28.9 kHz for chamber 'B') was kept constant while the z separation was changed. Therefore under these conditions the value of $Z(z)$ the acoustic pressure as a function of z separation (i.e. $\frac{q\pi}{2L}$) remains constant. Hence as the value of L increases the value of p must step through its associated values. Table 3.4 shows the band positions for chamber 'A' and Table 3.5 the band positions for chamber 'B' and the predicted mode frequencies for each L position.

	j_{mn} =	2.4	5.5	8.65
	c =	1530	1030	730
q	L/mm	f_{mnq}/kHz	f_{mnq}/kHz	f_{mnq}/kHz
1	10	41.23	35.01	32.13
3	28	43.77	36.39	32.89
5	53	39.23	33.96	31.56
$< f_{mnz} >$		42.50	35.70	32.51

Table 3.4 Predicted mode frequency as a function of Z position (L value) for chamber 'A'. The assumed value of j_{mn} and c are also included. In this case the cylinder radius, a, was 38 mm.

	j_{mn} =	2.4	5.5	8.65
	c =	1530	1030	730
q	L/mm	f_{mnq}/kHz	f_{mnq}/kHz	f_{mnq}/kHz
1	16	28.43	28.67	28.80
3	47	28.86	28.86	28.90
5	78	28.94	28.90	28.92
7	109	28.98	28.92	28.93
9	140	29.00	28.93	28.93
11	171	29.02	28.94	28.94
13	205	28.72	28.80	28.87
15	233	29.03	28.94	28.94
17	265	28.96	28.91	28.92
$< f_{mnz} >$		28.88	28.88	28.90

Table 3.5 Predicted mode frequency as a function of Z position (L value) for chamber 'B'. The assumed value of j_{mn} and c are also included. In this case the cylinder radius, a, was 38 mm.

The experimental results showed that the cell geometry was important in being able to generate cavitation at the surface. Further experiments were performed to discover whether other experimental factors were able to induce or enhance the cavitation and its associated effects.

3.4.3 Hydrogen evolution

It has been seen that the atmospheric conditions in the cell can have an effect on the 'bubble activity' observed and the position of the resonance bands. To discover whether other factors can affect the number of 'bubble events' a further set of experiments were performed. In these experiments a negative potential of -2.2 V *vs.* stainless steel was applied to the titanium working electrode. At this potential hydrogen gas was evolved at the working electrode. The effect of this gas evolution was to seed the cavitation events at the electrode surface. A broadening of the active bands is seen, with a small number of events observed where the cell is not exactly at the resonance point. The activity profile is shown in Figure 3.20.

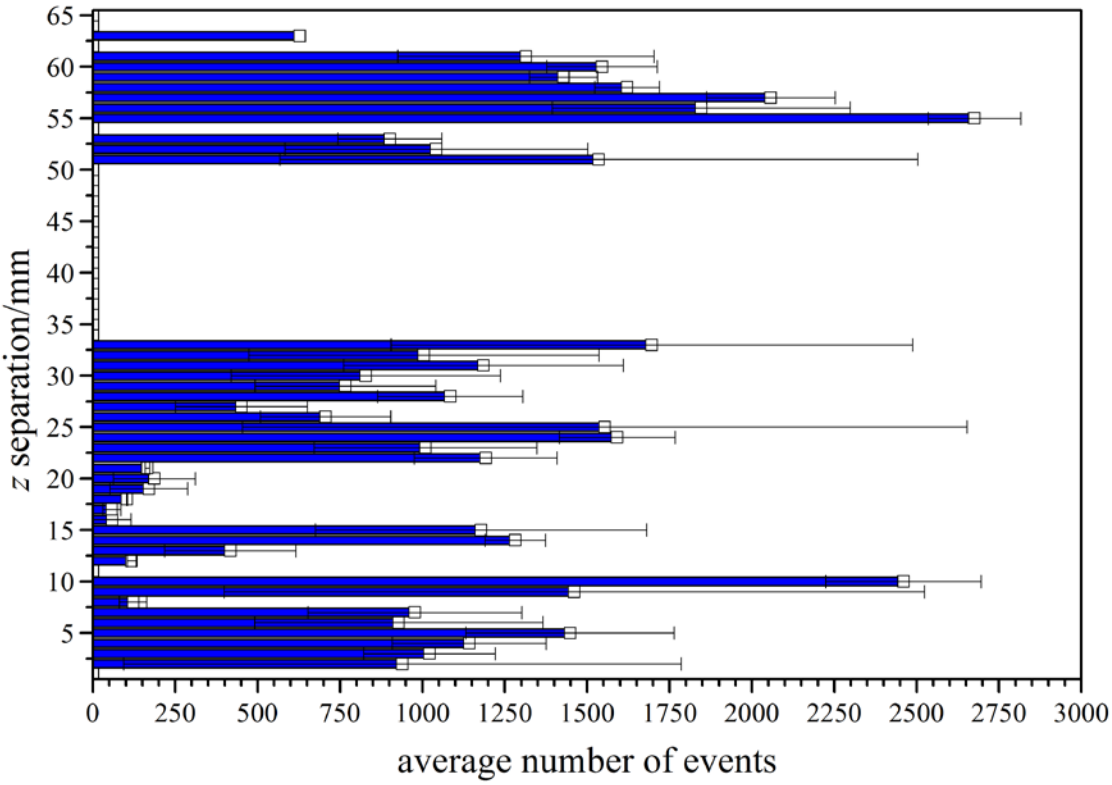

Figure 3.20 Plot of the number of events (■) as a function of *z* separation for an 80 µm diameter titanium disc within a resin support at -2.2 V *vs.* stainless steel and a stainless steel case as a reference electrode. Each event number is an average of three separate experiments performed at each height. Experiments were performed over a number of days with an electrolyte solution of 0.5 M Na_2SO_4 at a temperature from 21 – 23 °C in aerobic conditions. Data from individual scans was acquired with a 500 kHz sample rate.

This result was expected as both a suitable sound field and nucleation events are required for bubble activity. At the borders of the band, the sound field pressure is less than the inertial limit. However, bubble events are possible if seeded with an appropriate nuclei as shown in Figure 3.20.

In order to provide complementary evidence for this seeding effect, another series of experiments were then performed. For these experiments, the disc was held at a constant *z* separation of 28 mm and the potential of the working electrode was decreased from 0.0 V *vs.* stainless steel to -2.2 V *vs.* stainless steel in increments of 0.1 V. The *z* separation of 28 mm was chosen as a distance at which a stable cluster reliably forms without hydrogen gas seeding the cavitation. The activity profile for this series of experiments is shown in Figure 3.21.

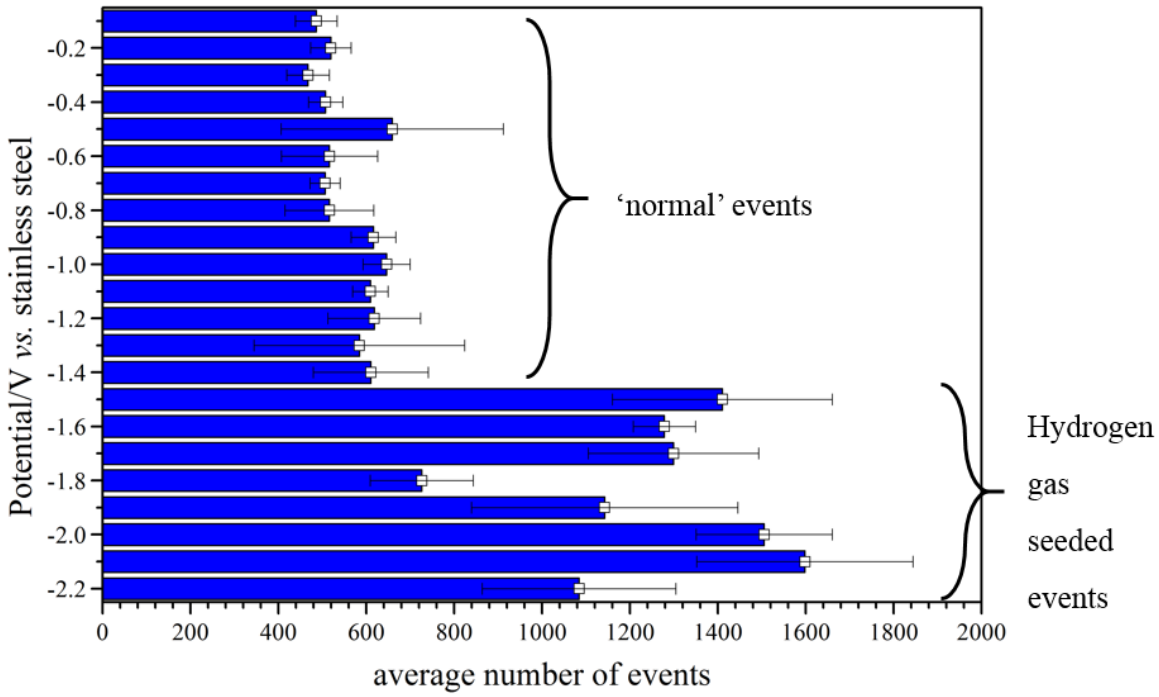

Figure 3.21 Plot of the number of events (■) as a function of electrode potential for an 80 µm diameter titanium disc within a resin support at a *z* separation of 28 mm and a stainless steel case as a reference electrode. Each event number is an average of three separate experiments performed at each height. Experiments were performed over a number of days with an electrolyte solution of 0.5 M Na_2SO_4 at a temperature from 21 – 23 °C in aerobic conditions. Data from individual scans was acquired with a 500 kHz sample rate.

A clear increase in the number of calculated events was seen at -1.5 V *vs.* stainless steel. This enhancement in the number of events, indicates that at a potential of -1.5 V *vs*. stainless steel the number of bubbles at or near the surface of the electrode has increased. Therefore this potential is likely the onset potential for hydrogen gas evolution of titanium with respect to stainless steel.

3.4.4 Cyclic Voltammetry

In order to correlate these results with the electrochemistry at the titanium electrode, a set of cyclic voltammograms were performed. Figure 3.22 shows three such voltammograms recorded at 0.0 V *vs.* stainless steel to -2.2 V *vs.* stainless steel. The onset potential of hydrogen evolution is measured at ~ -1.4 V *vs.* stainless steel. Therefore below this potential there will be additional gas at or near the electrode surface resulting in a larger number of events being recorded under the same acoustic conditions.

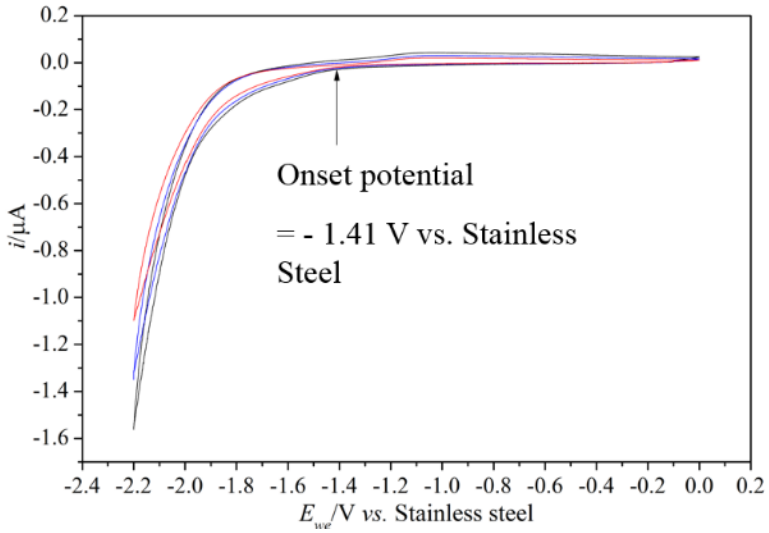

Figure 3.22 A plot of current, *i*, as a function of potential for an 80 µm diameter titanium disc within a resin support and a stainless steel case as a reference electrode. Cyclic voltammetry sweeps were performed at sweep rates of 50 mV s^{-1} (—), 100 mV s^{-1} (—) and 200 mV s^{-1} (—). The electrolyte solution was 0.5 M Na_2SO_4 at 21 °C and aerobic conditions.

This correlates well with the count of erosion/corrosion activity at the electrode with decreasing potential. A gas evolution onset potential of -1.4 V *vs.* stainless steel indicates that below this potential there will be additional gas on the electrode surface due to hydrogen evolution. The enhanced number of cavitation ‘events’ was measured from a potential of -1.5 V *vs.* stainless steel.

3.4.5 Using a microphone to measure acoustic output

It has been previously noted that the magnitude of the cylindrical cell sound output was increased and decreased as the reflector was moved up though the cylindrical cell. This meant that as well as measuring the observed bubble activity, surface cavitation could be monitored by measuring the acoustic output from the chamber. This was achieved using a microphone positioned near the curved wall of the cylindrical chamber (chamber ‘B’, see Figure 2.22). The acoustic output was recorded as a function of time then post processed

using a fast Fourier transform (FFT). The result was plotted as signal amplitude against frequency in Hz. An example plot at a reflector height of 16 mm is shown in Figure 3.23.

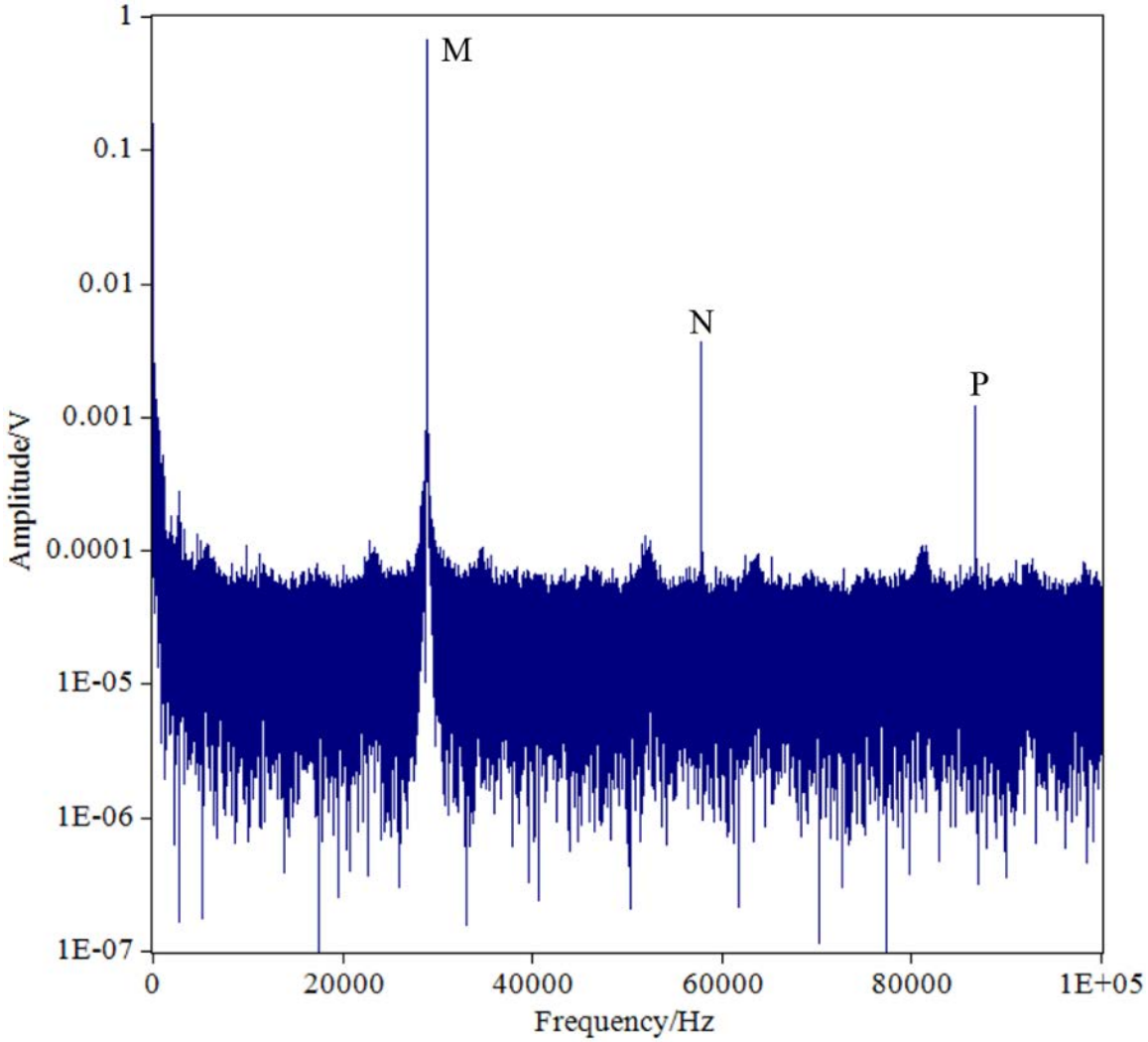

Figure 3.23 A plot of microphone amplitude against frequency (—). This is an FFT of the amplitude vs. time data captured. The reflector was at a *z* separation of 16 mm and the ultrasound was applied to the cell at a frequency of 28.9 kHz with an amplification of 38 dB from the power amplifier. The time domain data was captured with a sample rate of 1 MHz and 1,000,000 data points were captured in the sample. The solution in the chamber is an aqueous solution of 0.5 M Na_2SO_4 in aerobic conditions at room temperature (23 °C) and pressure.

In this plot (Figure 3.23) a series of regularly spaced peaks are observed. The largest of these peaks, labelled M, has a frequency of 28.9 kHz. This is the fundamental frequency of the applied ultrasound. A peak is expected to be seen at this frequency as the bubbles created during cavitation oscillate in resonance with the driving ultrasound frequency. The higher frequency peaks, labelled N and P, correspond to frequencies of 57.8 kHz and 86.7 kHz respectively. These frequencies are the first and second harmonics of the fundamental frequency (28.9 kHz). The amplitude of these frequency peaks was recorded

for each reflector height. Figure 3.24 shows the amplitude of the 28.9 kHz and 57.8 kHz frequency points as a function of reflector height. The resonance peak amplitude is seen to increase as the cell undergoes cavitation. These positions are the positions at which the pressure wave reaches a maximum at the reflector. The positioning of these acoustic resonance peaks is the same as the positions at which bubble activity was observed at the electrode surface using the same resonance chamber.

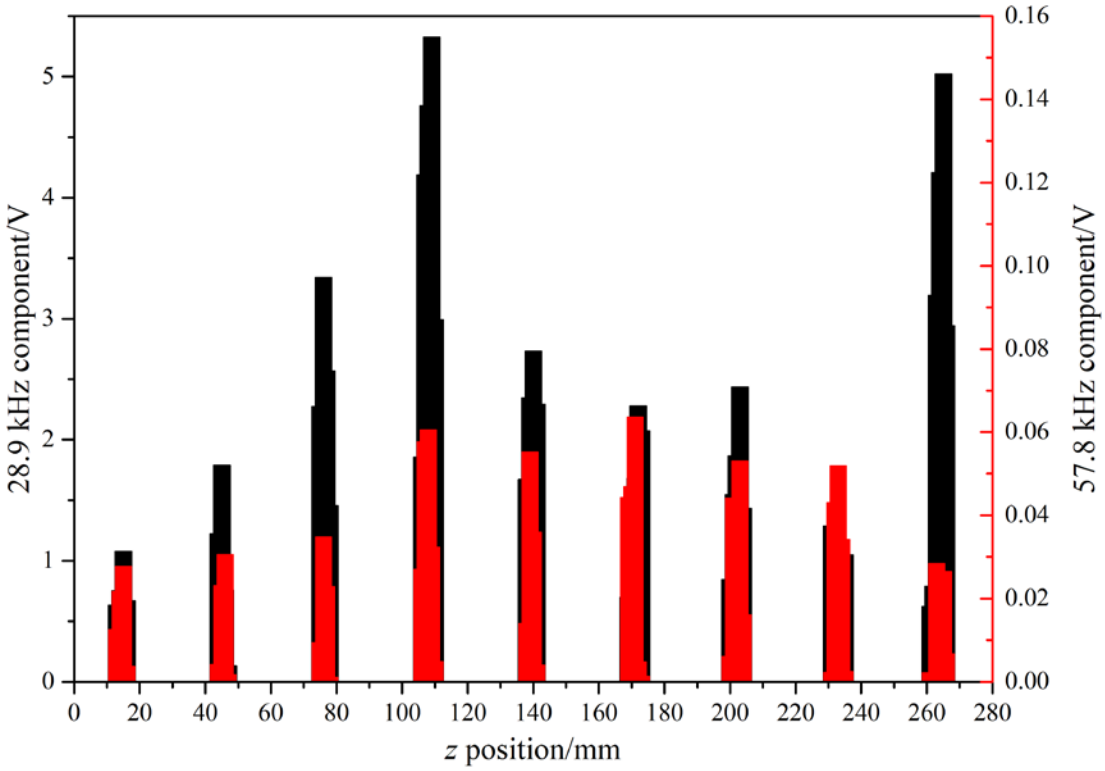

Figure 3.24 A plot of microphone amplitude as a function of reflector height (*z* position) at 28.9 kHz (—) and 57.8 kHz (—). The solution in the chamber is an aqueous solution of 0.5 M Na_2SO_4 in aerobic conditions at room temperature (23 °C) and pressure.

These acoustic measurements support the mathematical model for chamber resonance proposed in Chapter 1.6 and discussed in Chapter 3.4.2. In this model the assumptions made about the boundary conditions suggested that the curved walls and base of the chamber were a pressure release (air-like) boundary and the metal reflector was a solid boundary. These boundary conditions lead to equation 3.3 for resonance positions (f_{mnq}) which depended on the dimensions of the chamber (radius, a and height, L)

$$f_{mnq} = \left(\frac{c}{2\pi}\right)\sqrt{\left(\frac{j_{mn}}{a}\right)^2 + \left(\frac{q\pi}{2L}\right)^2} \quad (3.3)$$

where the Bessel function, j_{mn} takes values j_{01} = 2.5, j_{02} = 5.5 and j_{03} = 8.65 and q is an integer which takes odd integer values q = 1, 3, 5 etc. As the height of the chamber L is increased the value of $\frac{q\pi}{2L}$ (the acoustic pressure as a function of z) has to remain constant and therefore the integer value of q increases with increasing L (z separation). As seen in Figure 1.14, the position of each resonance position is related to the wavelength of the sound wave (λ) by $\frac{q\lambda}{4}$. Thus each resonance position is separated by a distance equal to half a wavelength, with the first resonance position at a quarter of a wavelength.

The positions at which resonance is observed could be altered by changing one of the boundary conditions. To test this a reflector disc was made with a polystyrene disc ~ 2 mm in thickness fixed to the base of a steel plunger. The assumption was made that this changed the upper boundary condition from a solid-liquid boundary to an air-liquid (pressure release boundary).

The acoustic output of the cylindrical cell with an upper air boundary was recorded as a function of time for varying z separations. The positions of the high amplitude points were shifted for the air boundary case so the peaks appear partway between those seen for the solid boundary. A plot comparing the peak amplitudes at 58.7 kHz for the air boundary and solid boundary is shown in Figure 3.25.

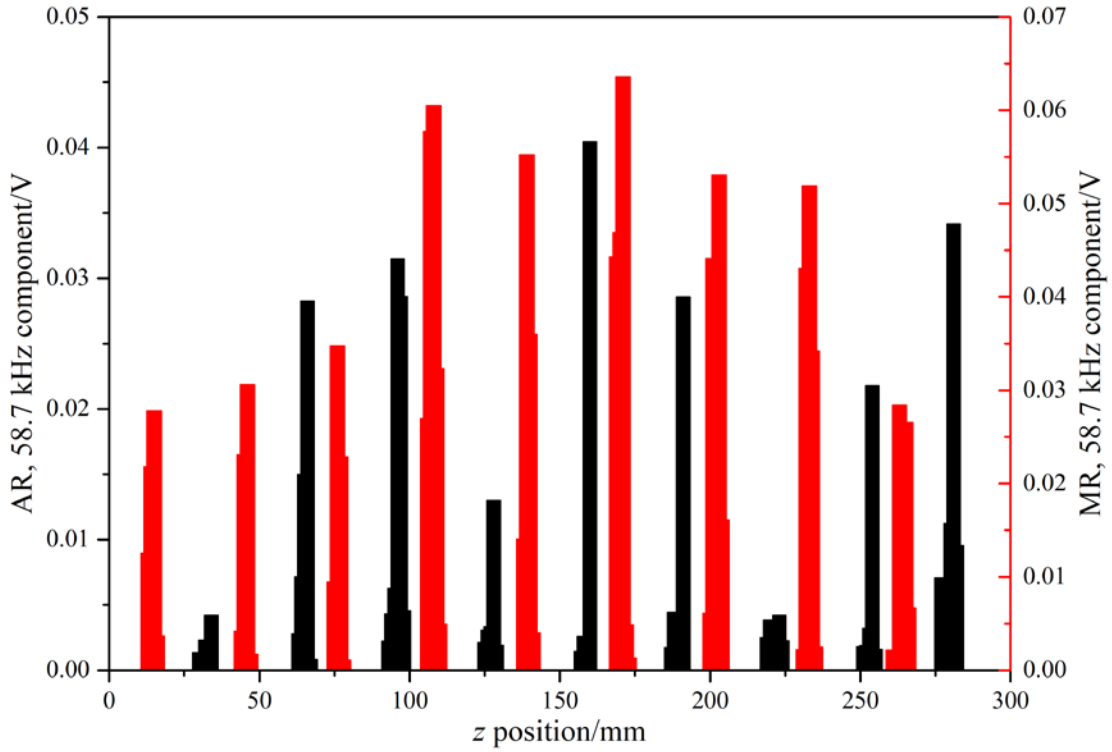

Figure 3.25 A plot of microphone amplitude as a function of reflector height at 57.8 kHz for an air reflector (—) and solid reflector (—). The solution in the chamber is an aqueous solution of 0.5 M Na_2SO_4 in aerobic conditions at room temperature (23 °C) and pressure.

These experiments can be compared to the model proposed in Chapter 1.6. In this model, changing the upper boundary condition changes the *z* positions at which resonance modes are observed. The chamber resonance f_{mnp} is now described by equation 3.4

$$f_{mnp} = \left(\frac{c}{2\pi}\right)\sqrt{\left(\frac{j_{mn}}{a}\right)^2 + \left(\frac{p\pi}{L}\right)^2} \qquad (3.4)$$

where *p* takes whole integer values 1, 2, 3 etc. The change in acoustic pressure as a function of z means that now the resonance positions are related to the wavelength of the acoustic wave by $\frac{p\lambda}{2}$. Therefore the first resonance position is now at half the wavelength of the acoustic wave and are then spaced at half wavelength intervals.

Table 3.6 shows the band positions for chamber 'B' with an upper air boundary and the predicted mode frequencies for each *L* position recorded in Figure 3.25.

	j_{mn} =	2.4	5.5	8.65
	c =	1530	1030	730
p	L/mm	f_{mnp}/kHz	f_{mnp}/kHz	f_{mnp}/kHz
1	32	28.43	28.67	28.80
2	68	27.25	28.15	28.54
3	90	29.78	29.29	29.11
4	109	32.01	30.33	29.65
5	125	34.25	31.42	30.21
6	158	32.87	30.75	29.86
7	190	32.11	30.38	29.67
8	222	31.57	30.12	29.54
9	255	31.07	29.89	29.42
< f_{mnz}>		31.04	29.89	29.42

Table 3.6 Predicted mode frequency as a function of z position (L value) for chamber 'B' with an upper air boundary. The assumed value of j_{mn} and c are also included. In this case the cylinder radius, a, was 38 mm.

This result is similar to that presented for chambers 'A' and 'B' with a solid upper boundary condition (Table 3.4and Table 3.5). The key finding here is the resonance frequency predicted at the z positions (given from the experimental data) closely matches the real applied ultrasound frequency of 28.9 kHz. This verifies the assumptions made by the model are correct. It also shows that the cell geometry and boundary conditions are important in creating the right acoustic field to generate acoustic cavitation.

The work with cylindrical chambers presented in this chapter shows that transient cavitation can be generated and recorded under the correct acoustic conditions. The cavitation was observed only in bands at high acoustic pressure. To generate cavitation bubbles within the chamber, it was therefore necessary to create a standing wave within the chamber by changing the position of the acoustic reflector. With a solid upper boundary reflector, cavitation was observed at the electrode embedded in the surface of this reflector only at these regions of high acoustic pressure. Where the reflector was not at the correct z position to form a region of high acoustic pressure at the reflector surface no acoustic cavitation was observed. It was also observed that changing the boundary conditions of this reflector changed the z positions of the high acoustic pressure regions. This would be important to consider, for example, in the design of a cylindrical device intended to use ultrasound to generate acoustic cavitation and clean surfaces. In such a device the chamber geometry, ultrasound frequency and boundary conditions at the walls of the chamber would all important to consider in order for such a device to be successful.

The sound field described in chapter 3 is just one example of a sound field in which acoustic cavitation can be generated. The next three chapters will look at an alternative acoustic field employing an ultrasonic horn as a piston-like emitter.

Chapter 4 Ultrasonic Horn (PLE) as a Sound emitter

4.1 Monitoring bubble motion from a PLE

The ultrasonic horn, or piston-like emitter (PLE), was used as a sound source to produce and excite cavitation bubbles in an electrolyte. Unlike the cylindrical chamber, here a bubble cluster was not formed on the electrode/reflector surface but over the tip of the horn. The schematic in Figure 4.1 shows where cavitation bubbles were observed in these experiments. Bubbles were observed breaking away from this cluster and moving onto the surface of the resin (polished to mirror finish with 0.3 µm Al_2O_3 slurry, diameter (ϕ) 20 mm). From there the bubbles were then detected as they moved and oscillated across the solid support and the working electrode surface. The motion of these bubbles on the resin and working electrode surface is indicated in Figure 4.1.

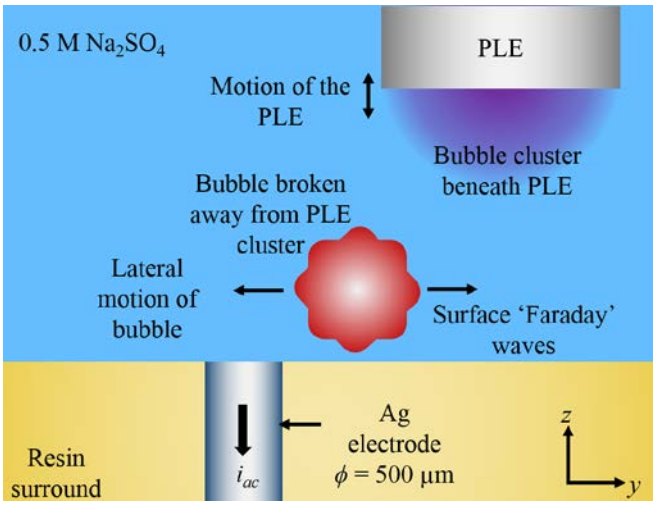

Figure 4.1 A schematic showing the cluster of bubbles formed underneath the ultrasonic horn or piston-like emitter (PLE) and bubbles moving across the polished surface of the Ag disc working electrode and resin surround. The diameter of the Ag electrode was 500 µm and experiments were performed in 0.5 M Na_2SO_4 at room temperature and pressure in aerobic conditions. The picture is not drawn to scale.

The horn was positioned at a variety of *z* separations, distance between the PLE and resin surface, and y separations, the lateral position of the PLE relative to the centre of the Ag (ϕ = 500 µm) working electrode. The origin of the axis used was taken to be the position where the PLE was directly above the working electrode and touching the electrode surface (see Figure 4.2). The surface bubble activity, measured as a function of *x* and *y* separation, will be explored further in Chapter 4.3.

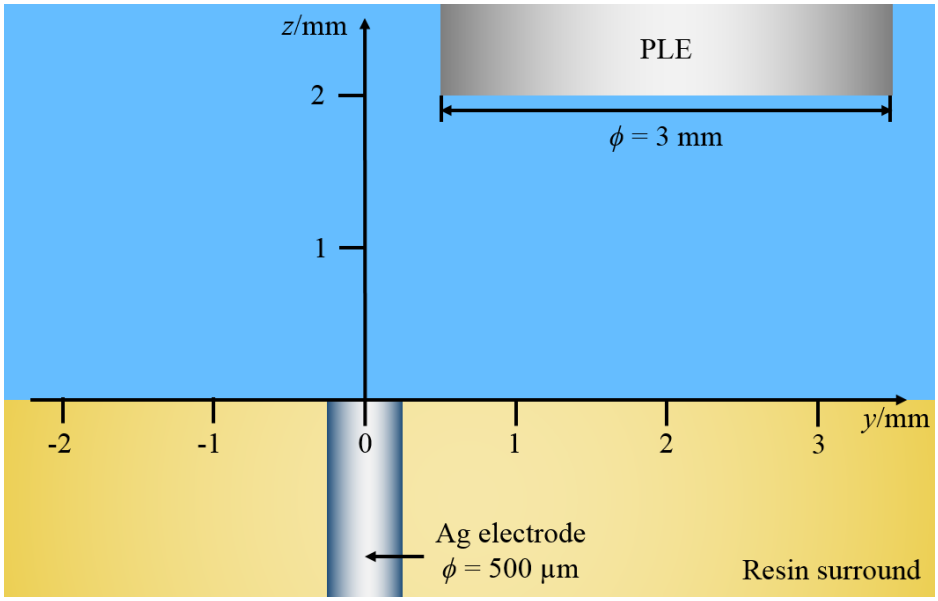

Figure 4.2 A cartoon illustration of the *y* and *z* axes used to record the position of the PLE tip (ϕ = 3 mm) relative to the Ag working electrode (ϕ = 500 µm). The origin of the axes was placed at the centre of electrode surface. The *z* separation was measured as the distance from the electrode surface to the bottom surface of the PLE. The *y* separation was recorded from the centre of the electrode to the centre of the PLE tip. The PLE is here positioned at a *y* separation of 2 mm and *z* separation of 2mm. The illustration is drawn to scale.

The bubble motion (or 'activity') was measured using the novel high-speed impedance technique described in Chapter 2.3. In the experiments performed here the working electrode used was an Ag disc electrode (ϕ = 500 µm). An AC perturbation of 25 mV zero-to-peak was applied across the Ag working electrode and stainless steel counter reference electrode at a frequency of 50 kHz. The AC potential input and AC current response was recorded at a sample rate of 1 MHz (one data point every 1 µs). By decreasing the sample rate for AC current time and AC potential time recording and applied AC perturbation by a factor of 10, data could be recorded over longer periods of time with fewer data points then in the experiments performed in the cylindrical resonance cell (see Chapter 3 for further details of previous experiments). Figure 4.3 shows the differences between using a 50 kHz perturbation compared to a 500 kHz perturbation which are key to the interpretation of the results collected.

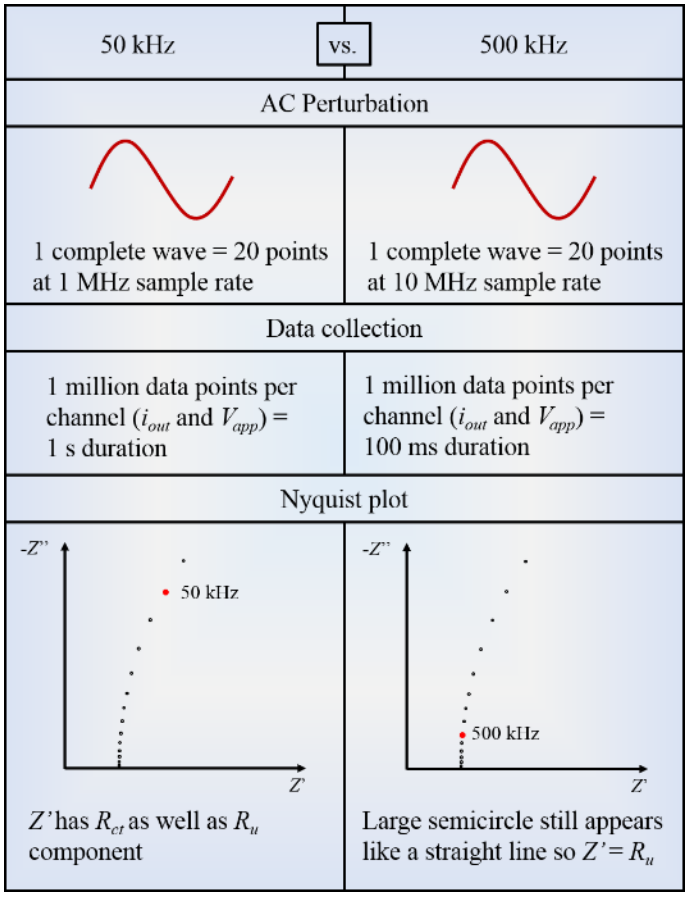

Figure 4.3 Showing the key differences between using a 50 kHz AC perturbation to using a 500 Hz perturbation for the same electrochemical setup.

As illustrated by Figure 4.3, decreasing the frequency of the perturbation affected the values of the real and imaginary components of impedance, *Z'* and *Z''*. By decreasing the perturbation frequency, the real impedance, *Z'*, is no longer equal to the uncompensated resistance alone (as it approximately was at 500 kHz) and contains a component due to the charge transfer resistance, R_{ct}. This would mean that the simple RC circuit model used would no longer be an accurate representation from which to interpret the impedance results. For this reason, an electrode with a larger surface area was also employed for these experiments (ϕ = 500 µm compared to ϕ = 250 µm or ϕ = 100 µm in Chapter 3). The result of increasing the electrode surface area was that the electrode capacity was increased. This resulted in a decrease in the magnitude of the capacitive resistance, the imaginary component of the impedance, and so the recorded phase angle, θ, between applied potential and current response was small (see Figure 4.4). Decreasing the imaginary component of impedance in this way allows us to continue using the RC circuit model as a good approximation. The data reported from the calculated impedance (Figures 4.5 and 4.6) therefore shows only the uncompensated resistance and not capacitance changes as *Z''* was too small to accurately determine *C* and R_u was approximately equivalent to *Z*.

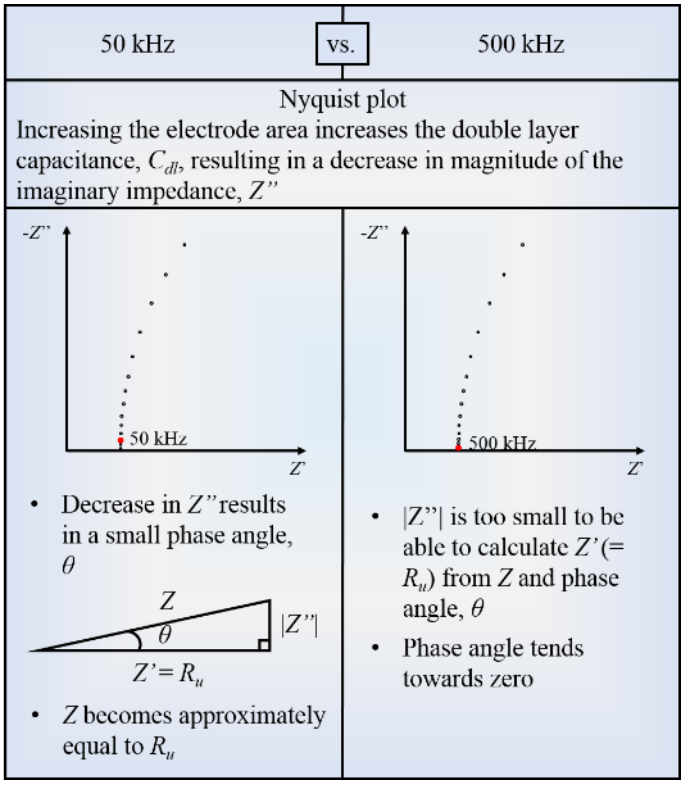

Figure 4.4 Showing the key differences between using a 50 kHz AC perturbation to using a 500 kHz perturbation for a larger diameter electrode e.g. ϕ = 500 µm.

4.2 High-Speed Camera

In conjunction with these high-speed impedance studies of the electrode surface (eg. Figures 4.5 and 4.6), high-speed imagery was also employed to investigate the bubble motion. This provided a useful tool to verify the assertions made about the cavitation bubble motion from the high-speed impedance studies. A trigger system was setup to allow for simultaneous capture of impedance data by the data capture program (Microsoft Visual Basic 2010, National Instruments Measurement Studio) and high-speed camera video (see Chapter 2.2, Table 2.2 for further information about camera). The resistance transients from the high-speed AC impedance can then be matched up in time to high-speed camera footage, confirming the presence or absence of bubbles over the electrode surface at appropriate times in the resistance time traces. Images from such experiments are shown in Figure 4.7. These figures are a composite of individual images taken from the same experiment which yielded the data displayed in Figure 4.5.

Figure 4.5 shows one section from a 1 s long resistance time data capture taken with a sample frequency of 50 kHz with images from the accompanying high-speed video footage (Figure 4.7).

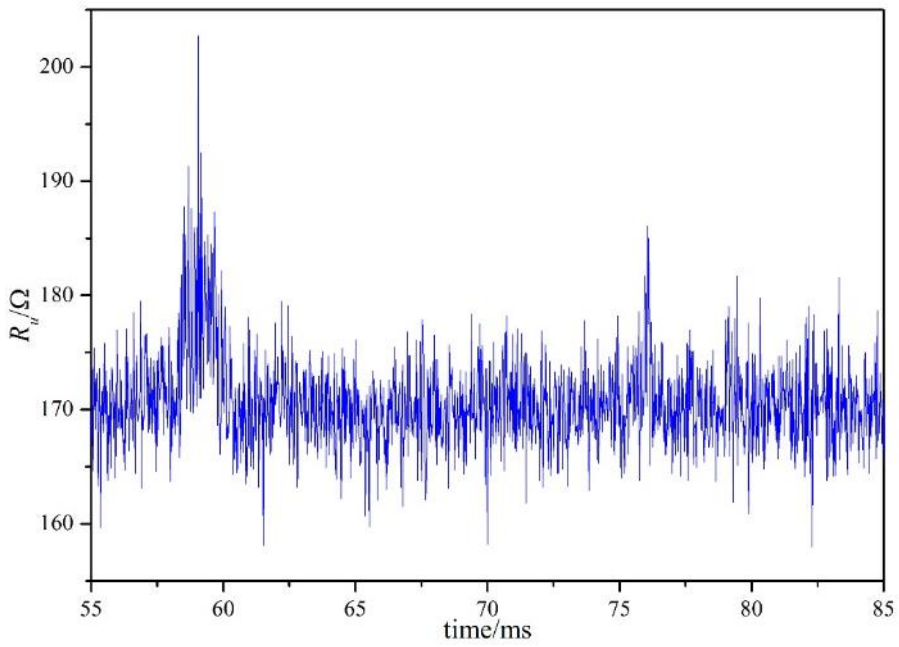

Figure 4.5 A plot of resistance, R_u, (—) as a function of time at a sample rate of 50 kHz. The working electrode used was a 500 µm diameter Ag disc electrode and stainless steel was used as a pseudo reference counter electrode. The electrolyte used in this experiment was 0.5 M Na_2SO_4. The temperature was 24.9 °C and the experiment was carried out at atmospheric pressure and in aerobic conditions.

The resistance transient seen in Figure 4.5 shows transient peaks in resistance as a function of time, as was observed in the resistance time plots recorded inside the cylindrical resonance cell (see Chapter 3). We attribute these transients to 'bubble activity' over the electrode surface. Unlike the transients recorded inside the cylindrical resonance cell (see Chapter 3) the resistance time transients shown here (Figures 4.5 and 4.6) in are more symmetrical in shape. This was an indication that a different type of bubble motion, other than bubble collapse in inertial cavitation, was being observed here. Figure 4.6 shows the section between 58 ms and 60 ms where transient resistance spikes were observed compared to the resistance spikes observed in the cylindrical resonance cell. From this figure the resistance spikes observed from the experiments using the PLE as the ultrasonic source have a more symmetrical shape than those seen in the cylindrical resonance cell. The Faradaic current recorded for both experiments is also included in the plots on Figure 4.6. When the collapsing bubbles eroded the aluminium surface spikes in Faradaic current were observed as the passive layer reformed (as seen in Figure 4.6 b)). Figure 4.6 a) taken from the PLE experiment shows no such current spikes. Both the shape of the resistance transients and appearance of the current time plot indicated that the bubble motion observed at the electrode from the PLE was not inertial cavitation as observed in the cylindrical resonance cell.

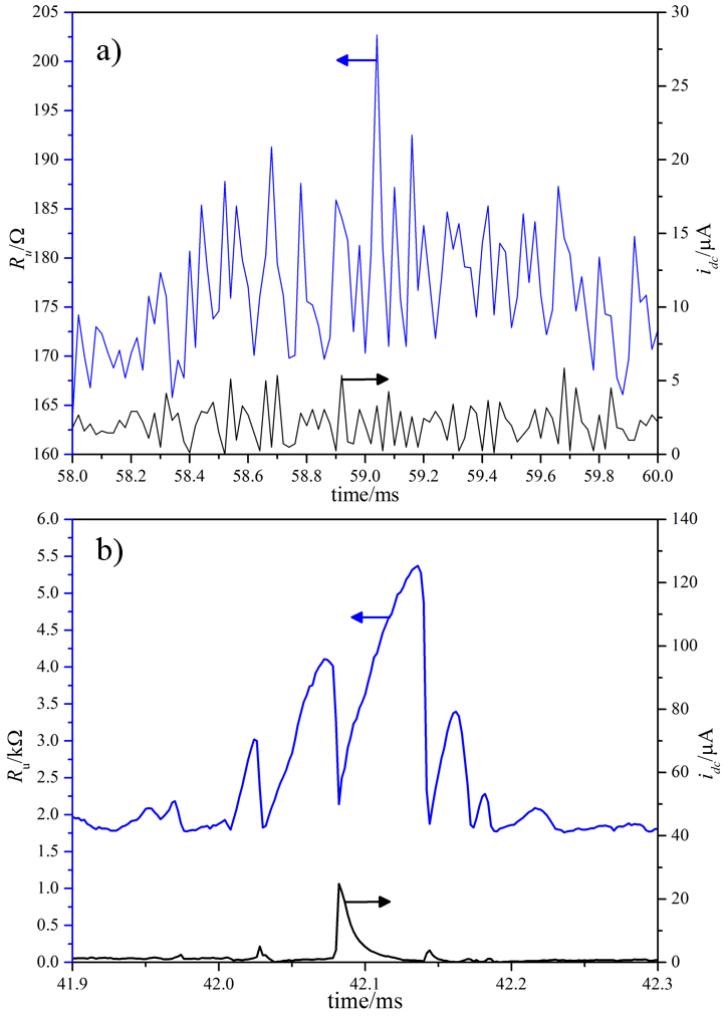

Figure 4.6 a) A plot of resistance, R_u, (—) and Faradaic current, i_{dc}, (—) as a function of time at a sample rate of 50 kHz. The working electrode used was a 500 μm diameter Ag disc electrode and stainless steel was used as a pseudo reference counter electrode. The electrolyte used in this experiment was 0.5 M Na_2SO_4. The temperature was 24.9 °C and the experiment was carried out at atmospheric pressure and in aerobic conditions. **b)** Plot showing the resistance, R_u, (—) and Faradaic current, i_{dc}, (—) as a function of time for a 100 μm diameter Al disc within a resin support and a stainless steel outer case acting as a reference counter electrode. The solution in the resonant chamber was 0.2 M Na_2SO_4. The frequency applied to the transducer from the amplifier is 37.97 kHz and the *z* separation was 32 mm. The solution temperature was 22 °C and the experiment was performed in aerobic conditions. Data acquired with a 500 kHz sample rate.

In conjunction with these high-speed impedance studies of the electrode surface, high-speed imaging of the PLE and electrode assembly was also employed to investigate the bubble motion. This provided a useful tool to verify the assertions made about the cavitation bubble motion from the high-speed impedance studies. A trigger system was setup to allow for simultaneous capture of impedance data by the Visual Basic program and high-speed camera video. The resistance transients from the high-speed AC impedance can then be matched up in time to high-speed camera footage, confirming the presence or absence of bubbles over the electrode surface at appropriate times in the resistance time

traces. The high-speed camera recording is presented as a composite of individual images taken from the video footage. Figure 4.7 shows the bubble activity over the electrode in the same time window as the resistance time data shown in Figure 4.5.

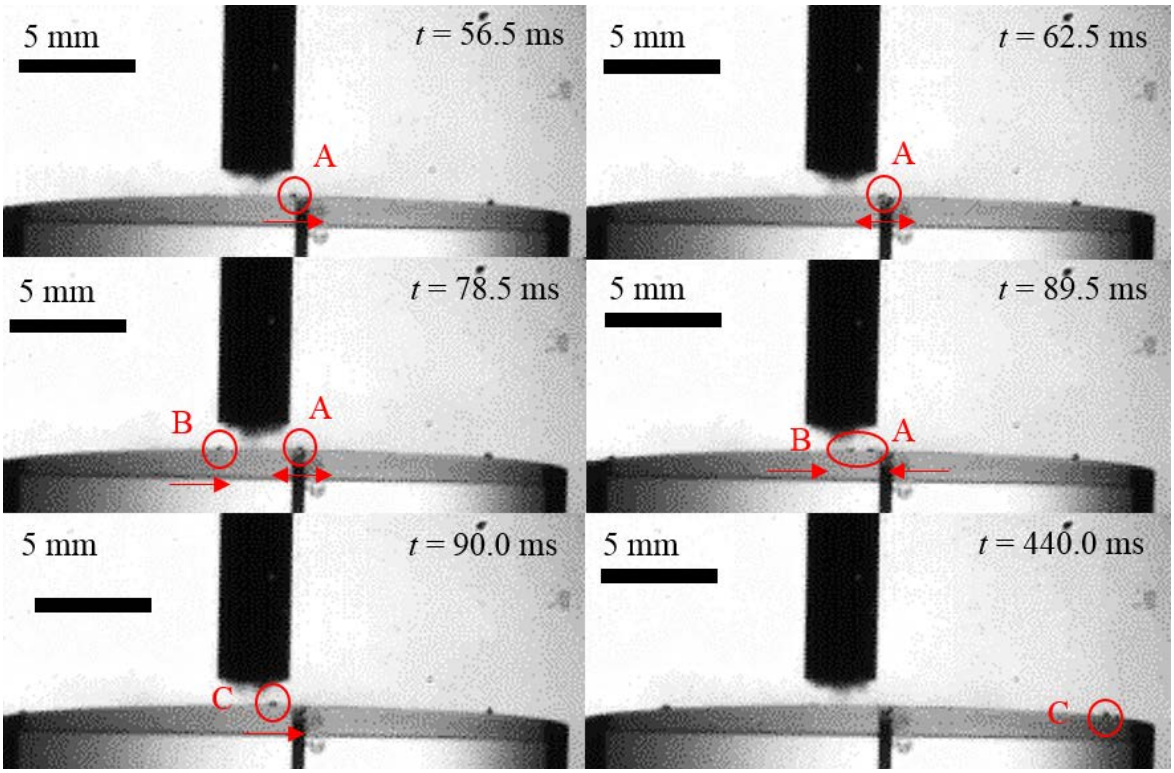

Figure 4.7 A composite of images from the high-speed camera video footage recorded. The horn is positioned at a *z* separation of 2 mm and *y* separation of -2 mm. The camera data was recorded at 2000 frames per second. The video footage accompanying this figure can be found at: https://doi.org/10.5258/SOTON/D0674.

The first two images shown in Figure 4.7 taken at t = 56.5 ms and t = 62.5 ms showed a bubble, labelled ‘A’, moving backwards and forwards across the working electrode. This corresponds in time to a series of resistance peaks observed in Figure 4.5. Bubble ‘A’ remained close to the working electrode for the next 15 ms and crossed over the electrode again at t = 78.5 ms. A second moving bubble, labelled ‘B’, was also observed to appear at this point. The two bubbles ‘A’ and ‘B’ were pulled in towards each other (t = 89.5 ms) and joined together to form one single bubble (t = 90.0 ms) labelled ‘C’. This larger bubble continued to move across the resin surface for approximately 350 ms until it eventually stopped towards the edge of the resin surround. This stationary bubble ‘C’ can be observed in the image at t = 440.0 ms.

The position the bubbles moving across the electrode surface relative to the PLE suggests that the bubbles being interrogated in these experiments are of non-inertial cavitation. These bubbles grow, shrink and move in response to the forces impacted on them from the

sound field, the surfaces (and bubble images) and the flow of liquid induced by acoustic streaming and streamer formation. These are all as a result of the action of the PLE.

Using the high-speed camera images alongside the high-speed impedance data it was possible to correlate the transient resistance peaks observed in the high-speed data capture to the motion of bubbles moving on or around the working electrode surface. The high-speed camera does however have certain limitations. As the frame rate was increased in order to capture more mechanistic details of the bubble motion the number of pixels available for the recorded image decreased. This meant that for better quality images at high frame rates it was necessary to decrease the area imaged. The decrease in image quality with increasing frame rate means that smaller bubbles on/near the electrode surface were often not clearly visible in the images recorded. The high-speed resistance data capture was at a clear advantage over the images in recording these small bubbles as this technique was sensitive enough to be able to detect small changes in resistance (ΔR_u = 10 to 15 Ω) due to these smaller bubbles.

4.3 Bubble activity as function of horn to electrode distance

The motion of the PLE has been shown to stimulate cavitation in the liquid which generated bubbles. These were seen in a semi-circular cluster underneath the PLE tip. Bubbles from this cluster were observed breaking away from the cluster and moving down onto the resin surround of the electrode. As the bubbles skated across the surface of the Ag working electrode (ϕ = 500 µm) mounted in the resin block (ϕ = 20 mm) transient spikes in uncompensated resistance were recorded. The bubble activity recorded in the resistance transients was seen to change depending on the position of the PLE relative to the working electrode.

It was observed that over time the cavitation bubbles came to a stop in a circular ring with the PLE in the centre of the ring. This is seen in the image in Figure 4.8.

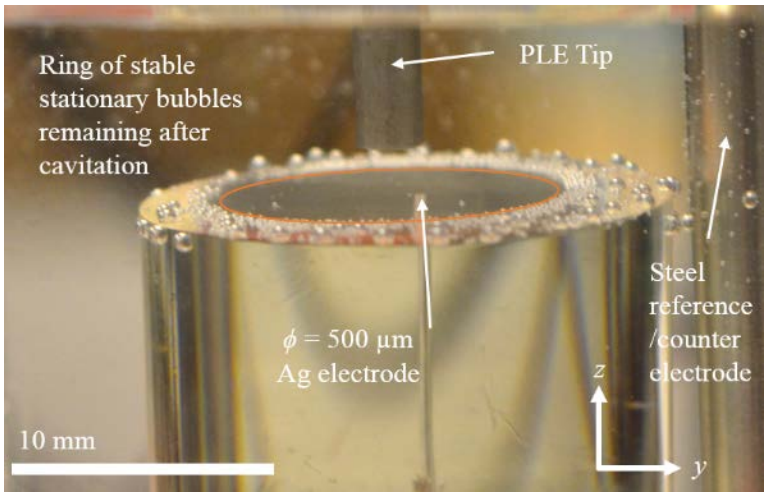

Figure 4.8 Showing the stationary ring of bubbles forming on the resin surface after ~ 2 mins of exposure to ultrasound.

In order to quantify this observation of bubble activity, a series of experiments were performed in which a set of resistance time measurements were gathered over a fixed time window. From these measurements, the number of transient peaks ('bubble events') was counted as a function of *y* and *z* separation between the PLE and the working electrode (see Figure 4.2 for axes employed). The number of peaks observed was used as an indication of the level of bubble activity at the electrode. Figures 4.9, 4.10 and 4.11 are plots of the average number of resistance peaks within 10 s as a function of *y* separation at *z* separations of 2.5 mm. 5.0 mm and 7.5 mm respectively. The resistance data was recorded at a sample frequency of 50 kHz (500,000 data points in 10 s) and an average of two data captures used to gather the appropriate bubble activity.

For each data set captured, the number of transients in resistance was determined using a peak finder routine (see Chapter 3.4 for further explanation). Two data captures were made at each distance and the averages at each distance plotted in the graph below. The standard error (generated from statistical analysis in Microsoft Excel) is given as an error for each of these calculations.

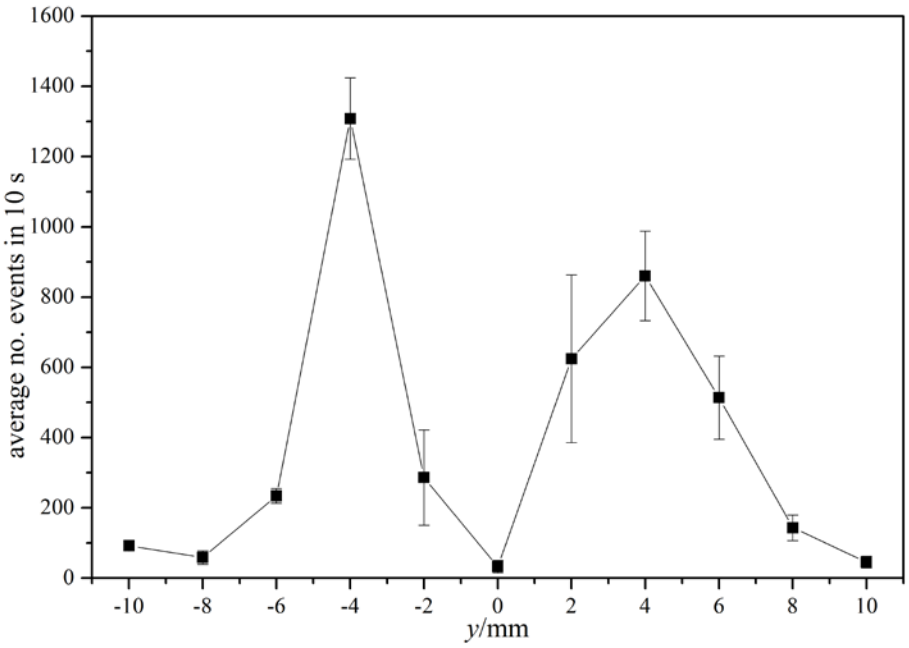

Figure 4.9 A plot showing the average number of 'bubble events' (■) in 10 s as a function of *y* separation from the silver disc (ϕ = 500 µm) at a *z* separation of 2.5 mm. Captures were made in 2 mm incremental distances from the electrode and the averages were made over 2 data captures at each distance. The error quoted in each case is the standard error for the two data captures. The working electrode was an Ag disc (ϕ = 500 µm) and the reference/counter was a stainless steel rod. The electrolyte used was 0.5 M Na_2SO_4 at room temperature (18.4 °C) and pressure under aerobic conditions.

Figure 4.9 showed that with the horn at a height of 2.5 mm above the resin surface the largest number of resistance peaks, or 'bubble events' was found for these conditions at a *y* separation of ± 4 mm. The decrease in 'bubble events' when the *y* separation was increased quantitatively showed that the bubbles lost kinetic energy as the moved further away from the PLE source. This supports the previous observations made where the loss of bubble energy caused larger stable bubbles to form a static ring on the resin surface (Figure 4.8). Figure 4.9 also shows that directly below the PLE there were relatively few bubble events.

In Figure 4.10, the *z* separation was 5.0 and here the largest number of 'bubble events' was observed at a *y* separation of ± 6 mm. As was observed at *z* = 2.5 mm the number of events radially further from the PLE still decreases. However, in the size of the area beneath the PLE where 'bubble events' were diminished was also increased, with no events recorded between *y* = ± 2 mm.

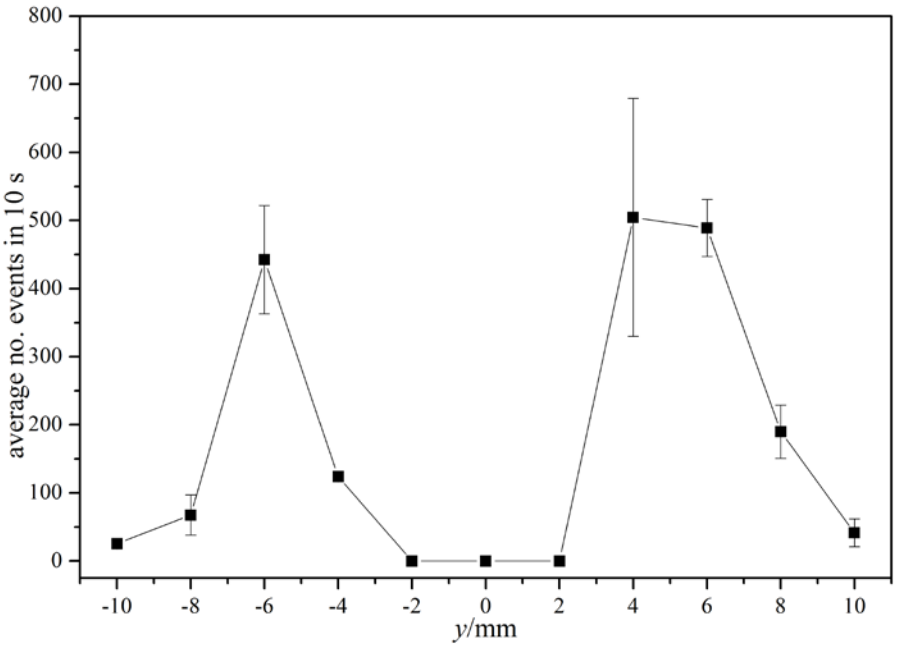

Figure 4.10 A plot showing the average number of 'bubble events' (■) in 10 s as a function of *y* separation from the silver disc (ϕ = 500 µm) at a *z* separation of 5.0 mm. Captures were made in 2 mm incremental distances from the electrode and the averages were made over 2 data captures at each distance. The error quoted in each case is the standard error for the two data captures. The working electrode was an Ag disc (ϕ = 500 µm) and the reference/counter was a stainless steel rod. The electrolyte used was 0.5 M Na_2SO_4 at room temperature (18.4 °C) and pressure under aerobic conditions.

As the *z* separation was increased further the size of this 'dead zone' was seen to increase. Figure 4.11 shows that at a *z* separation of 7.5, there were essentially no bubble events recorded between $y = \pm 4$ mm.

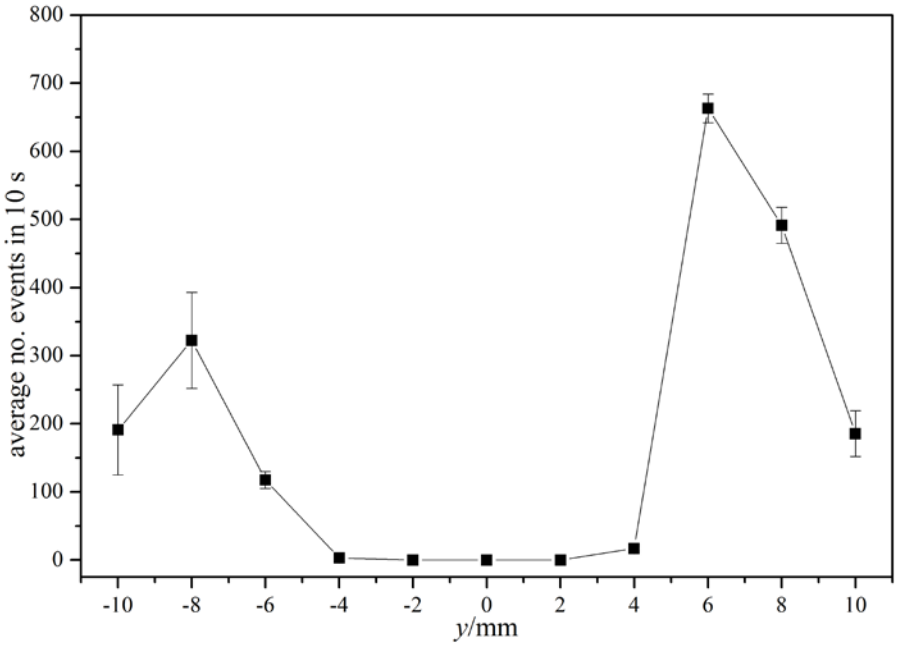

Figure 4.11 A plot showing the average number of 'bubble events' (■) in 10 s as a function of *y* separation from the silver disc (ϕ = 500 µm) at a *z* separation of 7.5 mm. Captures were made in 2 mm incremental distances from the electrode and the averages were made over 2 data captures at each distance. The error quoted in each case is the standard error for the two data captures. The working electrode was an Ag disc (ϕ = 500 µm) and the reference/counter was a stainless steel rod. The electrolyte used was 0.5 M Na_2SO_4 at room temperature (18.4 °C) and pressure under aerobic conditions.

This decrease in activity below the sound emitter may be due to the flow of liquid below the horn and over the large electrode support. A picture illustrating the flow of bubbles from the horn down onto the resin surface is shown in Figure 4.12.

The arrows (→) in Figure 4.12 show the direction in which the bubbles streaming from the horn were observed to travel. The results suggest that as the cavitation bubbles travel down from the PLE towards the surface they are pushed radially outwards. For this reason, with the horn relatively close to the electrode surface, the bubbles cannot reside for any great length of time directly beneath the PLE, as observed in the plot in Figure 4.9 (with a *z* separation of 2.5 mm), where no events were recorded at a *y* separation of 0 mm. In this plot the number of bubble events recorded at *y* separations of ± 2 mm was also reduced by this effect compared to *y* = ± 4 mm.

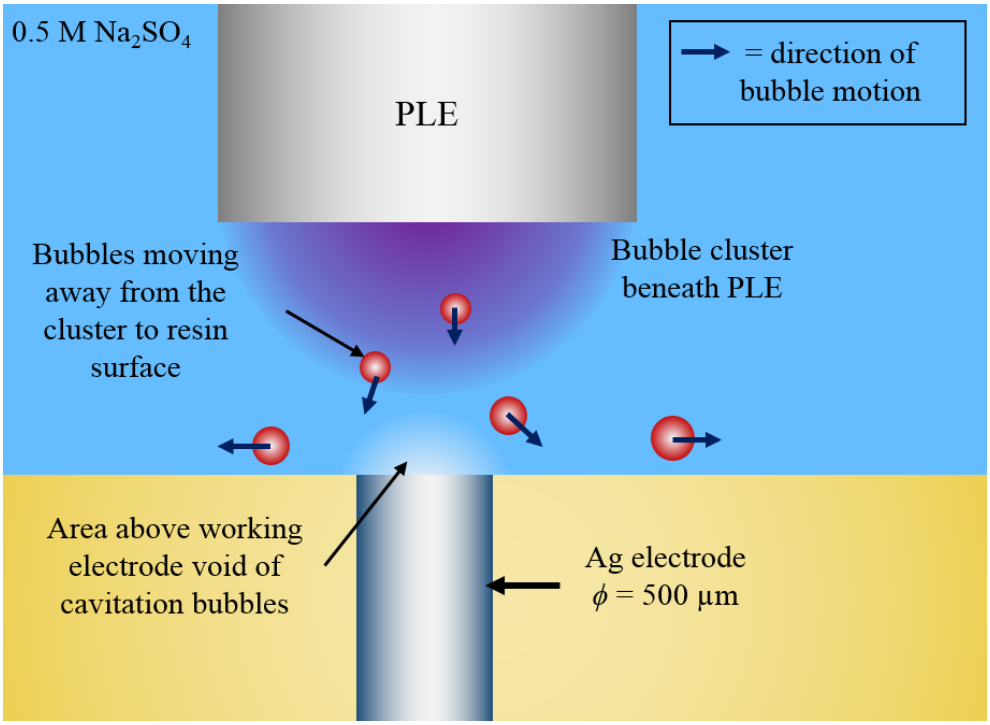

Figure 4.12 An illustration of the ultrasonic horn and Ag (ϕ = 500 µm) in a wide resin surround (ϕ = 20 mm) showing the direction of the bubbles moving radially outwards from underneath the ultrasonic horn. The electrolyte used in the cell was 0.5 M Na_2SO_4 at room temperature (~ 20°C) and pressure and under aerobic conditions. The ultrasonic horn was placed 2.5 mm above the surface of the resin. The picture is not drawn to scale.

As the *z* separation between the PLE and the working electrode was increased, the motion of the gas bubbles changed. It was observed that fewer bubbles from the cluster reached the resin surface (the maximum number of events recorded at both z = 5.0 mm and z = 7.5 mm is nearly half that recorded at z = 2.5 mm) directly below the PLE. However, bubbles were observed to reach the surface at extended radial distances from the PLE centre. This trend becomes more extreme the greater the distance (z) between the PLE surface and the solid electrode substrate.

4.4 Particle impact on an electrode

The novel high-speed impedance technique has been shown to be effective at measuring the activity of cavitation bubbles as they move across a working electrode surface. However as the technique is simply measuring the local change in solution resistance above a working electrode and effective active surface area, the technique could also be applied to other experimental systems. As an example of how this technique could be used in other systems, experiments were performed using sand particles and carbon micro particles in fluid jets, to act as insulating and conducting particles respectively. The effect

of these particles on the electrochemical environment around the electrode could then be characterised.

The experimental setup for such particle impact experiments can be seen in Figure 4.13, showing a sand loaded jet impinging on an aluminium electrode (ϕ = 250 µm). In this setup the electrolyte was pumped from the electrochemical cell, used as a reservoir, and through a glass pipette which was loaded with sand (or carbon) particles as a jet. The jet was positioned close to the surface of the aluminium working electrode. An AC perturbation of 50 mV zero-to-peak was applied across the working electrode and stainless steel reference/counter electrode at a frequency of 100 kHz. The current was recorded as function of time at a sample rate of 10 MHz (one data point every 0.1 µs) during the particle impact and the data processed using the FFT method described in detail in Chapter 2.3.

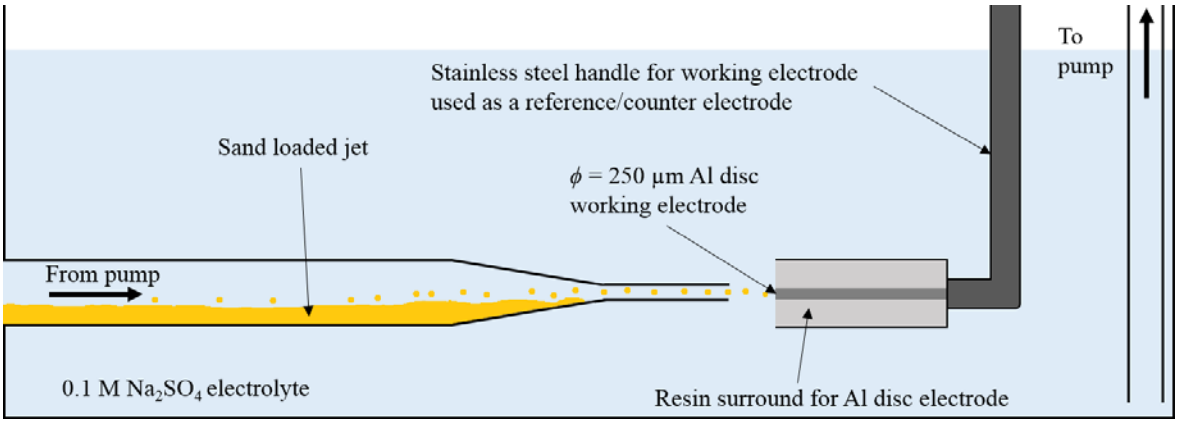

Figure 4.13 A cartoon showing the setup used in the particle impact experiments. The electrolyte (0.1 M Na_2SO_4) was pumped from the cell used to perform the experiments and through a glass pipette which was pre-loaded with the particles for the impact experiments (in this case sand). The working electrode was an aluminium disc (ϕ = 250 µm) mounted in an epoxy resin surround. The stainless steel handle of the electrode was used as the reference/counter electrode for the experiments. An AC perturbation was applied across the working and reference/counter electrodes of 50 mV zero-to-peak at 100 kHz and the AC current at the working electrode recorded at a sample rate of 10 MHz. Experiments were performed at room temperature (24 – 26 °C) and atmospheric pressure and under aerobic conditions.

The high speed AC impedance measurements of the impact of sand particles on the electrode elucidated similar results to the bubbles moving across the electrode. This was expected, as like the gas bubbles, the sand particles are insulators and thus would appear similar in terms of their impact on the local electrochemical environment. Figure 4.14 shows a plot of the uncompensated resistance (R_u), effective electrode capacitance (C), phase angle (θ) and Faradaic current (i_{dc}) measured as a function of time during sand particle impact on a 250 µm Al disc electrode.

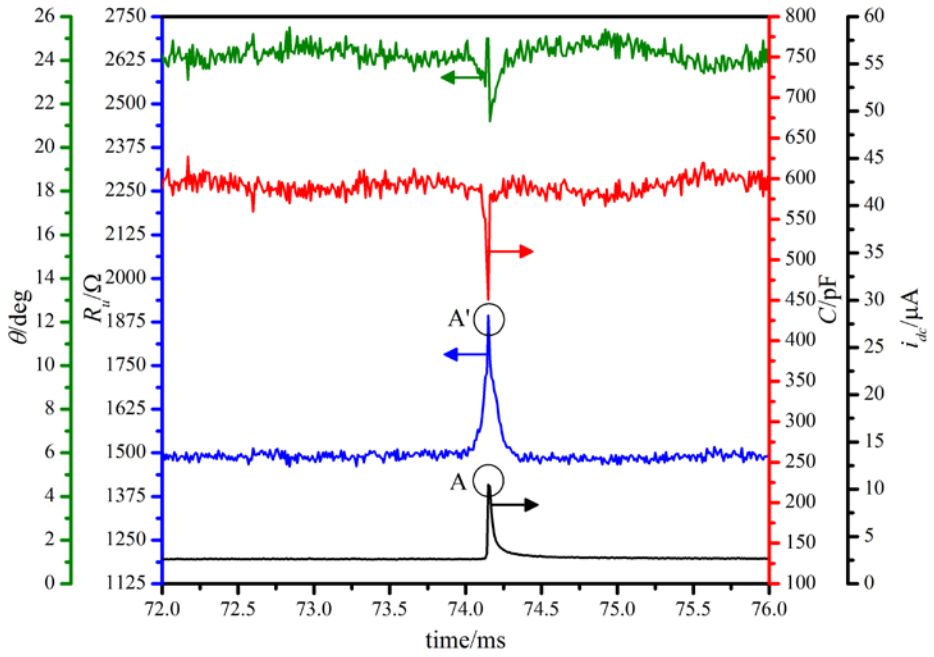

Figure 4.14 A plot of uncompensated resistance (R_u, —), effective electrode capacitance (C, —), Faradaic current (i_{dc}, —) and phase angle (θ, —) as a function of time at a sample rate of 100 kHz on impact with sand particles. The working electrode used was a 250 µm diameter Al disc electrode. The stainless steel casing was used as a pseudo reference counter electrode. The experiment was carried out in an aqueous electrolyte of 0.1 M Na_2SO_4 at 26.04 °C and at atmospheric pressure in aerobic conditions.

A transient peak was observed in Faradaic current, labelled ‘A’. As discussed in Chapter 3 this current transient indicates the erosion/corrosion processes which occur at the electrode as a result of the impact of the sand particle onto the surface of the aluminium. In this particular experiment the resistance transients therefore show the times at which individual sand particles struck the working electrode surface. The sand particle impact causes erosion of surface aluminium oxide from the electrode. This accounts for the shape of the current transient observed in Figure 4.14. As the sand particle strikes the surface some of the aluminium oxide surface layer is removed. An increase in Faradaic current was observed when the aluminium was exposed, followed by an exponential decay in current as the surface forms a new oxide layer using dissolved oxygen from the electrolyte solution. The baseline current recorded in each experiment should be zero, as the AC potential perturbation was centred around 0 V *vs.* the reference/counter electrode, which was an electrochemically inactive region. However, a current offset of 2.5 µA was recorded across multiple experiments using this setup. This systematic error was accounted for by the operational amplifier used by the custom made high-speed current follower employed in this system. Similar systematic shifts had been recorded in previous experiments carried out with this same operational amplifier[91].

As the sand particle from the jet moved towards the working electrode surface an increase in resistance was also measured. At the same time the working electrode capacitance was decreased as the sand particle effectively partially blocks the electrode surface. The time period over which resistance transients were recorded was longer than for cavitation bubble motion. For example, the width of the peak labelled A' in Figure 4.14 was approximately 0.35 ms. By comparison, the average length of the resistance transients observed in the non-inertial bubble motion experiments (Figures 4.5 and 4.6) was 0.05 ms. Thus it can be deduced that the particle/electrode encounters were occurring over a longer time period compared to bubble growth and collapse, which was driven by the applied ultrasonic source.

From the resistance transient data collected, it would be possible to calculate the size of the individual sand particles as they approach and strike the working electrode surface. This could be achieved by using a mathematical model. This model would need to account for the electrode diameter and sand particle size as the size of the resistance change will depend on the relative size of the sand particle relative to the electrode diameter[79]. However, the ΔR_u observed with the presence of an insulating particle has been shown in simulations to vary radially across the electrode surface the greatest change observed when the particle is closest to the edge of the disc[79]. The model used would therefore also need to account for the distance between the working electrode and sand particle in the encounter. Therefore, to accurately measure the sand particle size, images of the electrode surface during the jet impact would also be required. Thus the particle size calculated from the resistance change can only truly be considered as an estimate as the radial position of the particle as it hit the electrode surface was unknown.

This same system was also used to measure the change in resistance and capacitance upon impact with conducting particles. For these experiments, glassy carbon micro-particles with a particle size between 2 – 12 µm were chosen as the conducting particles.

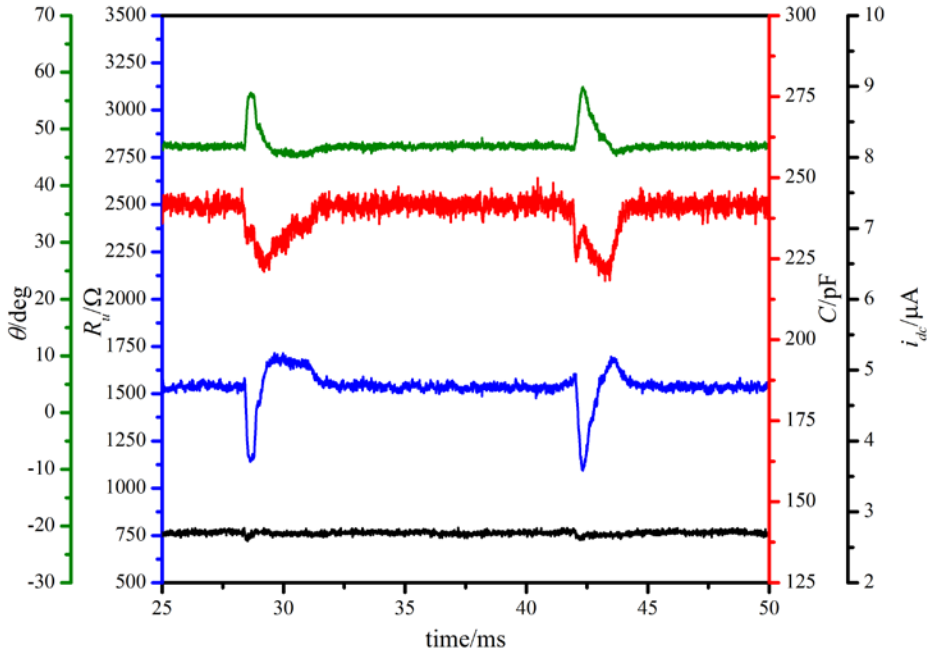

Figure 4.15 A plot of uncompensated resistance (R_u, —), effective electrode capacitance (C, —), Faradaic current (i_{dc}, —) and phase angle (θ, —) as a function of time at a sample rate of 100 kHz on impact with spherical glassy carbon particles with a particle size ranging between 2 – 12 μm. The working electrode used was a 200/250 μm diameter Al disc electrode. The stainless steel casing was used as a pseudo reference counter electrode. The experiment was carried out in an aqueous electrolyte of 0.1 M Na_2SO_4 at 24.4 °C and at atmospheric pressure in aerobic conditions.

The impact of carbon particles elucidated different results. First, due to their conductive nature, as the particles hit the surface of the electrode a decrease in resistance was observed. An example of two such transients can be seen in Figure 4.15. Second, as the carbon particles were smaller and lighter than the sand particles, the particle/electrode encounters have not resulted in the erosion of the Al working electrode surface. As a result the Faradaic current remains constant (0 A) during the particle jet impact.

The changes in R_u and C observed here for the sand and carbon particles can be easily rationalised, and attributed to some physical aspect of the system. This is therefore an indication that the impedance method developed can be applied to other simple electrochemical setups and yield useful information about the electrode surface and the impinging particle.

4.5 Control experiments

A series of control experiments were performed to check the validity of the high-speed impedance method employed. The range of experiments performed were used to measure electrode resistance and capacitance changes under various conditions and make comparisons between the novel method devised and commercial systems.

4.5.1 Connecting External Resistors

In the experiment devised, an electrochemical cell was set up with a 250 µm diameter aluminium working electrode and stainless steel reference counter electrode in 0.5 M Na_2SO_4. Using the high-speed impedance system, 50 mV zero-to-peak amplitude AC perturbations were applied across the two electrodes and the AC current response recorded. This was performed at five different AC frequencies, 200 kHz, 400 kHz, 800 kHz, 1 MHz and 2 MHz. These frequencies were chosen as they covered the frequency range employed in the many bubble activity investigations carried out. It was necessary to choose these exact frequencies owing to the nature of the data capture system used. Further discussion on the limitations in data recording and hence choice of frequencies can be found in Chapter 2.4. Using the FFT approach described in Chapter 2.3, the uncompensated resistance and working electrode capacitance was elucidated from the comparison between applied potential and current response. This was then repeated with an external resistance of 500 Ω and 1kΩ connected in series with the working electrode. Figure 4.16 shows a plot of uncompensated resistance as function of perturbation frequency with no added external resistance and with the two external resistors added.

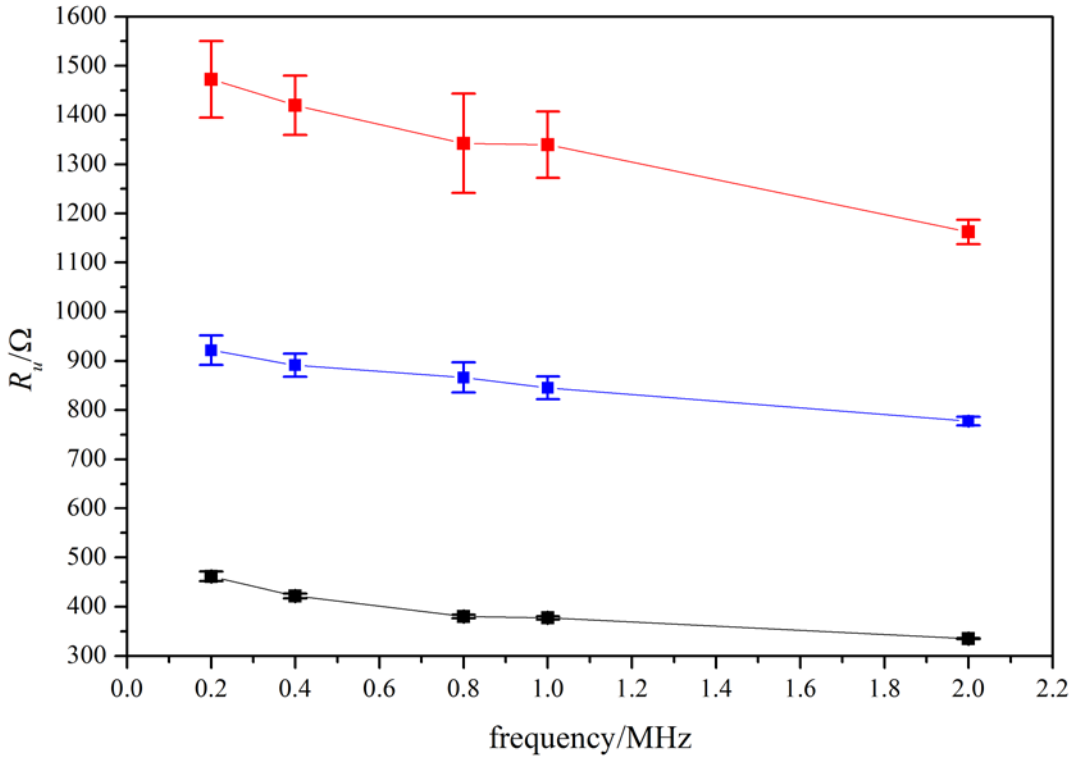

Figure 4.16 A plot of uncompensated resistance as a function of AC potential frequency for a 250 µm diameter aluminium working electrode (—) and for the same electrode with a 500 Ω resistor connected in series (—) and a 1 kΩ resistor connected in series (—). The magnitude of this AC perturbation was 50 mV zero-to-peak. The experiments were performed in 0.5 M Na_2SO_4 with a stainless steel reference counter electrode. The solution temperature was 21 °C and the experiments were performed at atmospheric pressure and aerobic conditions.

From Figure 4.16, the addition of an external resistor caused a shift in calculated uncompensated resistance as expected. The size of this observed shift is approximately equal to the size of the added external resistor. In order to show this more clearly, Figure 4.17 shows the same uncompensated resistance, R_u, data as Figure 4.16 with the value of the external resistors, R, removed from the two data sets in which the resistors were employed. From this plot it can be clearly observed that the measured value of the solution uncompensated resistance was not altered by the addition of other resistors. This is important to note as it indicates that the variance in resistance observed during bubble interaction with the electrode surface is a real effect and not as result of the calculation method employed.

The range in the calculated resistance values seen in Figure 4.17 was greatest at 2 MHz with a range of 173 Ω compared to a range of 38.6 Ω at 1 MHz. The calculated values at this perturbation frequency are less accurate as the system was at its detection limit at this frequency. It is also important to note that the reported error in R_u decreased in magnitude as the frequency of the perturbation increased. This is because the measured phase angle, θ, between the applied potential and current response decreased as the frequency of the perturbation increased (only 3.3° at 2 MHz compared to 19° at 800 kHz and 50° at 200 kHz). For further details of how the error in these values was calculated and how the error in R_u changes as a function of θ, see Appendix 4.

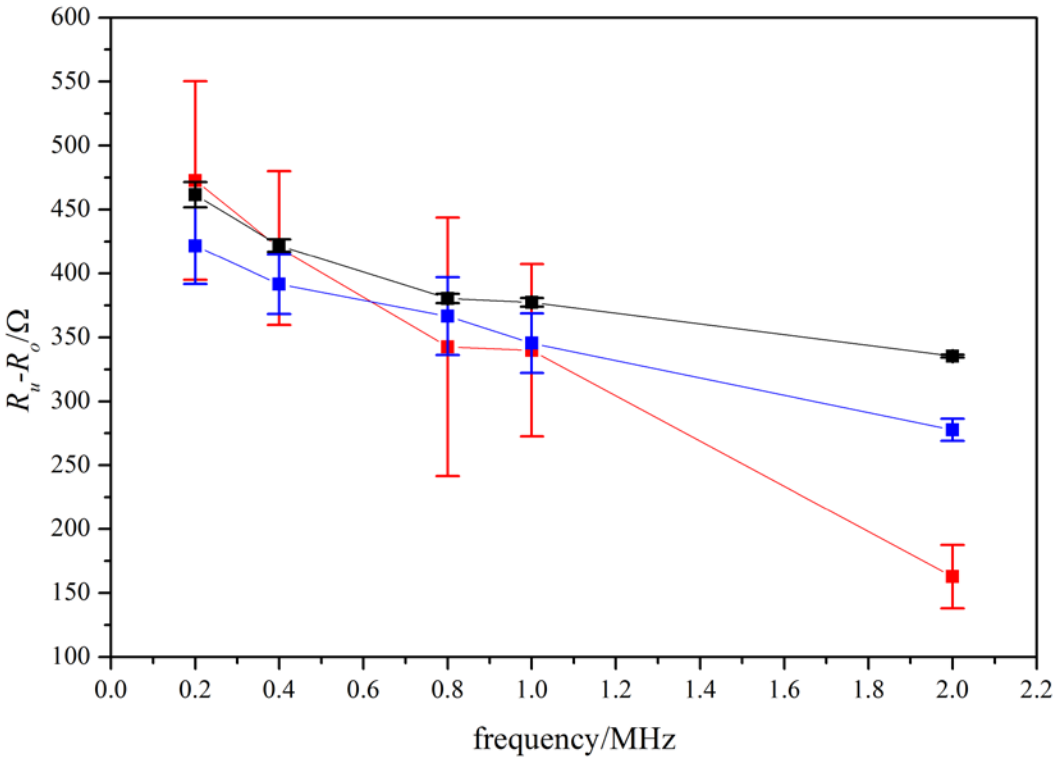

Figure 4.17 A plot of uncompensated resistance minus the added external resistance ($R_u - R_o$) as a function of AC potential frequency for a 250 µm diameter aluminium working electrode (—) and for the same electrode with a 500 Ω resistor with the value of the external resistor subtracted (—) and a 1 kΩ resistor with the value of the external resistor subtracted (—). The magnitude of this AC perturbation was 50 mV zero-to-peak. The experiments were performed in 0.5 M Na_2SO_4 with a stainless steel reference counter electrode. The solution temperature was 21 °C and the experiments were performed at atmospheric pressure and aerobic conditions.

The plot of resistance against applied frequency (Figures 4.16 and 4.17) also showed that the measured resistance is not the same at all perturbation frequencies and decreases with the increase of perturbation frequency. This is because the working electrode surface is not a perfect capacitor as is assumed in the mathematical model for these calculations (Figure 2.6). In the ideal model of an RC circuit the *Z'* term of impedance is independent of frequency and so the expected plot of imaginary against real impedance is a straight line with a constant *Z'*. By looking at plot of the real against the imaginary component of the impedance at these frequencies (Figure 4.18) at lower frequencies the electrode behaviour become less like the straight line expected for the resistor capacitor and started to resemble a large semi-circular curve.

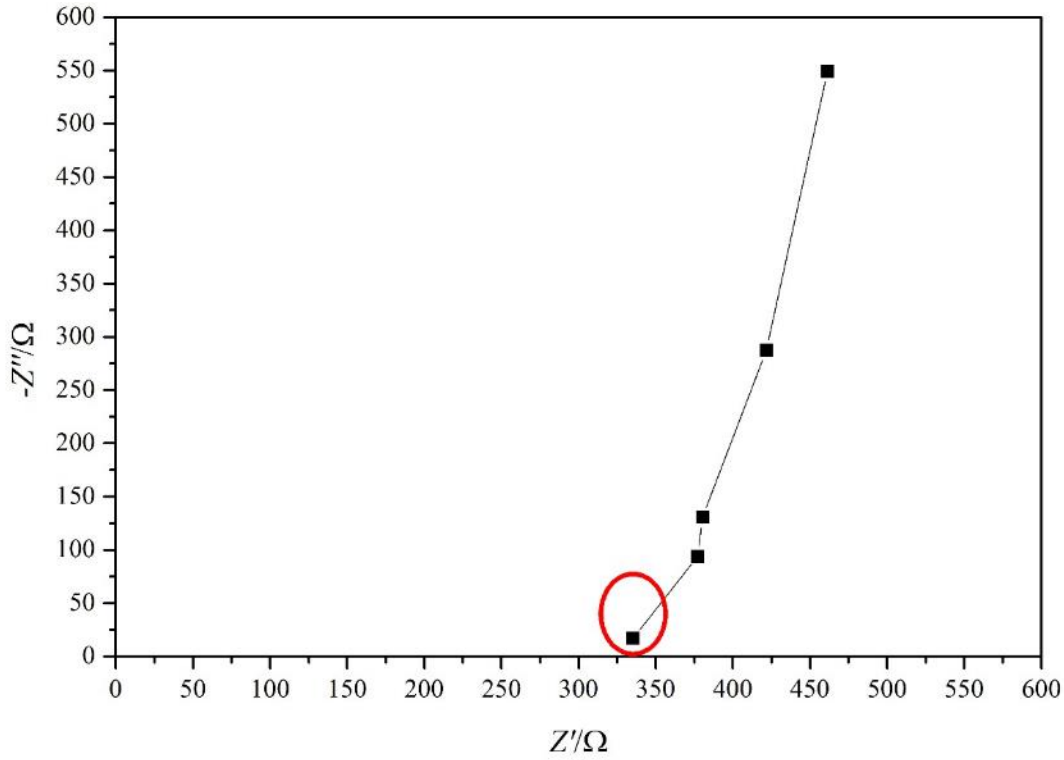

Figure 4.18 A plot of the imaginary component of impedance, *Z''*, against the real component of impedance, *Z'*, for a 250 µm diameter aluminium electrode. The reference counter electrode was a stainless steel rod and the electrolyte was 0.5 M Na_2SO_4. The temperature was 21 °C and the experiments were performed at atmospheric pressure and under aerobic conditions.

The first value on this curve corresponds to the value for *Z'* and *Z''* at 2 MHz. This point has been highlighted as anomalous. As was seen in the R_u against frequency plots of Figures 4.16 and 4.17 the accuracy of the calculation of *Z''* decreases at higher perturbation frequencies owing to the small θ therefore the error on the value plotted here is much greater than at lower frequencies (see earlier discussion on propagation of errors) and is not indicative of any trend. In addition, as the frequency range is increased the accuracy of the electronics employed may also be an issue. As a result, getting accurate measurements to 1 MHz potential perturbations is the limit under these conditions.

Using the data collected from this set of experiments the electrode capacitance calculated was also examined as a function of the external resistance added and frequency of the applied potential. In Figure 4.19 the calculated capacitance was plotted as a function of the ratio of uncompensated resistance with the added external resistors, *R*, over the resistance with no external resistors, R_o. For a system if the electrode surface acts as a perfect capacitor the value of the capacitance recorded was expected to stay the same regardless of the resistance added.

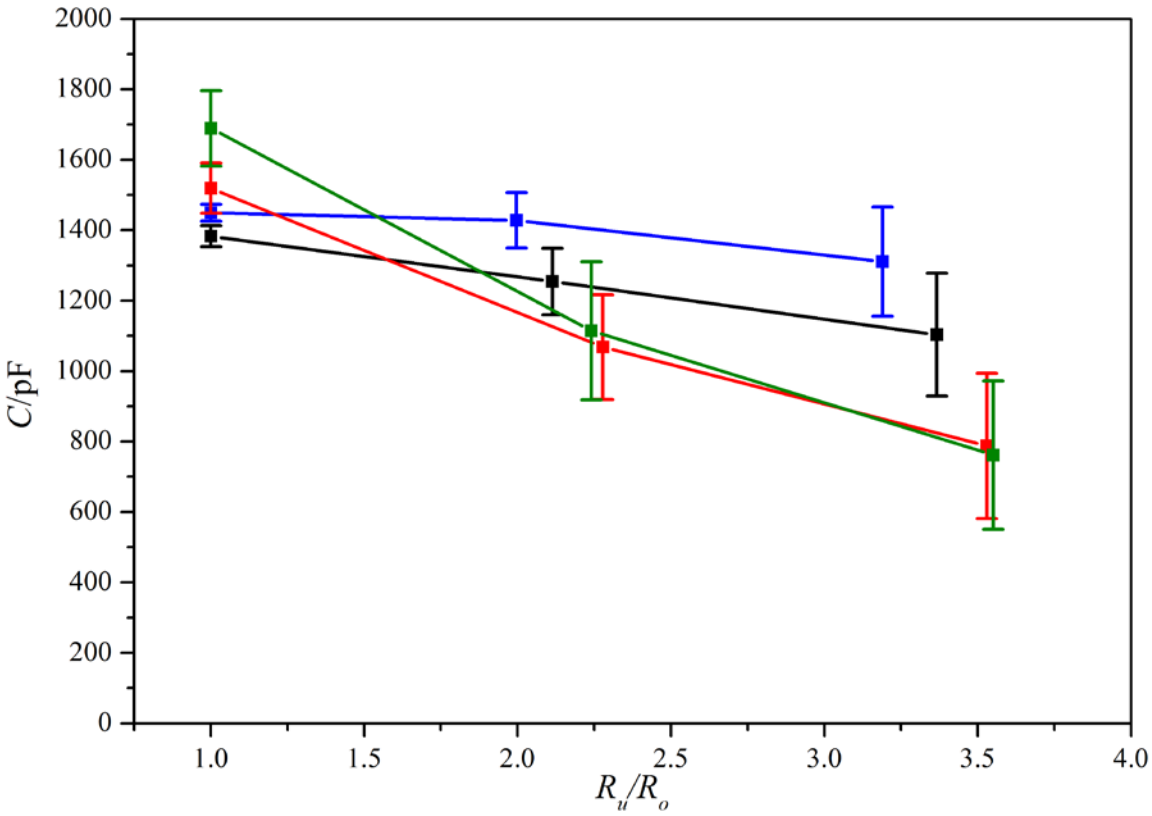

Figure 4.19 A plot of electrode capacitance as a function of the ratio of measured resistance, R_u, against resistance without an added external resistor, R_o. The plots given are for an AC potential perturbation of 200 kHz (—), 400 kHz (—), 800 kHz (—) and 1 MHz (—). The working electrode was a 250 µm diameter aluminium and the reference counter electrode was a stainless steel rod and the electrolyte was 0.5 M Na_2SO_4. The temperature was 21 °C and the experiments were performed at atmospheric pressure and under aerobic conditions.

Figure 4.19 shows a decrease in calculated capacitance as the ratio of R_u/R_o was increased. The change in capacitance measured also increased with increasing AC potential frequency, 110 pF at an AC frequency of 200 kHz and 706 pF at 1 MHz. The implication of this is that there is a constant phase element present, CPE, in the electrode capacitance measured. For the complete determination of the actual electrode capacitance this constant phase element needs to be accounted for when examining the results of capacitance change in the bubble/particle motion studies presented elsewhere in this thesis. However, it should be noted that over the range stated (R_u/R_o ~ 3.5), the magnitude of the capacitance change is of the order of 100 pF on a baseline of 1500 pF (at 400 kHz). This corresponds to <10 % change over this resistance perturbation. It should also be noted here that the error in capacitance values recorded increases with both increasing uncompensated (higher R/R_o recorded here) and also increasing frequency of AC perturbation. This is because increasing either or both of these two parameters results in a decrease in the phase angle, θ. The decrease in phase angle results in a decrease in an increase in error for the capacitive

resistance, X_C (Z'') and thus a very large error in capacitance, C, at small angles (for R_u/R_o = 1, θ = 50° at 200 kHz and θ = 14° at 1 MHz and for R_u/R_o = 3.5, θ =22° at 200 kHz and θ = 8.9° at 1 MHz). Further details of how the capacitance errors were calculated and their variance with phase angle can be found in Appendix 5.

It is now possible to compare these values with the experimental data recorded at an electrode in the presence of cavitation bubbles induced by ultrasound. Take as an example, in the capacitance transients observed in Figure 3.11 reproduced here in Figure 4.20. Here the maximum ratio of the uncompensated resistance change observed was 2.98. Under these conditions the capacitance (determined by applying the 'perfect' capacitor model), was found to change from ~ 600 pF to ~ 100 pF. This corresponds to a change in capacitance of ~ 500 pF.

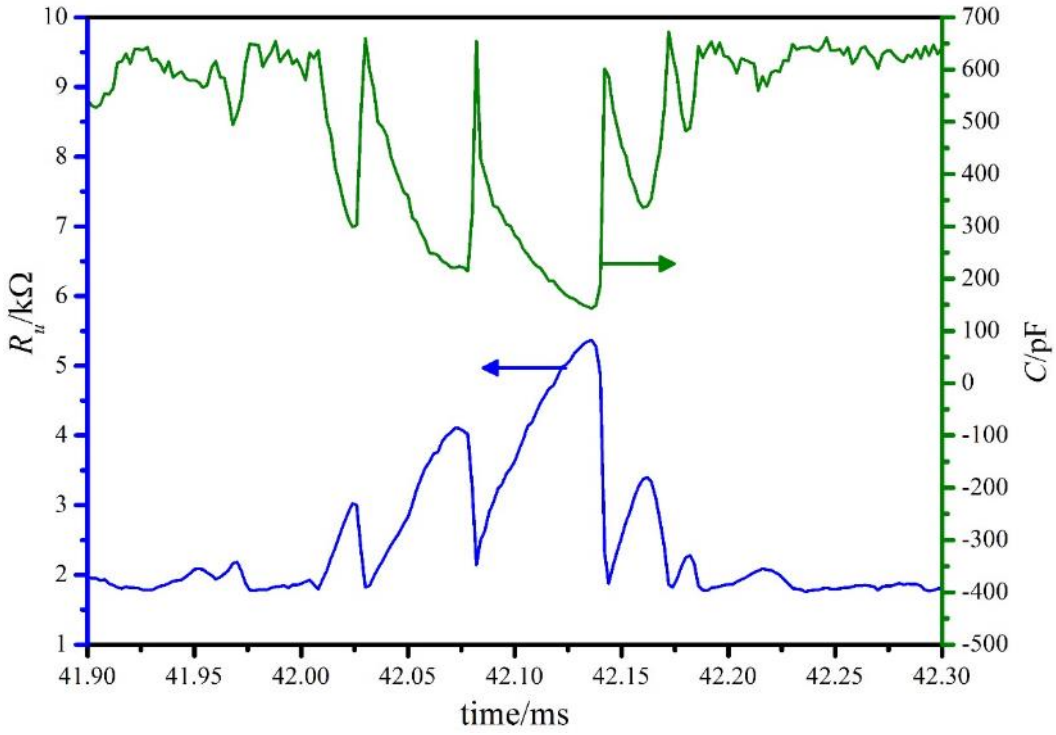

Figure 4.20 Plot showing the resistance, R_u, (—) and capacitance, C, (—) for a 100 µm diameter Al disc within a resin support and a stainless steel outer case acting as a reference counter electrode. The solution in the resonant chamber was 0.2 M Na_2SO_4. The frequency applied to the transducer from the amplifier is 37.97 kHz and the z separation was 32 mm. The solution temperature was 22°C and the experiment was performed in aerobic conditions. Data acquired with a 500 kHz sample rate.

A comparison in the changes in capacitance observed in the bubble event (Figure 4.20) to the shift observed owing to the CPE (Figure 4.19) was then made to determine the extent to which the observed capacitance change was due to the CPE. Using the data of Figure 4.19, for R_u/R_o = 2.98 the approximate capacitance change was 175 pF and for R_u/R_o = 1.27

was 33.4 pF. Therefore, it is possible that some of the capacitance change measured by the system may not be due to the change in double layer capacitance from bubble. In the absence of further experiments on the dynamic bubble system involving use of multiple frequencies of AC perturbation, these two characteristics cannot be separated from one another in the data collected. However as shown by Figure 4.19, the percentage change in capacitance owing to the CPE effect is not a significant percentage of the total (> 10 %) and thus the capacitance change observed here (Figure 4.20) can be assumed to be a mostly real effect.

4.5.2 Approach Curves

In the bubble/particle motion investigations presented elsewhere in this thesis, the magnitude of resistance change is often used to either determine the size of the bubble/particle or explain bubble growth over the electrode it is interacting with. As will be shown here, the magnitude of resistance and capacitance change is also dependent on the position of the interrogating bubble/particle to the electrode. This was investigated using a sealed glass pipette (ϕ ~ 1500 µm) as an insulating material interacting with a working electrode (Ag, ϕ = 500 µm inside a 1000 µm recess). The same glass pipette was positioned at different z separations (distance between the end of the pipette and top of the recess, as shown in the schematic of Figure 4.21) using a micro-positioning system. At chosen *z* separations, the current response to a 50 mV zero-to-peak AC potential perturbation at 10 kHz, 500 kHz, 1 MHz and 2 MHz was investigated. Using the high-speed AC impedance system (see Chapter 2.3) the resistance and capacitance (using the series model) was elucidated for each frequency of potential perturbation and plotted as a function of *z* separation. The pipette was positioned centrally over the electrode in each case. This was confirmed by measuring the electrode resistance with the pipette at a *z* separation of 20 µm for different lateral positions, also controlled by a micro-positioner. Figure 4.21 is a schematic of this experimental setup. The picture is for illustration only and not drawn to scale.

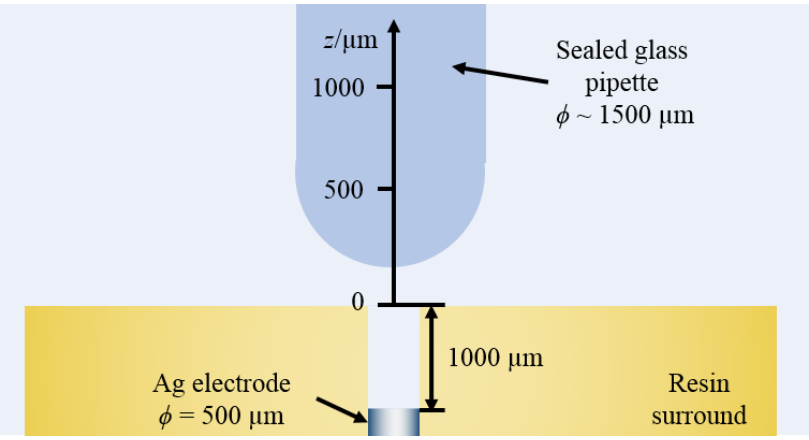

Figure 4.21 A schematic showing the experimental setup used to measure the uncompensated resistance at an Ag electrode (ϕ = 500 µm, inside a 1000 µm recess) as an insulator (glass pipette ϕ ~ 1500 µm) approached the mouth of the recess. A stainless steel rod (ϕ = 6 mm) was used as a counter reference electrode. The electrolyte was 0.5 M Na_2SO_4 at atmospheric temperature and pressure and under aerobic conditions. This image is an illustration only and is not drawn to scale.

As the resistance increases as the insulator approaches the electrode surface, the position at which the highest resistance was recorded was the position at which the pipette was central over the electrode surface. To validate the measurements from the high-speed AC impedance system, a commercial system (Bio-Logic, SP-150, using EC-Lab v10.44) was also employed. The resistance values obtained from this system were calculated using the EC-Lab Z Fit program. In this Z fit the Nyquist plots were fitted to an equivalent circuit of a resistor (Z_1/Ω) and constant phase element (Q_1/F s^{a-1}) Three readings were recorded at each z separation for each AC perturbation and using the EC-Lab system. The results recorded in Figure 4.22 are an average of the three measurements and the error quoted is the 95 % confidence level calculated using Excel ‘Data Analysis’.

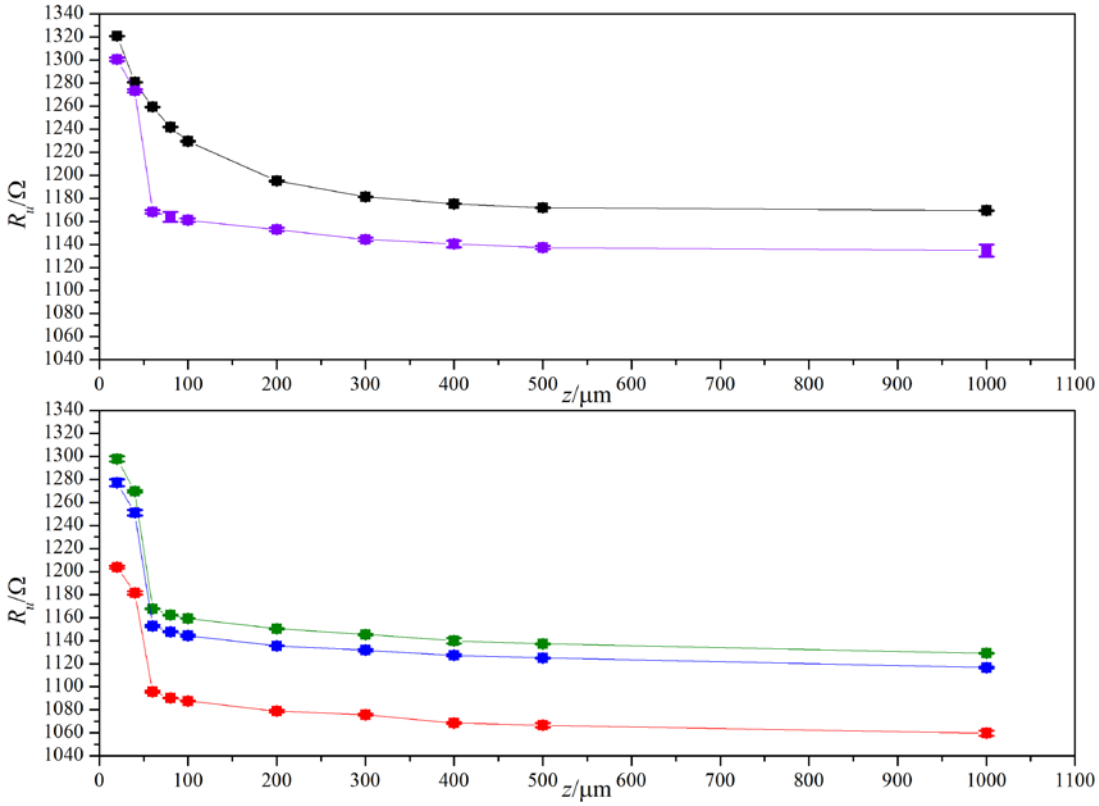

Figure 4.22 A plot of uncompensated resistance as a function of z separation with an AC perturbation frequency of 10 kHz (●), 500 kHz (●), 1 MHz (●) and 2 MHz (●) EC-lab Z Fit (●). The working electrode was a 500 µm diameter Ag disc electrode inside a 1000 µm recess and the reference counter electrode was stainless steel. The experiments were performed in an aqueous electrolyte of 0.5 M Na_2SO_4. The solution temperature was 22°C and the experiment was performed at atmospheric pressure in aerobic conditions.

The results of these approach experiments can be seen in Figure 4.22. Each plot shows that when the glass pipette was > 500 µm – 1000 µm, the measured uncompensated resistance measured was not significantly altered by the presence of the insulator. However, as the glass pipette moved closer to the Al electrode surface the resistance increased. The resistance rose steadily until the glass pipette reached a *z* separation of 60 µm. As the *z* separation decreased below this value the increase in resistance became more rapid (as seen in Figure 4.22).

These approach curves show that the resistance measured between the working electrode and reference/counter electrode is dependent on the position of the insulator (or cavitation bubble) relative to the electrode surface. Therefore the size of the resistance changes measured in our cavitation experiments is dependent on the bubble position as well as the diameter of the bubble. Without other complementary data, such as high-speed camera images in which the bubble position can be tracked, it is difficult to distinguish these two parameters from the impedance data. The change in resistance with *z* separation appears to

have a reciprocal relationship, so the change in resistance decreases rapidly with increasing insulator to electrode *z* separation.

The expected uncompensated resistance for this working electrode (Ag, ϕ = 500 µm inside a 1000 µm recess) within the absence of an insulator between the working and counter reference electrodes was 1091 Ω. This value was calculated based on the assumption that the total resistance is a linear combination of the resistance in the recess (R_{ch}, with $R_{ch} = l/\kappa A$, where l is the length of the recess, κ the solution conductivity and A the area of the end of the channel) and the electrochemical environment at the recess mouth (R_h, with $R_h = 1/4\kappa a$ where a is the radius of the recess mouth). The high-speed AC impedance measurements which most closely resembled the results from the EC-Lab fitting were those recorded at 500 kHz. The uncompensated resistance with the glass rod at a *z* separation of 1000 µm for both these methods was higher than the expected resistance (at 500 kHz R_u = 1134 Ω, for Z Fit R_u = 1129 Ω). Considering the experimental setup and the approximations of the model (temperature control etc.), the agreement between the experimental data and the theoretical value (40 Ω) is excellent (<5%). As the frequency of the perturbation was increased to 1 MHz and 2 MHz, so the measured θ between the applied AC potential and current response dropped (as seen in Chapter 4.5.1). The decrease in θ again resulted in a less accurate calculation of uncompensated resistance.

The discrepancy seen between recorded uncompensated resistance values at different frequency perturbations indicates that the RC model chosen is in reality too simplistic. It is however necessary to use to perform the calculations required for the chosen high-speed system. Hence the R_u and C_{dl} calculated here are an approximation, however the values become a closer approximation at higher perturbation frequencies owing to the reduction in CPE effect observed (see discussion in Chapter 4.5.1).

The plot in Figure 4.23 shows the Nyquist plot of impedance performed using the Bio-Logic instrument with the glass pipette at a *z* separation of 1000 µm for a 250 µm diameter Al electrode. The frequency range used for the AC potential perturbation was from 10 kHz to 500 kHz. It can be seen from this plot that the electrode response has a slight curve which is most significant at lower frequencies and as it approaches higher frequencies starts to become more vertical. This is typical of real electrode/electrolyte interfaces where CPE models are often employed to accurately depict the experimental conditions.

However, in the work presented in the thesis, we are concerned with the dynamic changes around the electrode and hence some compromise is required.

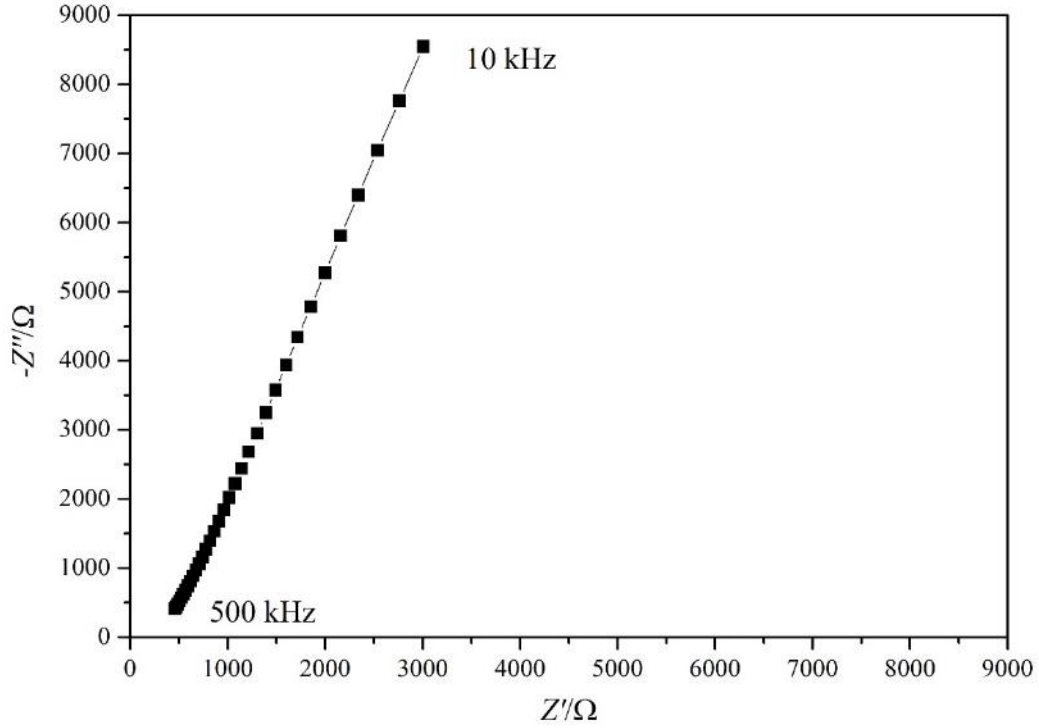

Figure 4.23 A Nyquist plot of impedance for a 250 µm diameter Al disc electrode. The reference counter electrode used was a stainless steel rod and the experiment was performed in 0.5 M Na_2SO_4. A glass pipette used as an insulator to change the impedance of the solution was held at a *z* separation of 1000 µm from the electrode surface. The experiment was performed at a temperature of 22 °C in aqueous and aerobic conditions at atmospheric pressure.

4.5.3 Scanning Experiments

In the previous chapter (4.5.2) it was determined that the measured uncompensated resistance increased as an insulator (glass pipette) approached the surface of an electrode. These investigations were carried out with the glass pipette held centrally over an electrode surface, however it was noted that the lateral position of the insulator relative to the electrode also affected the resistance measured. In order to quantify this observation, a series of experiments performed a sealed glass pipette (ϕ ~ 1500 µm) was used as an insulator and moved across the surface of a variety of electrodes at different *z* separations from the surface. The pipette was moved to different *x* and *y* positions and the resistance and capacitance measured at each position using the same AC impedance method as described in Chapter 2.3 with a 100 mV zero-to-peak perturbation at 500 kHz. The position of the working electrode (position at which the resistance was greatest) was determined by performing a course scan (one data point every 500 µm over distances of 2000 µ in *x* and *y* direction) and the origin set so the centre of the working electrode lay in the centre of the

scanning range. This technique has similarities to the high-frequency impedance scanning electrochemical microscopy performed by Gabrielli *et al.* on microelectrodes (ϕ = 10 µm)[94]. It also bears similarities to an ion conductance microscopy technique employed by Klenerman *et al.* to reveal topographical information of biological cells[95].

Figure 4.24 is a schematic of the experimental setup used showing the directions of the *x*, *y* and *z* axes and the chosen origin. This schematic is given for illustration purposes and is not shown to scale.

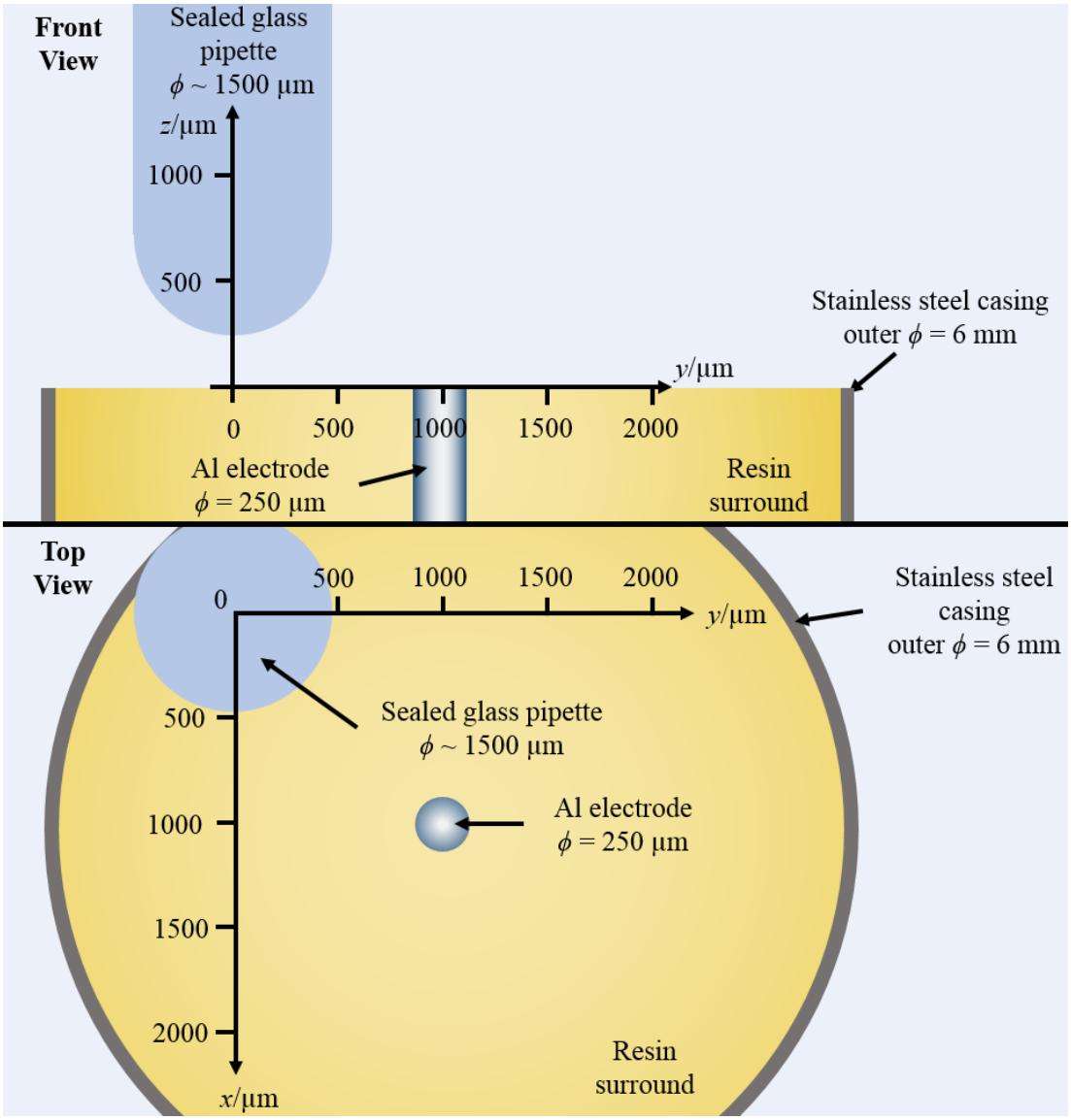

Figure 4.24 A schematic of the experimental setup used in the surface scanning experiments as viewed from the front and top. The centre of the working electrode, Al ϕ = 250 µm, was approximately in the centre of the 2000 µm x 2000 µm *x*/*y* scanned region, and the origin of the *z* axis was chosen as the surface of the electrode. The stainless steel outer case of the electrode surround was used as a counter reference electrode. The experiments were performed in an electrolyte of 0.5 M Na_2SO_4 at atmospheric temperature and pressure and under aerobic conditions. This image is an illustration only and is not drawn to scale.

Using the high-speed AC impedance method the uncompensated resistance, R_u, and apparent capacitance, C, was calculated and 2-D surface maps were generated from these values. The results of one such set of experiments is shown in Figures 4.25 and 4.26 showing the change in resistance and capacitance respectively for an aluminium working electrode (ϕ = 250 µm).

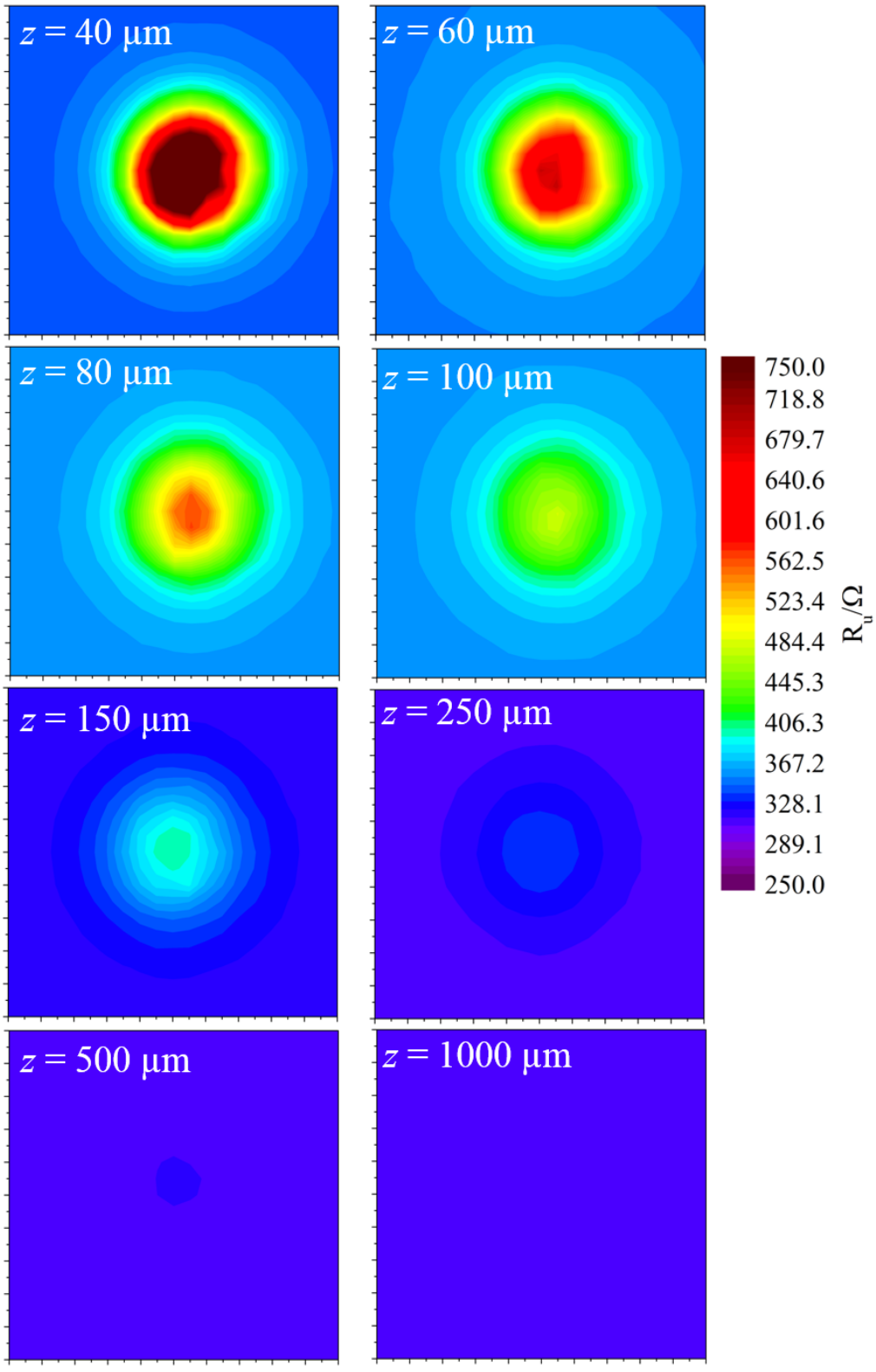

Figure 4.25 2-D plots of resistance from the scanning experiments. The working electrode was a 250 µm diameter aluminium electrode. A stainless steel rod was used as a pseudo reference counter electrode and the experiments were performed in 0.5 M Na_2SO_4. The applied AC perturbation applied across the electrodes was 100 mV zero-to-peak at 500 kHz. The same key was used for each plot. The image resolution was 100 µm created by moving the glass pipette in this increment in both *x* and *y* dimensions to form a 20 by 20 point grid. The *x* and *y* scales on each plot range from 0 to 2000 µm with major divisions of 200 µm. The experiments were carried out at 25.2 °C and at atmospheric pressure and in aerobic conditions.

From the measured uncompensated resistance plots (Figure 4.25) the extent to which the insulator effects the solution resistance measured between a 250 µm aluminium electrode and stainless steel electrode was observed as a function of *x*, *y* and *z* separation. The origin point of each scan was chosen so that the centre of the working electrode lay approximately in the centre of the 2000 µm x 2000 µm area scanned by the glass pipette. Successive experiments were all performed starting from the same starting position using a program controlled micro positioning system to control the *x* and *y* movement of the glass pipette.

These plots showed increasing resistance as the glass rod came closer to the electrode producing a 2-D plot with circular bands of increasing resistance as the pipette reaches the centre of the electrode. By plotting all of the data from each scan on the same colour scale, the change in resistance perturbation made by the insulator could be observed. As the *z* separation between glass pipette and electrode surface was increased the extent to which the resistance was perturbed lessened so the range of resistance change decreased.

At 1000 µm *z* separation the resistance was not noticeably altered by the movement of the glass pipette over the working electrode. As the *z* separation increased the measured resistance did not just decrease in the region where the glass pipette was above the working electrode but also where the pipette is further laterally from the electrode, such as at the origin. This indicates that the region over the electrode in which the glass pipette insulator has an effect on the resistance measurement forms a hemispherical region around the electrode. In relating these results to the transients observed in bubble motion captures the size of the resistance changes observed could not only indicate the size of the collapsing or oscillating bubble but also the proximity of the bubble to the electrode surface. As the working electrode capacitance will be altered by changing the active area of the working electrode, an accurate measurement of the change in capacitance will be useful in determining how close the bubbles were to the electrode surface.

The measured capacitance as a function of *x*, *y* and *z* separation was also plotted in the same way as the uncompensated resistance. The plots in Figure 4.26 show how the capacitance of the 250 µm diameter aluminium electrode changes over the same range as shown in the resistance plots of Figure 4.25.

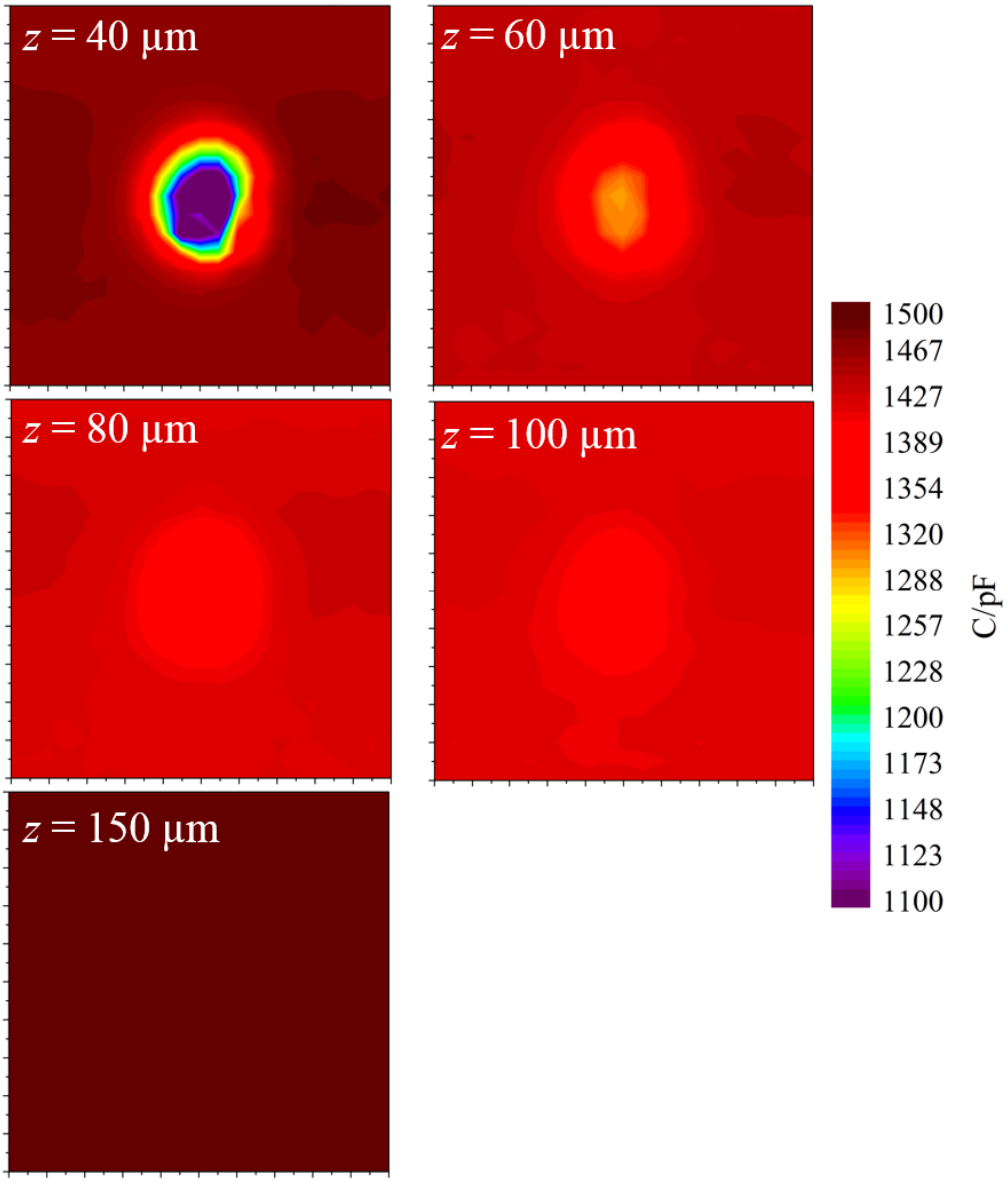

Figure 4.26 2-D plots of capacitance from the scanning experiments. The working electrode was a 250 µm diameter aluminium electrode. A stainless steel rod was used as a pseudo reference counter electrode and the experiments were performed in 0.5 M Na_2SO_4. The applied AC perturbation applied across the electrodes was 100 mV zero-to-peak at 500 kHz. The same key was used for each plot. The image resolution was 100 µm created by moving the glass pipette in this increment in both *x* and *y* dimensions to form a 20 by 20 point grid. The *x* and *y* scales on each plot range from 0 to 2000 µm with major divisions of 200 µm. The experiments were carried out at 25.2 °C and at atmospheric pressure and in aerobic conditions.

As the glass pipette was moved across the electrode the measured capacitance decreased creating a pattern similar to that observed with the resistance plots. The range over which the electrode to insulator separation caused a significant change in electrode capacitance was lower than that observed for resistance. This can be seen in Figure 4.26 where at a *z* separation of 150 µm no significant change in electrode capacitance was measured as the glass pipette was moved across the electrode in *x* and *y*.

The results reported on in this chapter show how the high-speed impedance technique developed can be used to measure the activity of cavitation bubbles from a PLE source. The technique developed was also validated by the use of a number of control experiments in which the high-speed impedance technique was compared to a commercial impedance system. A series of surface and line scans with an insulating glass rod were also performed. These showed how the change in resistance and capacitance observed varied as a function of insulator (or bubble) to electrode distance. The surface scans also showed that the relative changes in capacitance were smaller than the observed changes in resistance and that such changes in capacitance were only observed when the insulator was very close to the electrode surface. In the following chapter the impedance technique will be explored further to reveal further mechanistic details of the bubble motion.

Chapter 5 Bubble Capture and Cleaning

5.1 Cleaning of a resin surface using a PLE

In the previous chapter an ultrasonic horn was used as a piston-like emitter (PLE), as an energy source to generate cavitation bubbles. The primary focus of this chapter was to investigate how the high-speed impedance method developed (Chapter 2.3) could be employed to monitor the activity of bubbles generated in such a manner. This second chapter dedicated to the ultrasonic horn as a PLE will concentrate on how this same impedance technique can reveal mechanistic detail of the bubble motion and explore practical applications of the cavitation. More specifically, the role in which the oscillations of the bubble wall play in the cleaning of contaminate material from a flat surface will be investigated.

In experiments inside the cylindrical resonance chamber (Chapter 3) it was observed that high energy cavitation bubbles exhibit transient cavitation, where the bubbles grow then rapidly collapse. In this bubble collapse, material was eroded from the electrode being used to probe the bubble activity. The ability for transient cavitation bubbles to erode surfaces shows these bubbles have great potential for removing contaminant material from a surface. However, experiments in which cavitation bubbles were generated using a PLE (see Chapter 4 for further details), the bubbles probed at the electrode surface were ‘stable’ cavitation bubbles. These bubbles had kinetic energy to move across the electrode surface (see Chapter 4.2 and Figure 4.7) and to oscillate. Although less explosively energetic than the transient cavitation bubbles, the motion of the stable cavitation bubbles can also be employed to loosen and remove material from a surface.

An experiment was devised to investigate the cleaning of surfaces using cavitation bubbles from the PLE. In this experiment, a finely sanded resin surface of a circular resin block (ϕ = 42 mm, epofix resin see Table 2.1 for further details) was ‘contaminated’ by coating it in an even and thin layer of petroleum jelly (Vaseline) and aluminium oxide powder (0.3 µm particle size, see Table 2.1 for further information). The solid resin block was fixed to the base of an electrochemical cell and submerged in an electrolyte solution of 0.5 M Na_2SO_4. The PLE was placed centrally over the resin disc with the tip at 1.5 mm from the surface of the resin. The resin block was then exposed to ultrasonic activity for approximately 3 minutes. An annotated picture of the experimental setup and image of the

contaminated resin block during exposure to cavitation bubble from the PLE can be seen in Figure 5.1.

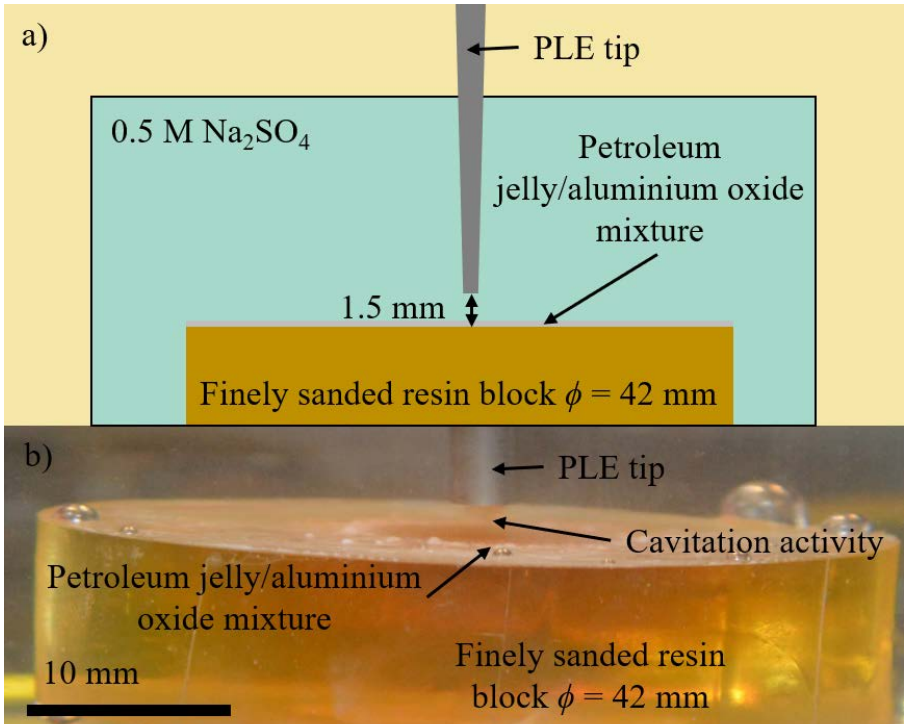

Figure 5.1 a) An annotated image of the experimental setup employed in the cleaning experiment. **b)** An image of the contaminated resin block during exposure to cavitation activity.

Images of the resin disc employed, before and after exposure to cavitation bubbles from the PLE is shown in Figure 5.2 a) and b).

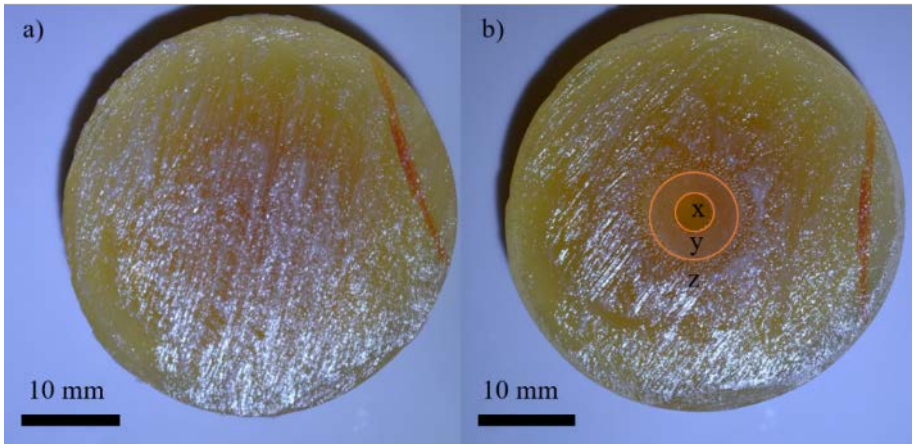

Figure 5.2 a) An image of the resin disc contaminated with petroleum jelly and aluminium oxide powder. **b)** An image of the same contaminated resin disc after exposure to cavitation from a PLE source.

The image of the resin surface after exposure to cavitation (Figure 5.2 b)) shows that the kinetic motion of the bubbles has indeed succeeded in removing the ‘contaminant’ material from the resin surface. The removal of material occurred in a circular pattern. This shows

that the bubbles generated from the PLE moved away from the source in a radial direction (such motion was also observed in the high-speed images captured, see Chapter 4 for further information). The bubbles in the high-speed images were also observed to lose kinetic energy as they moved radially further away from the source. This can be observed in the circular pattern of contaminant material removed from the resin surface. In the image (Figure 5.2 b)), three distinct regions of surface cleaning can be observed. In the first region (labelled x in Figure 5.2 b)), all the petroleum jelly/aluminium oxide mixture had been removed from the resin surface. This region was the region of resin directly underneath the PLE where the cavitation bubbles have the greatest kinetic energy. This observation can be rationalised as the piston motion of the ultrasonic horn tip (PLE) does not allow bubbles to reside for any period of time directly underneath it (for further details of this piston motion see discussion in Chapter 4.3 with reference to Figure 4.12). Therefore, all the contaminant material is cleared from this region along with the high energy cavitation bubbles. The second region (Figure 5.2 b)), labelled y, shows partial cleaning of the petroleum jelly/aluminium oxide. In this region the cavitation bubbles still had reasonably high kinetic energy and so their lateral motion and oscillation (see Chapters 4 and 5.2 for further details of bubble motion) was able to remove some contaminant material from the resin surface. The third region, labelled z, shows no removal of contaminant from the resin surface. This was because the cavitation bubbles lost kinetic energy as they moved radially further away from the PLE.

The quantity of bubble activity observed was observed to vary as a function of the PLE to surface distance (see Chapter 4). Therefore it would follow that the quality of surface cleaning would also be affected by this PLE to resin (*z* separation). The variation of this the z separation on surface cleaning was investigated. In the investigation a finely sanded circular resin block (ϕ = 42 mm, epofix resin see Table 2.1 for further details) was spread with an aqueous slurry of aluminium oxide particles (0.3 µm particle diameter, see Table 2.1 for further details). The aluminium oxide paste was allowed to dry onto the surface of the resin. The resin was then submerged into a container of water and the PLE tip placed at a known *z* separation over the centre of the disc. The disc was then exposed to cavitation bubbles for 1 minute. The *z* separation was then altered at the experiment repeated. Between each repeat experiment the resin surface was thoroughly cleaned and re-coated with the aluminium oxide particle slurry. Images were recorded of the resin surface before and after each exposure to cavitation. Figures 5.3, 5.4 and 5.6 show images of the

resin block before and after exposure the cavitation with the PLE tip at *z* separations of 2.5 mm, 5.0 mm, and 7.5 mm respectively.

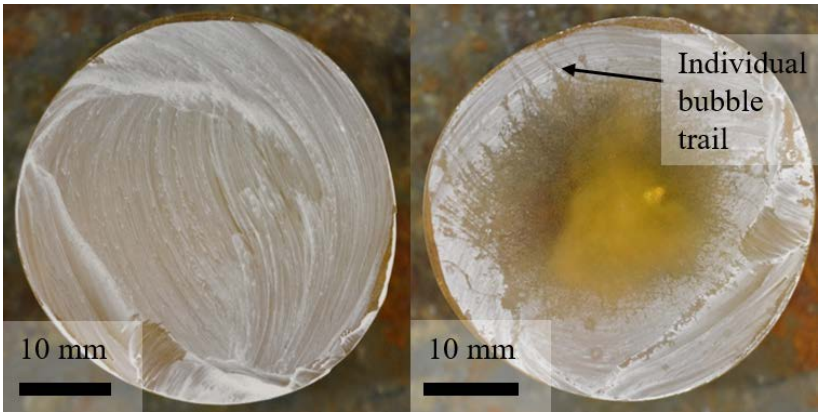

Figure 5.3 Images of the aluminium oxide powder covered resin before and after exposure to cavitation bubbles. The cavitation bubbles were generated by a PLE oscillating at approximately 23 kHz in a basin of purified water (see Table 2.1 for further details of purification process). The PLE tip was positioned at a *z* separation of 2.5 mm.

At $z = 2.5$ all the contaminating material was removed from the centre of the disc out to form a clear approximately circular area with a diameter of ~ 17.6 mm. As the PLE tip was close to the resin surface, the material from directly under the PLE was forced radially outwards, as was observed in the previous cleaning experiment (Figure 5.3). The motion of the stable cavitation bubbles then carried the contaminant material further away from the centre of the resin. The trails of individual bubbles carrying aluminium oxide powder away from below the PLE tip can be seen at the edge to the central clean section.

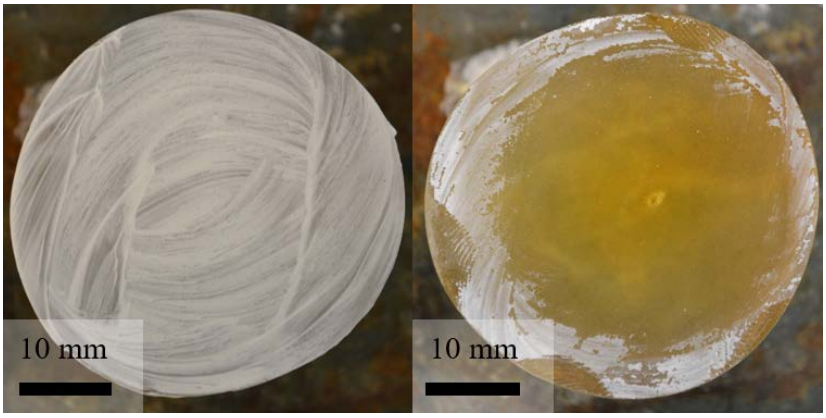

Figure 5.4 Images of the aluminium oxide powder covered resin before and after exposure to cavitation bubbles. The cavitation bubbles were generated by a PLE oscillating at approximately 23 kHz in a basin of purified water (see Table 2.1 for further details of purification process). The PLE tip was positioned at a *z* separation of 5.0 mm.

With the *z* separation at 5.0 mm (Figure 5.4), a larger area (ϕ ~ 29 mm) of aluminium oxide powder was cleared from the resin surface. However close inspection of the surface inspection of the resin surface shows that some aluminium oxide powder remained behind

across the entire resin surface. The inference drawn from this was that the increased *z* separation was that the cavitation bubbles generated at the PLE had spread further radially outwards from the surface before reaching the resin surface. A schematic showing the movement of the cavitation bubbles away from the cluster and the apparent 'beam angle' of bubble motion can be seen in Figure 5.5.

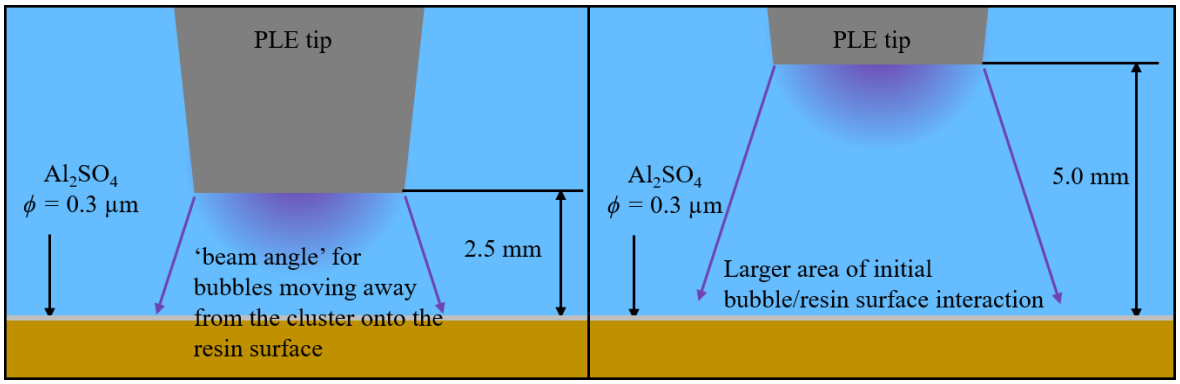

Figure 5.5 A schematic showing the movement of cavitation bubble cluster below the PLE cluster down to the resin surface at a *z* separation of 2.5 mm and 5.0 mm.

The *z* separation between PLE tip and resin surface was then increased to 7.5 mm. The images of the contaminated disc before and after exposure to cavitation can be seen in Figure 5.6. At this *z* separation the surface area cleared of resin all resin decreased in comparison to that cleaned with the smaller *z* separations (a circular area of approximately 15 mm in diameter).

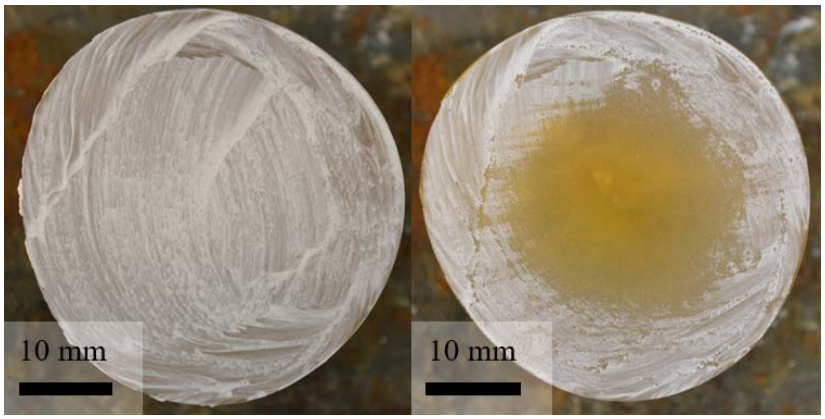

Figure 5.6 Images of the aluminium oxide powder covered resin before and after exposure to cavitation bubbles. The cavitation bubbles were generated by a PLE oscillating at approximately 23 kHz in a basin of purified water (see Table 2.1 for further details of purification process). The PLE tip was positioned at a *z* separation of 7.5 mm.

The diminishing effectiveness of the cavitation bubbles to clean the surface can be attributed to two factors. First, the cavitation bubbles were generated at the PLE tip rather than on the resin surface. Therefore by increasing the distance between the place where the

bubbles were generated and surface to be cleaned fewer of the bubbles reached the surface. Second, the bubbles that reached the resin surface were now further from the driving force of the PLE. The increase in distance from the driving force resulted in a decrease in bubble oscillations, the kinetic motion of which helped to clean the surface. The nature of these bubble oscillations will be explored further in Chapter 5.2. The decrease in surface activity with increasing z separation was observed in Chapter 4.3, where the 'bubble activity' observed at the electrode surface decreased with increasing distance between the PLE tip and the electrode (Ag disc, ϕ = 500 µm).

5.2 Mechanistic details of bubble motion from a PLE source

High-speed images of the electrode surface have revealed that some of the cavitation bubbles generated at the PLE leave the cluster below the PLE tip and move across the polished resin surface of the electrode. This 'bubble activity' has also been detected by changes in resistance at the working electrode (Ag disc, ϕ = 500 µm) recorded as a function of time (see Chapter 4.3 for initial discussion). The magnitude of such resistance changes is dependent on two qualities of the bubble, the separation between bubble and electrode surface and the relative size of the electrode and bubble.

The dependence of the resistance change on the distance between the bubble and the working electrode is true for any insulator interacting with a working electrode surface (see approach curves and scanning experiments in Chapter 4.5.3). The physical distance between bubble and electrode surface is difficult to measure in situ owing to the fast motion of the bubbles and their small size which limits the quality of images which can be taken of the cell during experiments. The changes in resistance due to changing bubble size is easier to observe. In the previous section (5.1) it was stated that the cavitation bubbles oscillated in resonance with the frequency of the PLE. If this is the case, then increases in recorded resistance should be observed as the bubbles move closer to the working electrode. Such resistance increases should not however be one peak as the bubble moves across the electrode but the resistance should oscillate with the size of the bubble as the bubble walls expand and contract. Figure 5.7 shows the motion exhibited by the bubble as it moves across the working electrode. As well as moving laterally across the surface of the electrode, the walls of the bubble expand and contract (indicated by the blue arrows). This oscillation is driven by the frequency of the PLE (*f*). The bubble walls may also exhibit

'rippling' known as Faraday waves[2,43]. These waves oscillate at the first subharmonic of the driving frequency ($f/2$)[96].

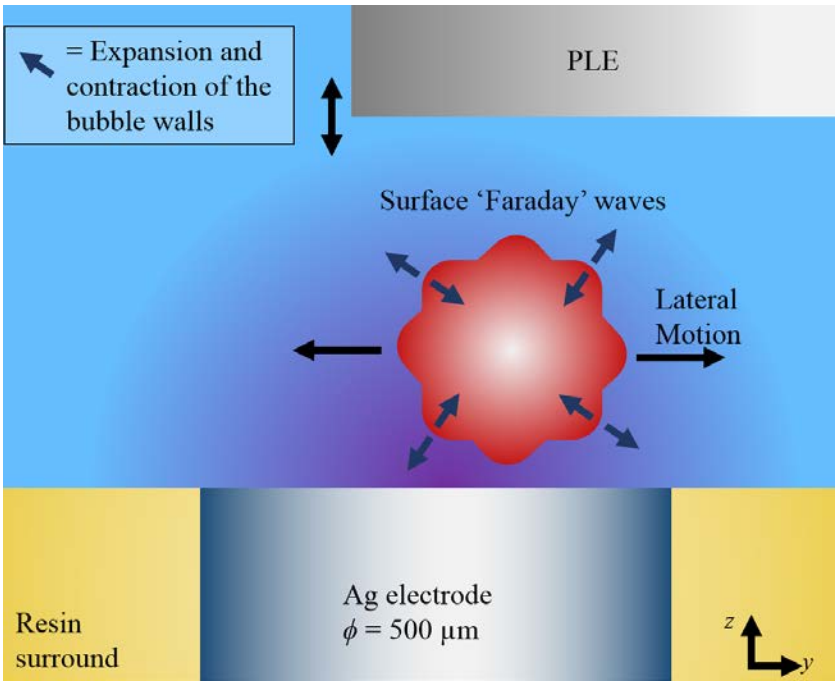

Figure 5.7 A schematic showing the different types of motion exhibited by the cavitation bubble as it travels across the electrode surface.

Using the high-speed AC impedance technique (see Chapter 2.3 for details of technique), a plot of uncompensated resistance as a function of time was recorded. The 500 µm diameter electrode was chosen such that the changes in uncompensated resistance were approximately equal to impedance changes and the capacitances changes could not be determined. Further discussion of the choice of electrode size using this technique can be found in Chapter 4.1. The uncompensated resistance vs time plot of the data showed that as the bubbles moved over the working electrode spikes in resistance were observed. In this setup multiple spikes are seen clustered together, referred to as 'event clusters'. The spacing of these spikes in resistance forms a regular pattern as shown in Figure 5.8.

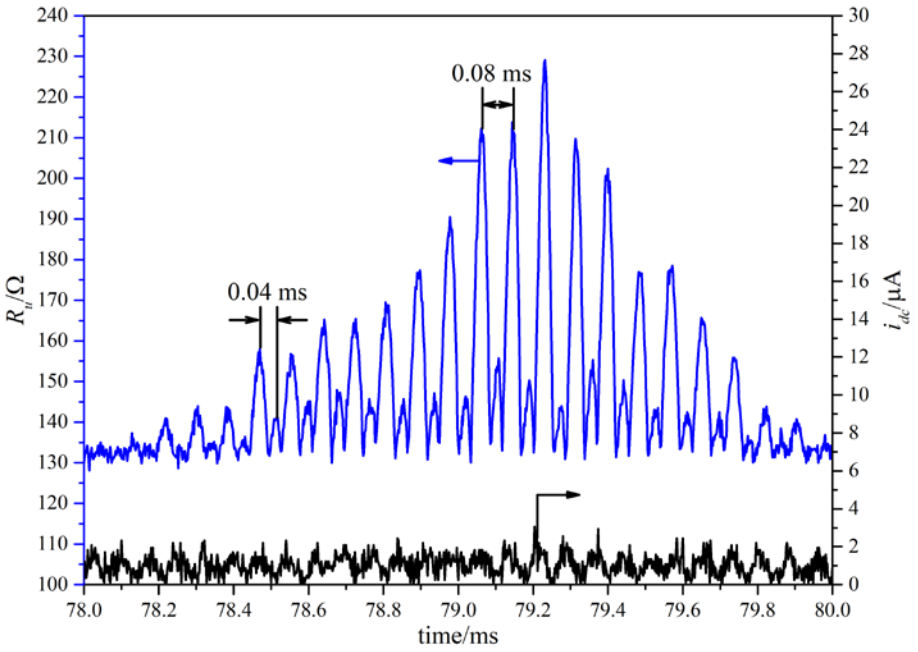

Figure 5.8 Plot showing the resistance, R_u, (—) and Faradaic current, i_{dc}, (—) as a function of time for a 500 μm diameter Ag disc within a resin support and a stainless steel rod acting as a reference counter electrode. The solution in the resonant chamber was 1 M NaCl. The frequency applied to the ultrasonic horn was 23.65 kHz. The *z* separation was 2.5 mm and the *y* separation was - 1.9 mm. The solution temperature was 23.5 °C and the experiment was performed in aerobic conditions. Data acquired with a 500 kHz sample rate.

A regular alternating pattern of larger and smaller spikes in resistance can be clearly seen in the data presented Figure 5.8. The time interval between each resistance spike was measured. The average time interval between the larger spikes was found to be 0.08 ms and the average time difference between the large and small spikes was 0.04 ms. These time intervals correspond to frequencies of 11.81 kHz and 25.00 kHz respectively. These frequencies are close to the fundamental frequency of the applied ultrasound (f = 23.65 kHz) and the first subharmonic of the applied ultrasound frequency ($f/2$ = 11.83 kHz). This indicates that the peaks observed are descriptive of the motion of the bubble walls as the frequencies of oscillation are the same as those expected for the typical modes of bubble oscillation described in Figure 5.7. No such change is observed in the Faradaic current is observed, which provides further evidence that the bubbles observed here are stable rather than transient cavitation bubbles. In the case of transient cavitation, the energy released in the bubble collapse would be expected to erode the electrode surface resulting is a change in Faradaic current at the electrode surface as the surface chemistry is altered.

This same oscillatory bubble motion was also observed in an experiment in which a gas bubble was injected onto the surface of a Pt disc (ϕ = 100 μm) electrode and forced to

resonate by positioning the PLE at a *z* separation of 3 mm from the electrode surface. The bubble remained stationary on the surface of the electrode and oscillated in resonance with the applied ultrasound frequency of the PLE. Images of this bubble from the high-speed camera reveal two types of bubble wall motion, both the 'breathing' mode of expansion and contraction of the bubble and surface waves on the bubble (Faraday waves).

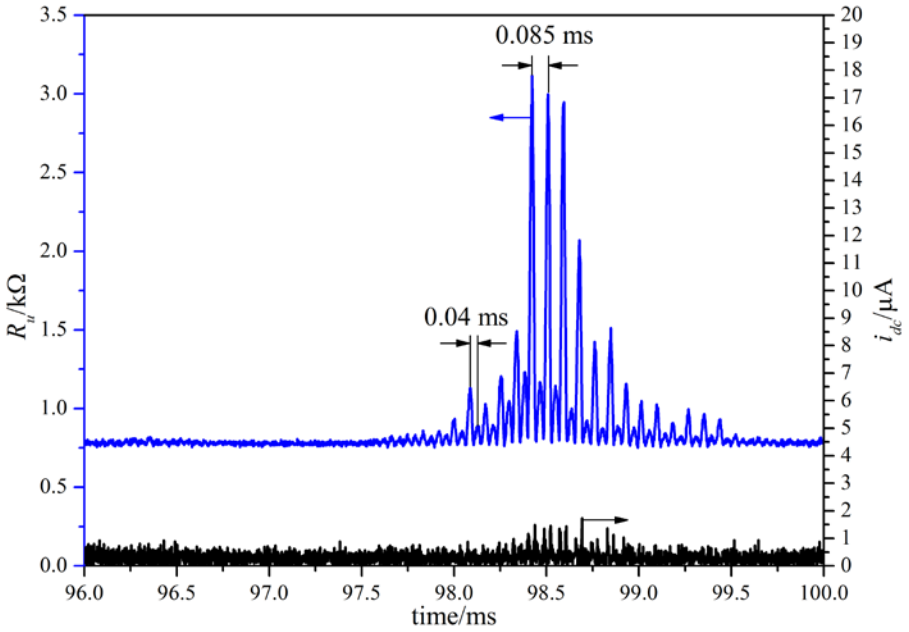

Figure 5.9 Plot showing the resistance, R_u, (—) and Faradaic current, i_{dc}, (—) as a function of time for a 100 μm diameter Pt disc within a resin support and a stainless steel rod acting as a reference counter electrode. The solution in the chamber was 0.5 M Na_2SO_4. The frequency applied to the ultrasonic horn was 23.697 kHz. The *z* separation was 3 mm. The solution temperature was 25.7 °C and the experiment was performed in aerobic conditions. Data acquired with a 500 kHz sample rate.

Figure 5.9 shows the uncompensated resistance as a function of time as well as the Faradaic current at the working electrode over the same time period. Transient resistance peaks were observed as the size of the bubble over the working electrode surface increased and decreased in volume. The regular pattern of the peaks indicates that this motion is driven by the regular oscillation of the PLE. The pattern observed is the same as observed in Figure 5.8 with alternating large and small resistance peaks. The average separation between large peaks was 0.085 ms (11.8 kHz = *f*/2) and between large and small peaks was 0.04 ms (23.7 kHz = *f*). This is a further indication that the bubble oscillations are a combination of two different frequencies. The inclusion of the Faradaic current in this plot shows that no significant change in current passed at the electrode is observed when the bubble oscillates over the electrode surface. This indicates that no erosion of the electrode surface is occurring as was observed in the presence of transient cavitation bubbles (for example of transient cavitation see Figure 3.11). Some very small changes in current are

observed, likely due to oxygen reduction as the experiment was performed in aerobic conditions. A series of frames from a high-speed video of a bubble exhibiting these bubble wall oscillations is shown in Figure 5.10.

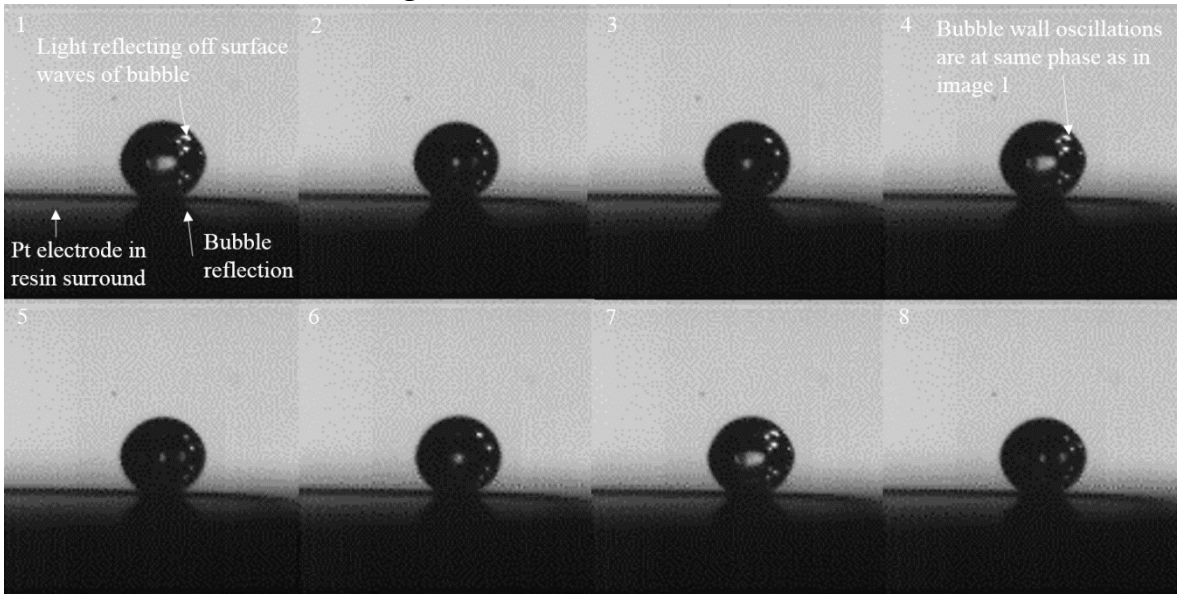

Figure 5.10 Still images from a high-speed video recording showing a bubble oscillating in sympathy with an external ultrasonic source (PLE). The time between each frame is 0.43 ms. No scale is shown on these images as no reference point could be used to scale the images. Each image is shown with the same magnification. The bubble is estimated to be ~500 µm in diameter. The video footage accompanying this figure can be found at: https://doi.org/10.5258/SOTON/D0674.

The eight frames shown in Figure 5.10 show two complete cycles of surface oscillations of the bubble walls. This bubble oscillation is driven by the PLE (positioned 3.0 mm above the surface of the electrode). The spots of light reflected off the bubble wall indicate that the bubble walls are oscillation. This oscillation has a frequency of half the driving ultrasound frequency. Every four images in the sequence shown the light reflects off the same positions of the bubble. This indicates that the surface wave is at the same point in the wave cycle. This is indicated in images 1 and 4 of Figure 5.10. The ‘breathing’ mode of oscillation can also be observed in these images where the bubble walls expand and contract in sympathy with the changes in pressure caused by the acoustic field. The frequency of these oscillations is the same as the driving ultrasound frequency.

5.3 Data Signal Post-Processing of Resistance time plots

It was suggested in Chapter 5.2 that the peaks observed in the uncompensated resistance time plots were a combination of two modes of bubble wall oscillation over the surface of the working electrode. To illustrate this more clearly a post-processing technique was applied to the uncompensated resistance *vs.* time data to produce an intensity plot with frequency as a function of time. The process applied to this data employed a fast Fourier

transform (FFT) technique is a similar manner to which the technique was applied to elucidate the uncompensated resistance as a function of time.

In this technique, an AC potential perturbation (V_{app}) and the AC current response ($V_{out} = i_{out}$ x 10^4 V A^{-1} gain) were recorded as a function of time at a sample rate of 10 MHz. An FFT algorithm was applied to the data recorded on a data window of 20 data points of both V_{app} and V_{out}. By moving the data window through the resistance *vs.* time data was elucidated. This process was then repeated with the uncompensated resistance *vs.* time data (effective sample frequency 500 kHz). The FFT algorithm was applied to the data in sections of 1000 data points to elucidate the magnitude of resistance as a function of frequency. This FFT window was then moved through the data in steps of 10 data points. The results of multiple FFT iterations were plotted as an intensity graph where the frequency components of the resistance oscillations were plotted as function of time with the uncompensated resistance providing the intensity scale. The intensity scale in this plot is the uncompensated resistance. The 1000 point data window was chosen for this post-processing to increase the resolution of frequency components elucidated. The smaller step (10 points) between each data window was required to increase the time resolution. If, as in the initial data processing, the data window was moved on by the length of the window each time then the intensity plot generated would have an effective sample frequency of 500 Hz (one data point only every 2 ms). By overlapping the windows, stepping by 10 points each time, the plot generated had an effective sample frequency of 50 kHz (one data point every 20 μs). Figure 5.11 shows a schematic detailing the AC impedance technique and post processing applied to the uncompensated resistance data to produce the intensity plot.

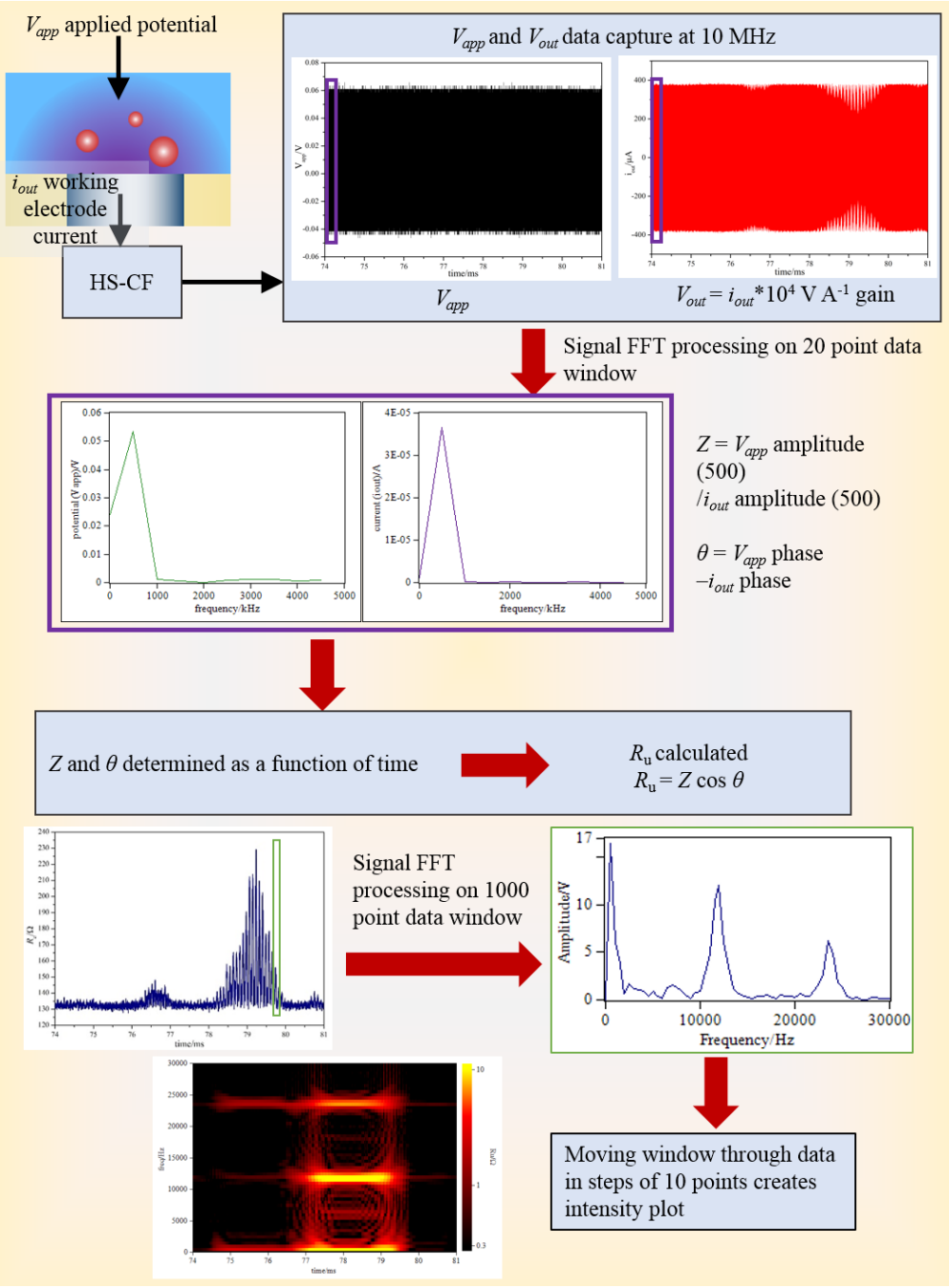

Figure 5.11 A schematic of the data processing routine in the AC impedance technique developed. The two signals captured (applied potential, $V_{app,}$ and current response, $V_{out} = i_{out}$*10^4 V A^{-1} gain) and data processing (FFT) applied to elucidate the amplitude of these two signals as a function of frequency. The impedance, Z, was calculated from ratio of potential and current amplitude at 500 kHz and the phase angle, θ, was calculated from the change in phase between V_{app} and i_{out}. The uncompensated resistance ($R_u = Z \cos \theta$) plot was then post processed to produce an intensity plot of frequency components of resistance as a function of time.

The intensity plots produced are shown in Figures 5.12 and 5.13. In Figure 5.12 the resistance vs time plot of the Ag disc electrode (Figure 5.8) and associated intensity plot are displayed side by side. The intensity peaks the post-processed data (Figure 5.12 b))

correspond in time to when series of resistance peaks are observed are observed in the AC impedance data.

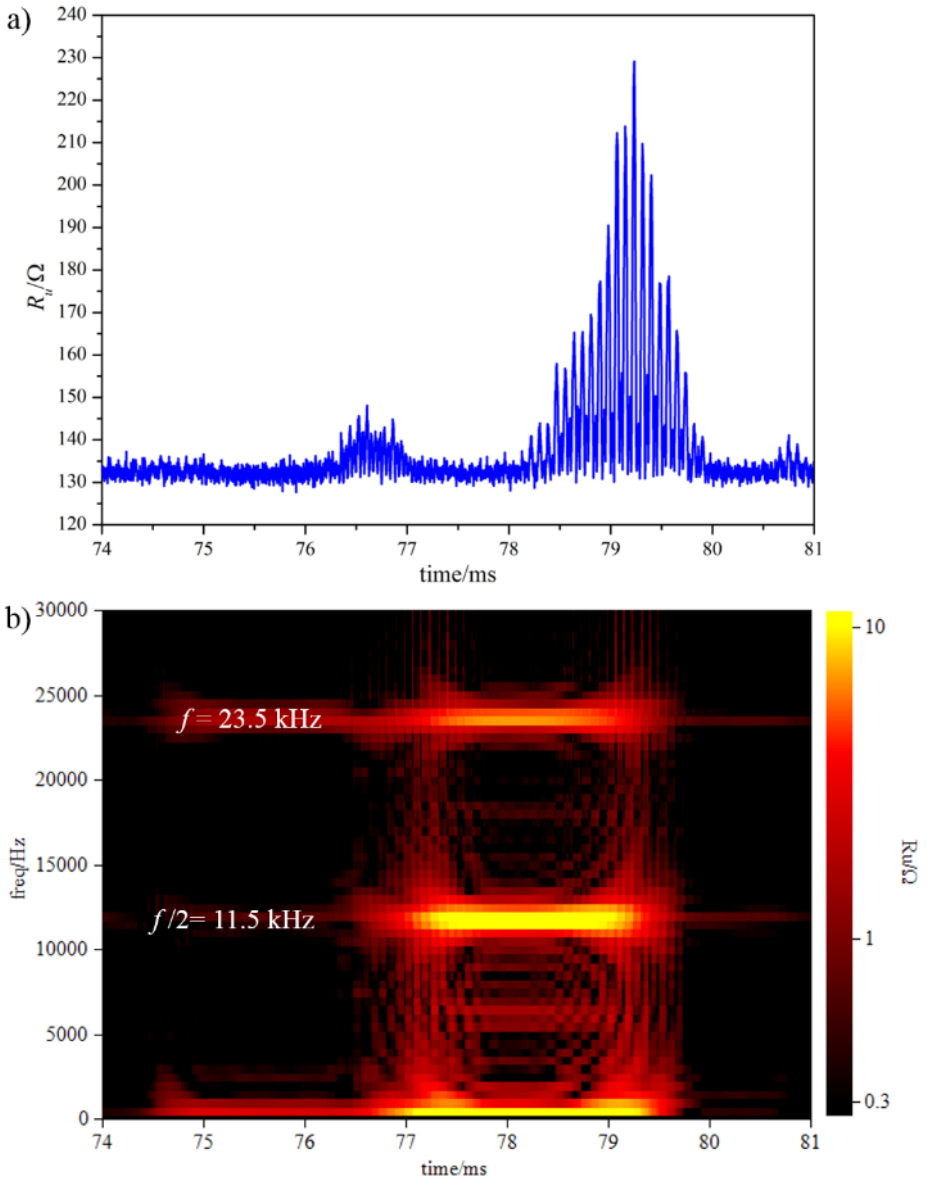

Figure 5.12 (a) A plot of resistance, R_u, (—) as a function of time for a 500 µm diameter Ag disc within a resin support and a stainless steel rod acting as a reference counter electrode. **(b)** FFT processed intensity plot for the same data set. The solution in the resonant chamber was 1 M NaCl. The frequency applied to the ultrasonic horn was 23.65 kHz. The *z* separation was 2.5 mm and *y* separation was 1.9 mm. The solution temperature was 23.5 °C and the experiment was performed in aerobic conditions. The resistance time data was acquired at a sample rate of 500 kHz.

The highest intensity regions are seen at 23.5 kHz (*f*) and 11.5 kHz (*f*/2). This indicates the frequency of the oscillations in resistance at these points. These frequencies correspond to the fundamental frequency and first sub-harmonic of the applied ultrasound frequency. As the changes in resistance indicate the movement of a bubble over the electrode the frequency of the resistance oscillations therefore indicates the frequency of the bubble

oscillations. This shows that the bubble movement depends upon the frequency of the applied ultrasound.

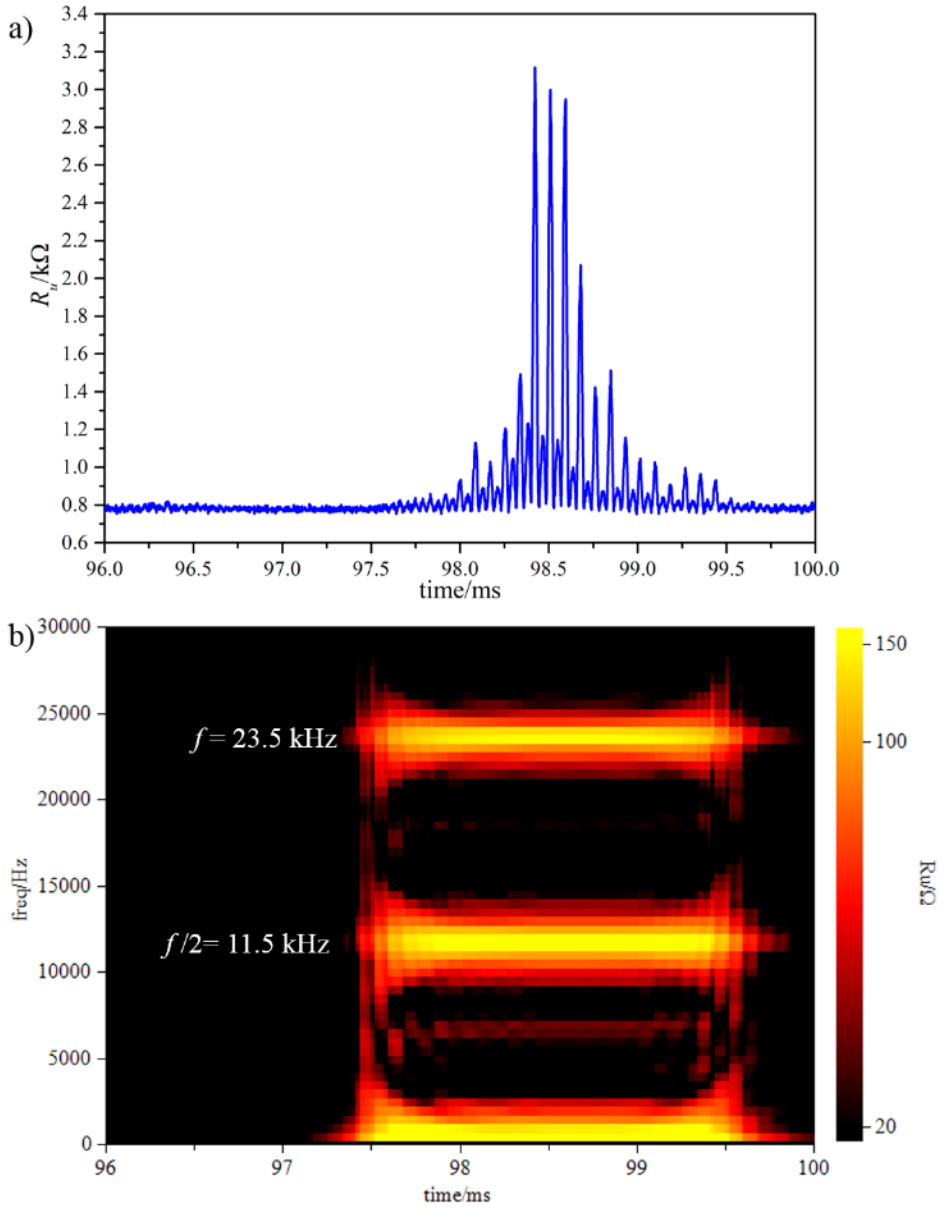

Figure 5.13 (a) A plot of resistance, R_u, (—) as a function of time for a 100 µm diameter Pt disc within a resin support and a stainless steel rod acting as a reference counter electrode **(b)** FFT processed intensity plot for the same data set. The solution in the resonant chamber was 0.5 M Na_2SO_4. The frequency applied to the ultrasonic horn was 23.697 kHz. The *z* separation between PLE tip and electrode surface was 3 mm. The solution temperature was 25.7 °C and the experiment was performed in aerobic conditions. The resistance time data was acquired at a sample rate of 500 kHz.

This same trend is observed in the intensity plot of the resistance vs. time plot of the fixed position bubble over a Pt disc electrode (Figure 5.9). Figure 5.13 shows the resistance *vs.* time data and associated intensity plot for the data present in Figure 5.9.

5.4 Bubble activity from a PLE source inside a pore

An extremely large threshold energy is required to generate cavitation bubbles inside a pure liquid (such as pure water). For this reason the generation of cavitation bubbles is generally assisted by impurities present in the liquid or vessel, for example surface defects in the liquid vessel or small particulates in solution such as salt ions. In the interest of generating cavitation bubbles to assist the cleaning of a surface it is therefore beneficial for the surface in question to be roughened in some way to assist the generation of bubbles by the input energy source. To investigate the motion of the bubbles generated inside crevices an electrode (Ag disc, ϕ = 500 µm) was etched in nitric acid to form a recessed electrode (see Chapter 2.5.3 for further information on electrode fabrication). Using the PLE as an ultrasonic sound source, cavitation bubbles were generated in a cluster below the PLE tip and inside the recess formed in the resin support of the Ag electrode. Figure 5.14 shows a picture of the set up used and the scale used indicates how the relative positions of the PLE tip and pore were recorded.

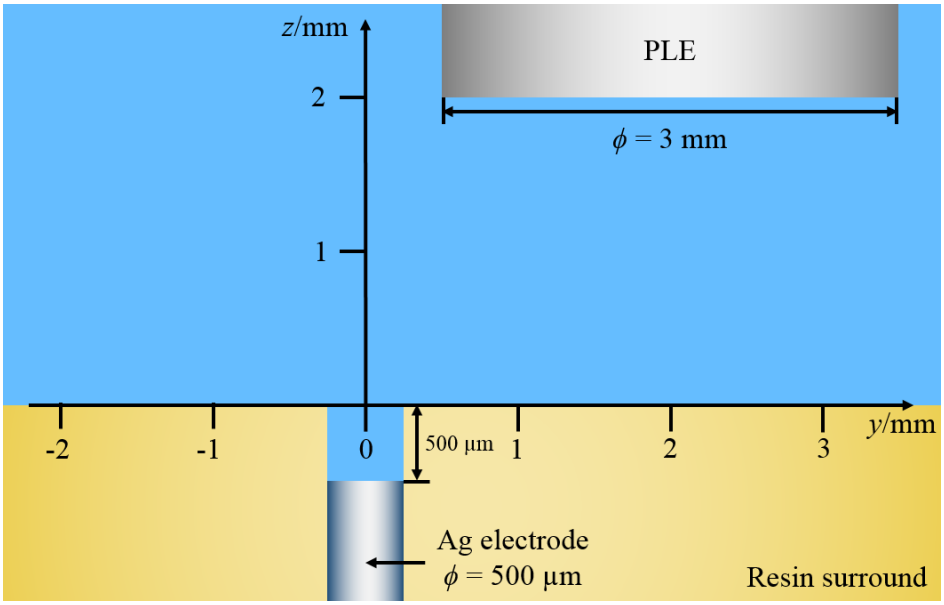

Figure 5.14 A cartoon illustration of the *y* and *z* axes used to record the position of the PLE tip (ϕ = 3mm) relative to the recessed Ag disc electrode (ϕ = 500 µm). The origin of these axes was chosen as the centre of the Ag electrode and the surface of the resin surround.

The bubble motion inside the pore was monitored electrochemically using the recessed Ag disc electrode as a working electrode. The high-speed AC impedance technique (described in Chapter 2.3) was employed to measure the change in resistance as a function of time. Figure 5.15 shows a short section of a resistance time transient for the bubbles generated inside this pore. The bubbles exhibit growth and collapse (as observed in the cylindrical

chamber experiments in Chapter 3, see Figure 3.11). Following the large growth and collapse resistance peaks a series of smaller rebound peaks were observed. Accompanying high-speed video footage simultaneously with the resistance time data. A series of images from this footage is shown along with the resistance time data in Figure 5.15. The amount of gas observed inside the pore correlates with the changes in resistance observed.

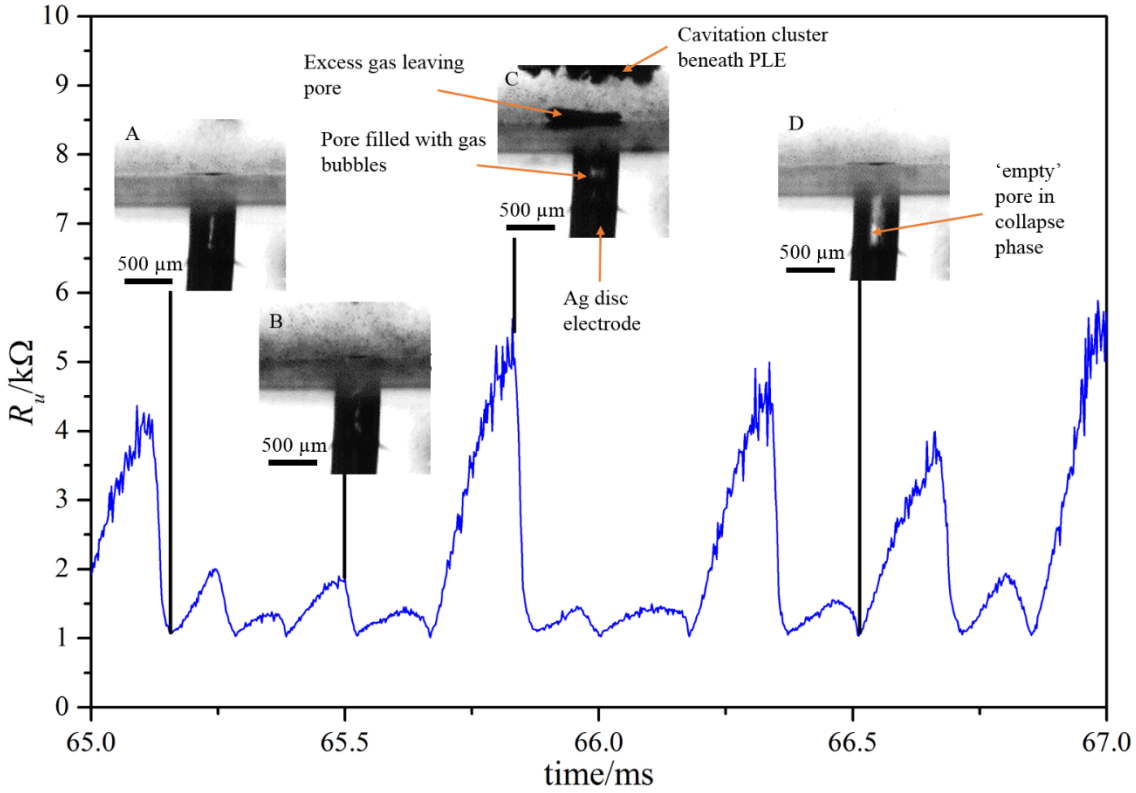

Figure 5.15 A plot of uncompensated resistance, R_u, (—) as a function of time with accompanying images taken from a high-speed camera video. The working electrode in this experiment was an Ag disc electrode (ϕ = 500 µm) inside a recess of depth 500 µm. The reference counter electrode in this experiment was a stainless steel rod and the electrolyte employed was aqueous 0.5 M Na_2SO_4 at room temperature and atmospheric pressure. The ultrasonic horn tip was positioned at a *y* separation of 0 mm and *z* separation of 1.46 mm. Resistance time data was recorded at a sample rate of 500 kHz. The high speed camera was recorded at 70 000 frames per second. The video footage accompanying this figure can be found at: https://doi.org/10.5258/SOTON/D0674.

The bubbles within the etched recess (pore) exhibit the same growth and collapse as observed in the cylindrical chamber experiments in Chapter 3 (see Figure 3.11) that of transient cavitation bubbles. The shape of the resistance transients revealed this bubble collapse process occurs in two stages. In the first stage, the bubble/bubbles grow to a maximum size, filling the pore with gas, as seen in the image labelled 'C' in Figure 5.15. At this position the uncompensated resistance measured is at a maximum. In the annotated image of the pore (labelled 'C') additional bubbles can be seen above the mouth of the recess as the bubbles have expanded and escaped the pore where they were generated from. The size of the bubble cluster below the PLE is also at a maximum size at this point

and the edge of this cluster is observed at the top edge of the image. The bubbles then collapsed rapidly, and the pore was left virtually free from gas and a rapid decrease in the uncompensated resistance was recorded. An example of the pore immediately after the bubble collapse can be observed at the image labelled 'A'. Following the large growth and bubble collapse a series of smaller uncompensated resistance peaks were observed. These peaks were termed 'rebound events'. Image 'B' shows how the recess refills with gas at the peak of one such rebound event before collapsing again leaving the recess virtually bubble free (image 'D').

At the positions at which the bubble appears free from bubbles, the uncompensated resistance recorded decreased to a 'background' resistance level. This 'background' level is the uncompensated resistance of the electrode without the interaction of additional insulators (e.g. bubbles). It should be noted that the uncompensated resistance in the data presented in Figure 5.15 was higher than that recorded for the flat disc electrode of the same diameter in the same electrolyte (Figure 5.8). This was due to the additional resistance cause by the diffusion of the electrolyte in and out of the recess. The uncompensated resistance term, $R_{ch,}$ added by the recess is proportional to the length of the recess, l, and inversely proportional to the end area of the channel, A, and electrolyte conductivity, κ, according to the equation $R_{ch} = l/ \kappa A$.

5.5 Surface Scanning experiment with Silver electrode inside a pore

In the surface scanning experiments reported in Chapter 4, the uncompensated resistance and double layer capacitance of a 250 µm diameter aluminium electrode was recorded as an insulating glass rod was moved across the electrode surface. This was repeated for the insulator at different heights above the electrode surface. This showed that the uncompensated resistance and capacitance recorded at the working electrode varied according to the position of the insulator relative to the working electrode. This result imitated the results observed as a cavitation bubble moved across the electrode surface, that as the bubble approached the working electrode, the measured uncompensated resistance was increased by the presence of an insulator and the capacitance decreased because of a decreased effective surface area (such as Figure 3.11 in Chapter 3). The results presented in Chapter 5.4 focussed on the resistance changes seen by bubble activity directly inside the pore, however as the uncompensated resistance measured between the working and reference/counter electrode is also influenced by insulating particles over the

mouth of the recess. This change in resistance due to bubbles/particles above the pore mouth is due to the local electrochemical environment around the pore mouth. The total uncompensated resistance measured is a linear combination of this hemispherical contribution and pore resistance as can be seen in Figure 5.16.

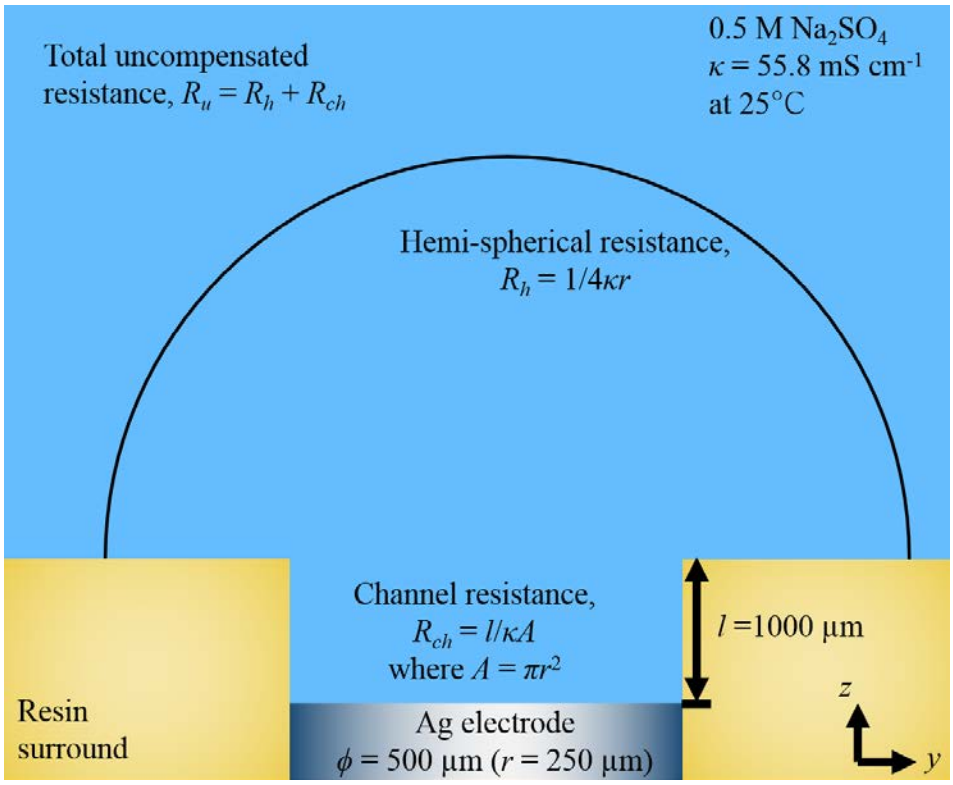

Figure 5.16 A picture showing the two separate resistance contributions to the overall uncompensated resistance. These comprise of the channel resistance, R_{ch} and hemi-spherical resistance, R_h, due to the electrochemical environment around the mouth of the channel.

To show how the interaction of an insulator (bubble or particle) over the mouth of the effects resistance and capacitance measured surface scanning experiments. This set of experiments was performed for a 500 µm diameter Ag disc electrode recessed inside a 1000 µm long pore. A sealed glass pipette (ϕ ~ 1500 µm) was used as an insulator for these experiments. The position of this pipette was controlled by a micro positioning system which was able to control the position of the pipette in *x*, *y* and *z* directions. At each pipette position the high-speed AC impedance technique (as described in Chapter 2.3) was employed with a 50 mV zero-to-peak perturbation at 500 kHz. From these R_u and C values 2-D surface maps were generated of the electrode surface. Figure 5.17 is a schematic showing the axes employed in these scanning experiments for reference purposes. The image is not drawn to scale.

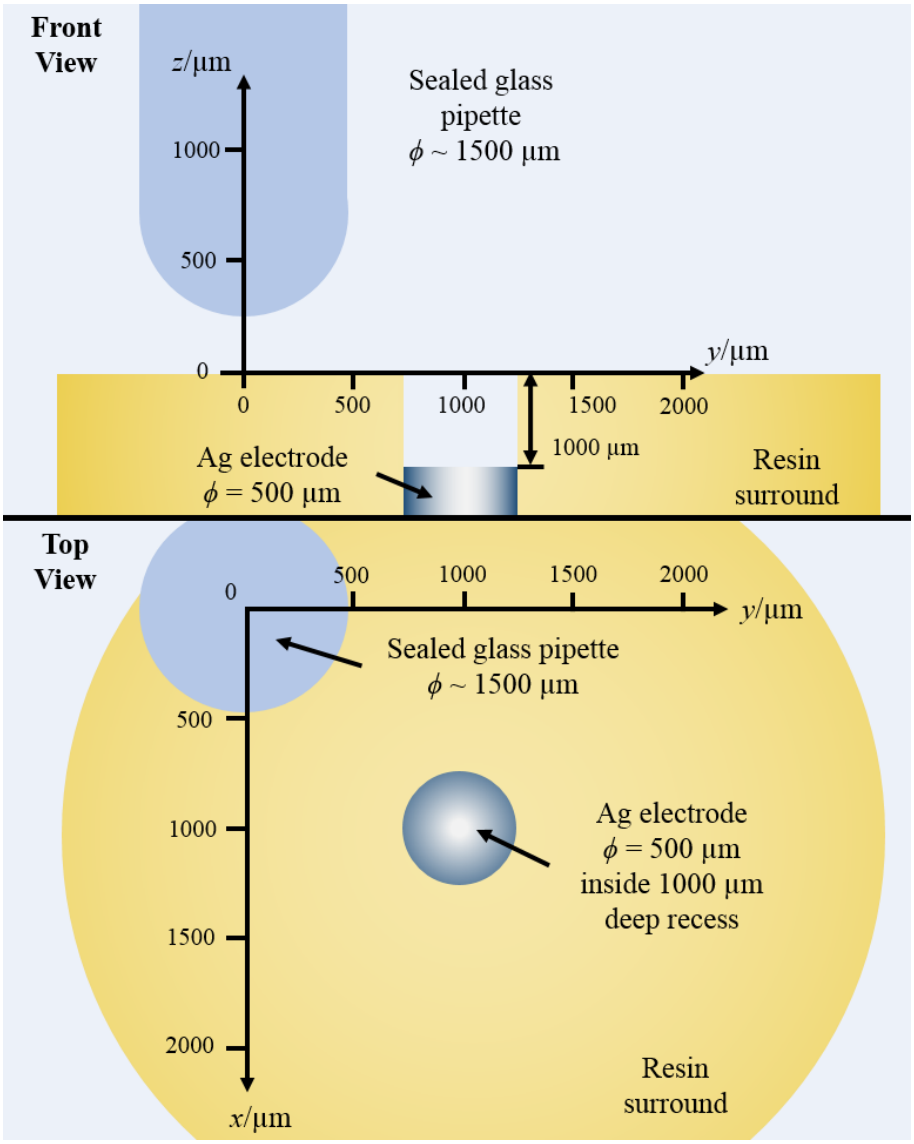

Figure 5.17 A schematic of the experimental setup used in the surface scanning experiments as viewed from the front and top. The centre of the working electrode, Ag ϕ = 500 µm inside a recess of depth 1000 µm, was approximately in the centre of the 2000 µm x 2000 µm *x*/*y* scanned region, and the origin of the *z* axis was chosen as the mouth of the recess. A stainless steel rod (ϕ = 6 mm) was used as a counter reference electrode. The experiments were performed in an electrolyte of 0.5 M Na_2SO_4 at atmospheric temperature and pressure and under aerobic conditions. This image is an illustration only and is not drawn to scale.

Figures 5.18 and 5.19 show the changing resistance plots as a function of *x*, *y* and *z* separation. The diameter of the glass rod used was larger than the diameter of the channel and hence measurements could not be made measuring the effect of an insulator inside the pore. The *z* separation recorded was therefore the distance between the end of the glass rod and the surface of the resin surround (as used in the axes in Figure 5.17).

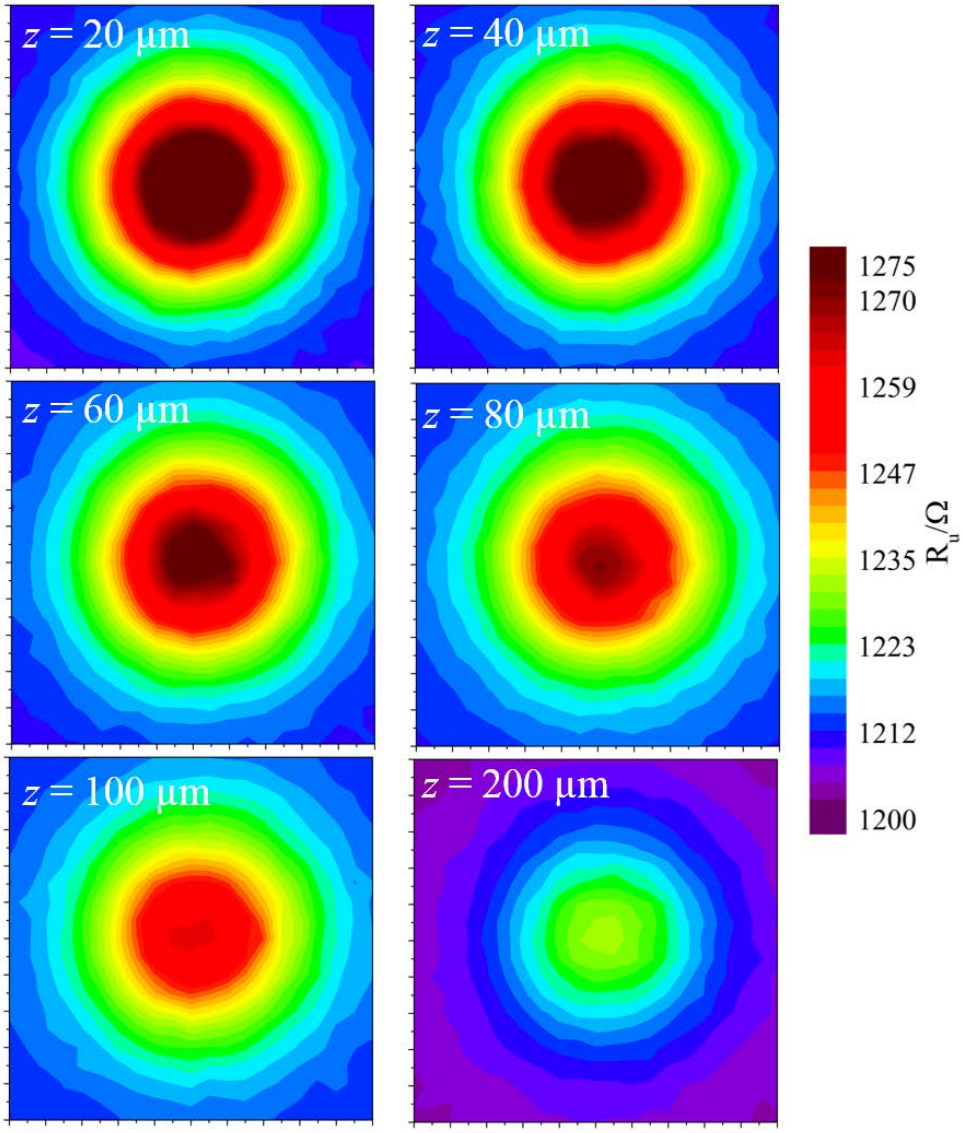

Figure 5.18 2-D plots of resistance from the scanning experiments. The working electrode was a 500 µm diameter silver electrode inside a 1000 µm deep pore. A stainless steel rod was used as a pseudo reference counter electrode and the experiments were performed in 0.5 M Na_2SO_4. The applied AC perturbation applied across the electrodes was 50 mV zero-to-peak at 500 kHz. The same key was used for each plot. The image resolution was 100 µm created by moving the glass pipette in this increment in both *x* and *y* dimensions to form a 20 by 20 point grid. The *x* and *y* scales on each plot range from 0 to 2000 µm with major divisions of 200 µm. The experiments were carried out between 24.4 °C and 26.3 °C at atmospheric pressure and in aerobic conditions.

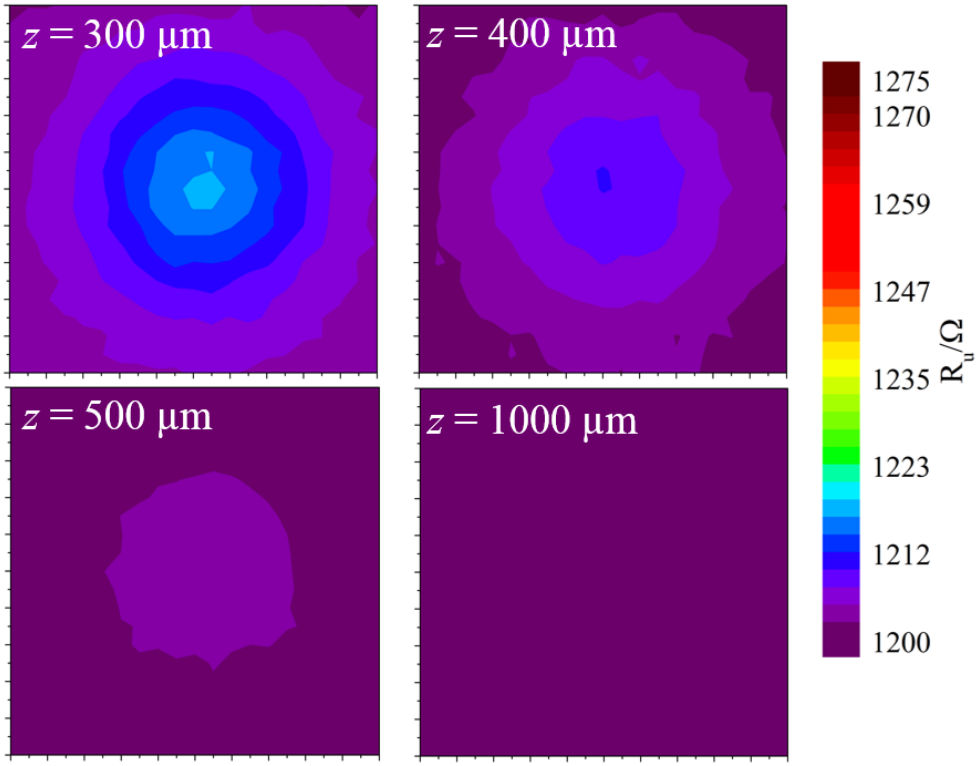

Figure 5.19 2-D plots of resistance from the scanning experiments. The working electrode was a 500 µm diameter silver electrode recessed by 1000 µm. A stainless steel rod was used as a pseudo reference counter electrode and the experiments were performed in 0.5 M Na_2SO_4. The applied AC perturbation applied across the electrodes was 50 mV zero-to-peak at 500 kHz. The same key was used for each plot. The image resolution was 100 µm created by moving the glass pipette in this increment in both *x* and *y* dimensions to form a 20 by 20 point grid. The *x* and *y* scales on each plot range from 0 to 2000 µm with major divisions of 200 µm. The experiments were carried out between 24.4 °C and 26.3 °C at atmospheric pressure and in aerobic conditions.

Despite the glass pipette not being as close to the surface of the electrode as for the aluminium disc scans, the proximity of the insulator to the pore mouth was still enough to cause changes in resistance. This was because the electrochemical environment at the pore mouth still forms a significant part of the resistance contribution for the working electrode in the electrochemical cell. This is further confirmation of the result observed in the line scan in Chapter 4.5.2 (Figure 4.22). Thus, when examining the resistance transients observed in experiments involving cavitation bubbles generated using a PLE it is important to note that changes in the recorded uncompensated resistance are not necessarily caused by bubble activity inside the recess, but the resistance recorded will also be changed by bubbles moving on the resin surface close to the mouth of the recess. Without additional measurements, such as the images of the electrode recorded, it is not always possible to attribute the changes in uncompensated resistance to bubble activity inside or outside of this recess.

The ‘bubble events’ inside and outside the recess could potentially be distinguished by examining the changes in apparent capacitance of the electrode. As the capacitance is proportional to the surface area of the electrode, changes to the capacitance for the recessed electrode would only be expected for insulating particles (or bubbles) inside the recess, as insulators above the mouth of the recess would be too far away from the electrode surface to affect the capacitance recorded (in Figure 4.26 capacitance changes were only observed up to a distance of 100 µm from the surface of the electrode). This was tested by examining the elucidated capacitance from the scanning experiments performed with the glass insulating rod above the recessed Ag electrode. The result of one such scanning experiment can be seen in Figure 5.20.

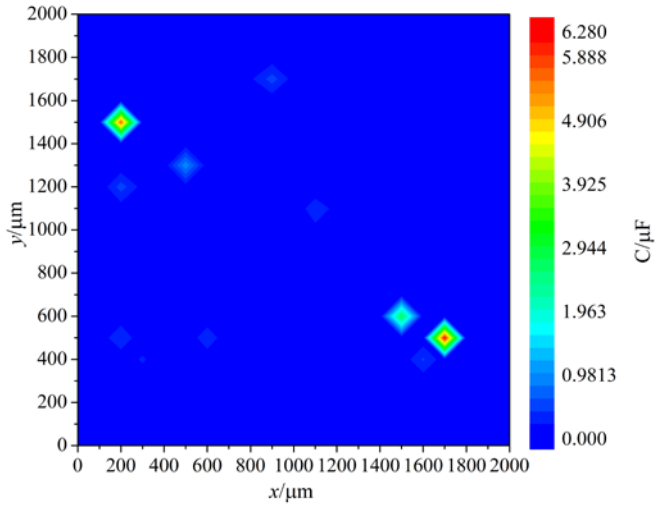

Figure 5.20 A 2-D plot of capacitance as a function of *x*/*y* position of a glass rod insulator (ϕ ~ 1500 µm) at a *z* separation of 20 µm above a 500 µm silver disc working electrode recessed by 1000 µm. A stainless steel rod was used as a pseudo reference counter electrode and the experiments were performed in 0.5 M Na_2SO_4. The applied AC perturbation applied across the electrodes was 50 mV zero-to-peak at 500 kHz. The image resolution was 100 µm created by moving the glass pipette in this increment in both *x* and *y* dimensions to form a 20 by 20 point grid. The experiment was carried out at 24.4 °C at atmospheric pressure and in aerobic conditions.

The capacitance plot shown in Figure 5.20 displays the capacitance measured as the *x* and *y* position of the glass rod is moved across the resin surface at a *z* separation of 20 µm from the resin surface. The size of the values recorded seem improbable by comparison. This is due to the frequency of the applied potential perturbation applied to this ϕ = 500 µm Ag electrode. By using a perturbation with a frequency of 500 kHz the measured phase angle, θ, between V_{app} and i_{out} is small leading to inaccurate calculation of capacitance. Further discussion of this can be found in Chapter 4.1. Even in the case that the capacitance could be accurately calculated, no change in capacitance would be expected.

In this chapter we have seen how the novel AC impedance method developed can be used to elucidate mechanistic detail of the motion exhibited by an acoustically driven bubble. Specifically, it was shown that the oscillating bubbles exhibit both the ‘breathing’ mode of expansion and contraction of the bubble walls and surface ‘Faraday’ waves on the surface. High-speed video recordings provided visual conformation of the presence this bubble motion. While this work has demonstrated that the technique is powerful, some limitations should be noted. For example, the data capture rate and data size is limiting when extended time periods are required. In order to circumvent this restriction, a new method was developed which relied on hardware demodulation of the experimental data. The development and testing of this approach will be covered in the next chapter.

Chapter 6 Impedance measurements from a demodulated current signal

6.1 Demodulated current signal

In the impedance experiments performed thus far an FFT algorithm has been employed to elucidate the impedance information as a function of time from the initial AC current response recorded after the application of a suitable voltage perturbation. This method was able to successfully elucidate the uncompensated resistance, electrode capacitance and Faradaic resistance of an electrochemical cell at an effective sample frequency of 500 kHz (2 µs time resolution). There are, however, a few drawbacks to this system.

First, the technique relies upon a number of stages of data processing to calculate this impedance data. The process can therefore prove time consuming, depending on the computer processing speed available and the desired data length. Second, the initial current response and applied potential have to be recorded at a very high sample rate (here 10 MHz was typically used) which requires high-speed data acquisition software. The data recording is therefore limited by the length of time it takes to gather, process and store long time windows (e.g. seconds). This data needs to be post-processed in order to get the impedance information from the current signal. This processing is achieved by applying the FFT to small data window equal to the number of data points in one wave of the AC perturbation (e.g. for data recorded at 10 MHz and an AC perturbation of 500 kHz the data window size would be 20 points). This results in processed data with an effective sample rate equal to the frequency of the AC perturbation. Therefore by increasing the frequency of the AC perturbation, the size of this window is decreased and thus the effective sample rate of the processed data is increased. However, a high-speed operational amplifier is required to monitor the current for data acquisition. Thus the experiment is also limited by the performance of this operational amplifier as the performance of the amplifier decreases in quality as the frequency of the AC perturbation (and hence AC current response) increases. Finally, owing to the post-processing nature of this technique it is more difficult to use this technique to record information ‘on the fly’ at suitable sample rates.

A new method of high-speed AC impedance data recording was devised in an effort to eliminate some of the disadvantages of the FFT method. In this alternative method, a

demodulation circuit was employed to allow for the change in amplitude of the AC current response to be recorded with respect to time. By comparison of this pseudo DC current to the amplitude of the applied potential the impedance[‡] of the working electrode could be plotted with respect to time. An additional correction factor, calibrated using model circuits equivalent to the electrochemical cell, was required to improve the accuracy of the impedance recorded.

This new technique allows for greater flexibility in the sample rate at which the impedance data can be reported. By the use of circuit elements within the demodulation circuit, some of the post processing required for the other reported technique (such as the FFT) can be eliminated. There are a number of advantages to this experimental approach. First, this allows us to record data over longer time frames as only one data channel is recorded during experiments. Second, by eliminating the time taken to post-process the AC current response of the system the impedance data can be reported much faster. Third, the reported impedance is now independent of the frequency of the applied potential within certain constraints.

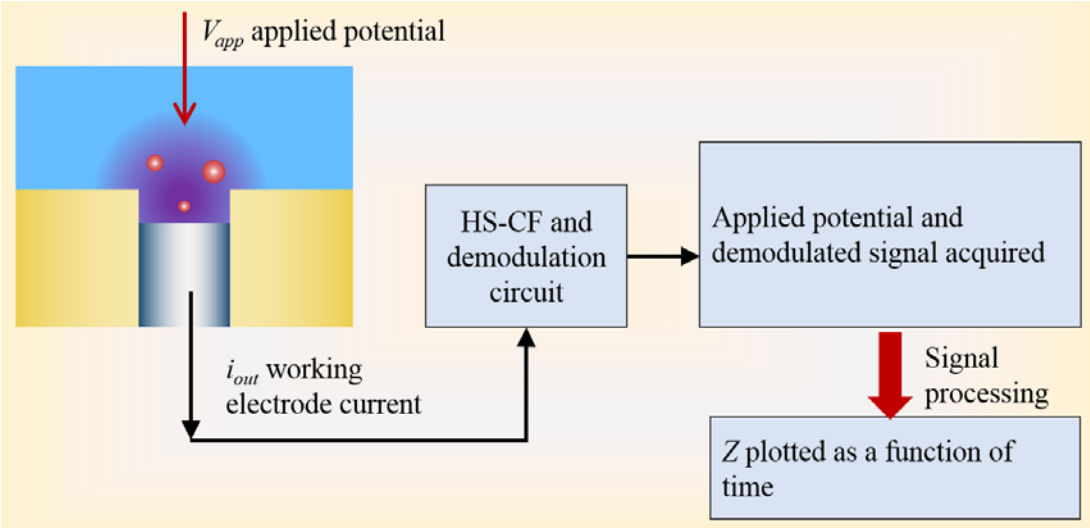

Figure 6.1 A Schematic of the data capture method and signal processing employed to record the impedance of the cell as a function of time with a sample frequency of 200 kHz (time resolution of 5 µs).

For the purpose of the experiments carried out and reported here, the excitation frequency and the size of the working electrode were chosen such that the reactive term (X_C) was small and therefore the phase angle, θ, between applied potential and current response was also small. This was chosen deliberately so that impedance changes in the cell could be

[‡] Note we are specifically measuring the impedance of the cell (and hence working electrode) in this case. This is a direct result of the approach adopted and the omission of phase data from the data acquisition process.

reported as changes in R_u. Figure 6.1 shows a schematic of how the signal was processed resulting in recording the impedance of the cell as a function of time. The results of studies using this approach are now presented.

6.2 Measuring Cavitation activity using Impedance from Demodulated signal

In Chapter 4, the number of uncompensated resistance transients in a 10 s time interval was used to quantify the level of bubble activity at the surface. As discussed in Chapter 6.1, the excitation frequency (1 MHz) and electrode size (ϕ 500 µm) were chosen so that the impedance was approximately equivalent to the uncompensated resistance. This system therefore was able to produce a repeat of the bubble activity experiments discussed in Chapter 4. In this set of experiments, a 500 µm Ag electrode set in a wide resin substrate (see Chapter 2 Figures 2.25 and 2.27 for the electrode and schematic of the experimental setup). The electrochemical system was exposed to ultrasonic activity from the PLE for 10 seconds at a time at a variety of chosen *z* and *y* separations (vertical distance from resin surface to PLE tip and horizontal distance between the centre of the PLE tip and centre of the Ag disc electrode respectively). The number of transient peaks in uncompensated impedance (effectively uncompensated resistance) in ten seconds were counted and plotted as a function of *y* separation and *z* separation.

Figure 6.2 shows the average number of events counted in ten seconds at a *z* separation of 2.5 mm, 5.0 mm and 7.5 mm plotted as a function of *y* separation (see Chapter 2, Figure 2.27 for schematic of experimental setup). The resulting plot shows the same trend as seen in Chapter 4 Figure 4.9 (where this system was investigated using the high-speed AC impedance technique described in Chapter 2.3). In the earlier case no peaks or 'bubble events' were observed at a *y* separation of zero and then the largest number of 'bubble events' was observed at small *y* separations and the events decreased in number as the magnitude of *y* separation increased.

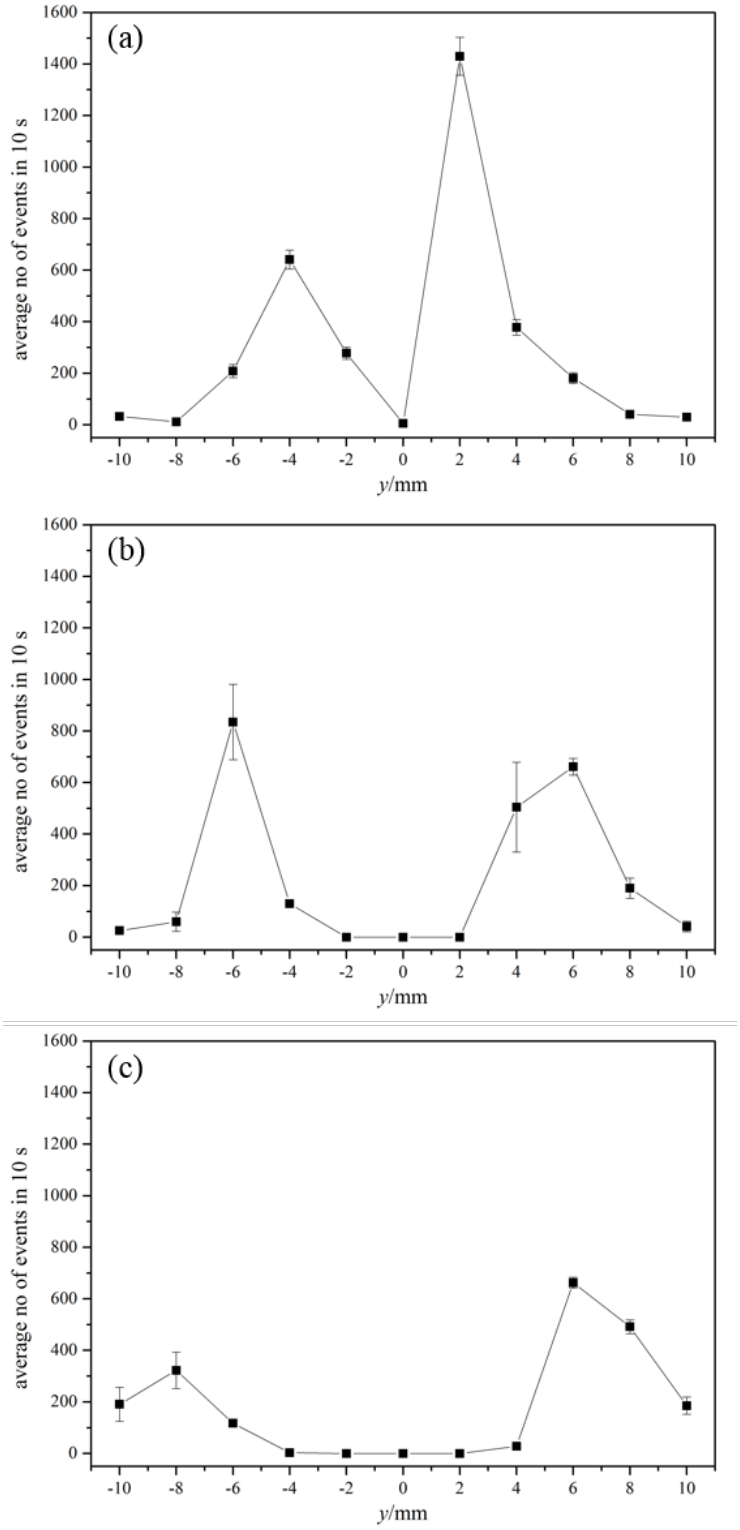

Figure 6.2 (a) A plot showing the average number of 'bubble events' (■) in 10 s as a function of distance from the silver disc (ϕ = 500 µm) at a *z* separation of 2.5 mm. **(b)** A plot showing the average number of 'bubble events' (■) in 10 s as a function of distance from the silver disc (ϕ = 500 µm) at a *z* separation of 5.0 mm. **(c)** A plot showing the average number of 'bubble events' (■) in 10 s as a function of distance from the silver disc (ϕ = 500 µm) at a *z* separation of 7.5 mm. Captures were made in 2 mm incremental distances from the electrode and the averages were made over 2 data captures at each distance. The error quoted in each case is the standard error for the two data captures. The working electrode was an Ag disc (ϕ = 500 µm) and the reference/counter was a stainless steel rod. The electrolyte used was 0.5 M Na_2SO_4 at room temperature (20.9°C) and pressure under aerobic conditions.

As the *z* separation was increased the same result as previously (see Chapter 4.3) was observed. With the increasing *z* separation, the central region in which no 'bubble events' were observed expanded. At a *z* separation of 5 mm (Figure 6.2 (b)), no events were observed between a *y* separation of ± 2 mm. At a *z* separation of 7.5 mm (Figure 6.2 (c)) this inactive region covered from a *y* separation between ± 4 mm. These results agree closely with the result using the FFT (DSP), detailed in Chapter 4.3, to calculate uncompensated resistance, thus proving the validity of the demodulated technique used here.

6.3 Using Demodulated data to dimension a channel

As well as using these impedance measurements to measure the change in impedance as a function of time, this system can be used as a measure of the uncompensated resistance of a variety of electrode geometries. The AC perturbation frequency (1 MHz) was chosen as at this frequency the reactive term was small (as discussed in Chapter 6.1). Thus the measured impedance can be approximated to the uncompensated resistance of the working electrode (here a 500 µm x 500 µm square) in Na_2SO_4 (0.5 M). Knowing the dimensions of the channels will be shown to be useful for calculating the volume of gas entering and leaving the pore during exposure to acoustic cavitation. This will be explored in Chapter 6.5.

The measurement of uncompensated resistance for a bubble-free channel is very useful for determining the length of the channel interrogated. A model was developed which accounted for the different resistance contributions to the overall uncompensated resistance. A three-dimensional image of the recessed square electrode annotated with the contributions to measured electrochemical cell resistance is given in Figure 6.3.

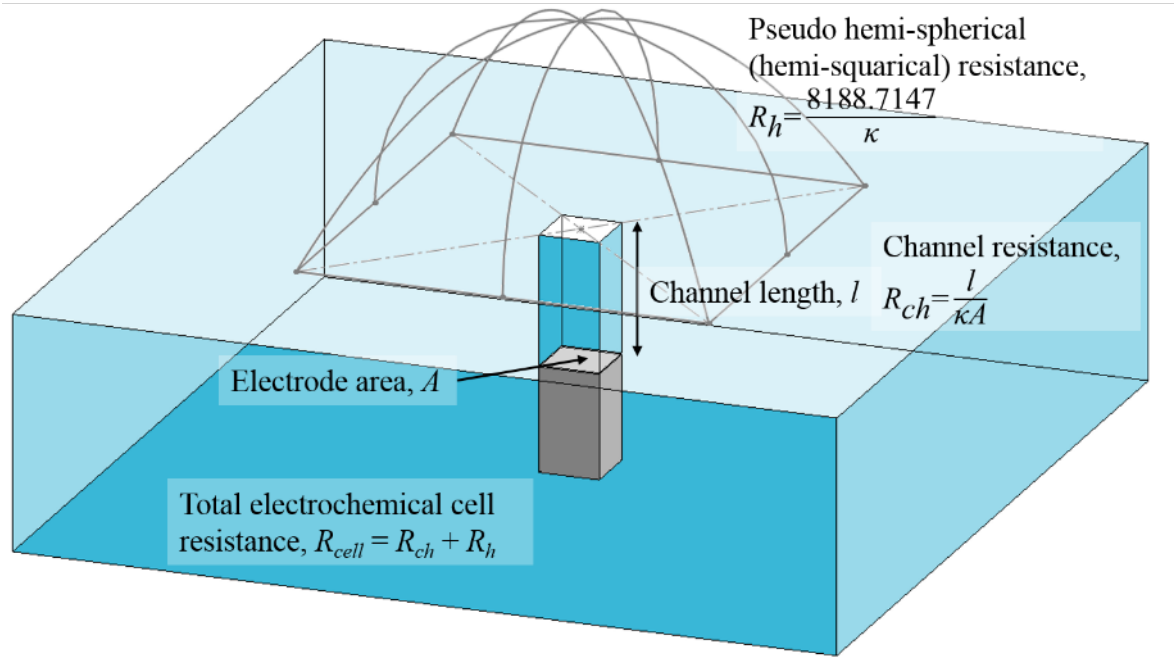

Figure 6.3 A 3-D representation of a recessed square electrode. The electrochemical cell resistance is a combination of two resistance contributions, from the channel (R_{ch}) and the pseudo hemi-spherical diffusion to the mouth of the channel (R_h). This image is for illustration purposes only and is not drawn to scale.

The channel resistance can be easily calculated based on the length of the channel, surface area and conductivity of the solution using equation 6.1

$$R_{ch} = \frac{l}{\kappa A} \tag{6.1}$$

With R_{ch} the resistance of the channel, l the length of the channel, κ the conductivity of the solution and A the area of the electrode. The measured resistance in the electrochemical system used will also depend upon a pseudo-hemispherical diffusion term. Using a COMSOL simulation the relationship between solution conductivity and pseudo hemi-spherical resistance contribution was elucidated (see Appendix 6). The resistance is given by equation 6.2.

$$R_h = \frac{8188.7147}{\kappa} \tag{6.2}$$

With R_h the pseudo-hemispherical resistance and κ the solution conductivity in mS cm^{-1}. The overall resistance measured in the electrochemical cell will therefore be a linear combination of the hemispherical and channel resistances (equation 6.3).

$$R_{cell} = R_{ch} + R_h \tag{6.3}$$

With R_{cell} the uncompensated resistance of the cell. By measuring the electrochemical cell resistance for a bubble free channel the channel length can therefore be calculated using equations 6.1 – 6.3.

Figure 6.4 plots the cell resistance as a function of solution conductivity for recessed square electrodes inside channels of depth 610 µm, 1100 µm and 2100 µm. This experimental data (■) is presented along with the results of the COMSOL simulation of the channel resistance (—) as a function of channel length at selected conductivities in the same range as the experimental data.

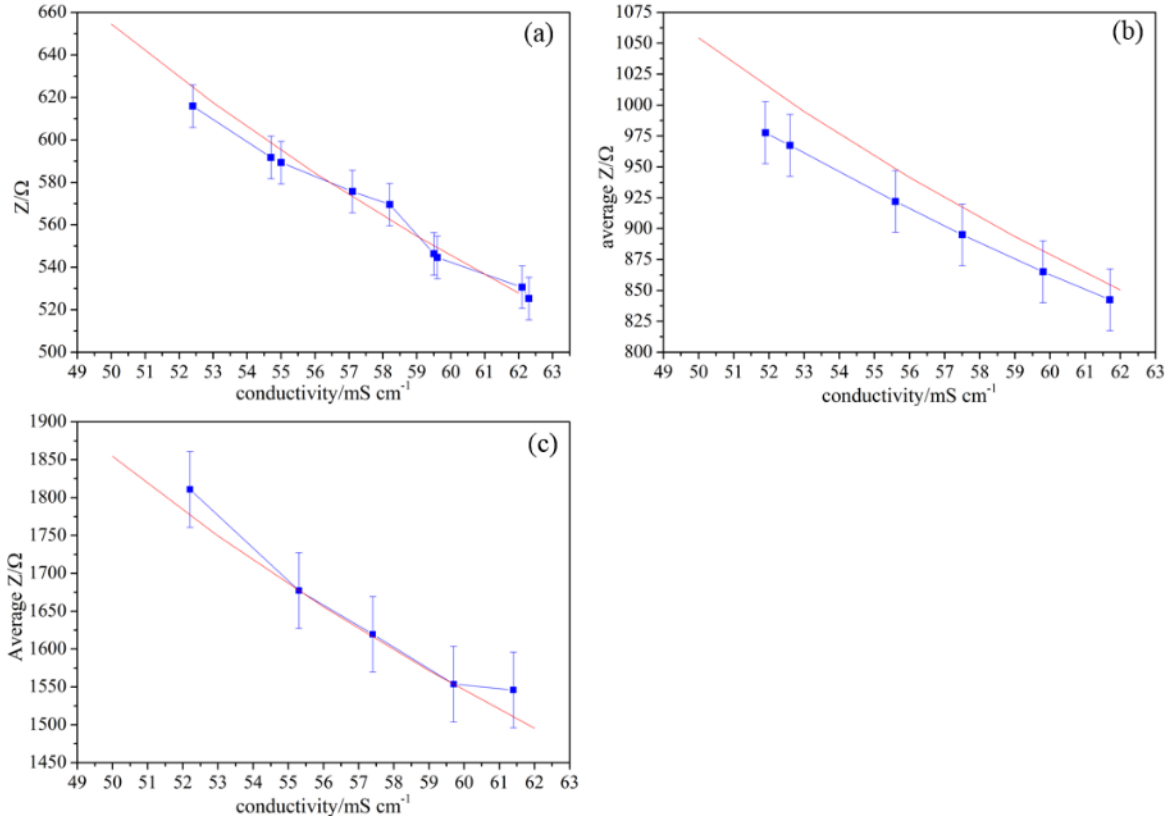

Figure 6.4 (a) Showing the cell resistance, *Z*, (■) as a function of conductivity for a 500 µm square Ag electrode inside a 500 µm x 500 µm x 610 µm resin channel and simulated resistance (—) over the same conductivity range. **(b)** Showing the cell resistance, *Z*, (■) as a function of conductivity for a 500 µm square Ag electrode inside a 500 µm x 500 µm x 1100 µm resin channel and simulated resistance (—) over the same conductivity range. **(c)** Showing the cell resistance, *Z*, (■) as a function of conductivity for a 500 µm square Ag electrode inside a 500 µm x 500 µm x 2100 µm resin channel and simulated resistance (—) over the same conductivity range. A stainless steel rod was used as a reference counter electrode. The solution in the resonant chamber was 0.5 M Na_2SO_4. The conductivity of the solution was varied by changing the temperature of the solution inside a water jacketed glass cell. The experiment was performed in aerobic conditions.

Some deviation between the experimental results and COMSOL model were observed for the 1100 µm channel (Figure 6.4 (b)). This deviation was observed as the magnitude of the AC perturbation was incorrectly measured by the data acquisition program. In this set of data, the potential amplitude, V_{app}, was determined by using an FFT algorithm to calculate

the amplitude at 1 MHz (the frequency of the AC potential). The frequency from the function generator used however was not precisely 1 MHz or a constant frequency (the function generator used relied on an oscillator circuit, which although noise free, was dependent on temperature and component value). Therefore, there was an inaccuracy in the amplitude of the applied AC potential (V_{app}) reported by the FFT processed data, resulting in a systematic error in the impedance values recorded. The error in the resistance values here was ± 25 Ω reflecting the spread of the data points collected at this resistance.

The experimental data in Figure 6.4 (a) (with the 610 µm channel) and Figure 6.4 (c) (with the 2100 µm channel) is presented with data point spreads of ± 10 Ω and ± 30 Ω respectively. These values were estimated from the spread of the data points collected in the demodulated signal. For these two data sets, V_{app} was acquired using an alternative method, not susceptible to the issues of the FFT approach. Specifically, an rms measurement of the true AC excitation potential was utilised. This method was found to be more reliable than the FFT approach for determining the real V_{app} in this case. The result was that the resistance values were calculated with greater accuracy and have a close agreement with the results of the simulation.

The use of resistance measurements to calculate channel length is however just one possible method of measuring the etched channels. In order to provide supporting evidence to these calculations, microscope images were taken of each of the three channels. The length of the channels were then measured from the images taken. Figure 6.5 shows images of the 610 µm, 1100 µm and 2100 µm channels.

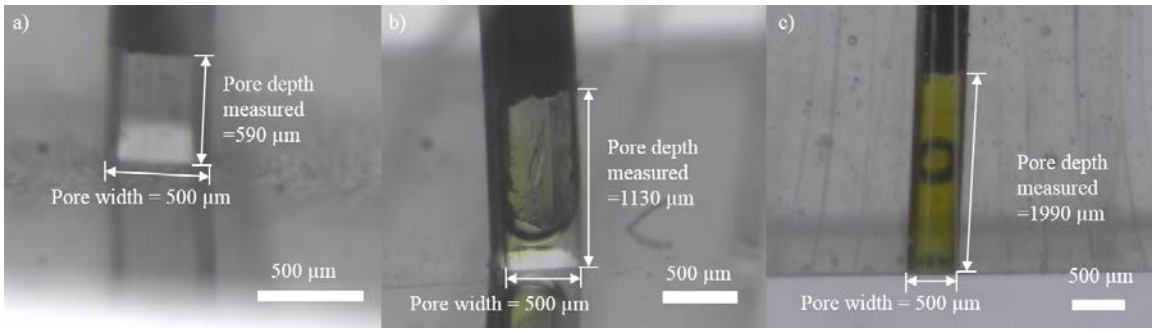

Figure 6.5 a) An image of the 610 µm depth channel imaged using a microscope camera. The channel depth as measured from this image is 590 µm. **b)** An image of the 1100 µm depth channel imaged using a microscope camera. The channel depth as measured from this image is 1130 µm. **c)** An image of the 2100 µm depth channel imaged using a microscope camera. The channel depth as measured from this image is 1990 µm.

A summary of the measured lengths of the three channels using both the impedance data and images is given in Table 6.1. Further details of how the measured impedance was used to calculate the channel length can be found in Appendix 7.

Channel length calculated from impedance data, l/μm	Channel length measured from image, l/μm	Difference between measurements, Δl/μm
610 ± 4.6	590 ± 9.1	20 ± 14
1100 ± 7.3	1130 ± 13	30 ± 20
2100 ± 18	1990 ± 9.4	110 ± 27

Table 6.1 A table of the measured channel lengths for the three recessed square electrodes. The channel lengths were calculated from the recorded impedance and also from images of the electrodes taken using a microscope camera.

It seems likely that the camera images were less accurate for recording the channel length than using the recorded resistance. There are two challenges to producing these images which reduce the accuracy of these measurements. First, the electrode was imaged at a slight angle using a lens with a shallow depth of field. Thus the boundaries (channel mouth and electrode position) are ambiguous. Second, it proved challenging to position the electrode so that the flat channel wall was perpendicular to the camera lens. Therefore the observed width (used to scale the images) appeared narrower in the images due to this misalignment.

6.4 Monitoring the impedance changes inside a channel

The demodulation technique made it possible to process impedance time information at a faster sample rate of 1 MHz (compared to the 500 kHz sample rate at which the previous FFT approach was most accurate). The new technique also allows for impedance to be recorded over longer time periods.

In order to investigate how well this system worked, an electrochemical system was chosen in which a silver electrode was recessed to form a sensor at the bottom of a channel. In this case a depth of 1100 μm was deployed (as dimensioned in Chapter 6.3). This structure was exposed to short pulses of ultrasound from an ultrasonic horn. The shape of the impedance plot during ultrasound exposure follows a reproducible and predictable pattern. This pattern is shown in Figure 6.6 along with a series of cartoon images of the bubble activity.

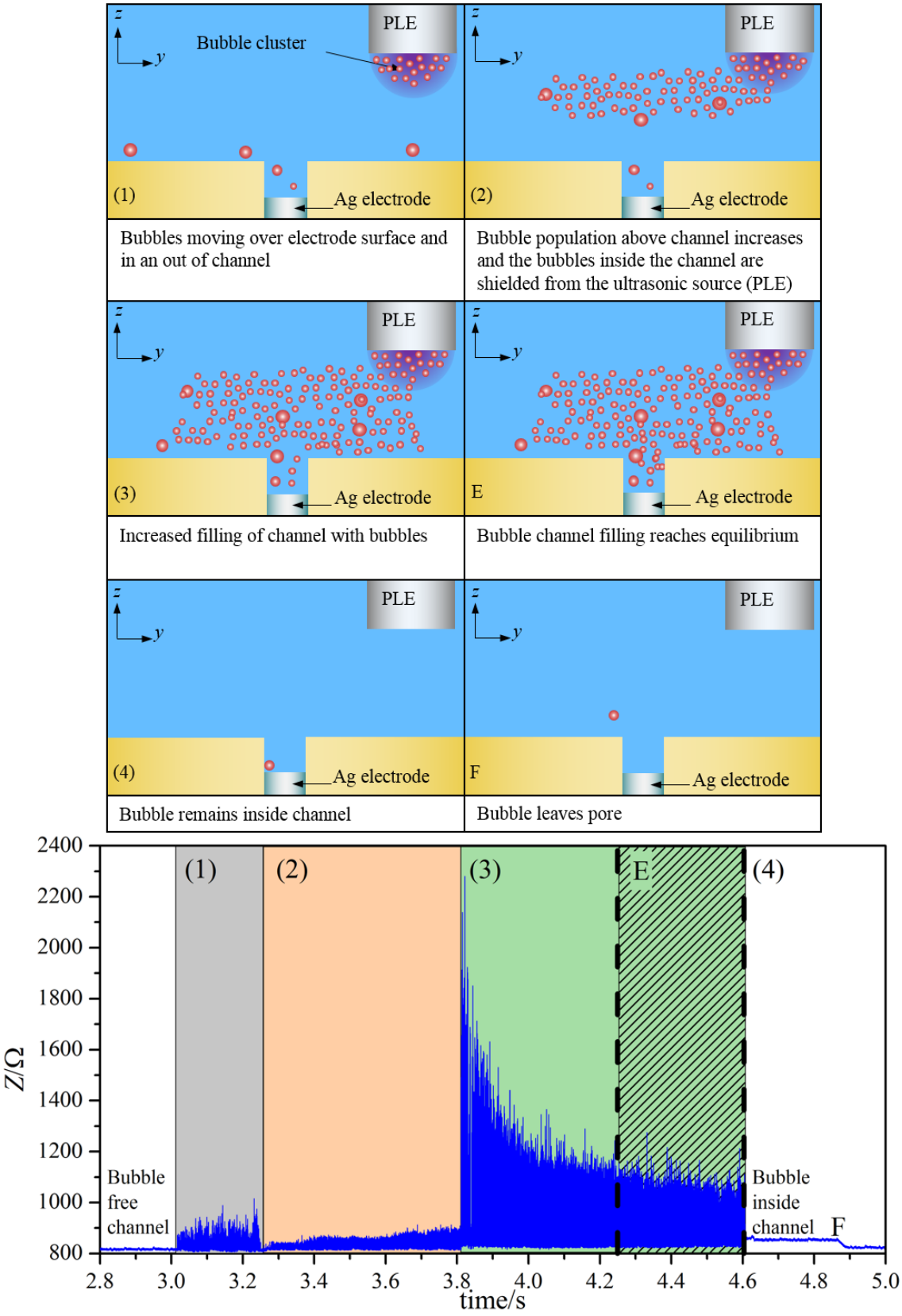

Figure 6.6 Showing the demodulated impedance, *Z*, (—) as a function of time for a 500 µm square Ag electrode inside a 500 µm x 500 µm x 1.1 mm resin channel. A stainless steel rod was used as a reference counter electrode along with cartoon images of the electrochemical cell. The solution in the resonant chamber was 0.5 M Na_2SO_4. The frequency applied to the ultrasonic horn was approximately 23 kHz. The horn tip was positioned at a *z* separation of 2 mm and *y* separation of 2 mm from the channel mouth. The solution temperature was 21.9 °C and the experiment was performed in aerobic conditions.

This impedance time plot can be split into three distinct regions. In the grey shaded region (1) immediately after the ultrasonic horn was turned on, cavitation bubbles are seeded inside the channel (as seen in cartoon image (1)). This was also confirmed by high-speed imaging (see Chapter 6.6). These bubbles grow and collapse which in turn cause regular spikes in the impedance time profile. The changes observed are attributed to the bubble oscillation, where the impedance increases during bubble growth and decreases as the bubbles are compressed inside the channel.

With continued ultrasound excitation, the cavitation cluster below the piston was observed to increase in size. This resulted in an increase of the bubble population in the solution above the recessed electrode (cartoon (2)). The effect of increasing bubble population shields the bubbles inside the channel from the effects of the ultrasound. The effect of this shielding is seen in the orange shaded region (2) of Figure 6.6. In this region the amplitude of the impedance transients (and hence amplitude of bubble oscillations) is decreased due to the decrease in pressure amplitude acting on them.

In the green shaded section (3), the increased gas population in the solution above the channel begins to push bubbles into the channel. As the gas inside the channel fills up the impedance spikes measured increase drastically in size (cartoon (3), Figure 6.6). As the gas filling region continued to grow larger however as a steady state was reached in which the impedance peaks observed levelled out to a plateau. This can be observed in Figure 6.6 and is highlighted as section E. This indicates that relatively little extra gas was entering the channel and so the bubbles left behind after the ultrasonic field was terminated are all of a similar size regardless of the ultrasound exposure period used.

After the ultrasonic pulse from the PLE ended, some of the gas from the cavitation bubbles remained inside the channel. Imaging of the channel showed this gas amalgamating into a single gas bubble (cartoon (4), Figure 6.6). This gas bubble either remained inside the channel or rose out under buoyancy. The presence of gas inside the channel after ultrasound pulsing can be seen the impedance time plots by comparing the measured impedance before and after the ultrasound pulse, as the gas inside the pore increased the measured impedance. As a gas bubble rose out of the channel a step change in impedance was recorded. Such a step change can be seen in the impedance plot and is labelled F in Figure 6.6 and in cartoon ‘F’ of Figure 6.6. It was possible to use the change in impedance to calculate the size of the gas bubbles. This is explored further in Chapter 6.5.

6.5 Using Demodulated data to calculate void fraction

As was mentioned in Chapter 6.3 the dynamic volume of gas inside these recessed or channel structures can also be calculated from the impedance data captured. This was achieved by modelling the system used in a similar way to the model used to calculate the channel length in Chapter 6.3. This model used accounts for how changes to the dimensions of the channel, solution conductivity and gas bubble volume altered the measured cell impedance which in turn, is assumed to be dominated by the cell resistance. From this it is then possible to calculate the fraction of the channel occupied by bubbles, or in other words the void fraction of the channel. It is then possible to determine the dimensions of the bubbles inside the channel and, under appropriate conditions, their size as they rise out of the electrode structure.

In order to account for the inclusion of gas within the recessed electrode structure or 'channel', equation 6.4 can be derived.

$$\kappa' = \frac{l}{(R_{cell}\text{-}R_h)A} \tag{6.4}$$

where κ' represents the conductivity of the bubble/solution in the system. From this the void fraction, α, of the channel can be calculated using equation 6.5[97,98]. For further information on these equations see Appendix 8.

$$\alpha = \frac{2(1-\kappa')}{\kappa'+2} \tag{6.5}$$

The value of α can take values from 0 to 1 with a value of 0 indicating no bubbles are present and 1 indicating the whole channel is filled with bubbles.

The model described here was applied to the demodulated resistance data captured to discover how the void fraction of the channel changes as a function of time. Figure 6.7 shows the void fraction time plot calculated from the data set depicted in Figure 6.6.

Clearly, as gas bubbles are generated inside or captured by the channel during exposure to ultrasound, the void fraction is seen to increase. The oscillatory motion (expansion and contraction) of the bubbles as a result of the action of the sound field on those moieties causes the void fraction to oscillate.

It was observed from the impedance plots (e.g. Figure 6.6) that as the length on the ultrasonic pulse was increased (typically 2-3 s in length) the peak impedance values plateaued. Using a void fraction plot (such as in Figure 6.7) the volume of the channel the bubbles fill in this region (labelled ‘e’) can now be calculated.

The base level for the void fraction in this plot is less than zero. This is not a physical possibility and thus this indicates that there were some problems with the data processing which resulted in this systematic error. The likely source of this error was in the original calculation of impedance from the demodulated current signal. This error was discussed in relation to the resistances calculated in Figure 6.6 in which the amplitude of the input AC potential is not correctly determined. This error is systematically carried through each calculation of impedance from the demodulated current. For the purposes of measuring bubble sizes and gas volume inside the channel the systematic nature of this error means that it can be accounted for and the change in void fraction used to calculate the relevant information from the data presented.

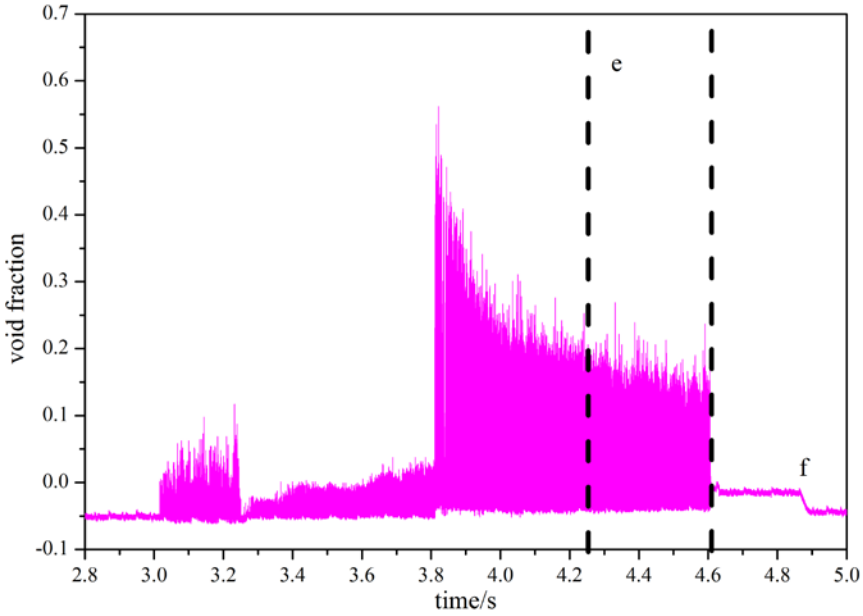

Figure 6.7 Showing the void fraction (—) as a function of time for a 500 µm square Ag electrode inside a 500 µm x 500 µm x 1.1 mm resin channel. A stainless steel rod was used as a reference counter electrode. The solution in the resonant chamber was 0.5 M Na_2SO_4. The frequency applied to the ultrasonic horn was approximately 23 kHz. The horn tip was positioned at a *z* separation of 2 mm and *y* separation of 2 mm from the channel mouth. The solution temperature was 21.9 °C and the experiment was performed in aerobic conditions.

As discussed previously in Chapter 6.4, a bubble seen to rise out of the channel after the pulse under buoyancy. This is labelled to occur in Figure 6.7 at point ‘f’. With a change in void fraction of 0.0315 ± 0.0099, the volume of the bubble can be calculated as $8.66 \times 10^{-6} \pm 2.71 \times 10^{-6}$ cm^3. Assuming the bubble is spherical this means the bubble has a

diameter of 255 ± 28.3 µm. Further repeat experiments showed a bubble radius of between 250 µm to 280 µm to be an average size for bubbles formed inside this 500 µm x 500 µm x 1100 µm channel. Conformation of this method of measuring bubble sizes was provided from images taken using a high-speed camera.

Investigations in which the impedance was recorded as a function of time during ultrasound pulses were also performed with channels of different sizes. The ultrasonic activity was generated using the same ultrasonic horn oscillating at the same frequency of 23 kHz. The purpose of using different sized channels was therefore to investigate whether the channel size would have any bearing on the size of the bubbles generated or if this was dictated solely by the ultrasonic source. Figure 6.8 shows the impedance time and void fraction time plot for ultrasonic pulsing on a channel with a depth of 610 µm.

The oscillation of impedance (—) during ultrasonic pulses was seen again as in the previous impedance time plot of Figure 6.6. The base uncompensated impedance (resistance) level was decreased from 820 ± 14 Ω to 620 ± 17 Ω. This change was due to the decrease of the length of the channel (see equation 6.1).

The channel length as calculated in Chapter 6.3 was used to calculate the void fraction (—) of the channel during the ultrasonic pulsing. Between the pulses the void fraction calculated was greater than zero indicating that there was a bubble trapped inside the channel. During ultrasonic pulses, the baseline void fraction approaches zero. This indicated that in the compression phase of the acoustic wave the gas bubbles were compressed making it appear as though the channel was bubble free (below the limit of detection for our system). An example of this can be seen between 0 – 2 s in Figure 6.8.

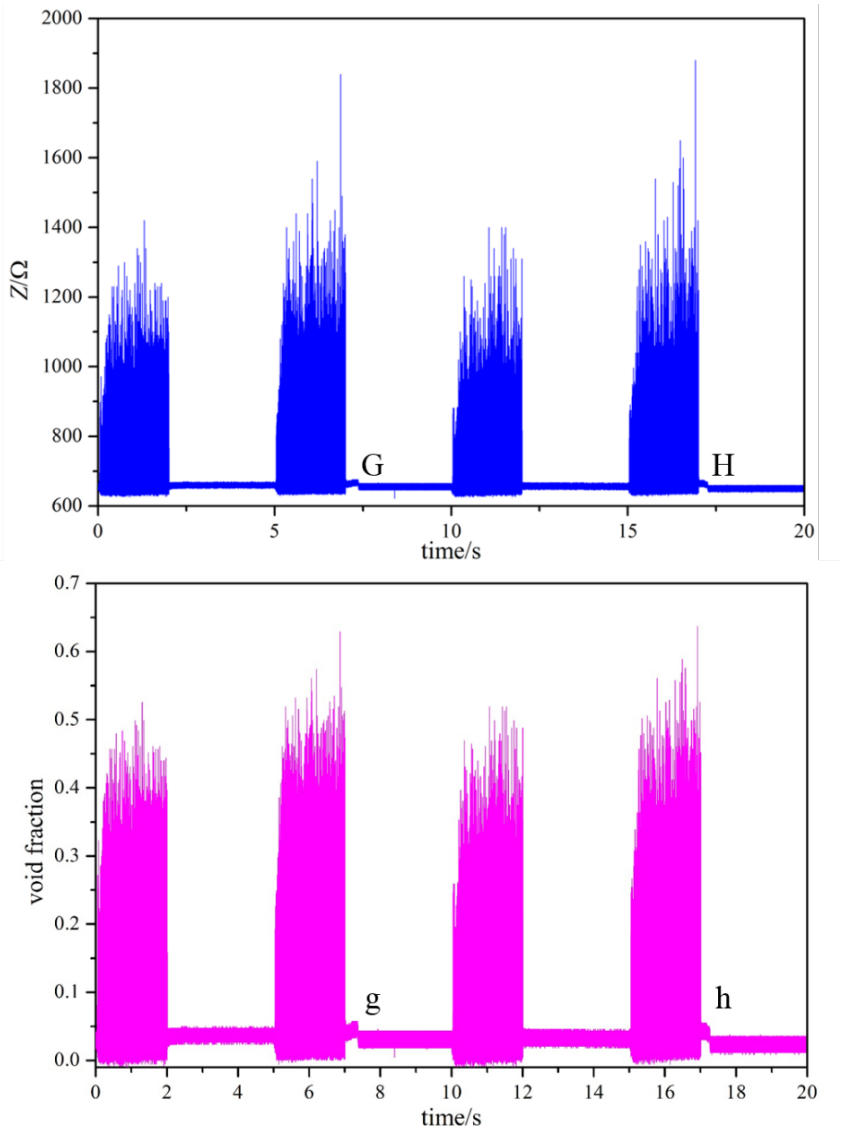

Figure 6.8 Showing the impedance (—) and void fraction (—) as a function of time for a 500 µm square Ag electrode inside a 500 µm x 500 µm x 610 µm resin channel. A stainless steel rod was used as a reference counter electrode. The applied AC potential amplitude was 54.0 mV from zero to peak. The solution in the resonant chamber was 0.5 M Na_2SO_4. The frequency applied to the ultrasonic horn was approximately 23 kHz. The horn tip was positioned at a *z* separation of 3 mm and *y* separation of 2 mm from the channel mouth. The solution temperature was 21.9 °C and the experiment was performed in aerobic conditions.

Two bubbles were observed leaving the channel after the ultrasonic exposure of the electrode assembly had been terminated. These are labelled ‘G’ and ‘H’ in the impedance time plot and ‘g’ and ‘h’ in the void fraction time plot (Figure 6.8). By using the change in void fraction and the known volume of the channel the volume of these bubbles was calculated. Table 6.2 summarises the results of these calculations.

Bubble	Void fraction	Bubble volume/cm^3	Bubble diameter/µm
'g'	0.017 ± 0.014	$2.59\text{x}10^{-6} \pm 2.19\text{x}10^{-6}$	170 ± 49.8
'h'	0.020 ± 0.019	$3.00\text{x}10^{-6} \pm 2.91\text{x}10^{-6}$	179 ± 43.7

Table 6.2 A table of the void fraction changes observed when a gas bubble leaves the 500 µm x 500 µm x 610 µm channel along with the calculated gas bubble volume and bubble diameter.

These bubbles are smaller than those seen leaving the 1100 µm deep channel. It is important to note however, that the void fraction (Figure 6.8, (—)) does not decrease to zero after the bubbles leave the channel at points 'g' and 'h'. This indicates that there is still some gas trapped inside the channel. Measuring the change in void fraction from before the bubbles left the channel at 'g' and 'h' and 0 (bubble free channel) the gas volume remaining in the channel after the ultrasonic pulse is $4.7\text{x}10^{-6} \pm 4.0\text{x}10^{-6}$ cm^3 and $3.5\text{x}10^{-6} \pm 3.5\text{x}10^{-6}$ cm^3 for 'g' and 'h' respectively. This volume is equivalent to the volume of the bubble seen leaving the 1100 µm length channel in Figure 6.7. Two different conclusions could be drawn from this observation. First is that the gas seen leaving the 1100 µm channel in Figure 6.7 is comprised of multiple bubbles leaving the channel simultaneously. Second, although the total gas volume is the same in both channels, the gas in the smaller channel is more likely to fragment into smaller sized bubbles.

Further to this, experiments were also performed in a channel with a depth of 2100 µm. The impedance time and void fraction time plots for this channel are displayed in Figure 6.9. It should be noted in this figure that the error in recorded impedance is much larger for this channel (around ± 50 Ω, compared to ± 10 Ω for the 610 µm deep channel). This increase in recorded error was a result of the channel resistance. The larger channel results in a larger cell resistance owing to the increase in the R_{ch} component of the total resistance (see equations 6.1 and 6.3). In the experiments presented in Figures 6.8 and 6.9, the amplitude of the applied AC potential was 54.0 mV and 55.9 mV respectively. As the applied potential to the cell was similar in both experiments, the demodulated current signal from the electrochemical setup using the 2100 µm channel was much smaller owing to the higher channel resistance. This resulted in a higher signal to noise ratio in the data (Figure 6.9).

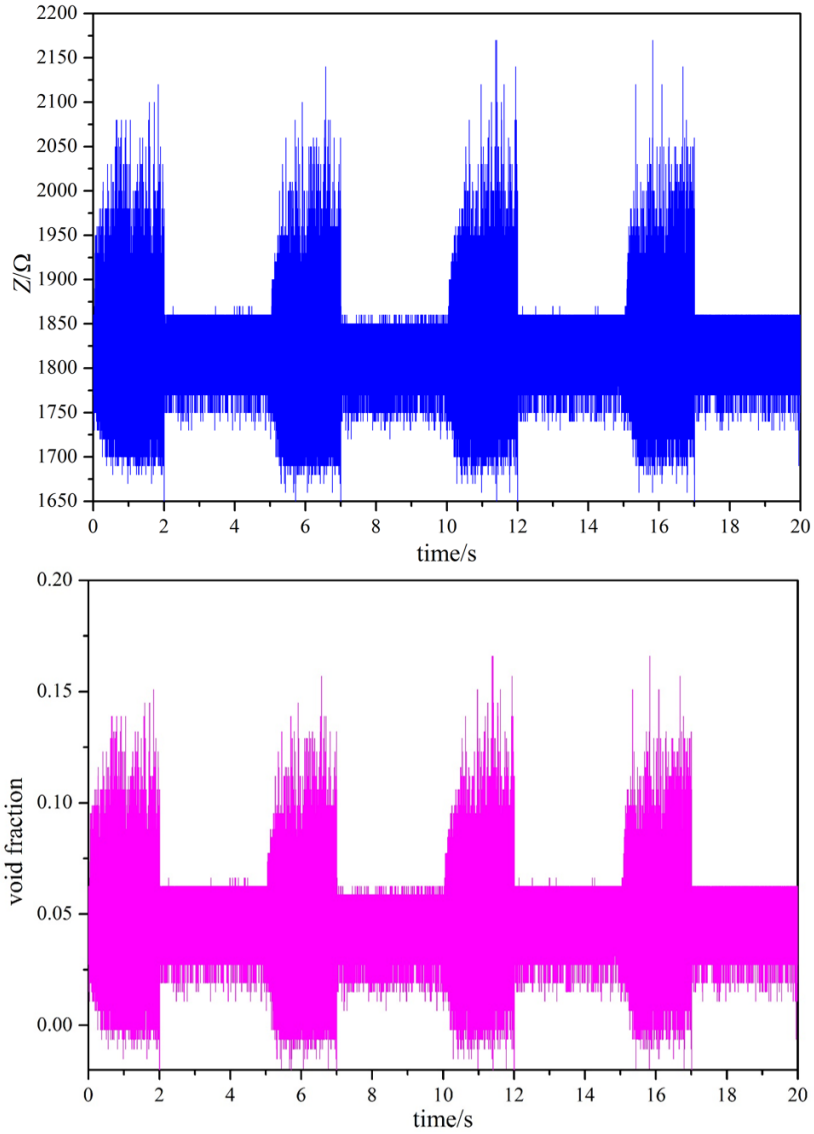

Figure 6.9 Showing the impedance (—) and void fraction (—) as a function of time for a 500 µm square Ag electrode inside a 500 µm x 500 µm x 2100 µm resin channel. A stainless steel rod was used as a reference counter electrode. The applied AC potential amplitude was 55.9 mV from zero to peak. The solution in the resonant chamber was 0.5 M Na_2SO_4. The frequency applied to the ultrasonic horn was approximately 23 kHz. The horn tip was positioned at a *z* separation of 3 mm and *y* separation of 2 mm from the channel mouth. The solution temperature was 21.9 °C and the experiment was performed in aerobic conditions

The void fraction between ultrasonic pulses in Figure 6.9 was 0.039. This means that the volume of gas which remained inside the channel between the pulses was 2.1×10^{-5} cm^3 (single bubble of diameter 340 µm). This is a larger volume of gas than for both of the other channel sizes. This may be indicative of a trend that the deeper the channel becomes the larger the gas bubbles are able to grow without becoming fragmented into clusters of smaller bubbles. This cannot be confirmed from the information presented. If gas bubbles had been seen rising out of the 2100 µm channel then their size as they left the channel could be measured by the change in void fraction.

In addition to measuring the gas volume remaining the channel after exposure to ultrasound, the void fraction data can also give us an indication of the fraction of the channel filled by gas during the ultrasonic exposure. A summary table of maximum void fraction and gas volume is given in Table 6.3.

Channel length/μm	**Maximum void fraction**	**'Average' void fraction during ultrasound exposure**	**Equilibrium volume of gas in channel during ultrasound exposure/cm^3**
610	0.5 – 0.6	0.4	6.10×10^{-5}
1100	0.3 – 0.4	0.2	5.50×10^{-5}
2100	0.1 – 0.15	0.1	5.30×10^{-5}

Table 6.3 A table of the maximum void fractions reported for channels of length 610 μm, 1100 μm and 2100 μm along with the calculated gas volume.

This table shows that for each channel of differing lengths, the fraction of the pore which is filled with gas is greater for the shorter channels. Thus the gas volume in the channel during exposure to ultrasound is shown to be independent of the channel length, as the volume of gas in each channel is similar.

As has been discussed in this section, certain assumptions have to be made about the bubble dynamics to interpret the impedance and void fraction results reported. Complementary evidence is therefore required to verify those assumptions. In the following section, high-speed imaging will be used to examine the bubble dynamics, and compare the visual observations to corresponding impedance time plots.

6.6 High-speed bubble imaging

The change in the amplitude of the impedance transients (such as seen in Figure 6.6) showed varying levels of 'bubble activity' observed at the silver recessed electrode. To provide additional information about the bubble environment around the electrode during ultrasonic exposure a series of high-speed video recordings were made. These were captured simultaneously with the recording of impedance time plots. The following section presents a series of images from these camera recordings along with the associated impedance time transients.

The first high-speed camera data was taken at a frame rate of 1000 frames per second. This frame rate was chosen so that images could be recorded for the entire 5 second window required to match the impedance data (without producing extremely large, and unnecessary, imaging files). In addition, this allows for the resolution of the images to be sufficient to view changes in the bulk fluid and the channel itself.

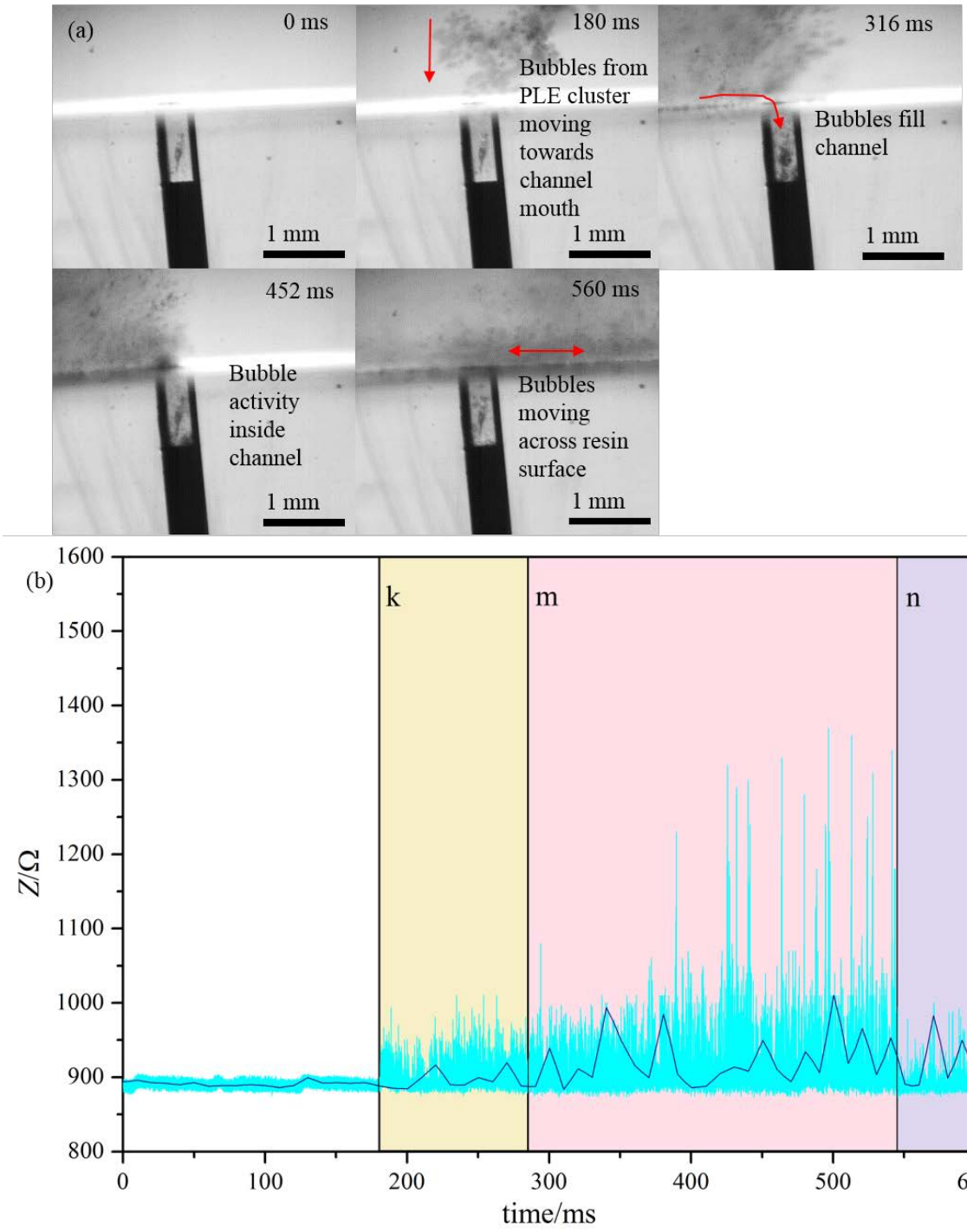

Figure 6.10 (a) A composite of images taken from the high-speed camera data recorded during ultrasonic agitation by the PLE. The camera data was recorded at a frame rate of 1000 fps and a shutter speed of 1/10000 s. The channel is square in shape with dimensions of 500 µm by 500 µm and depth of 1100 µm. The electrolyte is 0.5 M Na_2SO_4 at 24.5 °C and in aerobic conditions. The ultrasonic horn tip is positioned at a *z* separation of 3 mm and *y* separation of -2 mm. **(b)** Showing the demodulated impedance, *Z*, (—) and moving average of impedance (—, averaged over every 1000 data points) as a function of time for a 500 µm square Ag electrode inside a 500 µm x 500 µm x 1.1 mm resin channel. A stainless steel rod was used as a reference counter electrode. The solution in the resonant chamber was 0.5 M Na_2SO_4. The frequency applied to the ultrasonic horn was approximately 23 kHz. The horn tip was positioned at a *z* separation of 3 mm and *y* separation of 2 mm from the channel mouth. The solution temperature was 24.5 °C and the experiment was performed in aerobic conditions. The video footage accompanying this figure can be found at: https://doi.org/10.5258/SOTON/D0674.

The initial response of the system to the ultrasonic horn is shown in Figure 6.10 (a), showing a composite of images taken from the high-speed camera video footage. There is a delay between starting the recording of data and the start of the ultrasonic activity of 180 ms. The first bubble activity observed inside the cell was of bubbles streaming from the tip of the PLE (PLE not visible in these images, at a *z* separation of 3 mm and *y* separation of 2 mm) towards the resin surface of the electrode surround. The start of bubble activity above the channel mouth (as seen in the image in Figure 6.10, corresponds to the same point at which transient peaks were observed in the accompanying impedance time plot (yellow shaded region 'k', Figure 6.10). The bubbles then began to move over the resin surface and into the channel, as can be seen in the image at 316 ms in Figure 6.10 (a). This corresponds in time to an increase in the peak heights of the impedance time plot (pink shaded region 'm', Figure 6.10).

Over time the gas population above the electrode surround increased. This appeared to acoustically shield the central channel from the pressure wave from the PLE, and the bubble activity inside the channel decreased considerable in magnitude (t = 560 ms in Figure 6.10). The observed decrease in bubble activity inside the channel coincided with a decrease in the impedance peaks in Figure 6.10 (b), an indication that these transients were due to the bubble activity over the mouth of the channel.

After a period of 485 ms the growing population of gas above the mouth of the channel forced bubbles back into the channel (see image at 1237 ms in Figure 6.11 (a)). The refilling of the channel with gas coincided with an increase in the transient peaks seen in the impedance time plot (see shaded region in Figure 6.11 (b)). The volume of gas contained inside the channel then appeared to reach a steady state, where the percentage of the channel occupied by gas bubbles remained constant. This residual gas can be seen in the image at 1990 ms in Figure 6.11. Here the ultrasonic irradiation has been terminated. The impedance time plot also supported these observations (see shaded area in Figure 6.11 (b)) as the Z perturbations under these conditions are approximately equal in magnitude.

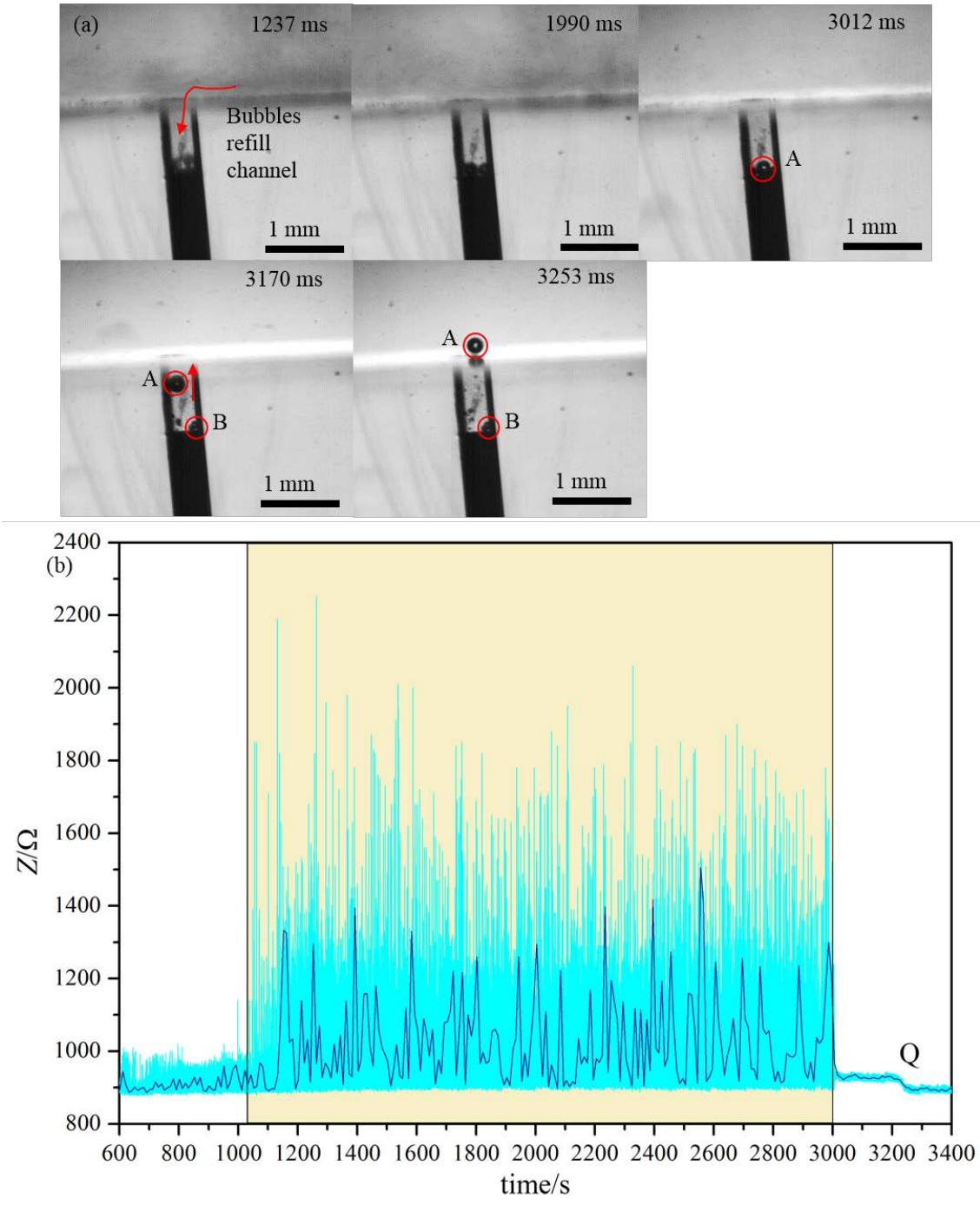

Figure 6.11 (a) A composite of images taken from the high-speed camera data recorded during ultrasonic agitation by the PLE. The camera data was recorded at a frame rate of 1000 fps and a shutter speed of 1/10000 s. The channel is square in shape with dimensions of 500 µm by 500 µm and depth of 1100 µm. The electrolyte is 0.5 M Na_2SO_4 at 24.5 °C and in aerobic conditions. The ultrasonic horn tip is positioned at a *z* separation of 3 mm and *y* separation of -2 mm. **(b)** Showing the demodulated impedance, *Z*, (—) and moving average of impedance (—, averaged over every 2000 data points) as a function of time for a 500 µm square Ag electrode inside a 500 µm x 500 µm x 1.1 mm resin channel. A stainless steel rod was used as a reference counter electrode. The solution in the resonant chamber was 0.5 M Na_2SO_4. The frequency applied to the ultrasonic horn was approximately 23 kHz. The horn tip was positioned at a *z* separation of 3 mm and *y* separation of 2 mm from the channel mouth. The solution temperature was 24.5 °C and the experiment was performed in aerobic conditions. The video footage accompanying this figure can be found at: https://doi.org/10.5258/SOTON/D0674.

After the ultrasonic agitation was terminated, a small cluster of bubbles remained inside the channel (image at 3012 ms in Figure 6.11 (a)). The largest of these bubbles is labelled ‘A’ in Figure 6.11 (a). This bubble was large enough that it was able to rise out of the channel under buoyancy forces (see image at 3170 ms) and settle at the mouth of the channel (see image at 3253 ms) leaving a smaller cluster of bubbles inside the channel (labelled ‘B’).

The presence of bubbles inside the channel and escape of bubble ‘A’ was also captured in the impedance time data (see Figure 6.11 (b)). The impedance level immediately after termination of ultrasonic activity was higher than the base level observed at the start (bubble free channel) of the data capture (925 Ω at t = 3050 ms compared to 885 ms at t = 0 ms). This increased impedance can now clearly be seen to be due to the presence of captured gas inside the channel. As the largest bubble, ‘A’, left the channel the measured impedance dropped to 889 Ω. This step change is marked in Figure 6.11 (b) by ‘Q’. By calculating the void fraction of the channel from the recorded impedance the change in void fraction was used to calculate the size of bubble ‘A’. The void fraction calculation yielded a bubble diameter for bubble ‘A’ of 250 µm. The bubble was also measured from the high-speed camera image. From the image, the bubble diameter was calculated to be 220 ± 8 µm.

The high-speed videos presented in Figures 6.10 (a) and 6.11 (a) were able to provide supporting evidence for the shape of the impedance transients observed in Figures 6.10 (b) and 6.11 (b). However, further information about the bubble motion in and out of the channel could be determined by recording images at a higher frame rate but at appropriate parts of the experiment. The time over which the electrochemical cell was exposed to ultrasonic activity was decreased to accommodate the size of the imaging file generated. In addition, an external trigger pulse system was setup so that the PLE, impedance data recording and high-speed camera recording were all triggered simultaneously. In addition a pulse system was then employed to turn the PLE ‘on’ and ‘off’ again at determined intervals controlled by a program written in Visual Basic 2010. The trigger pulse setup used is explained in the timeline in Figure 6.12.

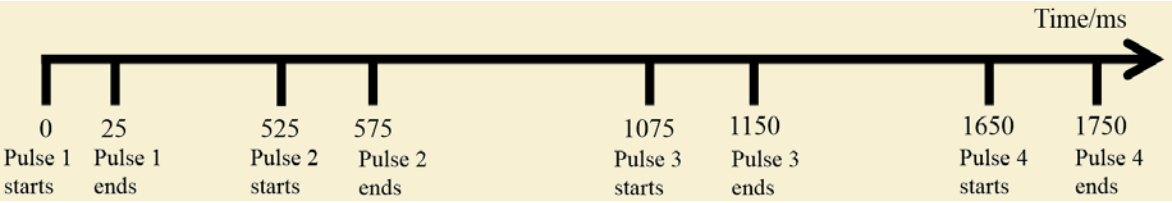

Figure 6.12 A timeline showing the sequence of pulses of ultrasonic energy imparted to the electrochemical cell. The timeline is given for illustration purposes only and is not drawn to scale.

Figure 6.13 shows the demodulated impedance (—) and a moving average (—, taken over 1000 data points) for the impedance time data recorded. The electrochemical system was exposed to four separate pulses of ultrasonic activity in the time window displayed with the region in which each pulse occurred highlighted in Figure 6.13 and labelled a) – d).

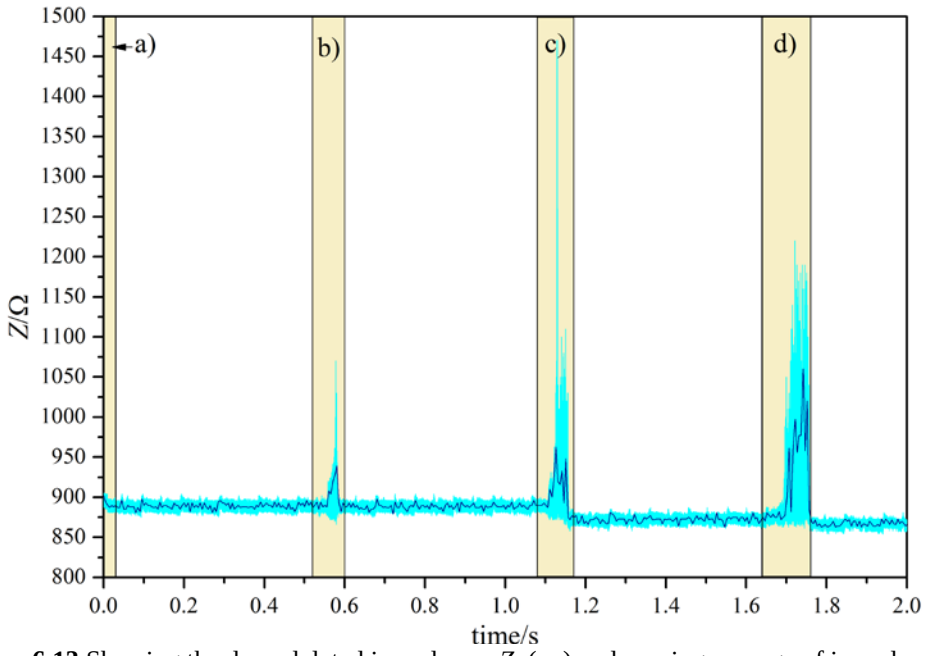

Figure 6.13 Showing the demodulated impedance, *Z*, (—) and moving average of impedance (—, taken over 1000 data points) as a function of time for a 500 µm square Ag electrode inside a 500 µm x 500 µm x 1.1 mm resin channel. A stainless steel rod was used as a reference counter electrode. The solution in the resonant chamber was 0.5 M Na_2SO_4. The frequency applied to the ultrasonic horn was approximately 23 kHz. The horn tip was positioned at a *z* separation of 3 mm and *y* separation of 2 mm from the channel mouth. The solution temperature was 25.0 °C and the experiment was performed in aerobic conditions.

A short series of images from the high-speed camera footage during the first ultrasonic pulse is shown in Figure 6.14. No discernible impedance activity was observed during the ultrasonic impulse (region a) in Figure 6.13). The camera footage, however, shows that there were two bubbles present around the recessed Ag working electrode, one at the mouth of the channel (labelled ‘A’) and one inside the channel (labelled ‘B’). The evidence of a bubble inside the channel could also be observed in Figure 6.13 by comparing the base

resistance level in region a) the resistance level after the third and fourth ultrasonic pulses (regions c) and d) in Figure 6.13).

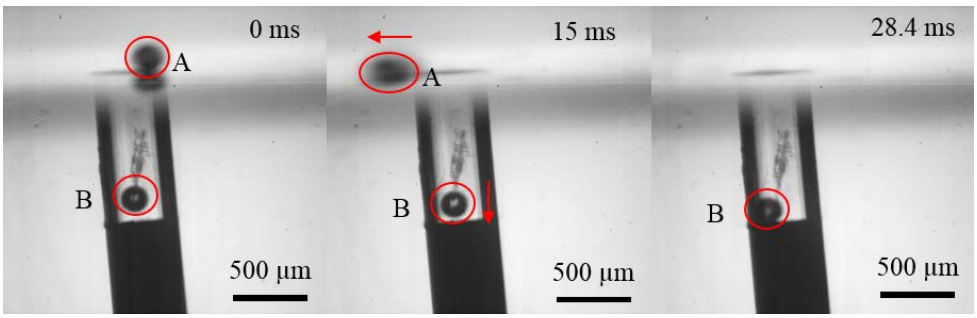

Figure 6.14 A composite of images taken from the high-speed camera data recorded during the first ultrasonic pulse. The camera data was recorded at a frame rate of 5000 fps and a shutter speed of 1/10000 s. The channel is square in shape with dimensions of 500 µm by 500 µm and depth of 1100 µm. The electrolyte is 0.5 M Na_2SO_4 at 25.0 °C and in aerobic conditions. The ultrasonic horn tip is positioned at a *z* separation of 3 mm and *y* separation of 2 mm. The video footage accompanying this figure can be found at: https://doi.org/10.5258/SOTON/D0674.

The ultrasonic energy input exerted by the PLE caused the bubble at the edge of the channel to oscillate and be moved away from the channel mouth by the pressure wave exerted on the bubble. The direction of the motion of bubble 'A' can be seen in Figure 6.14. At the same time the bubble inside the channel was also pushed further into the channel and after the pulse ended was left sitting on the Ag working electrode at the bottom of the channel.

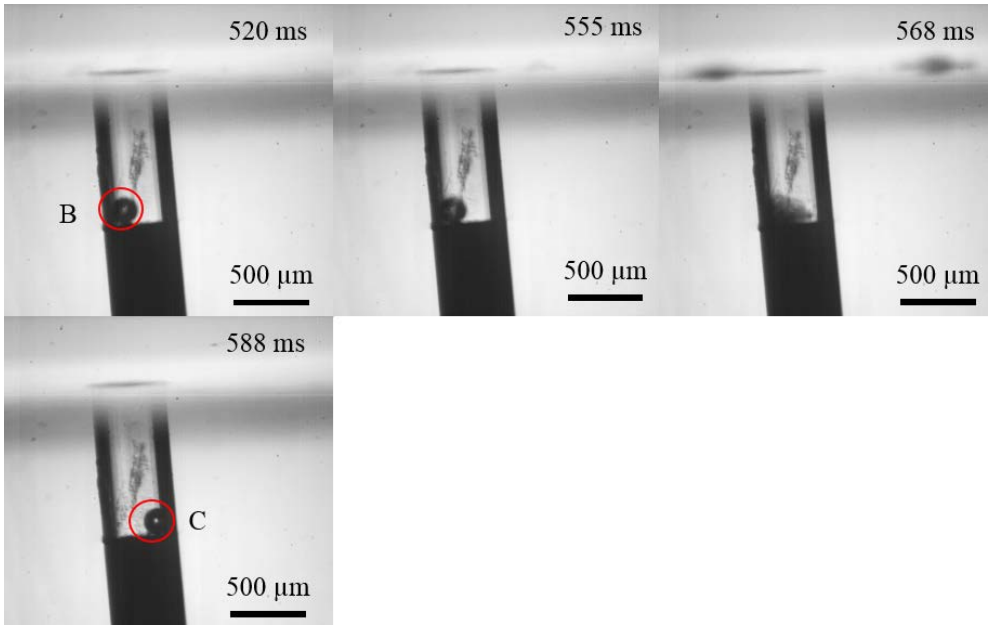

Figure 6.15 A composite of images taken from the high-speed camera data recorded during the second ultrasonic pulse. The camera data was recorded at a frame rate of 5000 fps and a shutter speed of 1/10000 s. The channel is square in shape with dimensions of 500 µm by 500 µm and depth of 1100 µm. The electrolyte is 0.5 M Na_2SO_4 at 25.0 °C and in aerobic conditions. The ultrasonic horn tip is positioned at a *z* separation of 3 mm and *y* separation of 2 mm. The video footage accompanying this figure can be found at: https://doi.org/10.5258/SOTON/D0674.

The bubble inside the channel (labelled ‘B’) was still present at the start of the second ultrasonic pulse as can be seen in the first image of Figure 6.15. The pulse of ultrasonic energy caused the bubble to oscillate and then to fragment into a series of smaller bubbles. The bubble oscillations were also observed in the spikes in the impedance time transient (section b) in Figure 6.13). After the end of the pulse the bubbles inside the channel coalesced again to form a single bubble, labelled ‘C’ in Figure 6.15.

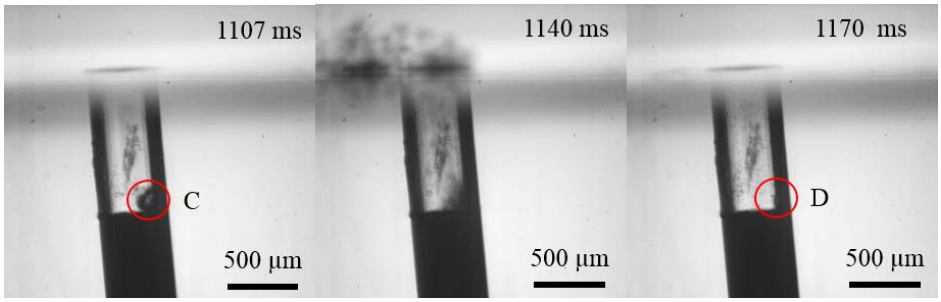

Figure 6.16 A composite of images taken from the high-speed camera data recorded during the third ultrasonic pulse. The camera data was recorded at a frame rate of 5000 fps and a shutter speed of 1/10000 s. The channel is square in shape with dimensions of 500 µm by 500 µm and depth of 1100 µm. The electrolyte is 0.5 M Na_2SO_4 at 25.0 °C and in aerobic conditions. The ultrasonic horn tip is positioned at a *z* separation of 3 mm and *y* separation of 2 mm. The video footage accompanying this figure can be found at: https://doi.org/10.5258/SOTON/D0674.

The third ultrasonic pulse caused bubble ‘C’ to fragment again and the fragments of the bubble were observed rising out of the channel (image at 1140 ms in Figure 6.16). This bubble activity was also observed in the transient impedance peaks in region c) of Figure 6.13. After the ultrasonic impulse ended the channel was left almost free of bubbles with one small bubble barely visible on the right wall of the channel. This bubble is labelled ‘D’ in Figure 6.16. The change in gas content inside the channel before and after this pulse can also be observed in the impedance data (see Figure 6.13). In comparing the baseline resistance before and after the shaded region c) in which the pulse occurred it can be seen that the resistance decreased after the pulse ended. By measuring the change in resistance and using the change in channel void fraction (see Chapter 6.5) the volume of gas that left the channel during this pulse was calculated to be 4.6×10^{-6} cm^3.

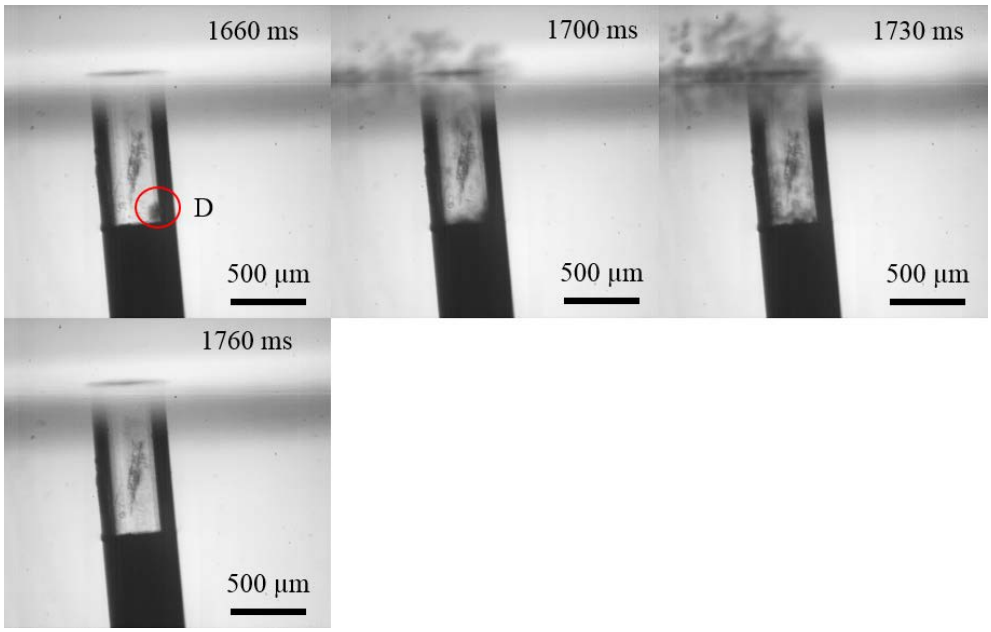

Figure 6.17 A composite of images taken from the high-speed camera data recorded during the fourth ultrasonic pulse. The camera data was recorded at a frame rate of 5000 fps and a shutter speed of 1/10000 s. The channel is square in shape with dimensions of 500 µm by 500 µm and depth of 1100 µm. The electrolyte is 0.5 M Na_2SO_4 at 25.0 °C and in aerobic conditions. The ultrasonic horn tip is positioned at a *z* separation of 3 mm and *y* separation of 2 mm. The video footage accompanying this figure can be found at: https://doi.org/10.5258/SOTON/D0674.

At the start of the fourth ultrasonic pulse, the bubble left inside the channel ('D') is broken into fragments and the bubble fragments were observed rising out of the channel (see image at 1700 ms in Figure 6.17). At the same time bubbles which had broken away from the cluster from the PLE (PLE not visible in the image) were observed moving across the surface of the resin and falling into the channel (see image at 1730 ms in Figure 6.17). After the pulse ended the channel was left free of bubbles. This change in gas content inside the channel could also be observed in the impedance data (Figure 6.13), although the change in base impedance before and after the pulse in region d) is very slight. The moving average was included in this plot to aid the observation of change in impedance.

6.7 Using a hydrophone to measure pressure changes during cavitation

Additional information about the bubble motion during ultrasonic pulsing was provided using a hydrophone. This was used to measure the change in the amplitude of the pressure in the liquid during the ultrasonic pulses. Figure 6.18 is an image of the setup used showing the recessed Ag working electrode (square 500 µm x 500 µm), the PLE (ultrasonic horn) and hydrophone. Experiments in which the hydrophone was used to monitor pressure changes was carried out in tandem with the impedance studies. In the image shown (Figure 6.18) the PLE is shown at a *y* separation of 2 mm and *z* separation of 2mm. The hydrophone was held at a fixed distance of 11 mm from the centre of the

working electrode recess. Thus the separation between PLE and hydrophone in Figure 6.18 was 9 mm.

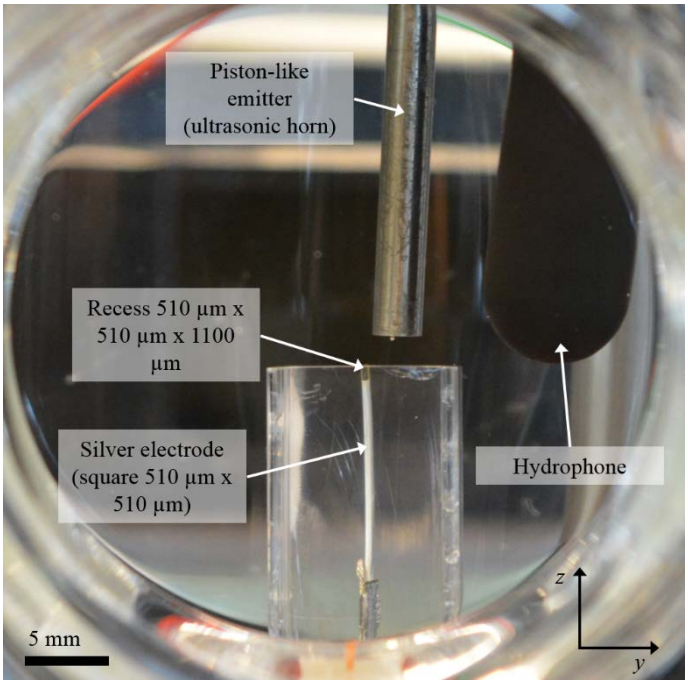

Figure 6.18 An image of the electrochemical cell showing the recessed Ag working electrode (500 µm x 500 µm) inside a channel of length 1100 µm, the PLE and hydrophone. Experiments were carried out in 0.5 M Na_2SO_4 at room temperature and atmospheric pressure. The solution was kept in aerobic conditions.

Figure 6.19 shows the impedance time plot from Figure 6.6 with the corresponding hydrophone data using the setup shown in Figure 6.18. The pressure signal from the hydrophone shows that the ultrasonic horn was active from 2.5 s until 4.6 s. The hydrophone pressure changes show a there was a 500 ms gap between the PLE starting to agitate the solution and significant change in the electrode impedance. This first region is labelled ‘A’ in Figure 6.19. The lack of impedance activity suggests that in this region no bubbles could be observed around the working electrode. The pressure changes measured by the horn in this region were therefore caused by the disturbance of the solution by the motion of the PLE unimpeded by the presence of cavitation bubbles.

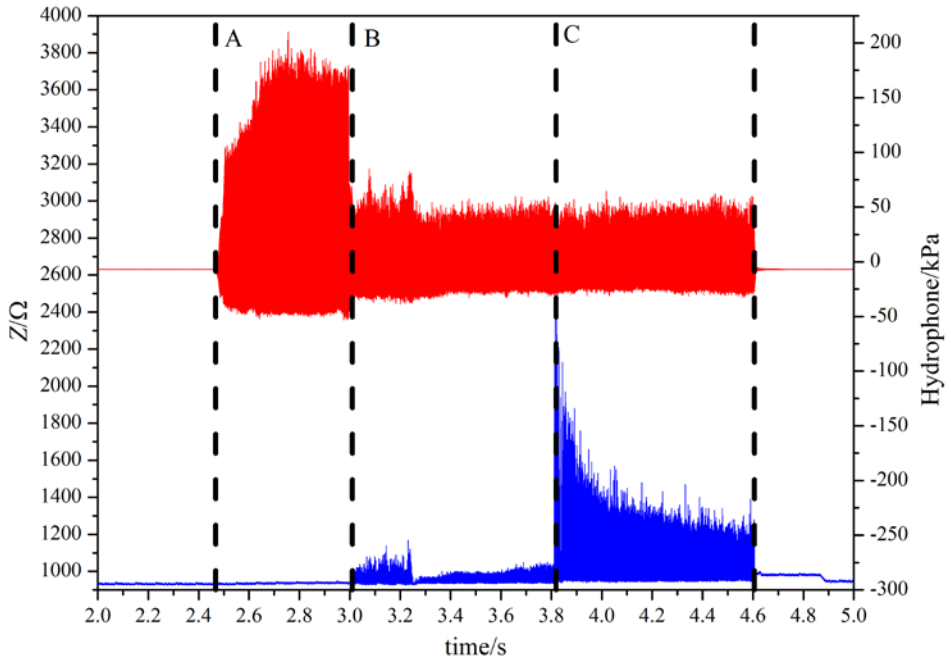

Figure 6.19 Showing the demodulated impedance, *Z*, (—) and hydrophone pressure (—) at a distance of 11 mm from the centre of the recess as a function of time for a 500 µm square Ag electrode inside a 500 µm x 500 µm x 1100 µm recess. A stainless steel rod was used as a reference/counter electrode. The solution in the resonant chamber was 0.5 M $NaSO_4$. The frequency applied to the ultrasonic horn was approximately 23 kHz. The horn tip was positioned at a *z* separation of 2 mm and *y* separation of 2 mm from the channel mouth. The solution temperature was 21.9 °C and the experiment was performed in aerobic conditions.

In the second region, labelled B in Figure 6.19, the amplitude of the hydrophone pressure signal decreased. The impedance time data also shows transient spikes. This indicated that the bubble population beneath the PLE had increased. An image of the cavitation cluster formed below the PLE is shown in Figure 6.20 shows an image of the electrochemical cell during ultrasonic agitation. From this image it is clear to see that the cavitation bubble cluster was shielding the hydrophone from the pressure change effects of the PLE.

The third region during ultrasonic agitation of the cell, labelled ‘C’ in Figure 6.19, the size of the transient impedance peaks increased. This increase in peaks was thought to be due to the gas filling of the channel, as seen in the high-speed camera images in Chapter 6.6. The amplitude of the hydrophone pressure changes shows no discernible changes in this region. This indicates that the hydrophone was still shielded from the pressure changes from the PLE tip by the cavitation bubble cluster.

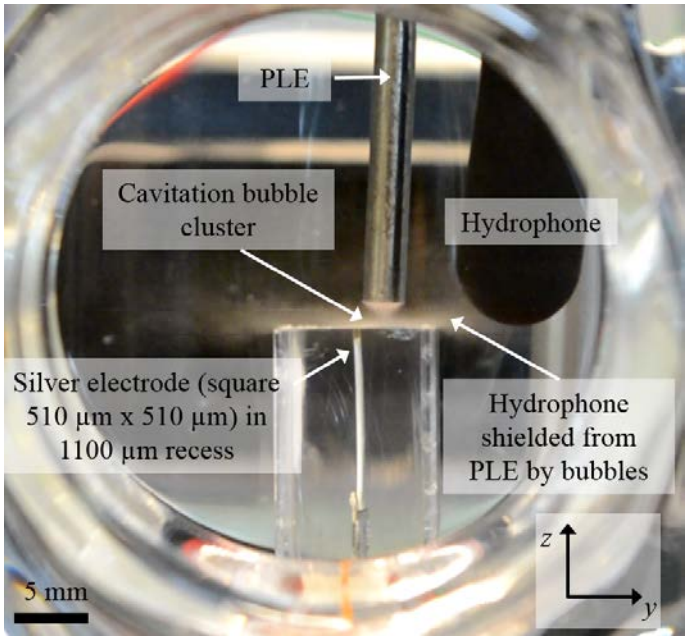

Figure 6.20 An image of the electrochemical cell showing the recessed Ag working electrode (510 µm x 510 µm) inside a channel of length 1100 µm, the PLE and hydrophone, during cell excitation from the PLE. Experiments were carried out in 0.5 M Na_2SO_4 at room temperature and atmospheric pressure. The solution was kept in aerobic conditions.

In using the impedance data in conjunction with the hydrophone signal useful information could be inferred about the generation of cavitation bubbles and their typical pattern of motion inside the channel. This is interesting in the context of using ultrasonic sources as a method of cleaning materials. It can be seen from the data presented that cavitation bubbles can be generated inside a channel and the motion of these bubbles, both in stable and transient cavitation, would be able to remove material stuck inside the channel. The nature of this bubble motion inside the channel can be supported using high-speed imaging of the channel during ultrasonic pulsing.

6.8 Data signal processing (DSP) using fast Fourier transform

Post processing (DSP) was applied to the impedance time and hydrophone pressure time data sets. In this post processing the fast Fourier transform algorithm was applied to the data using a custom designed program (Microsoft Visual Basic 2010 and National Instruments Measurement Studio, see Appendix 9, 9.9.2, for further information). Intensity plots were produced from this DSP in which the frequency components of the impedance or hydrophone pressure transients were plotted as a function of time. The intensity scale for these plots was provided by the impedance or hydrophone pressure amplitude. These plots showed how the frequency of the transient peaks in impedance and hydrophone pressure amplitude (e.g. Figure 6.19) changed as a function of time.

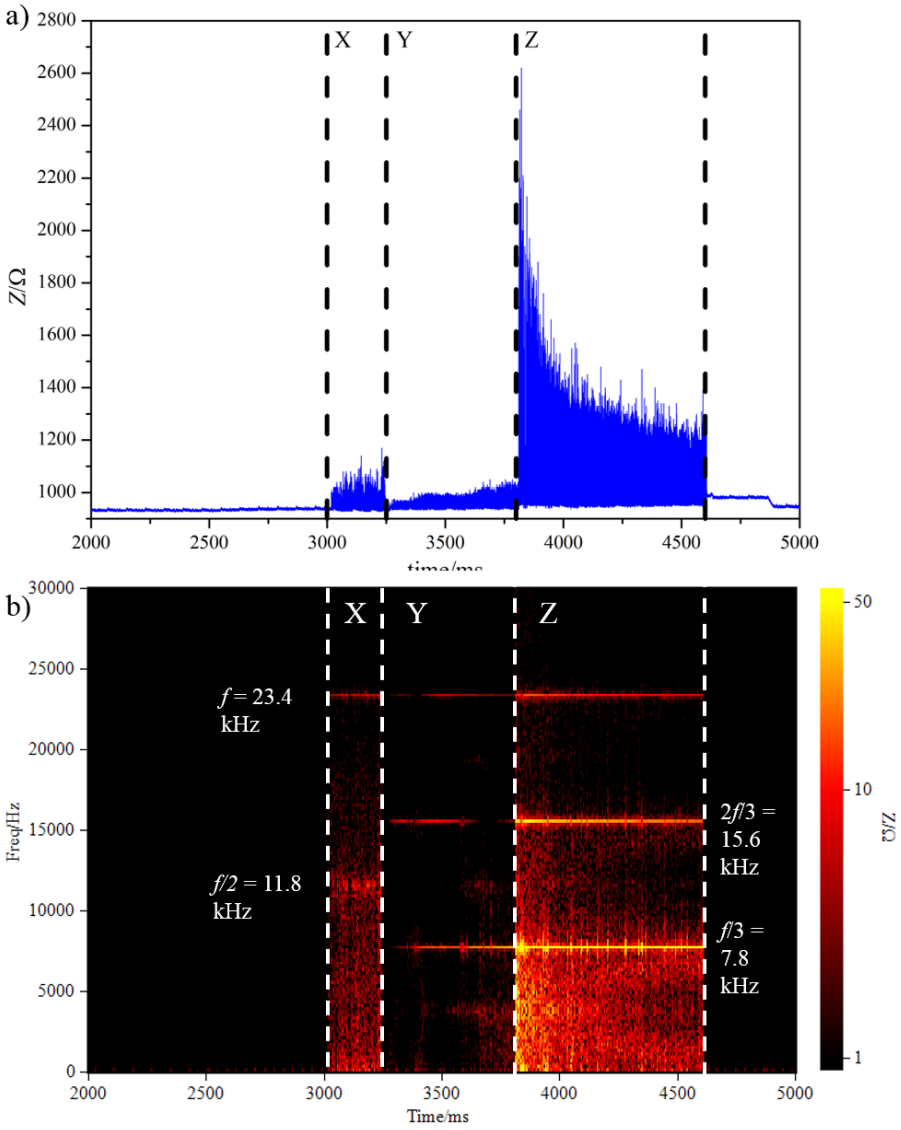

Figure 6.21 a) Showing the impedance (—) as a function of time for a 500 µm square Ag electrode inside a 500 µm x 500 µm x 1100 µm recess. A stainless steel rod was used as a reference/counter electrode. The solution in the resonant chamber was 0.5 M $NaSO_4$. The frequency applied to the ultrasonic horn was approximately 23 kHz. The horn tip was positioned at a *z* separation of 2 mm and *y* separation of 2 mm from the channel mouth. The solution temperature was 21.9 °C and the experiment was performed in aerobic conditions. **b)** FFT processed intensity plot for the impedance data shown.

Figure 6.21 a) shows the impedance data displayed in Figure 6.6 with the corresponding intensity plot (Figure 6.21 b)). From this figure it can be seen that the region containing intensity peaks (from 3000 – 4600 ms) corresponds to the same region in which impedance or 'bubble activity' was recorded. The intensity plot shows a peak at 23.4 kHz in this region. This is the same as the applied frequency of the ultrasonic wave from the PLE. The presence of this frequency peak indicates that the bubbles inside the channel are oscillating (expanding and contracting) with the same frequency as the applied ultrasound frequency from the PLE source (*f*).

The active region (from 3000 – 4600 ms) of the impedance and intensity plot can be divided into three distinct areas, in which different 'bubble activity' was observed. These regions have been labelled X, Y and Z in Figure 6.21. In the first highlighted region (3000 ms – 3300 ms, labelled X) small impedance transients were observed indicating the presence of cavitation bubbles close to the electrode and channel mouth. Two peaks were observed in the processed intensity plot at the fundamental frequency (*f*) and half the fundamental frequency, 11.8 kHz (*f*/2). The presence of this *f*/2 peak could be an indication of surface Faraday wave activity on the bubble walls as this activity is known to occur at the first subharmonic resonance frequency. The subharmonic resonance could also be an indication of the periodicity of the bubble cluster[99].

The positions of the subharmonic frequency intensity peaks in regions 'Y' and 'Z' indicated a change in the bubble resonance activity. In both regions, subharmonic peaks were observed at 7.8 kHz (*f*/3) and 15.6 kHz (2*f*/3). As Faraday waves are not observed at subharmonics of *f*/3 or 2*f*/3, the change in frequency is an indication that the subharmonics observed are symptomatic of a change in bubble cluster periodicity. This change in periodicity has been observed when the drive amplitude to the PLE is increased[99].

The input power to the ultrasonic horn was kept constant during the experiment. Thus the output power from the horn should be expected to be constant. However, the data presented here in Figures 6.19 and 6.21 indicated that the output power of the PLE was not constant over the duration of the ultrasonic pulse. This change in output power observed can be attributed to the mechanical construction of the PLE (ultrasonic horn) used in these experiments. The ultrasonic horn consists of a base unit, connected to a power amplifier, which drives the ultrasonic oscillations like a transducer (see Figure 6.22). To this unit a stainless steel tip was joined to the transducer by a threaded bolt. This steel tip acted as the PLE in the electrochemical cell. The thread used to connect the tip to the transducer was made from an insulating material with high tensile strength (PEEK, 30 % glass filled) and a thin washer made from the same material was also employed (as seen in Figure 6.22). The insulating thread and washer were required in these experiments in order to provide electrical shielding of the electrochemical cell from the power amplifier used to drive the oscillations of the ultrasonic horn.

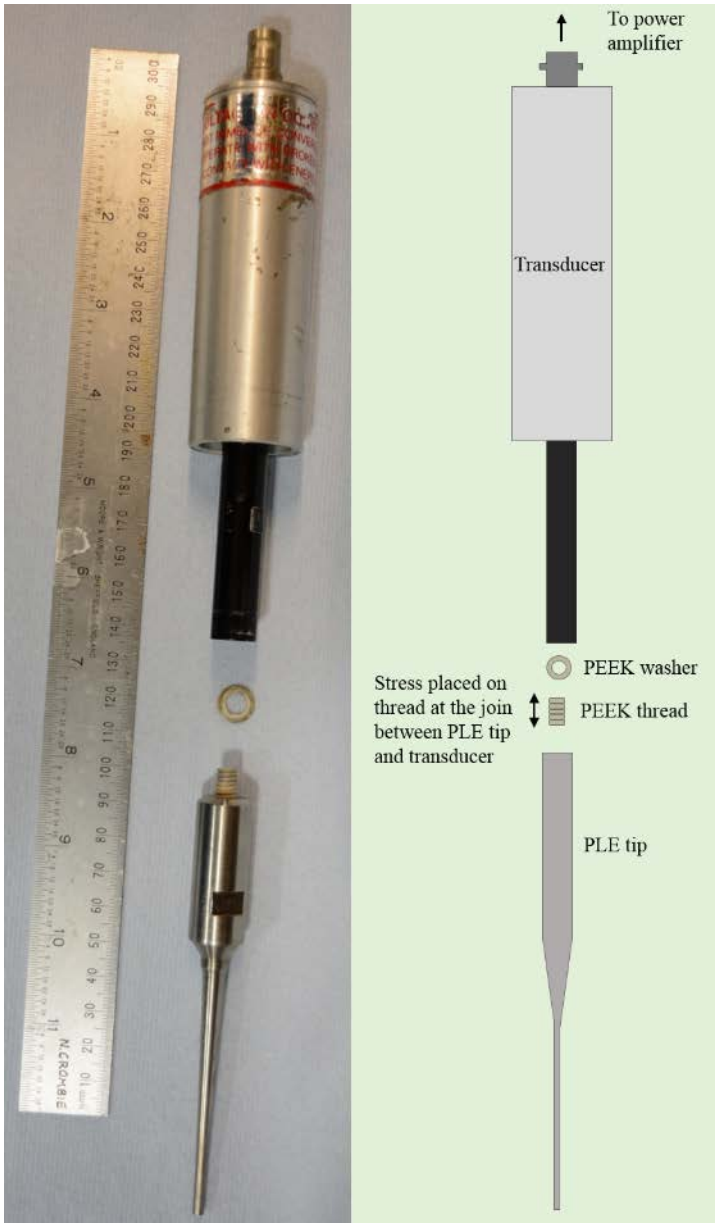

Figure 6.22 An image of the ultrasonic horn used as a piston-like emitter, showing the thread connecting the base transducer to the tip and washer used as additional electrical shielding between the power amplifier and tip in the electrochemical cell. The transducer oscillated at a frequency of 23.4 kHz.

Over time the PEEK thread became stretched by the oscillations of the transducer at the join between the transducer and stainless steel tip (Figure 6.22). This reduced how well the tip was able to mechanically couple to the oscillations of the transducer. Initially as the horn was turned on the lack of coupling between the PLE tip and transducer resulted in a lower than expected output power from the PLE. Over a period of transducer oscillations, the mechanical coupling between PLE and transducer improved and so the output power increased. This accounts for why the pressure changes at the hydrophone (Figure 6.19) was observed 500 ms before bubble activity was observed around the working electrode. As the

coupling between PLE tip and transducer improved further, the increase in power output resulted in a larger cavitation cluster below the PLE (section ‘Y’, Figure 6.21 a)) and a decrease in the bubble oscillation inside the channel. The increasing output power also accounts for the change in bubble periodicity observed as this same position (section ‘Y’, Figure 6.21 b)).

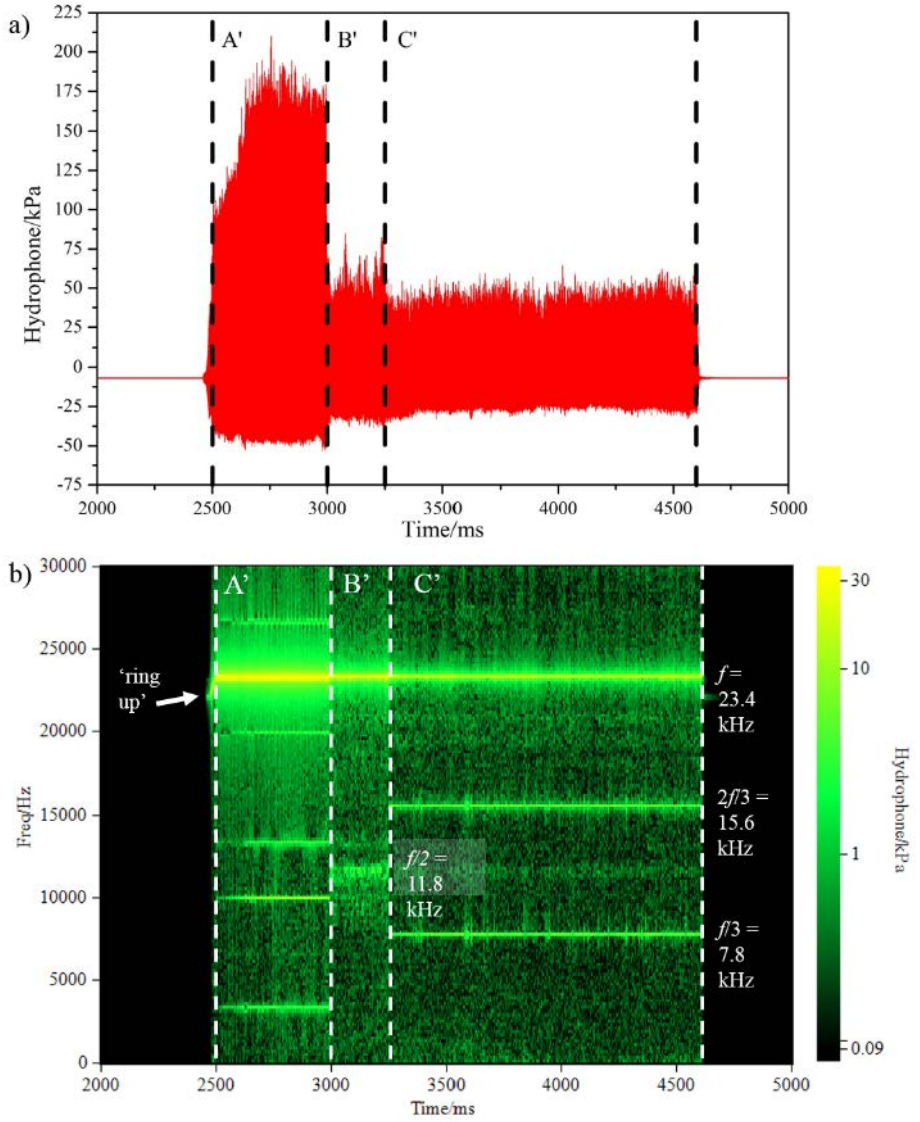

Figure 6.23 a) Showing the hydrophone pressure (—) as a function of time at a distance of 11 mm from the centre of the recess as a function of time for a 500 µm square Ag electrode inside a 500 µm x 500 µm x 1100 µm recess. The horn (PLE) tip was positioned at a *z* separation of 2 mm and *y* separation of 2 mm from the channel mouth. The solution temperature was 21.9 °C and the experiment was performed in aerobic conditions. **b)** FFT processed intensity plot for the hydrophone data shown.

Figure 6.23 shows the same FFT (DSP) algorithm applied to the hydrophone data recorded simultaneously with the impedance time signal (see Figure 6.19). Of interest in this intensity plot is the peak resonance as the ultrasound turns on at 2500 ms indicated by the white arrow and labelled ‘ring up’ in Figure 6.23. The fundamental frequency (*f*) peak here

started at 22.8 kHz and quickly rose to a frequency of 23.4 kHz. This shows that when turned the ultrasonic horn adjusted the frequency output and in effect 'self-tunes' to its resonance frequency. A peak in hydrophone pressure intensity was observed at the fundamental frequency f = 23.4 kHz. The other high intensity peaks observed in this region were at frequencies of 3.4 kHz, 10 kHz, 13.2 kHz, 20 kHz and 26.8 kHz. These frequencies are not harmonics of the fundamental frequency (f).

The subharmonic resonances observed are seen to change over the course of the ultrasound pulse. At the start of the pulse, in the region marked A', the strongest frequency peak is seen at 23.4 kHz. The absence of the impedance transients in this region indicated that the cavitation was not being generated near the electrode. As the cavitation bubbles were observed around the electrode, indicated by the presence of impedance transients and decrease of hydrophone pressure changes, a resonance peak at 11.8 kHz (f/2) emerged. This is labelled B' in Figure 6.23. This is the same region as the region in which the f/2 resonance mode was observed in the impedance data. This indicates that the bubbles in the cluster below the PLE tip (as seen by the hydrophone) were responding to the PLE stimulus in the same manner as those inside the channel (seen by the impedance plot). As the ultrasonic pulse continues and the gas population of the liquid increases the second subharmonic resonance mode is reached where peaks are observed at 7.8 kHz (f/3) and 15.6 kHz (2f/3). This region is labelled C'. This region is a mirror of the bubble resonance activity observed in the impedance data. Thus these results show that the bubble cluster below the PLE exhibits the same periodicity as the bubbles observed around the working electrode. This was to be expected as the driving force for all bubble oscillations comes from the PLE source.

The demodulated technique described in this chapter was able to report mechanistic details of the cavitation bubble motion. The results seen were similar to those shown in Chapter 5 using the other high-speed impedance technique. These results indicate that the bubble wall oscillations seen in stable cavitation as well as transient cavitation is important in the cleaning of surfaces using cavitation. The oscillatory bubble activity observed inside a recessed electrode in this chapter also indicates how cavitation bubbles can be particularly effective in cleaning rough textured surfaces or pores. The bubbles formed are small enough to be able to enter such recesses in the surface to be cleaned and with their oscillatory motion dislodge and remove debris. In fact, it may be beneficial to have

structured surfaces when cleaning using cavitation as the pores and crevices in the surface act as nucleation sites for the cavitation bubbles to form.

Chapter 7 Conclusions and Further Work

7.1 Concluding remarks

This thesis presents a new method for measuring electrochemical cell impedance as a function of time. This method was able to successfully elucidate the uncompensated resistance, R_u, electrode double layer capacitance, C_{dl}, and Faradaic current, i_{dc}, to a 2 µs time resolution. The novel technique developed was used to measure the activity of bubbles generated in acoustic cavitation. A number of different acoustic environments were investigated and complementary studies performed to provide conformation for the results observed from the high-speed AC impedance technique.

In Chapter 3, the acoustic environment chosen was a cylindrical cell and the sound source was an ultrasonic transducer fixed to the base of the chamber. The acoustic properties of the chamber are known to depend on the cell geometry and the frequency of the acoustic source. It was shown that acoustic cavitation occurred at the upper reflector surface of the cell when the acoustic pressure at the surface was at a maximum. The changes in acoustic pressure at the reflector surface were achieved by adjusting the *z* separation (the distance between the base of the cell and the reflector). The number of transient resistance peaks observed during the resonance cell exposure to ultrasound was used as an indication of the bubble 'activity'. The level of bubble activity observed using this impedance method was found to depend on the *z* separation between the upper reflector and the base of the cell. The bubble activity was also observed to increase when additional gas was electrochemically generated inside the cell. The *z* positions at which cavitation was observed was also observed to depend on the physical properties of the cell, the driving frequency of the ultrasonic transducer and the material properties of the reflector. The bubble activity measurements made using the high-speed AC impedance technique were confirmed by measuring the magnitude of the cell's acoustic output using a microphone. This was possible as the oscillating cavitation bubbles act as secondary sound sources.

The shape of the uncompensated resistance and electrode capacitance transients was also to characterise the behaviour of the cavitation bubbles during 'erosion/corrosion events' at the electrode surface. The shape of the resistance peaks showed us that the bubble grows over the surface relatively slowly and then rapidly collapses, eroding electrode material. In

experiments employing aluminium as the electrode material, current spikes were seen after the spike in resistance as the newly exposed surface oxidises.

The capacitance decreases as the bubble grows over the surface, opposite to the resistance, as capacitance varies linearly with surface area. As the bubble grows over the electrode it decreases the active surface area of the electrode and so the capacitance is decreased. This increase in electrode capacitance was also noted for an electrode not exposed to transient cavitation which had been made rough artificially using different polishing media.

In Chapters 4 and 5 the high-speed AC impedance technique was used to measure bubble activity generated using an ultrasonic horn as a sound source. The ultrasonic horn acts as a piston-like emitter (PLE) which oscillates vertically inside the cell creating a cluster of cavitation bubbles on the tip of the piston (see Figure 4.1). The bubble activity was measured at electrodes positioned underneath the bubble cluster on the PLE tip as bubbles broke away from the cluster and moved with an oscillatory motion across the electrode surface. The level of cavitation activity measured at the electrode surface was measured by counting the number of transient uncompensated resistance peaks in a period of 10 s. The measurements were made varying the vertical distance between electrode surface and PLE tip (*z* separation) and the lateral distance between the centre of the electrode and centre of the PLE tip (*y* separation), see Figure 4.2. These investigations found that the bubble activity at the electrode surface increased as the PLE tip approached the electrode, but that there was a ‘dead zone’ where the PLE tip was directly above the electrode. This dead zone was caused by the fluid flow beneath the PLE which pushed the bubbles radially outward. The size of this dead zone increased radially as the *z* separation was increased.

This experimental setup also allowed us to elucidate mechanistic detail about stable cavitation bubbles (compared to the transient bubbles observed in Chapter 3). Clusters of transient resistance peaks were observed as a bubble moved across the surface of the electrode. This was thought to be due to the oscillations of the bubble walls driven by the acoustic source (PLE). The resistance transients were post-processed using an FFT algorithm to elucidate the frequency components contained within the peak clusters (see Figure 5.12). This post-processing revealed that the cluster of peaks was a superposition of two oscillatory motions, one at the driving frequency of the PLE (fundamental frequency, *f*) and at half the driving frequency (first subharmonic of the fundamental, *f*/2). These frequencies are associated with two modes of bubble oscillation. The fundamental

frequency oscillation indicates the ‘breathing’ mode, the expansion and contraction of the bubble walls and the first sub-harmonic indicates waves on the surface walls of the bubble known as ‘Faraday waves’. Conformation of the bubble motion proposed by the uncompensated resistance transients was provided by complementary high-speed video recorded simultaneously with the impedance data.

In Chapter 4, the high-speed AC impedance technique was also used to measure particle impacts on an electrode surface using sand and carbon particles in a jet impinging on an electrode surface. Fluid flow was provided by a pump.

In Chapter 6, a demodulated current signal was used to produce impedance data as a function of time. This provided an alternative method of elucidating the cell impedance and hence information about the electrode surface to the high-speed AC impedance (FFT) approach. The principle advantage of this technique over the FFT approach is that it is possible to collect the data at a faster sample rate with less sacrifice on the accuracy of the data. However, the demodulation signal can only be used to record the impedance and not uncompensated resistance and capacitance separately. This limits the electrode and cell setups for which this can be used for.

7.2 Further work

The technique developed for elucidating R_u, C and i_{dc} as a function of time has shown some promising results, however the technique still has some limitations (for example in the speed of data processing and performance of the circuit elements). With further work there is potential to be able to extend this technique to be able to more accurately record data at smaller time resolutions, or increase the size of the data window. Currently the technique is also reliant on the simplicity of the electrochemical setup to provide meaningful results. There are therefore many more complex electrochemical environments in which adjustments would need to be made to the current technique in order to produce sensible results.

Chapter 8 References

1. A. Philipp and W. Lauterborn, *J. Fluid Mech.*, 1998, **361**, 75-116.
2. W. Lauterborn and T. Kurz, *Rep. Prog. Phys.*, 2010, **73**, 88.
3. K. S. Suslick, *Science*, 1990, **247**, 1439-1445.
4. W. Lauterborn and C. D. Ohl, *Ultrason. Sonochem.*, 1997, **4**, 65-75.
5. T. G. Leighton, *The acoustic bubble*, Academic Press, London, 1994.
6. P. R. Birkin, D. G. Offin, C. J. B. Vian and T. G. Leighton, *J. Acoust. Soc. Am.*, 2011, **130**, 3379-3388.
7. L. A. Crum, *Nature*, 1979, **278**, 148-149.
8. C. K. Holland and R. E. Apfel, *IEEE T. Ultrason. Ferr.*, 1989, **36**, 204-208.
9. P. R. Birkin, H. M. Hirsimaki, J. G. Frey and T. G. Leighton, *Electrochem. Commun.*, 2006, **8**, 1603-1609.
10. T. Kurz, D. Kroninger, R. Geisler and W. Lauterborn, *Phys. Rev. E*, 2006, **74**, 7.
11. E. B. Flint and K. S. Suslick, *Science*, 1991, **253**, 1397-1399.
12. P. R. Birkin, D. G. Offin and T. G. Leighton, *Phys. Chem. Chem. Phys.*, 2005, **7**, 530-537.
13. P. R. Birkin, R. O'Connor, C. Rapple and S. S. Martinez, *J. Chem. Soc. Faraday T.*, 1998, **94**, 3365-3371.
14. A. Kotronarou, G. Mills and M. R. Hoffmann, *J. Phys. Chem.*, 1991, **95**, 3630-3638.
15. A. Weissler, H. W. Cooper and S. Snyder, *J. Am. Chem. Soc.*, 1950, **72**, 1769-1775.
16. P. R. Birkin, J. F. Power, A. M. L. Vincotte and T. G. Leighton, *Phys. Chem. Chem. Phys.*, 2003, **5**, 4170-4174.
17. G. Mark, A. Tauber, L. A. Rudiger, H. P. Schuchmann, D. Schulz, A. Mues and C. von Sonntag, *Ultrason. Sonochem.*, 1998, **5**, 41-52.
18. L. A. Crum and G. T. Reynolds, *J. Acoust. Soc. Am.*, 1985, **78**, 137-139.
19. S. Putterman, P. G. Evans, G. Vazquez and K. Weninger, *Nature*, 2001, **409**, 782-783.
20. P. R. Birkin, D. G. Offin, P. F. Joseph and T. G. Leighton, *J. Phys. Chem. B*, 2005, **109**, 16997-17005.
21. B. Wolfrum, T. Kurz, R. Mettin and W. Lauterborn, *Phys. Fluids*, 2003, **15**, 2916-2922.
22. I. Hansson and K. A. Morch, *J. Appl. Phys.*, 1980, **51**, 4651-4658.
23. N. A. Madigan and L. A. Coury, *Anal. Chem.*, 1997, **69**, 5-15.
24. H. Zhang and L. A. Coury, *Anal. Chem.*, 1993, **65**, 1552-1558.
25. C. Otto, S. Zahn, F. Rost, P. Zahn, D. Jaros and H. Rohm, *Food Eng. Rev.*, 2011, **3**, 171-188.
26. L. W. M. van der Sluis, M. Versluis, M. K. Wu and P. R. Wesselink, *Int. Endod. J.*, 2007, **40**, 415-426.
27. B. Felver, D. C. King, S. C. Lea, G. J. Price and A. Damien Walmsley, *Ultrason. Sonochem.*, 2009, **16**, 692-697.
28. M. O. Lamminen, H. W. Walker and L. K. Weavers, *J. Membrane Sci.*, 2004, **237**, 213-223.
29. W. Yukio Tanimura and Kenji Yoshida and Yoshiaki, *Jpn J. Appl. Phys.*, 2010, **49**, 07HE20.
30. S. N. Patek, W. L. Korff and R. L. Caldwell, *Nature*, 2004, **428**, 819-820.
31. S. N. Patek and R. L. Caldwell, *J. Exp. Biol.*, 2005, **208**, 3655-3664.
32. D. G. Offin, P. R. Birkin and T. G. Leighton, *Phys. Chem. Chem. Phys.*, 2014, **16**, 4982-4989.
33. M. Hodnett, R. Chow and B. Zeqiri, *Ultrason. Sonochem.*, 2004, **11**, 441-454.
34. T. J. Matula, I. M. Hallaj, R. O. Cleveland, L. A. Crum, W. C. Moss and R. A. Roy, *J. Acoust. Soc. Am.*, 1998, **103**, 1377-1382.
35. S. C. Case, *Phys. Rev. E*, 2009, **79**, 026307.
36. V. Bouet, J. Fransaer, F. Huet, G. Maurin and J. P. Celis, *J. Electrochem. Soc.*, 1998, **145**, 436-446.
37. O. Louisnard, *Ultrason. Sonochem.*, 2012, **19**, 56-65.
38. T. G. Leighton, *Ultrasonics*, 2008, **48**, 85-90.
39. P. R. Birkin, T. G. Leighton, J. F. Power, M. D. Simpson, A. M. L. Vincotte and P. F. Joseph, *J Phys. Chem. A*, 2003, **107**, 306-320.
40. J. F. Power, PhD thesis, University of Southampton, 2003.
41. R. A. Roy, A. A. Atchley, L. A. Crum, J. B. Fowlkes and J. J. Reidy, *J. Acoust. Soc. Am.*, 1985, **78**, 1799-1805.
42. H. G. Flynn and C. C. Church, *J. Acoust. Soc. Am.*, 1984, **76**, 505-512.
43. F. R. Young, *Cavitation*, McGraw-Hill, London, 1989.
44. R. E. Apfel, *J. Acoust. Soc. Am.*, 1970, **48**, 1179-1186.
45. L. A. Crum, *Appl. Sci. Res.*, 1982, **38**, 101-115.
46. K. S. Suslick, D. A. Hammerton and R. E. Cline, *J. Am. Chem. Soc.*, 1986, **108**, 5641-5642.

47. M. Hodnett and B. Zeqiri, *Ultrason. Sonochem.*, 1997, **4**, 273-288.
48. L. Rayleigh, *The London, Edinburgh, and Dublin Philosophical Magazine and Journal of Science*, 1917, **34**, 94-98.
49. M. Harrison, *J. Acoust. Soc. Am.*, 1952, **24**, 776-782.
50. W. Güth, *Acta Acust. united Ac.*, 1954, **4**, 445-455.
51. T. M. Foley, PhD thesis, University of Southampton, 2014.
52. K. R. Rau, P. A. Quinto-Su, A. N. Hellman and V. Venugopalan, *Biophys. J.*, 2006, **91**, 317-329.
53. P. R. Birkin, J. F. Power, M. E. Abdelsalam and T. G. Leighton, *Ultrason. Sonochem.*, 2003, **10**, 203-208.
54. B. Zeqiri, S. C. Davies, P. N. Gelat, M. Hodnett and U. I. Lula, *2000 IEEE Ultrason. Symposium Proceedings, Vols 1 and 2*, 2000, 417-420.
55. E. A. Neppiras, *J. Acoust. Soc. Am.*, 1969, **46**, 587-601.
56. E. Cramer and W. Lauterborn, *Appl. Sci. Res.*, 1982, **38**, 209-214.
57. V. S. Moholkar, S. P. Sable and A. B. Pandit, *AIChE J.*, 2000, **46**, 684-694.
58. W. Lauterborn, *J. Acoust. Soc. Am.*, 1976, **59**, 283-293.
59. A. Prosperetti, L. A. Crum and K. W. Commander, *J Acoust. Soc. Am.*, 1988, **83**, 502-514.
60. D. F. Gaitan, L. A. Crum, C. C. Church and R. A. Roy, *J. Acoust. Soc. Am.*, 1992, **91**, 3166-3183.
61. B. P. Barber and S. J. Putterman, *Phys. Rev. Lett.*, 1992, **69**, 3839-3842.
62. P. R. Birkin, D. G. Offin and T. G. Leighton, *Wear*, 2005, **258**, 623-628.
63. C. E. Banks and R. G. Compton, *Chem. Anal.-Warsaw*, 2003, **48**, 159-180.
64. P. R. Birkin and S. SilvaMartinez, *J. Electroanal. Chem.*, 1996, **416**, 127-138.
65. M. E. Abdelsalam and P. R. Birkin, *Phys. Chem. Chem. Phys.*, 2002, **4**, 5340-5345.
66. P. R. Birkin, D. G. Offin and T. G. Leighton, *Electrochem. Commun.*, 2004, **6**, 1174-1179.
67. P. R. Birkin, J. F. Power, T. G. Leighton and A. M. L. Vinçotte, *Anal. Chem.*, 2002, **74**, 2584-2590.
68. P. R. Birkin, J. F. Power and T. G. Leighton, *Chem. Commun.*, 2001, 2230-2231.
69. G. O. H. Whillock and B. F. Harvey, *Ultrason. Sonochem.*, 1997, **4**, 23-31.
70. M. Sato, H. Itoh and T. Fujii, *Ultrasonics*, 2000, **38**, 312-315.
71. E. Maisonhaute, P. C. White and R. G. Compton, *J. Phys. Chem. B*, 2001, **105**, 12087-12091.
72. E. Maisonhaute, B. A. Brookes and R. G. Compton, *J. Phys. Chem. B*, 2002, **106**, 3166-3172.
73. W. E. Rowe and W. L. Nyborg, *J. Acoust. Soc. Am.*, 1966, **39**, 965-971.
74. J. Kolb and W. L. Nyborg, *J. Acoust. Soc. Am.*, 1956, **28**, 1237-1242.
75. C. W. Tobias, *J. Electrochem. Soc.*, 1959, **106**, 833-838.
76. D. P. Sutija and C. W. Tobias, *J. Electrochem. Soc.*, 1994, **141**, 2599-2607.
77. D. W. Dees and C. W. Tobias, *J. Electrochem. Soc.*, 1987, **134**, 369-377.
78. G. M. Whitney and C. W. Tobias, *AIChE J.*, 1988, **34**, 1981-1995.
79. J. Fransaer, V. Bouet, J. P. Celis, C. Gabrielli, F. Huet and G. Maurin, *J. Electrochem. Soc.*, 1995, **142**, 4181-4189.
80. Southampton Electrochemistry Group., *Instrumental methods in electrochemistry*, Ellis Horwood, Chichester, 2001.
81. A. J. Bard and L. R. Faulkner, *Electrochemical methods : fundamentals and applications*, Wiley, New York, 1980.
82. S. C. Case and S. R. Nagel, *Phys. Rev. Lett.*, 2008, **100**, 084503.
83. J. D. Paulsen, J. C. Burton and S. R. Nagel, *Phys. Rev. Lett.*, 2011, **106**, 114501.
84. J. D. Paulsen, J. C. Burton, S. R. Nagel, S. Appathurai, M. T. Harris and O. A. Basaran, *P. Natl. Acad. Sci. USA*, 2012, **109**, 6857.
85. H. Bouazaze, J. Fransaer, F. Huet, P. Rousseau and V. Vivier, *Electrochim. Acta*, 2010, **55**, 1645-1655.
86. C. Gabrielli, F. Huet and M. Keddam, *J. Electrochem. Soc.*, 1991, **138**, L82-L84.
87. L. E. Kinsler, *Fundamentals of acoustics*, Wiley, New York ; Chichester, 3rd edn., 1982.
88. I. G. Main, *Vibrations and waves in physics*, Cambridge University Press, Cambridge, 3rd edn., 1993.
89. *CRC Handbook of Chemistry and Physics*, CRC Press, 85th ed edn., 2004.
90. C. J. B. Vian, P. R. Birkin and T. G. Leighton, *J. Phys. Chem. C*, 2010, **114**, 16416-16425.
91. P. R. Birkin, T. M. Foley, J. L. Barber and H. L. Martin, *Chem. Commun.*, 2016, **52**, 11406-11409.
92. I. Smithsonian and W. E. Forsythe, *Smithsonian Physical Table. (9Th Rev. Ed.)*, 1954.
93. C. J. B. Vian, PhD thesis, University of Southampton, 2007.
94. C. Gabrielli, F. Huet, M. Keddam, P. Rousseau and V. Vivier, *J. Phys. Chem. B*, 2004, **108**, 11620-11626.
95. D. Klenerman, A. Shevchuk, P. Novak, Y. E. Korchev and S. J. Davis, *Philos. Tr. Roy. Soc. B*, 2013, **368**, 20120027.
96. D. Y. Hsieh, *J. Acoust. Soc. Am.*, 1974, **56**, 392-393.

97. E. Lamarre and W. K. Melville, *IEEE J. Oceanic Eng.*, 1992, **17**, 204-215.
98. J. C. Maxwell, *A Treatise on Electricity and Magnetism*, Clarendon Press, 1873, vol. 1, ch. IX, Article 314.
99. P. R. Birkin, T. M. Foley, T. T. Truscott, A. Merritt and S. Martini, *Phys. Chem. Chem. Phys.*, 2017, **19**, 6785-6791.
100. R. B. McCleskey, *J. Chem. Eng. Data*, 2011, **56**, 317-327.

Chapter 9 Appendices

9.1 Appendix 1: Solutions to Bessel functions

Figure 9.1 shows the 0th, 1st and 2nd order Bessel functions (m = 0, 1, 2 respectively). The crossing points of these functions with the x axis are the values of j_{mn} used in the sound model described in Chapter 1.6.

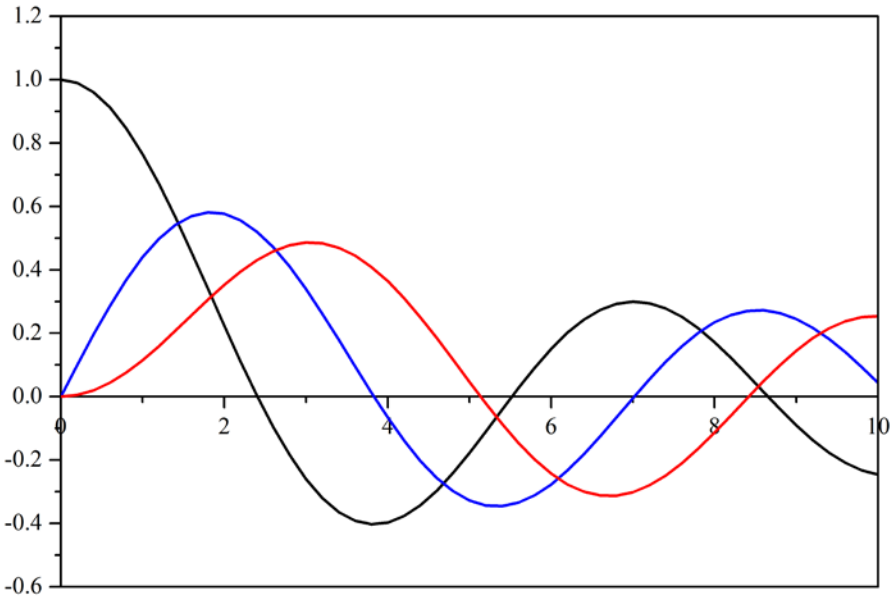

Figure 9.1 A graph of the 0th (—), 1st (—), and second order (—) Bessel functions

Table 9.1 gives the values of these crossing points (j_{mn}) for each value of m and n.

m \ n	1	2	3
0	2.40	5.52	8.65
1	3.83	7.02	10.17
2	5.14	8.42	11.62

Table 9.1 A table of j_{mn} values taken from the 0th, 1st and 2nd order Bessel functions.

9.2 Appendix 2: SEM image of Square Recessed electrode

The image shown below (figure 9.2) of a square recessed Ag electrode was taken using a scanning electron microscope (SEM).

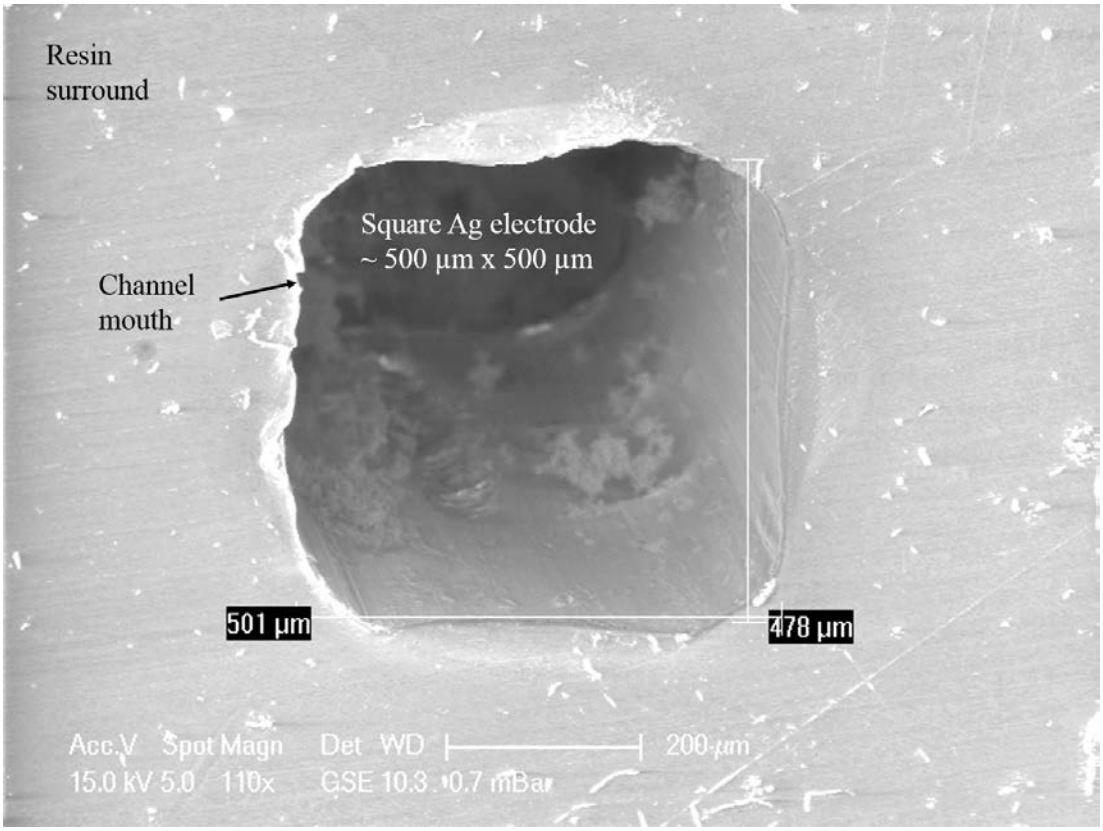

Figure 9.2 An SEM image of a recessed square Ag electrode. The etched channel has a depth of 1100 µm.

The recessed electrode was made by embedding a square Ag wire in epoxy resin (see Table 2.1 for further information) and then electrochemically etching the silver to form a channel. This SEM images shows that this wire has rounded corners rather than being perfectly square. The measurements of the channel mouth show that the channel has dimensions of approximately 500 µm x 500 µm.

9.3 Appendix 3: Circuit diagram for demodulator

Figure 9.3 is a circuit diagram of the electrical setup which allows us to monitor the AC current response to an AC potential perturbation and 'rectify' this current response to report a demodulated current signal.

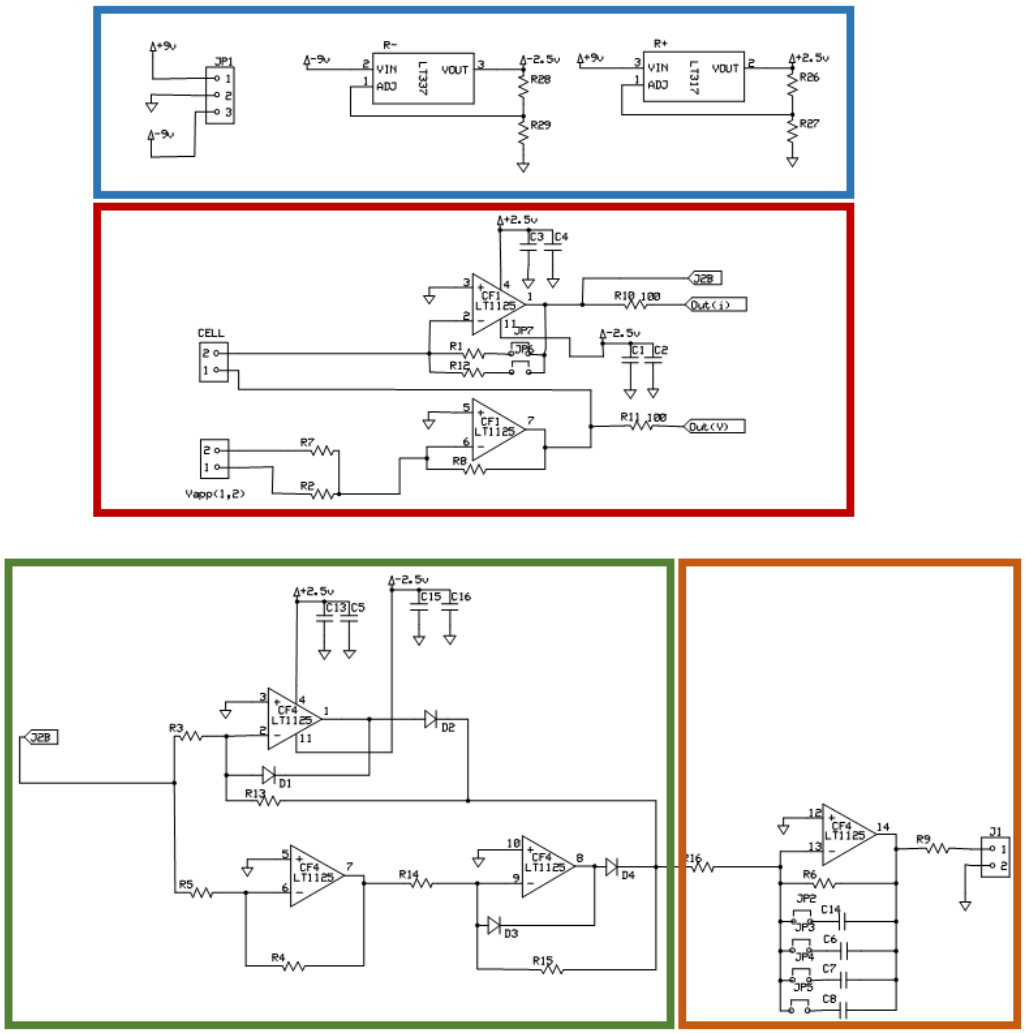

Figure 9.3 Schematic showing the power supply (—), adder and high-speed current follower (—), demodulator (—, —) incorporating a low pass filter (—) with a jumper selectable RC time constant. Note this system used two ADA4891 quad op-amp chips. The demodulator uses two 'precision rectifiers' to generate full wave rectification of the 1 MHz applied AC current signal.

This circuit setup was devised in collaboration with Dr Peter Birkin.

9.4 Appendix 4: Propagation of errors for Impedance data

For some general function, $y = f(x, z,\ldots)$, the standard deviation, s_y, is equal to

$$s_y = \sqrt{\text{variance}} = \left[\left\{\left(\frac{\partial y}{\partial x}\right)\partial x\right\}^2 + \left\{\left(\frac{\partial y}{\partial z}\right)\partial z\right\}^2 + \ldots\right]^{1/2}$$

Consider for impedance calculations using RC circuit as model equivalent circuit

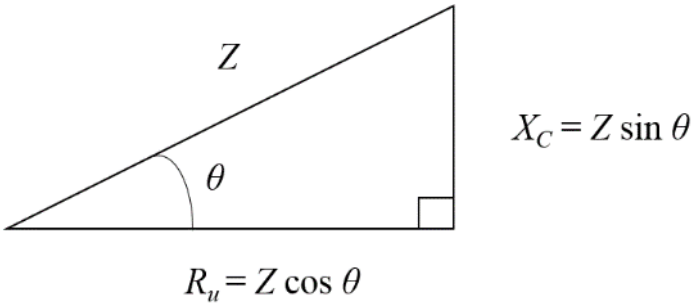

Figure 9.4 Showing the relation between the cell impedance, *Z*, and phase shift, θ, to the uncompensated resistance, R_u, and capacitive resistance, $X_C = 1/\omega C$, where ω is the angular frequency of the applied AC perturbation and C the electrode capacitance.

Standard deviation for X_C:

$$s_{X_C} = \left[\left\{\left(\frac{\partial X_C}{\partial Z}\right)\partial Z\right\}^2 + \left\{\left(\frac{\partial X_C}{\partial \theta}\right)\partial \theta\right\}^2\right]^{1/2}$$

Standard deviation for R_u:

$$s_{R_u} = \left[\left\{\left(\frac{\partial R_u}{\partial Z}\right)\partial Z\right\}^2 + \left\{\left(\frac{\partial R_u}{\partial \theta}\right)\partial \theta\right\}^2\right]^{1/2}$$

Differentials:

$$\frac{\partial X_C}{\partial Z} = \sin\theta \qquad \frac{\partial X_C}{\partial \theta} = Z\cos\theta \qquad \frac{\partial R_u}{\partial Z} = \cos\theta \qquad \frac{\partial R_u}{\partial \theta} = -Z\sin\theta$$

Therefore

$$s_{X_C} = [\{\sin\theta\ .\partial Z\}^2 + \{Z\cos\theta . \partial\theta\}^2]^{1/2}$$

and

$$s_{R_u} = [\{\cos\theta \,.\partial Z\}^2 + \{Z \sin\theta \,.\partial\theta\}^2]^{1/2}$$

So if $Z = 800 \pm 10\ \Omega$ and $\theta = 20° \pm 5°$ as typical values measured *in situ* (note equation requires angle in radians to work correctly) $\theta = 0.349 \pm 0.087$ radians)

$$s_{X_C} = [\{0.342 \times 10\}^2 + \{800 \times 0.940 \times 0.087\}^2]^{1/2}$$

$$s_{X_C} = 65.5\ \Omega$$

$$s_{R_u} = [\{0.940 \times 10\}^2 + \{800 \times 0.342 \times 0.087\}^2]^{1/2}$$

$$s_{R_u} = 25.7\ \Omega$$

Keeping $Z = 800 \pm 10\ \Omega$ and varying $\theta = 5° \pm 5°$ to $90° \pm 5°$

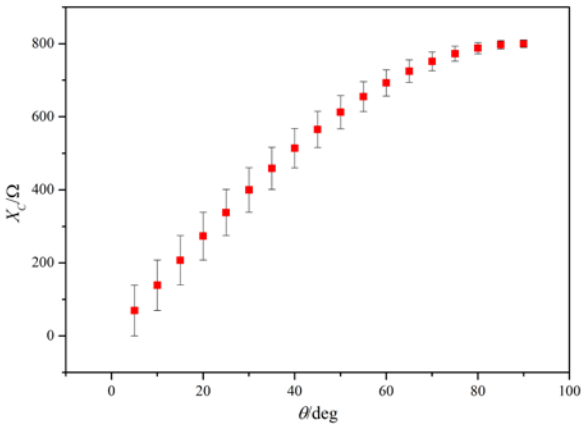

Figure 9.5 A plot of capacitive resistance, X_C (■), as a function of phase angle, θ, for a constant impedance, Z = 800 ± 10 Ω. The error in each θ was ± 5°.

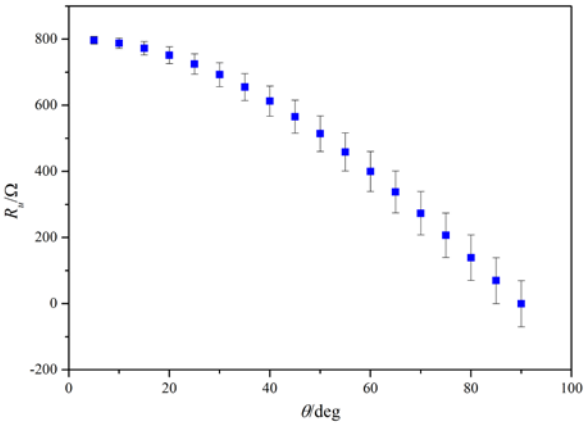

Figure 9.6 A plot of capacitive resistance, R_u (■), as a function of phase angle, θ, for a constant impedance, Z = 800 ± 10 Ω. The error in each θ was ± 5°.

Capacitance depends reciprocally on X_C:

$$C = \frac{1}{\omega X_C}$$

So standard deviation is

$$s_C = \frac{\partial C}{\partial X_C} \partial X_C$$

So

$$s_C = \left[\frac{1}{\omega {X_C}^2}\right] \partial X_C$$

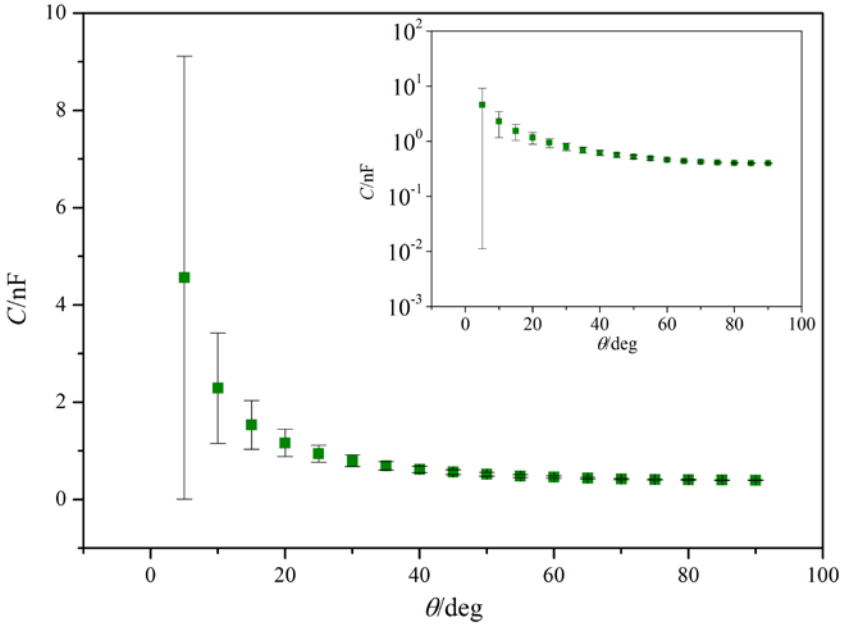

Figure 9.7 A plot of capacitance, C (■), as a function of phase angle, θ, for a constant impedance, $Z = 800 \pm 10\ \Omega$. The error in each θ was ± 5°.

9.5 Appendix 5: Extending the frequency range of the high-speed AC impedance technique

Owing to the high speed nature of the cavitation processes, a small time resolution was required so that a meaningful number of data points was recorded for individual 'bubble events'. In the experiments previously reported in this report an AC potential frequency of 500 kHz gave a time resolution of 2 µs. However on average, individual 'bubble events' last only around 30 µs and so ideally a shorter time resolution would be used.

By increasing the frequency of the applied AC signal, the time resolution of the impedance data calculated was improved. Tests were therefore carried out to see how this increase frequency affected the accuracy of the data calculated. To achieve this a series of idealised dummy cell experiments were performed with sample frequencies of 0.5 MHz, 1.0 MHz and 2.5 MHz. The dummy cell consisted of a resistor and capacitor connected in series. A 470 pF capacitor was used in all tests as this was close to the capacitance calculated inside the electrochemical cell from previous experiments. A range of resistors from 820 Ω to 10 kΩ was used. The results of the resistance accuracy tests are summarised in Table 9.2.

Resistance/kΩ	Sample frequency/MHz	Time resolution/μs	Resistance recorded/kΩ	% error
0.820	0.5	2.0	0.863	5.2
	1.0	1.0	0.833	1.6
	2.5	0.4	0.725	11.6
1.0	0.5	2.0	1.037	3.7
	1.0	1.0	1.007	0.7
	2.5	0.4	0.892	10.8
5.6	0.5	2.0	5.485	2.0
	1.0	1.0	5.264	6.0
	2.5	0.4	4.280	23.6
10	0.5	2.0	9.416	5.8
	1.0	1.0	8.464	15.4
	2.5	0.4	5.307	46.9

Table 9.2 A tabulation of the resistance results from the dummy cell tests performed with sample frequencies of 0.5 MHz, 1.0 MHz and 2.5 MHz. A range of resistors was used from 820 Ω to 10 kΩ. The recorded resistance is a mean average of all the points recorded in a 100 ms fixed time window. In all experiments the same capacitor with a value of 470 pF was used.

The resistance values of 0.820 kΩ and 1.0 kΩ were chosen as these were close to the baseline resistance previously measured inside the cell. The 5.6 kΩ resistor was chosen as this was a typical height for the resistance transients recorded and 10 kΩ represented the maximum height of the resistance transients measured. These results showed that while increasing the sample frequency allowed for a short time resolution, the accuracy of the resistance calculated decreased. The loss of accuracy was more significant as the resistance in the circuit increased. Similar calculations were made for the calculated capacitance

values. A summary of the capacitance calculated in each dummy cell is tabulated in Table 9.3.

Resistor in Dummy Cell	Capacitance/ pF	Sample frequency/MHz	Time resolution /μs	Capacitance recorded/pF	% error
0.820 kΩ	470	0.5	2.0	532	13.2
0.820 kΩ	470	1.0	1.0	1170	149
0.820 kΩ	470	2.5	0.4	3.20×10^{2}	6.81×10^{1}
1.0 kΩ	470	0.5	2.0	536	14.1
1.0 kΩ	470	1.0	1.0	1237	163
1.0 kΩ	470	2.5	0.4	1.44×10^{2}	6.93×10^{1}
5.6 kΩ	470	0.5	2.0	341	27.4
5.6 kΩ	470	1.0	1.0	187	60.2
5.6 kΩ	470	2.5	0.4	74.8	84.1
10 kΩ	470	0.5	2.0	148	68.4
10 kΩ	470	1.0	1.0	56.6	88.0
10 kΩ	470	2.5	0.4	22.0	95.3

Table 9.3 A tabulation of the capacitance results from the dummy cell tests performed with sample frequencies of 0.5 MHz, 1.0 MHz and 2.5 MHz. A range of resistors was used from 820 Ω to 10 kΩ. The recorded resistance is a mean average of all the points recorded in a 100 ms fixed time window. In all experiments the same capacitor with a value of 470 pF was used.

The capacitance values calculated from the high-speed AC impedance technique are less accurate than the calculated resistance values for all sample frequencies. This is particularly noticeable at sample frequencies of 1.0 MHz and 2.5 MHz, where the capacitance cannot be calculate with any accuracy.

9.6 Appendix 6: COMSOL Simulation

A COMSOL simulation was performed to model the change in impedance (Z) with the depth of the channel containing a square recessed working electrode. Figure 9.8 shows how the measured impedance increases with increasing recess depth. The non-zero value of impedance at 0 mm depth is a pseudo-hemispherical resistance contribution. The additional channel resistance is due to the channel.

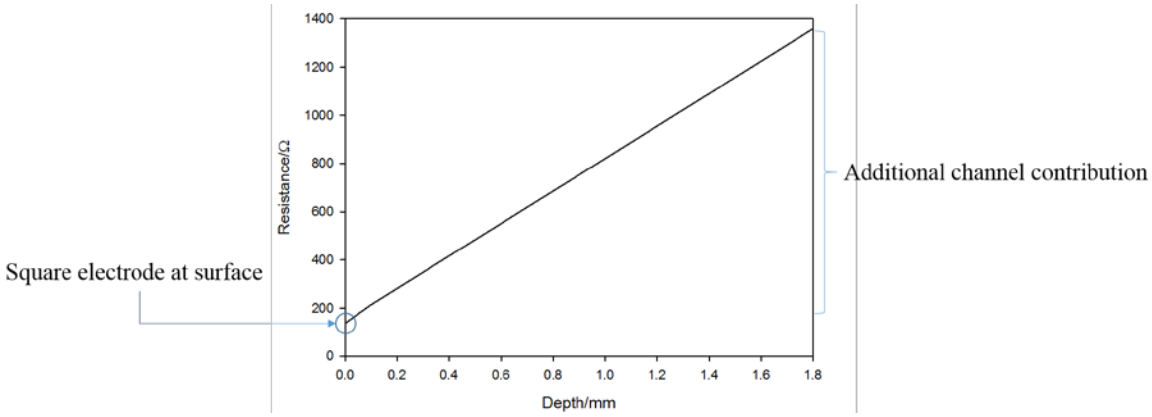

Figure 9.8 The modelled resistance for a square electrode (500 µm x 500 µm) contained within a recess as a function of the recess depth. The conductivity of the solution was 59.4 mS cm^{-1}.

Figure 9.9 shows the same information as Figure 9.8 plotted at various solution conductivities, showing that the impedance decreased as the solution conductivity (κ) increased.

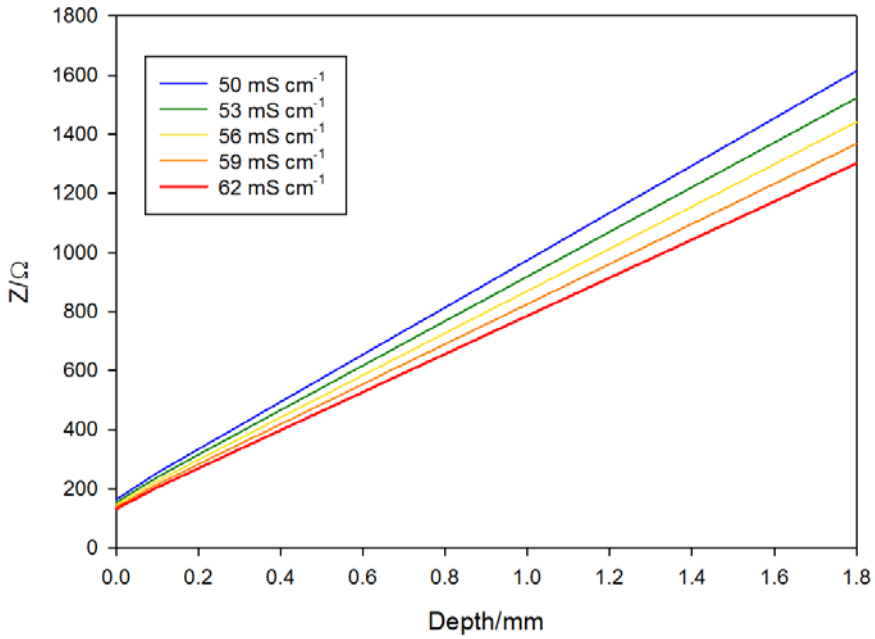

Figure 9.9 The impedance (Z) of a recessed square electrode (500 µm x 500 µm) with recess depth. Solution conductivities of 50, 53, 56, 59 and 62 mS cm^{-1} were used for these simulation results (see key on plot).

The values for impedance at a depth of 0 mm (non-recessed electrode) were then plotted against $1/\kappa$ to produce a linear plot. From this linear plot an equation describing how the magnitude of the pseudo-hemispherical impedance contribution varied with conductivity. This is shown in Figure 9.10.

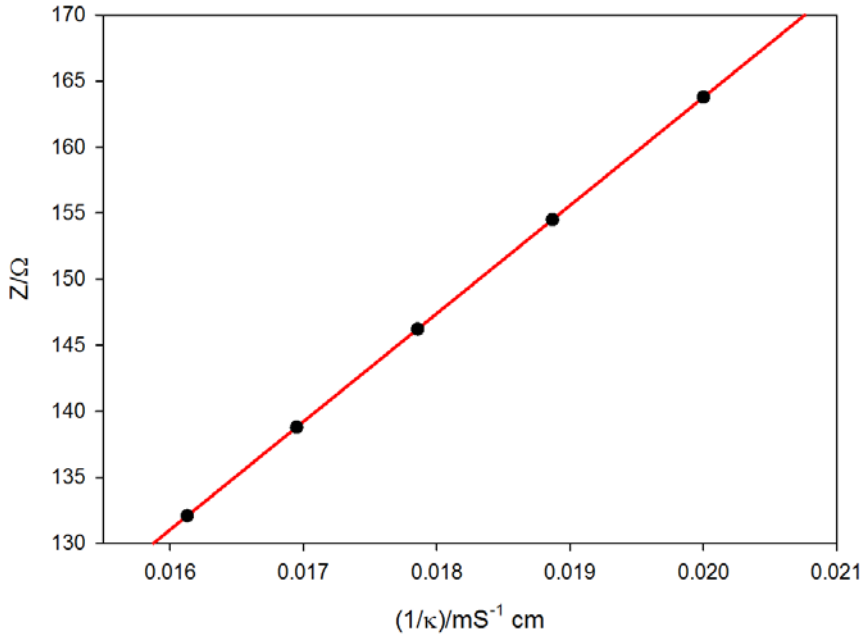

Figure 9.10 A plot of impedance (Z) as a function of $1/\kappa$ for a non-recessed square electrode (500 µm x 500 µm).

The gradient of the trendline (—) shown in figure 9.7 is 8188.7147. Therefore the pseudo-hemispherical impedance component can be described by the equation below

$$Z = \frac{8188.7147}{\kappa} \text{ mS cm}^{-1}$$

9.7 Appendix 7: Measuring channel resistance as a function of temperature to calculate channel length

Table 9.4 shows a series of resistance measurements recorded for a square silver electrode (500 µm x 500 µm) inside a square channel measured against a large stainless steel reference/counter electrode. The resistances were recorded in 0.5 M Na_2SO_4 and the temperature of the solution was controlled by carrying out the experiments in a water jacketed cell.

Temperature/°C	**Conductivity, κ /mS cm^{-1}**	**Electrochemical cell impedance, Z/Ω**	**R_h/Ω**	**Channel recess depth, l/µm**
21.5	51.7	628	158	610
21.5	51.7	628	158	610
22.1	52.4	616	156	600
24	54.7	592	150	600
24.3	55	589	149	610
26.1	57.1	576	143	620
27	58.2	570	141	620
28.1	59.5	546	138	610
28.2	59.6	545	137	610
30.3	62.1	531	132	620
30.5	62.3	525	131	610
		Average		**610**
		95 % Confidence Level		**4.6**

Table 9.4 A table showing how the channel length of a 610 ± 4.6 µm channel was calculated from the measured cell impedance. Measurements were made from 21.5 °C to 30.5 °C in 0.5 M Na_2SO_4. The solution conductivity values and R_h contribution were calculated based on the temperature of the solution.

The calculated lengths at different solution conductivities were then averaged giving an average channel length of 610 ± 4.6 µm. The conductivity values as a function of temperature used here were calculated using a polynomial relationship derived from conductivity values given by McCleskey.[100]

This approach was also applied to other etched channels of different lengths. Tables 9.5 and 9.6 show this same approach used for channel of depth 1100 µm and 2100 µm respectively. As expected the measured resistance of the electrochemical cell increases with the depth of the channel.

Temperature/°C	Conductivity, κ /mS cm^{-1}	Electrochemical cell impedance, Z/Ω	R_h/Ω	Channel recess depth, l/μm
21.6	51.9	977	158	1060
21.6	51.9	978	158	1060
22.1	52.4	970	156	1070
22.4	52.8	965	155	1070
24.7	55.5	924	148	1080
24.9	55.7	920	147	1080
26.4	57.5	895	142	1080
26.4	57.5	895	142	1080
28.4	59.8	865	137	1090
28.4	59.8	865	137	1090
30.0	61.7	842	133	1090
30.0	61.7	843	133	1100
		Average		**1080**
		95 % Confidence Level		**7.3**

Table 9.5 A table showing how the channel length of a 1080 ± 7.3 μm channel was calculated from the measured cell impedance. Measurements were made from 21.6 °C to 30.0 °C in 0.5 M Na_2SO_4. The solution conductivity values and R_h contribution were calculated based on the temperature of the solution.

Temperature/°C	Conductivity, κ /mS cm^{-1}	Electrochemical cell impedance, Z/Ω	R_h/Ω	Channel recess depth, l/μm
21.8	52.1	1820	157	2160
22.0	52.3	1810	157	2160
24.5	55.2	1680	148	2110
24.6	55.4	1680	148	2120
26.3	57.4	1620	143	2120
26.3	57.4	1620	143	2120
28.2	59.6	1550	137	2110
28.4	59.8	1560	137	2120
29.7	61.4	1550	133	2170
29.7	61.4	1550	133	2170
		Average		**2140**
		95 % Confidence Level		**18**

Table 9.6 A table showing how the channel length of a 2140 ± 18 μm channel was calculated from the measured cell impedance. Measurements were made from 21.8 °C to 29.7 °C in 0.5 M Na_2SO_4. The solution conductivity values and R_{hemi} contribution were calculated based on the temperature of the solution.

The information presented in Tables 9.4 – 9.6 was also used to produce plots of the resistance change as a function of solution conductivity.

9.8 Appendix 8: Calculating the channel void fraction from the change in conductivity

The overall uncompensated resistance (R_u) for the recessed electrode will be a combination of the resistance of the channel and the semicircular resistance at the channel mouth due to the local electrochemical environment (Figure 9.11).

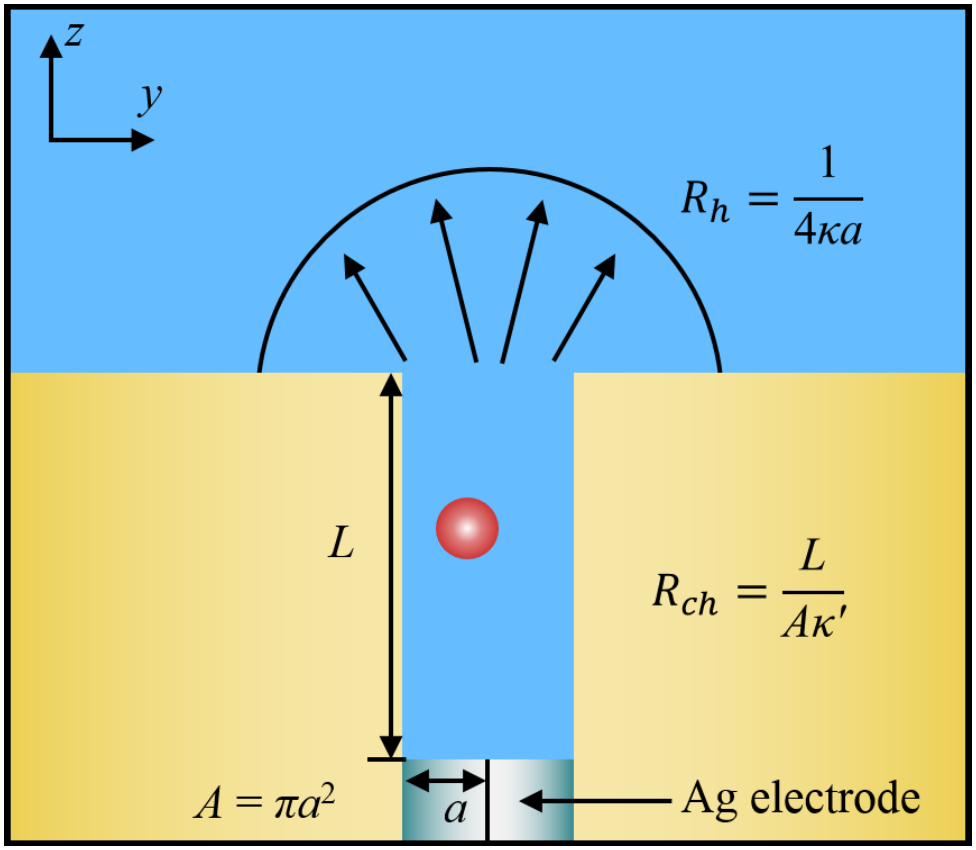

Figure 9.11 A schematic showing the channel resistance (R_{ch}) and hemispherical resistance (R_h) components which make up the overall uncompensated resistance measured.

The presence of a bubble/bubbles inside the channel will effectively change the conductivity inside the pore, therefore the uncompensated, R_u, can be expressed by the equation below

$$R_u = \frac{1}{4\kappa a} + \frac{L}{A\kappa'}$$

Expressing this in terms of κ':

$$\kappa' = \frac{L}{\left(R_u - \frac{1}{4\kappa a}\right)A}$$

Maxwell derived an expression for the effective conductivity, κ', of a homogenous suspension of spheres of conductivity κ_1 in a solution of conductivity κ_2[98]:

$$\kappa' = \frac{\kappa_1 + 2\kappa_2 + 2\alpha(\kappa_1 - \kappa_2)}{\kappa_1 + 2\kappa_2 - \alpha(\kappa_1 - \kappa_2)}\kappa_2$$

where α is the void fraction (volume occupied by the spheres). As the conductivity of air bubbles is much smaller than the conductivity of the electrolyte this expression can be simplified to[97]:

$$\kappa' = \frac{1 - \alpha}{1 + \alpha/2}\kappa$$

where κ is the conductivity of the electrolyte. Therefore for our system

$$\frac{1 - \alpha}{1 + \alpha/2}\kappa = \frac{L}{\left(R_u - \frac{1}{4\kappa a}\right)A}$$

And

$$\alpha = \frac{2(1 - \kappa')}{\kappa' + 2}$$

9.9 Appendix 9: Visual Basic programs

9.9.1 AC impedance

The main purpose of this program was to capture data and calculate the resistance and capacitance of the electrode using a fast Fourier transform. The FFT data is displayed in a separate form. The peak finder program, the program which runs when the ‘Peak finder’ button is clicked counts the number of events based on the number of resistance peaks and displays then in the box in the bottom left corner. A histogram of event distribution is also displayed on a third form. All graph data has a save routine on the main form.

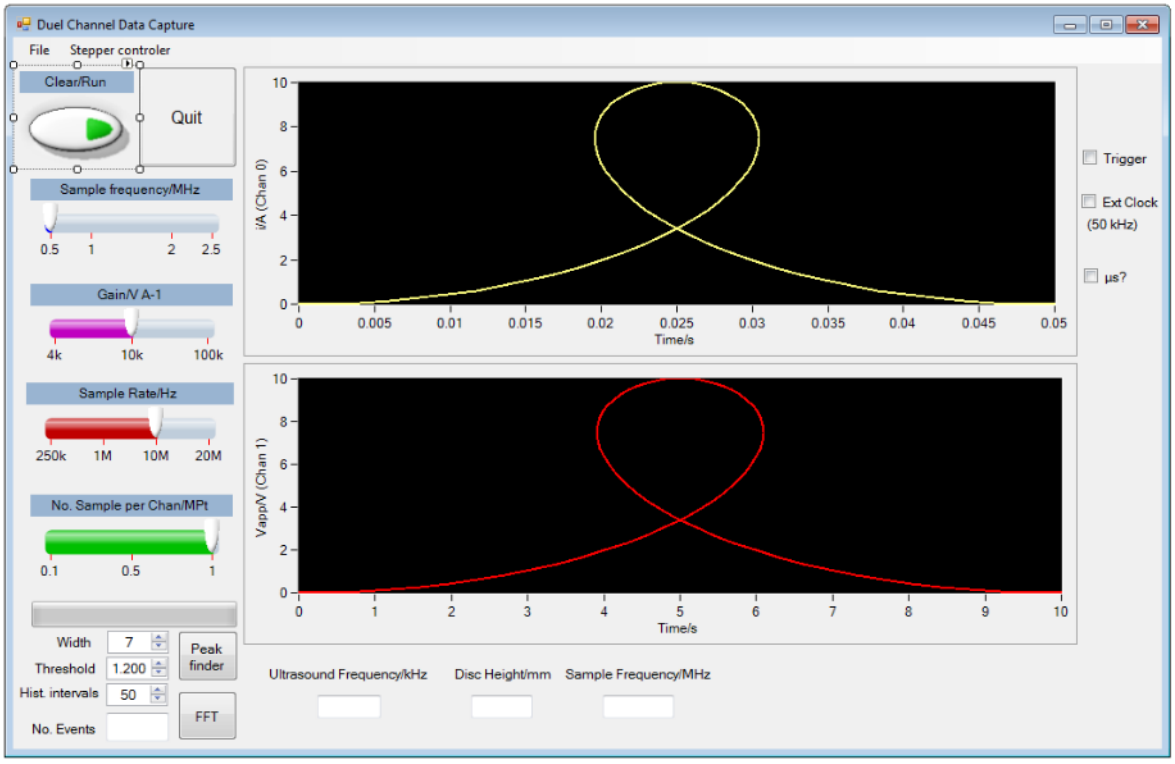

Figure 9.13 Main form, ULAI04, with raw data capture and FFT processing.

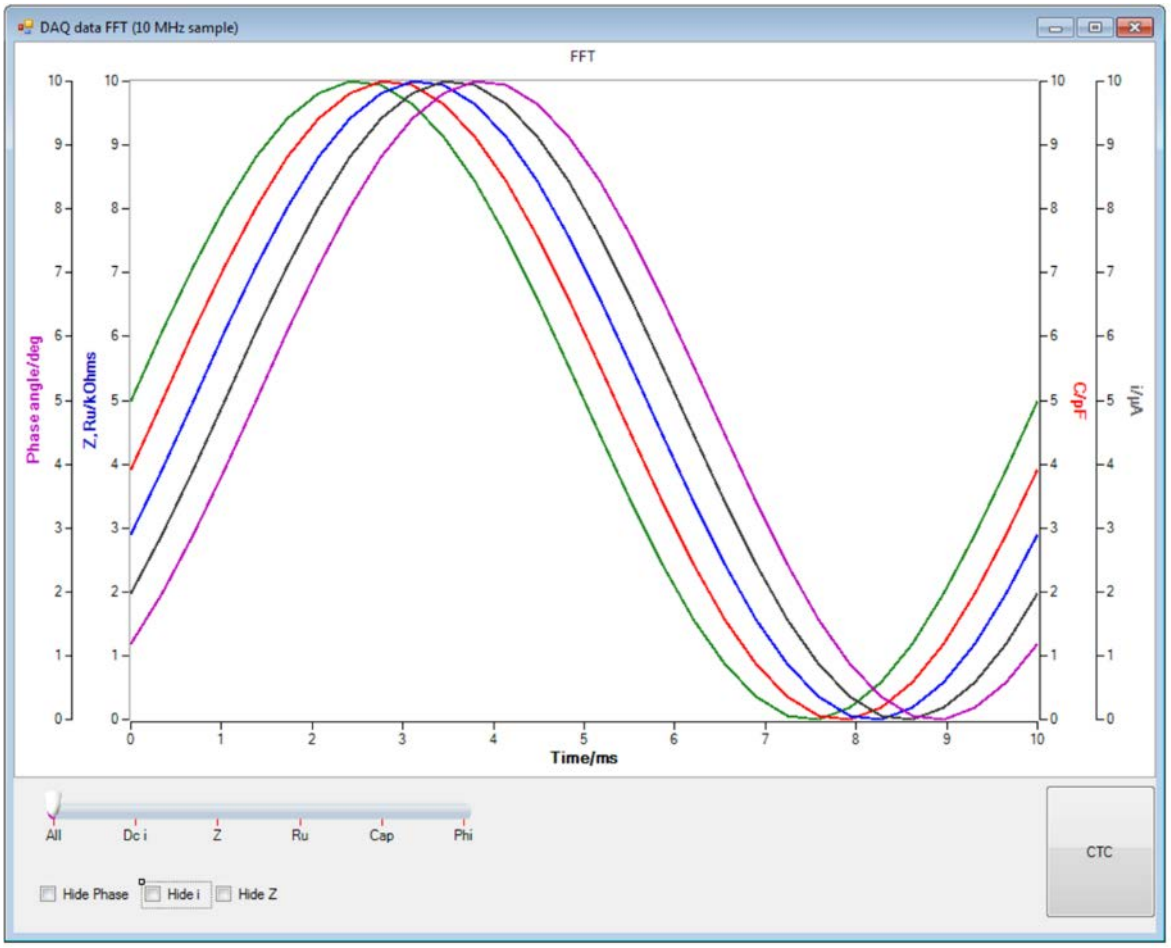

Figure 9.14 Form 1 displaying the results of the fast Fourier transform.

The code for this program is given below. This code was written in collaboration with Dr Peter Birkin.

```
File:                   ULAI04.VB - adapted PRB May 2015
' Library Call Demonstrated:    Mccdaq.MccBoard.AInScan() with Mccdaq.MccBoard.AConvertData()
' Purpose:                  Demonstrates the conversion of data values after they have been collected.
' Demonstration:            Collects data points from up to 8 analog inputs.
'                       Data points are collected as raw data values and
'                       (for devices that store channel tags) are converted
'                       from 16-bit composite data to channel numbers and
'                       12-bit data values using Mccdaq.MccBoard.AConvertData.
' Other Library Calls:        Mccdaq.MccBoard.GetStatus()
'                       Mccdaq.MccBoard.StopBackground()
'                       Mccdaq.MccBoard.ErrHandling()
' Special Requirements:       Analog signals on up to eight input channels.
'==========================================================================
Option Strict Off
Option Explicit On
'get this for the FFT, not sure really necessary?
Imports NationalInstruments.Analysis.SpectralMeasurements
'for file
Imports System.IO
Imports NationalInstruments.Analysis.Monitoring
Imports NationalInstruments.Analysis.Math
```

```
Public Class frmDataDisplay
    Inherits System.Windows.Forms.Form
    ' Create a new MccBoard object for Board 0
    Private DaqBoard As MccDaq.MccBoard = New MccDaq.MccBoard(1)
    Private Range As MccDaq.Range
    Private ADResolution, NumAIChans As Integer
    Private HighChan, LowChan, MaxChan As Integer
    Const NumPoints As Integer = 2000000  ' Number of data points to collect set to 20M for total to try
    Const FirstPoint As Integer = 0     ' set first element in buffer to transfer to array
    Dim ADData() As UInt16              ' dimension an array to hold the input values
    Dim datal As Integer
    Dim i As Integer
    Dim am(2499) As Double
    Dim ULStat As MccDaq.ErrorInfo
    Dim Options As MccDaq.ScanOptions
    Dim Rate As Integer
    Dim Count As Integer
    Dim unWrap As Boolean
    Dim p(2499) As Double
    Dim eng() As Double
    Dim eng_V() As Double
    Dim indd() As Object
    Dim engsingle() As Single
    'plotting slightly different - define an x sale
    Dim xscale() As Double
    Dim f As Double
    Dim sampr As Double
    Dim d, w, il As Integer
    'Dim lins As String
    Dim v() As Double
    Dim idaq() As Double
    Dim ip() As Double
    ' Dim sampr As Double
    Dim lc As Integer
    Dim z() As Double
    Dim timeplot() As Double
    Dim phi() As Double
    Dim ru() As Double
    Dim cap() As Double
    Dim izero() As Double
    Dim pha() As Double
    Dim ami(9) As Double
    Dim pi(9) As Double
    Dim amv(9) As Double
    Dim pv(9) As Double
    Dim samplerate As Double
    Dim histint() As Double
    Dim hisval() As Double
    Dim ph As Integer
    Dim hisl As Integer = 1
    Dim wind As Integer
    Private Sub InitUL()
        Dim ULStat As MccDaq.ErrorInfo
        ' declare revision level of Universal Library
        ULStat = MccDaq.MccService.DeclareRevision(MccDaq.MccService.CurrentRevNum)
        ' Initiate error handling
        '  activating error handling will trap errors like
        '  bad channel numbers and non-configured conditions.
        '  Parameters:
        '    MccDaq.ErrorReporting.PrintAll :all warnings and errors encountered will be printed
```

```
        '    MccDaq.ErrorHandling.StopAll   :if any error is encountered, the program will stop
        ReportError = MccDaq.ErrorReporting.PrintAll
        HandleError = MccDaq.ErrorHandling.StopAll
        ULStat = MccDaq.MccService.ErrHandling(ReportError, HandleError)
        If ULStat.Value <> MccDaq.ErrorInfo.ErrorCode.NoErrors Then
           Stop
        End If
    End Sub
#End Region
    Private Sub Switch1_StateChanged(ByVal sender As System.Object, ByVal e As
NationalInstruments.UI.ActionEventArgs) Handles Switch1.StateChanged
        'this is the main capture and fft section
        Dim gain As Integer
        Dim points As Integer
        Application.DoEvents()
        If Slide1.Value = 0 Then gain = 4000
        If Slide1.Value = 1 Then gain = 10000
        If Slide1.Value = 2 Then gain = 100000
        If Slide2.Value = 1 Then Rate = 250000
        If Slide2.Value = 2 Then Rate = 1000000
        If Slide2.Value = 3 Then Rate = 10000000
        If Slide2.Value = 4 Then Rate = 20000000
        If Slide3.Value = 0 Then points = 199999
        If Slide3.Value = 1 Then points = 999999
        If Slide3.Value = 2 Then points = 1999999
        datal = ((points + 1) / 2) - 1
        wind = (5 / Slide4.Value) * 4 'selects correct window size
        ReDim v(datal)
        ReDim idaq(datal)
        ReDim ip(datal)
        ReDim z((datal / wind) - 2)
        ReDim timeplot((datal / wind) - 2)
        ReDim phi((datal / wind) - 2)
        ReDim ru((datal / wind) - 2)
        ReDim cap((datal / wind) - 2)
        ReDim izero((datal / wind) - 2)
        ReDim pha((datal / wind) - 2)
        ReDim eng(datal)
        ReDim eng_V(datal)
        ReDim engsingle(points)
        'plotting slightly different - define an x sale
        ReDim xscale(datal)
        If Switch1.Value = False Then
           ProgressBar1.Value = 0
           ScatterGraph1.ClearData()
           ScatterGraph2.ClearData()
           Form1.WaveformGraph3.Plots(1).ClearData()
           Form1.WaveformGraph3.Plots(2).ClearData()
           Form1.WaveformGraph3.Plots(3).ClearData()
           Form1.WaveformGraph3.Plots(4).ClearData()
           Form1.WaveformGraph3.Plots(0).ClearData()
        Else
        End If
        LowChan = 0
        HighChan = 1
        If Switch1.Value = True Then
           Erase am, p
           Count = points + 1          ' total number of data points to collect
           Range = MccDaq.Range.Bip5Volts
           ' per channel sampling rate ((samples per second) per channel)
```

```
        If CheckBox1.Checked = False And CheckBox2.Checked = False Then Options =
MccDaq.ScanOptions.ConvertData
        If CheckBox1.Checked = True And CheckBox2.Checked = False Then Options =
MccDaq.ScanOptions.ConvertData Or MccDaq.ScanOptions.ExtTrigger
        If CheckBox1.Checked = True And CheckBox2.Checked = True Then Options =
MccDaq.ScanOptions.ConvertData Or MccDaq.ScanOptions.ExtTrigger Or MccDaq.ScanOptions.ExtClock
        If CheckBox1.Checked = False And CheckBox2.Checked = True Then Options =
MccDaq.ScanOptions.ConvertData Or MccDaq.ScanOptions.ExtClock
        If CheckBox2.Checked = True Then Slide2.Value = 0
        Application.DoEvents()
        ' collect data, external trigger and clock enabled
        LowChan = 0
        HighChan = 1
        'next line as normal
        ULStat = DaqBoard.AInScan(LowChan, HighChan, Count, Rate, Range, MemHandle, Options)
        If ULStat.Value <> MccDaq.ErrorInfo.ErrorCode.NoErrors Then Stop
        tmrCheckStatus.Enabled = True
        'get from memory
        ULStat = MccDaq.MccService.WinBufToArray(MemHandle, ADData, FirstPoint, NumPoints)
        If ULStat.Value <> MccDaq.ErrorInfo.ErrorCode.NoErrors Then Stop
        Dim x As Integer
        If CheckBox2.Checked = True Then Rate = 50000
        x = 0
        For i = 0 To points Step 2
           ULStat = DaqBoard.ToEngUnits(Range, ADData(i), engsingle(i))
           eng(x) = (engsingle(i) / gain)  ' note array eng is double so we can then plot the data
           ULStat = DaqBoard.ToEngUnits(Range, ADData(i + 1), engsingle(i + 1))
           eng_V(x) = engsingle(i + 1)
           xscale(x) = x * (wind / 20) * (1 / Rate)
           x = x + 1
        Next i
        ScatterGraph1.PlotXY(xscale, eng)
        ScatterGraph2.PlotXY(xscale, eng_V)
        Application.DoEvents()
        '*********************************************
        'just use the other processing stuff
        '*********************************************
        lc = 0
        sampr = 1 / Rate
        For d = 0 To ((points + 1) / 2) - (wind + 1) Step wind '(2 ^ 20) - 21 Step 20
           Dim fftdi(wind - 1) As Double
           Dim fftdv(wind - 1) As Double
           For w = 0 To wind - 1
              fftdv(w) = eng_V(w + d)
           Next
           'here's the expression for the FFT - note sequence
         NationalInstruments.Analysis.SpectralMeasurements.Measurements.AmplitudePhaseSpectrum(fftdv,
unWrap:=False, dt:=sampr, amplitudeSpectrum:=amv, phaseSpectrum:=pv, df:=f)
           For il = 1 To (wind / 2) - 1
              amv(il) = (Math.Sqrt(2)) * (amv(il))
           Next il
           'take 20 points here and then analyse
           For w = 0 To wind - 1
              fftdi(w) = eng(d + w)
           Next
           'here's the expression for the FFT - note sequence
          NationalInstruments.Analysis.SpectralMeasurements.Measurements.AmplitudePhaseSpectrum(fftdi,
unWrap:=False, dt:=sampr, amplitudeSpectrum:=ami, phaseSpectrum:=pi, df:=f)
           izero(lc) = ami(0) / 0.000001
           For il = 1 To (wind / 2) - 1
```

```
            ami(il) = (Math.Sqrt(2)) * (ami(il))
        Next il
        timeplot(lc) = lc * 0.000002
        z(lc) = (amv(1) / ami(1)) * 0.001 'impedance in kOhms
        phi(lc) = pi(1) - pv(1) 'phase angle
        Dim phases, phasec, xc As Object
        phases = Math.Abs(Math.Sin((pi(1)) - (pv(1))))
        phasec = Math.Abs(Math.Cos((pi(1)) - (pv(1))))
        xc = z(lc) * phases * 1000 'capacitive term
        ru(lc) = z(lc) * phasec 'uncomp r
        cap(lc) = 1 / (2 * (22 / 7) * (1 / (wind * sampr)) * xc) / 0.000000000001 'cap in pF
        'note this just converts to an angle
        Dim arc As Double
        arc = Math.Atan(-phasec / Math.Sqrt(-phasec * phasec + 1)) + 2 * Math.Atan(1)
        pha(lc) = (arc / (22 / 14)) * 90
        lc = lc + 1
        Erase ami, pi, fftdi, amv, pv, fftdv
        ProgressBar1.Value = (d / ((points + 1) / 2)) * 100
      Next d
      Form1.Visible = True
      'plot in ms
      Form1.WaveformGraph3.Plots(0).PlotY(z, 0, ((wind / Slide4.Value) * sampr / 0.001))
      Form1.WaveformGraph3.Plots(3).PlotY(izero, 0, ((wind / Slide4.Value) * sampr / 0.001))
      Form1.WaveformGraph3.Plots(2).PlotY(ru, 0, ((wind / Slide4.Value) * sampr / 0.001))
      Form1.WaveformGraph3.Plots(1).PlotY(cap, 0, ((wind / Slide4.Value) * sampr / 0.001))
      Form1.WaveformGraph3.Plots(4).PlotY(pha, 0, ((wind / Slide4.Value) * sampr / 0.001))
    Else
    End If
  End Sub
  Private Sub MenuStrip1_ItemClicked(ByVal sender As System.Object, ByVal e As
System.Windows.Forms.ToolStripItemClickedEventArgs) Handles MenuStrip1.ItemClicked
  End Sub
  Private Sub ScatterGraph1_PlotDataChanged(ByVal sender As System.Object, ByVal e As
NationalInstruments.UI.XYPlotDataChangedEventArgs) Handles ScatterGraph1.PlotDataChanged
  End Sub
  Private Sub InstrumentControlStrip1_ItemClicked(ByVal sender As System.Object, ByVal e As
System.Windows.Forms.ToolStripItemClickedEventArgs)
  End Sub
  Private Sub CheckBox2_CheckedChanged(ByVal sender As System.Object, ByVal e As
System.EventArgs) Handles CheckBox2.CheckedChanged
    Slide2.Value = 0
  End Sub
 Private Sub Slide2_AfterChangeValue(ByVal sender As System.Object, ByVal e As
NationalInstruments.UI.AfterChangeNumericValueEventArgs) Handles Slide2.AfterChangeValue
    If Slide2.Value > 0 Then CheckBox2.Checked = False
    If Slide2.Value = 0 Then Rate = 100000
    If Slide2.Value = 1 Then Rate = 250000
    If Slide2.Value = 2 Then Rate = 1000000
    If Slide2.Value = 3 Then Rate = 10000000
  End Sub
  Private Sub Slide1_AfterChangeValue(ByVal sender As System.Object, ByVal e As
NationalInstruments.UI.AfterChangeNumericValueEventArgs) Handles Slide1.AfterChangeValue
  End Sub
  Private Sub StepperControlerToolStripMenuItem_Click(ByVal sender As System.Object, ByVal e As
System.EventArgs) Handles StepperControlerToolStripMenuItem.Click
    Form2.Visible = True
    MsgBox("Find COM port")
  End Sub
  Private Sub CheckBox3_CheckedChanged(ByVal sender As System.Object, ByVal e As
System.EventArgs) Handles CheckBox3.CheckedChanged
```

```
        If CheckBox3.Checked = True Then
            Form1.WaveformGraph3.Plots(0).PlotY(z, 0, (20 * sampr / 0.000001))
            Form1.WaveformGraph3.Plots(3).PlotY(izero, 0, (20 * sampr / 0.000001))
            Form1.WaveformGraph3.Plots(2).PlotY(ru, 0, (20 * sampr / 0.000001))
            Form1.WaveformGraph3.Plots(1).PlotY(cap, 0, (20 * sampr / 0.000001))
            Form1.WaveformGraph3.Plots(4).PlotY(pha, 0, (20 * sampr / 0.000001))
            Form1.WaveformGraph3.XAxes(0).Caption = "Time/µs"
        End If
        If CheckBox3.Checked = False Then
            Form1.WaveformGraph3.Plots(0).PlotY(z, 0, (20 * sampr / 0.001))
            Form1.WaveformGraph3.Plots(3).PlotY(izero, 0, (20 * sampr / 0.001))
            Form1.WaveformGraph3.Plots(2).PlotY(ru, 0, (20 * sampr / 0.001))
            Form1.WaveformGraph3.Plots(1).PlotY(cap, 0, (20 * sampr / 0.001))
            Form1.WaveformGraph3.Plots(4).PlotY(pha, 0, (20 * sampr / 0.001))
            Form1.WaveformGraph3.XAxes(0).Caption = "Time/ms"
        End If
        If Form1.CheckBox2.Checked = True Then Form1.WaveformGraph3.Plots(4).Visible = False
        If Form1.CheckBox2.Checked = False Then Form1.WaveformGraph3.Plots(4).Visible = True
        If Form1.CheckBox2.Checked = True Then Form1.WaveformGraph3.YAxes(3).Visible = False
        If Form1.CheckBox2.Checked = False Then Form1.WaveformGraph3.YAxes(3).Visible = True
        If Form1.CheckBox1.Checked = True Then Form1.WaveformGraph3.Plots(0).Visible = False
        If Form1.CheckBox1.Checked = False Then Form1.WaveformGraph3.Plots(0).Visible = True
    End Sub
    Private Sub FileToolStripMenuItem_Click(ByVal sender As System.Object, ByVal e As
System.EventArgs) Handles FileToolStripMenuItem.Click
    End Sub
    Private Sub OpenToolStripMenuItem_Click_1(ByVal sender As System.Object, ByVal e As
System.EventArgs) Handles OpenToolStripMenuItem.Click
        'Dim myStream As Stream
        Dim openFileDialog1 As New OpenFileDialog()
        openFileDialog1.Filter = "txt files (*.txt)|*.txt|all files (*.*)|*.*"
        openFileDialog1.FilterIndex = 1
        openFileDialog1.RestoreDirectory = True
        ReDim xscale(NumPoints), eng(NumPoints), eng_V(NumPoints)
        If openFileDialog1.ShowDialog() = DialogResult.OK Then
            Dim sw1 As StreamReader = New StreamReader(openFileDialog1.OpenFile())
            Dim indat As String
            If (sw1 IsNot Nothing) Then
                indat = sw1.ReadLine()
                i = 0
                Do While sw1.Peek() >= 0
                    indat = sw1.ReadLine()
                    Dim indd() = Split(indat, ",")
                    xscale(i) = (indd(0))
                    eng(i) = (indd(1))
                    eng_V(i) = (indd(2))
                    i = i + 1
                Loop
                sw1.Close()
            End If
        End If
        ScatterGraph1.PlotXY(xscale, eng)
        ScatterGraph2.PlotXY(xscale, eng_V)
    End Sub
    Private Sub cmdStopConvert_Click_1(ByVal sender As System.Object, ByVal e As System.EventArgs)
Handles cmdStopConvert.Click
        Dim ULStat As MccDaq.ErrorInfo
        ' Free up memory for use by other programs
        ULStat = MccDaq.MccService.WinBufFreeEx(MemHandle)
        If ULStat.Value <> MccDaq.ErrorInfo.ErrorCode.NoErrors Then Stop
```

```
        End
    End Sub
    Private Sub Button1_Click_1(ByVal sender As System.Object, ByVal e As System.EventArgs) Handles
Button1.Click
        Dim points, gain As Integer
        If Slide1.Value = 0 Then gain = 4000
        If Slide1.Value = 1 Then gain = 10000
        If Slide1.Value = 2 Then gain = 100000
        If Slide2.Value = 0 Then Rate = 100000
        If Slide2.Value = 1 Then Rate = 250000
        If Slide2.Value = 2 Then Rate = 1000000
        If Slide2.Value = 3 Then Rate = 10000000
        If Slide3.Value = 0 Then points = 199999
        If Slide3.Value = 1 Then points = 999999
        If Slide3.Value = 2 Then points = 1999999
        lc = 0
        sampr = 1 / Rate
        datal = ((points + 1) / 2) - 1
        wind = (5 / Slide4.Value) * 4
        ReDim z((datal / wind) - 2), izero((datal / wind) - 2), ru((datal / wind) - 2), cap((datal / wind) - 2),
pha((datal / wind) - 2), timeplot((datal / wind) - 2), phi((datal / wind) - 2)
        For d = 0 To ((points + 1) / 2) - (wind + 1) Step wind '(2 ^ 20) - 21 Step 20
            Dim fftdi(wind - 1) As Double
            Dim fftdv(wind - 1) As Double
            For w = 0 To wind - 1
                fftdv(w) = eng_V(w + d)
            Next
           'here's the expression for the FFT - note sequence
NationalInstruments.Analysis.SpectralMeasurements.Measurements.AmplitudePhaseSpectrum(fftdv,
unWrap:=False, dt:=sampr, amplitudeSpectrum:=amv, phaseSpectrum:=pv, df:=f)
            For il = 1 To (wind / 2) - 1
                amv(il) = (Math.Sqrt(2)) * (amv(il))
            Next il
            'take 20 points here and then analyse
            For w = 0 To wind - 1
                fftdi(w) = eng(d + w)
            Next
            'here's the expression for the FFT - note sequence
NationalInstruments.Analysis.SpectralMeasurements.Measurements.AmplitudePhaseSpectrum(fftdi,
unWrap:=False, dt:=sampr, amplitudeSpectrum:=ami, phaseSpectrum:=pi, df:=f)
            izero(lc) = ami(0) / 0.000001
            For il = 1 To (wind / 2) - 1
                ami(il) = (Math.Sqrt(2)) * (ami(il))
            Next il
            timeplot(lc) = lc * 0.000002
            z(lc) = (amv(1) / ami(1)) * 0.001 'impedance
            phi(lc) = pi(1) - pv(1) 'phase angle
            Dim phases, phasec, xc As Object
            phases = Math.Abs(Math.Sin((pi(1)) - (pv(1))))
            phasec = Math.Abs(Math.Cos((pi(1)) - (pv(1))))
            xc = z(lc) * phases * 1000 'capacitive term
            ru(lc) = z(lc) * phasec 'uncomp r
            cap(lc) = 1 / (2 * (22 / 7) * (1 / (wind * sampr)) * xc) / 0.000000000001 'cap in pF
            'note this just converts to an angle
            Dim arc As Double
            arc = Math.Atan(-phasec / Math.Sqrt(-phasec * phasec + 1)) + 2 * Math.Atan(1)
            pha(lc) = (arc / (22 / 14)) * 90
           lc = lc + 1
            Erase ami, pi, fftdi, amv, pv, fftdv
            ProgressBar1.Value = (d / ((points + 1) / 2)) * 100
```

```
        Next d
        Form1.Visible = True
        'plot in ms
        Form1.WaveformGraph3.Plots(0).PlotY(z, 0, ((wind / Slide4.Value) * sampr / 0.001))
        Form1.WaveformGraph3.Plots(3).PlotY(izero, 0, ((wind / Slide4.Value) * sampr / 0.001))
        Form1.WaveformGraph3.Plots(2).PlotY(ru, 0, ((wind / Slide4.Value) * sampr / 0.001))
        Form1.WaveformGraph3.Plots(1).PlotY(cap, 0, ((wind / Slide4.Value) * sampr / 0.001))
        Form1.WaveformGraph3.Plots(4).PlotY(pha, 0, ((wind / Slide4.Value) * sampr / 0.001))
    End Sub
    Private Sub Button6_Click_1(ByVal sender As System.Object, ByVal e As System.EventArgs) Handles
Button6.Click
        Dim amplitudes() As Double = Nothing, locations() As Double = Nothing, secondDerivatives() As
Double = Nothing
        Dim initialThreshold As Double
        Dim initialWidth As Integer
        Dim endOfData As Boolean
        Dim peakDetector As New Analysis.Monitoring.PeakDetector
        Peakplot.ScatterGraph2.Plots(0).ClearData()
        Peakplot.ScatterGraph2.Plots(1).ClearData()
        Peakplot.ScatterGraph1.ClearData()
        ' Set initial state of peakDetector
        initialThreshold = NumericUpDown2.Value
        initialWidth = NumericUpDown1.Value
        peakDetector.Reset(initialThreshold, initialWidth, PeakPolarity.Peaks)
        endOfData = True
        ' Find location of amplitude, locations and second derivates of peaks in signalIn array
        peakDetector.Detect(ru, endOfData, amplitudes, locations, secondDerivatives)
        Dim locationtime(locations.Length - 1) As Double
        Dim pl As Integer
        For pl = 0 To locations.Length - 1
            locationtime(pl) = locations(pl) * 0.000002
        Next
        TextBox1.Text = amplitudes.Length
        Peakplot.Visible = True
        Peakplot.ScatterGraph2.Plots(0).PlotXY(locationtime, amplitudes)
        Peakplot.ScatterGraph2.Plots(1).PlotXY(timeplot, ru)
        Dim centerValues(9) As Double
        Dim histogramData() As Integer
        Dim histogramBase, histogramTop As Double
        Dim histogramIntervals As Integer
        histogramIntervals = NumericUpDown3.Value
        ' Get the minimum and maximum values in the array
        histogramBase = ArrayOperation.GetMin(amplitudes)
        histogramTop = ArrayOperation.GetMax(amplitudes)
        ' Calculate histogram
        histogramData = Statistics.Histogram(amplitudes, histogramBase, histogramTop, histogramIntervals,
centerValues)
        ReDim histint(histogramData.Length - 1)
        ReDim hisval(histogramData.Length - 1)
        Dim ph As Integer
        For ph = 0 To (histogramData.Length - 1)
            histint(ph) = (((histogramTop - histogramBase) / histogramIntervals) * ph) + histogramBase
            hisval(ph) = histogramData(ph)
        Next
        hisl = histogramData.Length - 1
        Peakplot.ScatterGraph1.PlotXY(histint, hisval)
    End Sub
    Private Sub SaveToolStripMenuItem_Click_1(ByVal sender As System.Object, ByVal e As
System.EventArgs) Handles SaveToolStripMenuItem.Click
        'Dim myStream As Stream
```

```
        Dim saveFileDialog1 As New SaveFileDialog()
        saveFileDialog1.Filter = "txt files (*.txt)|*.txt|all files (*.*)|*.*"
        saveFileDialog1.FilterIndex = 1
        saveFileDialog1.RestoreDirectory = True
        If saveFileDialog1.ShowDialog() = DialogResult.OK Then
            Dim sw As StreamWriter = New StreamWriter(saveFileDialog1.OpenFile())
            If (sw IsNot Nothing) Then
                sw.WriteLine("Time/s, Amplitude/A, Voltage/V")
                For i = 0 To datal
                    sw.WriteLine(Format(i * (wind / 20) * sampr, "0.00000e-00") + "," + Format(eng(i), "0.00e-00")
+ "," + Format(eng_V(i), "0.0000"))
                Next i
                sw.Close()
            End If
        End If
    End Sub
    Private Sub SaveFFTToolStripMenuItem_Click_1(ByVal sender As System.Object, ByVal e As
System.EventArgs) Handles SaveFFTToolStripMenuItem.Click
        Dim saveFileDialog1 As New SaveFileDialog()
        saveFileDialog1.Filter = "txt files (*.txt)|*.txt|All files (*.*)|*.*"
        saveFileDialog1.FilterIndex = 1
        saveFileDialog1.RestoreDirectory = True
        If saveFileDialog1.ShowDialog() = DialogResult.OK Then
            Dim sw As StreamWriter = New StreamWriter(saveFileDialog1.OpenFile())
            If (sw IsNot Nothing) Then
                sw.WriteLine("Sample Frequency/MHz" + "," + TextBox4.Text)
                sw.WriteLine("Ultrasound Frequency/kHz" + "," + TextBox2.Text)
                sw.WriteLine("Disc Height/mm" + "," + TextBox3.Text)
                sw.WriteLine("Time/ms, Ru/kOhms, Cap/pF, phase/deg, i/µA")
                For Me.lc = 0 To ((datal - 41) / 20)
                    sw.WriteLine(Format(lc * wind * sampr * 1000, "0.0000e-00") + "," + Format(ru(lc), "0.0000")
+ "," + Format(cap(lc), "0.0") + "," + Format(pha(lc), "0.0") + "," + Format(izero(lc), "0.0000"))
                Next lc
                sw.Close()
            End If
        End If
    End Sub
    Private Sub SaveHistogramToolStripMenuItem_Click_1(ByVal sender As System.Object, ByVal e As
System.EventArgs) Handles SaveHistogramToolStripMenuItem.Click
        Dim saveFileDialog1 As New SaveFileDialog()
        saveFileDialog1.Filter = "txt files (*.txt)|*.txt|All files (*.*)|*.*"
        saveFileDialog1.FilterIndex = 1
        saveFileDialog1.RestoreDirectory = True
        If saveFileDialog1.ShowDialog() = DialogResult.OK Then
            Dim sw As StreamWriter = New StreamWriter(saveFileDialog1.OpenFile())
            If (sw IsNot Nothing) Then
                sw.WriteLine("Resistance/Ohms, No. of events")
                For Me.ph = 0 To hisl
                    sw.WriteLine(Format(histint(ph), "0.000") + "," + Format(hisval(ph), "0.0"))
                Next
                sw.Close()
            End If
        End If
    End Sub
    Private Sub SaveEventNumberToolStripMenuItem_Click_1(ByVal sender As System.Object, ByVal e As
System.EventArgs) Handles SaveEventNumberToolStripMenuItem.Click
        SaveFileDialog1.Filter = "txt files (*.txt)|*.txt|All files (*.*)|*.*"
        SaveFileDialog1.FilterIndex = 1
        SaveFileDialog1.RestoreDirectory = True
        If SaveFileDialog1.ShowDialog() = DialogResult.OK Then
```

```
        Dim sw As StreamWriter = New StreamWriter(SaveFileDialog1.OpenFile())
        If (sw IsNot Nothing) Then
            sw.WriteLine("Number of events")
            For Me.ph = 0 To hisl
                sw.WriteLine((TextBox1.Text), "0")
            Next
            sw.Close()
        End If
    End If
  End Sub
  Private Sub Slide4_AfterChangeValue(ByVal sender As System.Object, ByVal e As
NationalInstruments.UI.AfterChangeNumericValueEventArgs) Handles Slide4.AfterChangeValue
    TextBox4.Text = Slide4.Value / 2
  End Sub
End Class
```

9.9.2 Demodulator

The purpose of this program was to capture the current (demodulated by the circuitry described in Appendix 2) and then process this data to report the impedance. Figure 9.15 shows the user interface for this program.

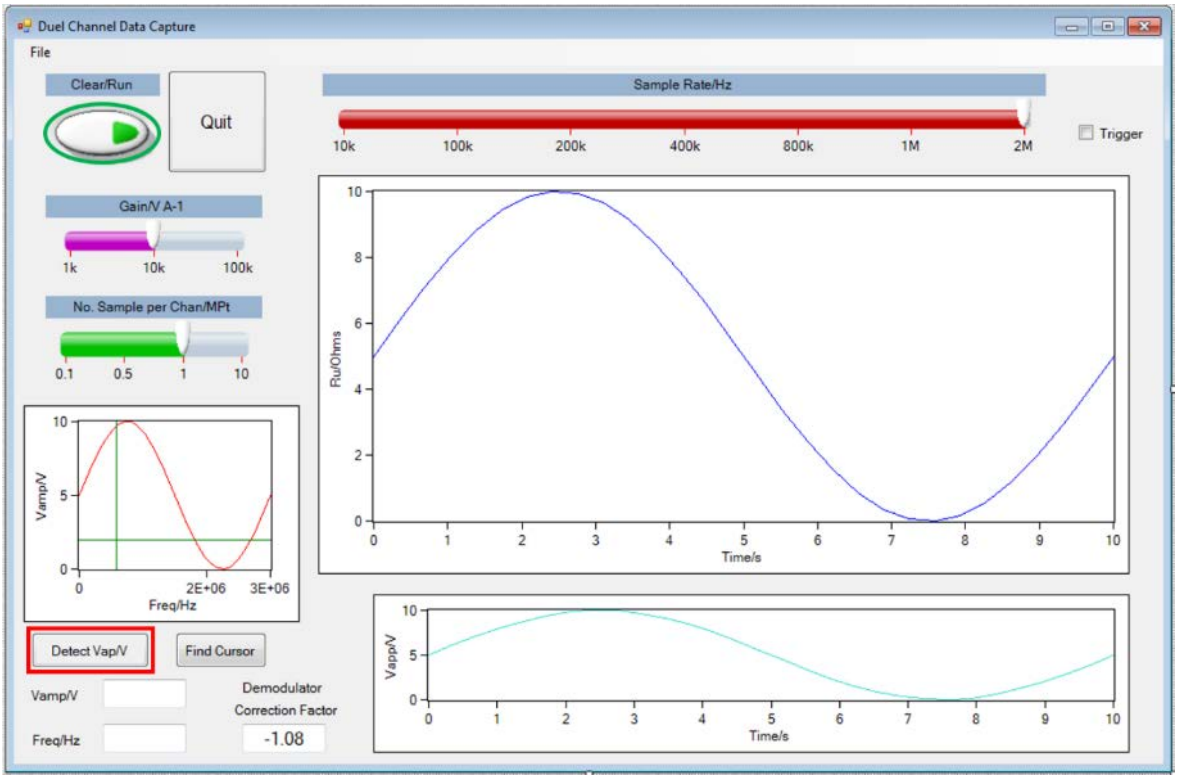

Figure 9.15 Form for data capture and processing of demodulated current to report and save impedance.

The ‘Detect Vap/V’ button (highlighted by the red box) took a short data capture of the applied AC potential and reported the magnitude of the applied signal. The reported value of AC potential was then used as a constant to convert the demodulated current captured in

the main capture routine (highlighted by green circle, Figure 9.15) to impedance. This data is displayed in the central graph with labelled *x* and *y* axes ‘Time/s’ and ‘Ru/Ohms’.

The code for this program is given below. This code was written in collaboration with Dr Peter Birkin.

```
'====================================================================================
' File:                    ULAI04.VB - adapted HLM March 2017
' Library Call Demonstrated:    Mccdaq.MccBoard.AInScan() with Mccdaq.MccBoard.AConvertData()
' Purpose:                  Demonstrates the conversion of data values
'                       after they have been collected.
' Demonstration:              Collects data points from up to 8 analog inputs.
'                       Data points are collected as raw data values and
'                       (for devices that store channel tags) are converted
'                       from 16-bit composite data to channel numbers and
'                       12-bit data values using Mccdaq.MccBoard.AConvertData.
' Other Library Calls:         Mccdaq.MccBoard.GetStatus()
'                       Mccdaq.MccBoard.StopBackground()
'                       Mccdaq.MccBoard.ErrHandling()
' Special Requirements:        Analog signals on up to eight input channels.
'====================================================================================
Option Strict Off
Option Explicit On
'get this for the FFT, not sure really necessary?
Imports NationalInstruments.Analysis.SpectralMeasurements
'for file
Imports System.IO
Imports NationalInstruments.Analysis.Monitoring
Imports NationalInstruments.Analysis.Math
Public Class frmDataDisplay
    Inherits System.Windows.Forms.Form
    ' Create a new MccBoard object for Board 0
    Private DaqBoard As MccDaq.MccBoard = New MccDaq.MccBoard(1)
    Private Range As MccDaq.Range
    Private ADResolution, NumAIChans As Integer
    Private HighChan, LowChan, MaxChan As Integer
    Const NumPoints As Integer = 10000000  ' Number of data points to collect set to 20M for total to try
    Const FirstPoint As Integer = 0     ' set first element in buffer to transfer to array
    Dim ADData() As UInt16              ' dimension an array to hold the input values
    Dim datal As Integer
    Dim i As Integer
    Dim am(2499) As Double
    Dim ULStat As MccDaq.ErrorInfo
    Dim Options As MccDaq.ScanOptions
    Dim Rate As Integer
    Dim gain As Integer
    Dim points As Integer
    Dim Count As Integer
    Dim unWrap As Boolean
    Dim p(2499) As Double
    Dim eng() As Double
    Dim eng_V() As Double
    Dim indd() As Object
    Dim amv() As Double
    Dim pv() As Double
    Dim xscale() As Double
    Dim engsingle() As Single
```

```
    'plotting slightly different - define an x sale
    Dim f As Double
    Dim sampr As Double
    Dim d, il, w As Integer
    'Dim lins As String
    Dim v() As Double
    Dim idaq() As Double
    Dim ip() As Double
    ' Dim sampr As Double
    Dim lc As Integer
    Dim samplerate As Double
    Dim ph As Integer
    Dim wind As Integer
#Region "Universal Library Initialization - Expand this region to change error handling, etc."
    Private Sub InitUL()
        Dim ULStat As MccDaq.ErrorInfo
        ' declare revision level of Universal Library
        ULStat = MccDaq.MccService.DeclareRevision(MccDaq.MccService.CurrentRevNum)
        ' Initiate error handling
        '  activating error handling will trap errors like
        '  bad channel numbers and non-configured conditions.
        '  Parameters:
        '    MccDaq.ErrorReporting.PrintAll :all warnings and errors encountered will be printed
        '    MccDaq.ErrorHandling.StopAll   :if any error is encountered, the program will stop
        ReportError = MccDaq.ErrorReporting.PrintAll
        HandleError = MccDaq.ErrorHandling.StopAll
        ULStat = MccDaq.MccService.ErrHandling(ReportError, HandleError)
        If ULStat.Value <> MccDaq.ErrorInfo.ErrorCode.NoErrors Then
            Stop
        End If
    End Sub
#End Region
    Private Sub Switch1_StateChanged(ByVal sender As System.Object, ByVal e As
NationalInstruments.UI.ActionEventArgs) Handles Switch1.StateChanged
        'this is the main capture and fft section
        Dim fidfac As Single
        Dim vamp As Single
        vamp = TextBox2.Text
        fidfac = TextBox1.Text
        Application.DoEvents()
        If Slide1.Value = 0 Then gain = 1000
        If Slide1.Value = 1 Then gain = 10000
        If Slide1.Value = 2 Then gain = 100000
        If Slide2.Value = 1 Then Rate = 10000
        If Slide2.Value = 2 Then Rate = 100000
        If Slide2.Value = 3 Then Rate = 200000
        If Slide2.Value = 4 Then Rate = 400000
        If Slide2.Value = 5 Then Rate = 800000
        If Slide2.Value = 6 Then Rate = 1000000
        If Slide2.Value = 7 Then Rate = 2000000
        If Slide3.Value = 0 Then points = 99999
        If Slide3.Value = 1 Then points = 499999
        If Slide3.Value = 2 Then points = 999999
        If Slide3.Value = 3 Then points = 9999990
        ReDim eng(points)
        ReDim engsingle(points)
        'plotting slightly different - define an x sale
        ReDim xscale(points)
        If Switch1.Value = False Then
            WaveformGraph2.ClearData()
```

```
        Else
        End If
        LowChan = 2
        HighChan = 2 'one channel
        If Switch1.Value = True Then
            Count = points + 1          ' total number of data points to collect
            Range = MccDaq.Range.Bip5Volts
            ' per channel sampling rate ((samples per second) per channel)
            If CheckBox1.Checked = False Then Options = MccDaq.ScanOptions.ConvertData
            If CheckBox1.Checked = True Then Options = MccDaq.ScanOptions.ConvertData Or
MccDaq.ScanOptions.ExtTrigger
            Application.DoEvents()
            ' collect data, external trigger and clock enabled
            LowChan = 2
            HighChan = 2
            'next line as normal
            ULStat = DaqBoard.AInScan(LowChan, HighChan, Count, Rate, Range, MemHandle, Options)
            If ULStat.Value <> MccDaq.ErrorInfo.ErrorCode.NoErrors Then Stop
            tmrCheckStatus.Enabled = True
            'get from memory
            ULStat = MccDaq.MccService.WinBufToArray(MemHandle, ADData, FirstPoint, NumPoints)
            If ULStat.Value <> MccDaq.ErrorInfo.ErrorCode.NoErrors Then Stop
            Dim xv As Integer
            xv = 0
            For i = 0 To points
                ULStat = DaqBoard.ToEngUnits(Range, ADData(i), engsingle(i))
                eng(xv) = (vamp * gain) / (engsingle(i)) / fidfac  ' note array eng is double so we can then plot the
data
                xscale(xv) = xv * (1 / Rate)
                xv = xv + 1
            Next i
            'End If
            WaveformGraph2.PlotY(eng, 0, (1 / Rate))
        End If
    End Sub
    Private Sub MenuStrip1_ItemClicked(ByVal sender As System.Object, ByVal e As
System.Windows.Forms.ToolStripItemClickedEventArgs) Handles MenuStrip1.ItemClicked
    End Sub
    Private Sub ScatterGraph1_PlotDataChanged(ByVal sender As System.Object, ByVal e As
NationalInstruments.UI.XYPlotDataChangedEventArgs)
    End Sub
    Private Sub InstrumentControlStrip1_ItemClicked(ByVal sender As System.Object, ByVal e As
System.Windows.Forms.ToolStripItemClickedEventArgs)
    End Sub
    Private Sub CheckBox2_CheckedChanged(ByVal sender As System.Object, ByVal e As
System.EventArgs)
        'Slide2.Value = 0
    End Sub
    Private Sub Slide2_AfterChangeValue(ByVal sender As System.Object, ByVal e As
NationalInstruments.UI.AfterChangeNumericValueEventArgs) Handles Slide2.AfterChangeValue
        If Slide2.Value = 0 Then Rate = 100000
        If Slide2.Value = 1 Then Rate = 250000
        If Slide2.Value = 2 Then Rate = 1000000
        If Slide2.Value = 3 Then Rate = 10000000
    End Sub
    Private Sub Slide1_AfterChangeValue(ByVal sender As System.Object, ByVal e As
NationalInstruments.UI.AfterChangeNumericValueEventArgs) Handles Slide1.AfterChangeValue
    End Sub
    Private Sub FileToolStripMenuItem_Click(ByVal sender As System.Object, ByVal e As
System.EventArgs) Handles FileToolStripMenuItem.Click
```

```
    End Sub
    Private Sub OpenToolStripMenuItem_Click_1(ByVal sender As System.Object, ByVal e As
System.EventArgs) Handles OpenToolStripMenuItem.Click
        If Slide2.Value = 1 Then Rate = 10000
        If Slide2.Value = 2 Then Rate = 100000
        If Slide2.Value = 3 Then Rate = 200000
        If Slide2.Value = 4 Then Rate = 400000
        If Slide2.Value = 5 Then Rate = 800000
        If Slide2.Value = 6 Then Rate = 1000000
        If Slide2.Value = 7 Then Rate = 2000000
        Dim openFileDialog1 As New OpenFileDialog()
        openFileDialog1.Filter = "txt files (*.txt)|*.txt|all files (*.*)|*.*"
        openFileDialog1.FilterIndex = 1
        openFileDialog1.RestoreDirectory = True
        ' ReDim xscale(NumPoints), eng(NumPoints), eng_V(NumPoints)
        If openFileDialog1.ShowDialog() = DialogResult.OK Then
            Dim sw1 As StreamReader = New StreamReader(openFileDialog1.OpenFile())
            Dim indat As String
            If (sw1 IsNot Nothing) Then
                'indat = sw1.ReadLine()
                il = 0
                Do While sw1.Peek() >= 0
                    indat = sw1.ReadLine()
                    il = il + 1
                Loop
                sw1.Close()
                ReDim xscale(il - 2), eng(il - 2)
                Dim sw2 As StreamReader = New StreamReader(openFileDialog1.OpenFile())
                For Me.i = 1 To il - 2
                    indat = sw2.ReadLine()
                    Dim indd() = Split(indat, ",")
                    xscale(i) = (indd(0))
                    eng(i) = (indd(1))
                Next i
                sw2.Close()
            End If
        End If
        WaveformGraph2.PlotY(eng, 0, 1 / Rate)
    End Sub
    Private Sub cmdStopConvert_Click_1(ByVal sender As System.Object, ByVal e As System.EventArgs)
Handles cmdStopConvert.Click
        Dim ULStat As MccDaq.ErrorInfo
        ' Free up memory for use by other programs
        ULStat = MccDaq.MccService.WinBufFreeEx(MemHandle)
        If ULStat.Value <> MccDaq.ErrorInfo.ErrorCode.NoErrors Then Stop
        End
    End Sub
    Private Sub SaveToolStripMenuItem_Click_1(ByVal sender As System.Object, ByVal e As
System.EventArgs) Handles SaveToolStripMenuItem.Click
        Dim saveFileDialog1 As New SaveFileDialog()
        saveFileDialog1.Filter = "txt files (*.txt)|*.txt|all files (*.*)|*.*"
        saveFileDialog1.FilterIndex = 1
        saveFileDialog1.RestoreDirectory = True
        If saveFileDialog1.ShowDialog() = DialogResult.OK Then
            Dim sw As StreamWriter = New StreamWriter(saveFileDialog1.OpenFile())
            If (sw IsNot Nothing) Then
                For i = 0 To points
                    sw.WriteLine(Format(xscale(i), "0.00e-00") + "," + Format(eng(i), "0.00e-00"))
                Next i
                sw.Close()
```

```
            End If
        End If
    End Sub
    Private Sub Button1_Click(ByVal sender As System.Object, ByVal e As System.EventArgs) Handles
Button1.Click
        Application.DoEvents()
        If Slide1.Value = 0 Then gain = 1000
        If Slide1.Value = 1 Then gain = 10000
        If Slide1.Value = 2 Then gain = 100000
        If Slide2.Value = 1 Then Rate = 100000
        If Slide2.Value = 2 Then Rate = 1000000
        If Slide2.Value = 3 Then Rate = 2000000
        If Slide2.Value = 4 Then Rate = 4000000
        If Slide2.Value = 5 Then Rate = 8000000
        If Slide2.Value = 6 Then Rate = 10000000
        If Slide2.Value = 7 Then Rate = 20000000
        If Slide3.Value = 0 Then points = 99999
        If Slide3.Value = 1 Then points = 499999
        If Slide3.Value = 2 Then points = 999999
        If Slide3.Value = 3 Then points = 9999990
        wind = 2000
        ReDim v(wind - 1)
        ReDim idaq(wind - 1)
        ReDim ip(wind - 1)
        ReDim eng_V(wind - 1)
        ReDim engsingle(wind - 1)
        'plotting slightly different - define an x scale
        ReDim xscale(wind - 1)
        LowChan = 1
        HighChan = 1 'one channel
        Erase am, p
        Count = points + 1          ' total number of data points to collect
        Range = MccDaq.Range.Bip1Volts
        ' per channel sampling rate ((samples per second) per channel)
        'If CheckBox1.Checked = False Then Options = MccDaq.ScanOptions.ConvertData
        'If CheckBox1.Checked = True Then Options = MccDaq.ScanOptions.ConvertData Or
MccDaq.ScanOptions.ExtTrigger
        Application.DoEvents()
        ' collect data, external trigger and clock enabled
        LowChan = 1
        HighChan = 1
        'next line as normal
        ULStat = DaqBoard.AInScan(LowChan, HighChan, Count, Rate, Range, MemHandle, Options)
        If ULStat.Value <> MccDaq.ErrorInfo.ErrorCode.NoErrors Then Stop
        tmrCheckStatus.Enabled = True
        'get from memory
        ULStat = MccDaq.MccService.WinBufToArray(MemHandle, ADData, FirstPoint, NumPoints)
        If ULStat.Value <> MccDaq.ErrorInfo.ErrorCode.NoErrors Then Stop
        Dim x As Integer
        'If CheckBox2.Checked = True Then Rate = 50000
        x = 0
        'If CheckBox2.Checked = True Then
        'For i = 0 To points - 1
        'ULStat = DaqBoard.ToEngUnits(Range, ADData(i), engsingle(i))
        'eng(x) = (engsingle(i) / gain)  ' note array eng is double so we can then plot the data
        'ULStat = DaqBoard.ToEngUnits(Range, ADData(i + 1), engsingle(i + 1))
        'eng_V(x) = engsingle(i + 1)
        'xscale(x) = x * (wind / 10) * (1 / Rate)
        'x = x + 1
        'Next i
```

```
        'Else
        For i = 0 To wind - 1
            ULStat = DaqBoard.ToEngUnits(Range, ADData(i), engsingle(i))
            eng_V(x) = (engsingle(i))
            xscale(x) = x * (1 / Rate)
            x = x + 1
        Next i
        WaveformGraph3.PlotY(eng_V, 0, (1 / Rate))
        sampr = 1 / Rate
        Dim fftdv(wind - 1) As Double
        For w = 0 To wind - 1
            fftdv(w) = eng_V(w)
        Next w
        'here's the expression for the FFT - note sequence
        NationalInstruments.Analysis.SpectralMeasurements.Measurements.AmplitudePhaseSpectrum(fftdv,
unWrap:=False, dt:=sampr, amplitudeSpectrum:=amv, phaseSpectrum:=pv, df:=f)
        For il = 1 To (wind / 2) - 1
            amv(il) = (Math.Sqrt(2)) * (amv(il))
        Next il
        WaveformGraph1.PlotY(amv, 0, f)
    End Sub
    Private Sub Button2_Click(ByVal sender As System.Object, ByVal e As System.EventArgs) Handles
Button2.Click
        TextBox2.Text = Format(WaveformGraph1.Cursors.Item(0).YPosition, "0.0000")
        TextBox3.Text = Format(WaveformGraph1.Cursors.Item(0).XPosition, "0")
    End Sub
    Private Sub CheckBox3_CheckedChanged(ByVal sender As System.Object, ByVal e As
System.EventArgs)
    End Sub
End Class
```

9.9.3 Double FFT data processing

The purpose of this program was to open files with impedance data recorded using the demodulator and to reprocess this data to produce an intensity plot. This same approach was used in similar programs to produce intensity plots from the uncompensated resistance measured using the high-speed AC impedance method. A discussion of the double FFT processing method can be found in Chapter 5.3. Later the option to include an additional data channel was added so that both the uncompensated resistance/impedance and hydrophone signal could be processed in this manner. Figure 9.16 shows the main form into which the original data is opened and displayed graphically from a text file.

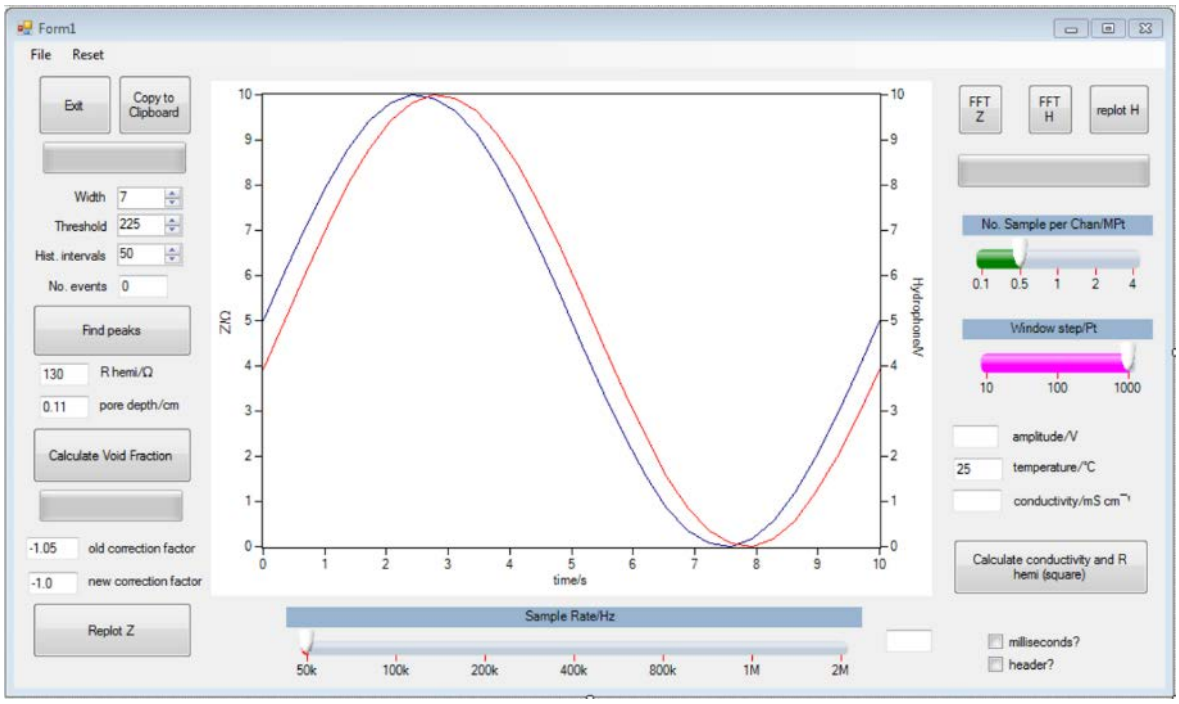

Figure 9.16 Main form for program with double FFT processing.

FFT processing of the uncompensated resistance/impedance and hydrophone data is achieved using the buttons ‘FFT Z’ and ‘FFT H’ respectively.

Figures 9.15 and 9.16 show the forms on which the intensity plot data for the impedance and hydrophone were displayed.

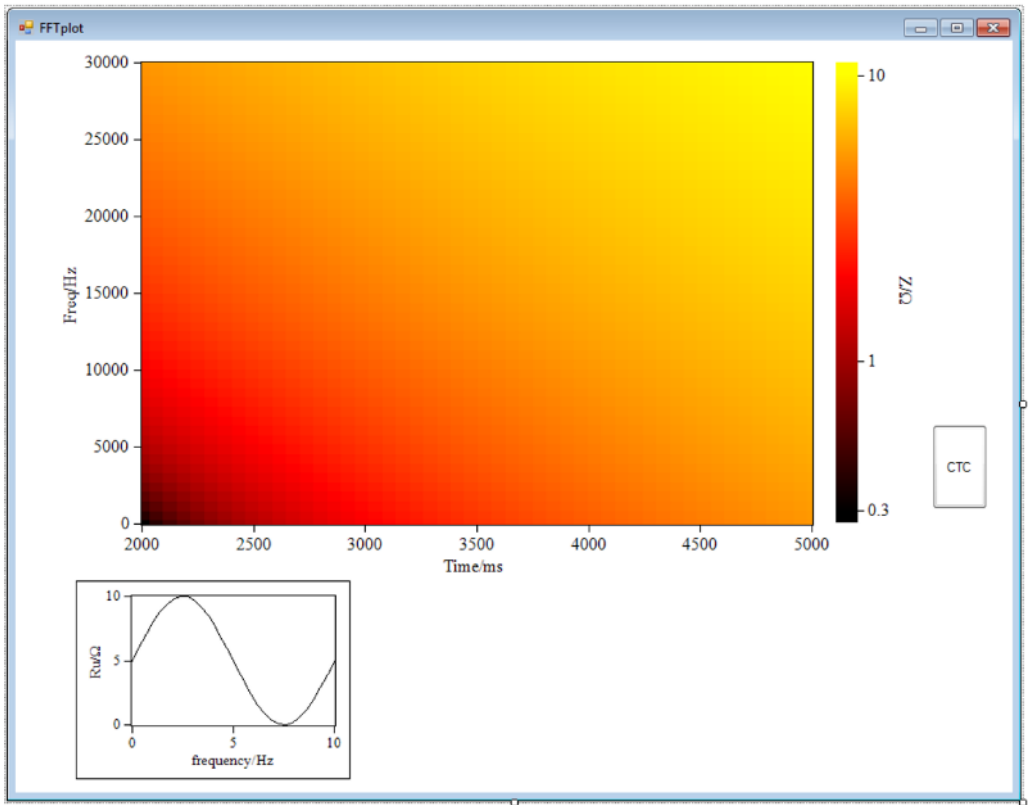

Figure 9.17 Form displaying intensity plot for impedance data.

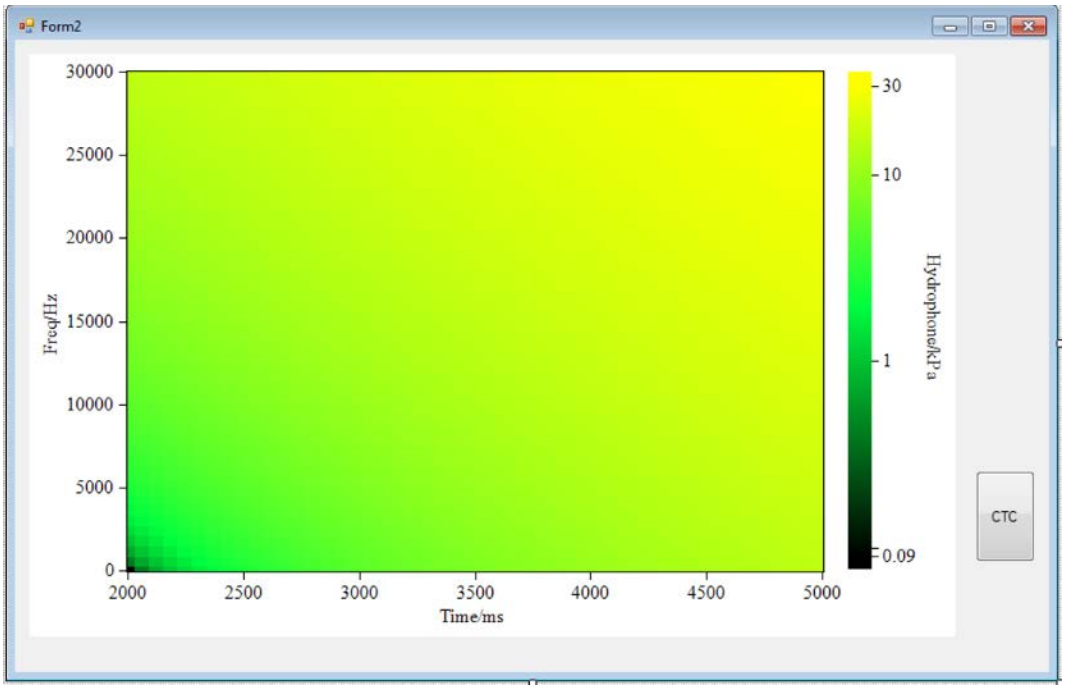

Figure 9.18 Form displaying intensity plot for hydrophone data.

This program was also used to calculate the channel void fraction from the impedance data for experiments performed with recessed electrodes. The form shown in Figure 9.19 displayed this void fraction plot. The program was also able to save this information as a text file to be exported into other graphics drawing software.

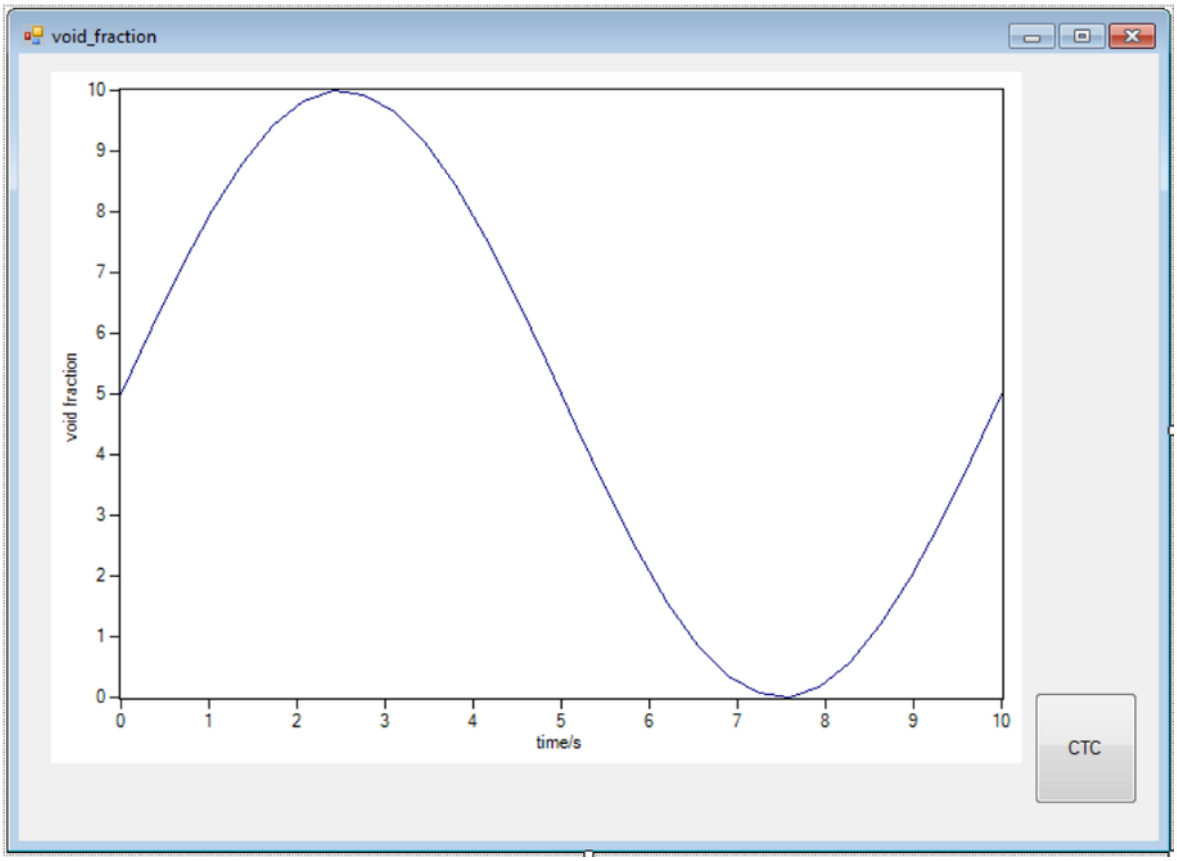

Figure 9.19 Form displaying the channel void fraction based on the impedance data.

The code for this program is given below. This program was written in collaboration with Dr Peter Birkin.

```
Option Strict Off
Option Explicit On
'get this for the FFT, not sure really necessary?
Imports NationalInstruments.Analysis.SpectralMeasurements
'for file
Imports System.IO
Imports NationalInstruments.Analysis.Monitoring
Imports NationalInstruments.Analysis.Math
Public Class Form1
    Const NumPoints As Integer = 19999999
    Dim xscale() As Double
    Dim ru() As Double
    Dim cap() As Double
    Dim phase() As Double
    Dim idc() As Double
    Dim i, ip, timm, lc, ik, im As Integer
    Dim indd() As Object
    Dim timeplot As Double
    Dim amr(points) As Double
    Dim rate As Integer
    Dim sampr As Double
    Dim f As Double
    Dim PV() As Double
    Dim points As Integer
```

```
    Dim amcon(10, 103) As Double
    Dim srfac As Double
    Dim winds As Integer
    Dim datal As Integer
    Dim lfac As Integer
    Dim xdiv As Integer
    Dim ydiv As Integer
    Dim windd As Integer
    Dim hyd() As Double
    Dim amplitudes() As Double = Nothing, locations() As Double = Nothing, secondDerivatives() As Double
= Nothing
    Dim initialThreshold As Double
    Dim initialWidth As Integer
    Dim endOfData As Boolean
    Dim peakDetector As New Analysis.Monitoring.PeakDetector
    Dim histint() As Double
    Dim hisval() As Double
    Dim hisl As Integer = 1
    Dim rufft() As Double
    Dim kappa, temp, Rhem, poreh, porea, hemi As Double
    Dim theta() As Double
    Dim alpha() As Double
    Dim Z() As Double
    Dim ffacold As Double
    Dim ffacnew As Double
    Private Sub OpenFFTToolStripMenuItem_Click(ByVal sender As System.Object, ByVal e As
System.EventArgs) Handles OpenFFTToolStripMenuItem.Click
        'Dim myStream As Stream
        Dim openFileDialog1 As New OpenFileDialog()
        openFileDialog1.Filter = "txt files (*.txt)|*.txt|all files (*.*)|*.*"
        openFileDialog1.FilterIndex = 1
        openFileDialog1.RestoreDirectory = True
        If openFileDialog1.ShowDialog() = DialogResult.OK Then
            Dim sw1 As StreamReader = New StreamReader(openFileDialog1.OpenFile())
            Dim head As String
            Dim indat As String
            If (sw1 IsNot Nothing) Then
                If CheckBox3.Checked = True Then
                    head = sw1.ReadLine()
                    ip = 0
                Else
                End If
                Do While sw1.Peek() >= 0
                    indat = sw1.ReadLine(
                    ip = ip + 1
                Loop
                sw1.Close()
            End If
            ReDim xscale(ip - 1), ru(ip - 1), cap(ip - 1)
            Dim sw2 As StreamReader = New StreamReader(openFileDialog1.OpenFile())
            WaveformGraph1.Caption = openFileDialog1.FileName
            If CheckBox3.Checked = True Then
                head = sw2.ReadLine()
                Dim indt() = Split(head, ",")
                TextBox7.Text = indt(0) 'Vamp
                TextBox5.Text = indt(1) 'fidfac
                TextBox2.Text = indt(2) 'temp
            Else
            End If
            For Me.i = 0 To ip - 1
```

```
            indat = sw2.ReadLine()
            Dim indd() = Split(indat, ",")
            xscale(i) = (indd(0))
            ru(i) = (indd(1))
            cap(i) = (indd(2))
            ProgressBar1.Value = (i / ip) * 100
        Next i
        sw2.Close()
        End If
    If ip = 100000 Then Slide3.Value = 0
    If ip = 500000 Then Slide3.Value = 1
    If ip = 1000000.0 Then Slide3.Value = 2
    If ip = 2000000.0 Then Slide3.Value = 3
    If ip = 4000000.0 Then Slide3.Value = 4
    If xscale(1) = (1 / 50000) Then Slide4.Value = 0
    If xscale(1) = (1 / 100000) Then Slide4.Value = 1
    If xscale(1) = (1 / 200000) Then Slide4.Value = 2
    If xscale(1) = (1 / 400000) Then Slide4.Value = 3
    If xscale(1) = (1 / 800000) Then Slide4.Value = 4
    If xscale(1) = (1 / 1000000) Then Slide4.Value = 5
    If xscale(1) = (1 / 2000000) Then Slide4.Value = 6
    timeplot = xscale(1)
    WaveformGraph1.Plots(0).PlotY(ru, 0, timeplot)
    WaveformGraph1.YAxes(0).Caption = "Z/Ω"
    WaveformGraph1.YAxes(0).CaptionForeColor = Color.Navy
    WaveformGraph1.Plots(0).LineColor = Color.Navy
    WaveformGraph1.Plots(1).PlotY(cap, 0, timeplot)
    WaveformGraph1.YAxes(1).Caption = "Hydrophone/V"
    WaveformGraph1.YAxes(1).CaptionForeColor = Color.Red
    WaveformGraph1.Plots(1).LineColor = Color.Red
  End Sub
  Private Sub Copy_Click(ByVal sender As System.Object, ByVal e As System.EventArgs) Handles
Copy.Click
    WaveformGraph1.ToClipboard()
  End Sub
  Private Sub Button1_Click(ByVal sender As System.Object, ByVal e As System.EventArgs) Handles
Button1.Click
    End
  End Sub
  Private Sub ResetToolStripMenuItem_Click(ByVal sender As System.Object, ByVal e As
System.EventArgs) Handles ResetToolStripMenuItem.Click
    WaveformGraph1.ClearData()
    WaveformGraph1.Caption = Format("")
    If FFTplot.Visible = True Then
        FFTplot.IntensityPlot1.ClearData()
        Me.ProgressBar2.Value = 0
    End If
    If Form2.Visible = True Then
        Form2.IntensityPlot1.ClearData()
        Me.ProgressBar2.Value = 0
    End If
    If void_fraction.Visible = True Then
        void_fraction.WaveformGraph1.ClearData()
        void_fraction.WaveformGraph1.Caption = Format("")
        Me.ProgressBar3.Value = 0
    End If
    If peakplot.Visible = True Then
        peakplot.ScatterGraph1.ClearData()
        peakplot.ScatterGraph2.ClearData()
        Me.ProgressBar3.Value = 0
```

```
        End If
        void_fraction.Visible = False
    End Sub
    Private Sub CheckBox1_CheckedChanged(ByVal sender As System.Object, ByVal e As
System.EventArgs) Handles CheckBox1.CheckedChanged
        If CheckBox1.Checked = False Then WaveformGraph1.XAxes(0).Caption = "time/s"
        If CheckBox1.Checked = True Then WaveformGraph1.XAxes(0).Caption = "time/ms"
    End Sub
    Private Sub Button2_Click(ByVal sender As System.Object, ByVal e As System.EventArgs)
    End Sub
    Private Sub Button3_Click(ByVal sender As System.Object, ByVal e As System.EventArgs) Handles
Button3.Click
        Dim timx As Integer
        Dim wfac As Integer
        Dim d As Integer
        If Slide3.Value = 0 Then points = 99999
        If Slide3.Value = 1 Then points = 499999
        If Slide3.Value = 2 Then points = 999999
        If Slide3.Value = 3 Then points = 1999999
        If Slide3.Value = 4 Then points = 3999999
        If Slide4.Value = 0 Then rate = 50000
        If Slide4.Value = 1 Then rate = 100000
        If Slide4.Value = 2 Then rate = 200000
        If Slide4.Value = 3 Then rate = 400000
        If Slide4.Value = 4 Then rate = 800000
        If Slide4.Value = 5 Then rate = 1000000
        If Slide4.Value = 6 Then rate = 2000000
        If Slide5.Value = 0 Then winds = 10 'window step
        If Slide5.Value = 1 Then winds = 100
        If Slide5.Value = 2 Then winds = 1000
        xdiv = (points + 1) / winds
        ydiv = (winds / 2) - 1
        ReDim amcon(xdiv, ydiv)
        datal = points + 1
        lc = 0
        sampr = 1 / rate
        timx = 0
        For d = 1 To datal - (winds + 1) Step winds
            Dim fftdr(winds - 1) As Double
            For w = 0 To (winds - 1)
                fftdr(w) = ru(w + d)
            Next
NationalInstruments.Analysis.SpectralMeasurements.Measurements.AmplitudePhaseSpectrum(fftdr,
unWrap:=False, dt:=sampr, amplitudeSpectrum:=amr, phaseSpectrum:=PV, df:=f)
            amcon(timx, 0) = 0.001
            amr(0) = 0.0001
            For il = 1 To ((winds / 2) - 1)
                amr(il) = (Math.Sqrt(2)) * (amr(il))
                amcon(timx, il) = amr(il)
            Next il
            ProgressBar2.Value = (d / datal) * 100
            timx = timx + 1
        Next d
        FFTplot.Visible = True
        FFTplot.WaveformGraph1.PlotY(amr, 0, f)
        FFTplot.IntensityGraph1.Plots(0).DefaultYIncrement = (200000.0 / winds)
        If Slide5.Value = 0 Then FFTplot.IntensityGraph1.Plots(0).DefaultXIncrement = 0.05
        If Slide5.Value = 1 Then FFTplot.IntensityGraph1.Plots(0).DefaultXIncrement = 0.5
        If Slide5.Value = 2 Then FFTplot.IntensityGraph1.Plots(0).DefaultXIncrement = 5
        FFTplot.IntensityGraph1.Plots(0).Plot(amcon, transposeZData:=False)
```

```
    End Sub
    Private Sub OpenIntensityPlotToolStripMenuItem_Click(ByVal sender As System.Object, ByVal e As
System.EventArgs) Handles OpenIntensityPlotToolStripMenuItem.Click
        Dim ph As Integer
        Dim dt As Integer
        Dim openFileDialog1 As New OpenFileDialog()
        openFileDialog1.Filter = "txt files (*.txt)|*.txt|All files (*.txt)|*.txt"
        openFileDialog1.FilterIndex = 2
        openFileDialog1.RestoreDirectory = True
        If openFileDialog1.ShowDialog() = DialogResult.OK Then
            Dim sw As StreamReader = New StreamReader(openFileDialog1.OpenFile())
            If (sw IsNot Nothing) Then
                Dim lins As String
                dt = 0
                Do While sw.Peek() >= 0
                    lins = sw.ReadLine()
                    Dim linff() = Split(lins, ",")
                    For ph = 0 To 10
                        amcon(ph, dt) = linff(ph)
                    Next
                    dt = dt + 1
                Loop
                sw.Close()
            End If
            FFTplot.Visible = True
            FFTplot.IntensityGraph1.Plots(0).DefaultYIncrement = 0.001
            FFTplot.IntensityGraph1.Plots(0).DefaultXIncrement = 2
            FFTplot.IntensityGraph1.Plots(0).Plot(amcon, transposeZData:=False)
        End If
    End Sub
    Private Sub SaveIntensityPlotToolStripMenuItem_Click(ByVal sender As System.Object, ByVal e As
System.EventArgs) Handles SaveIntensityPlotToolStripMenuItem.Click
        Dim saveFileDialog1 As New SaveFileDialog()
        Dim ph As Integer
        saveFileDialog1.Filter = "txt files (*.int)|*.int|All files (*.int)|*.int"
        saveFileDialog1.FilterIndex = 2
        saveFileDialog1.RestoreDirectory = True
        If saveFileDialog1.ShowDialog() = DialogResult.OK Then
            Dim sw As StreamWriter = New StreamWriter(saveFileDialog1.OpenFile())
            If (sw IsNot Nothing) Then
                For il = 1 To 499
                    For ph = 0 To 49998
                        sw.Write(Format(amcon(il, ph), "0.000e-00") + ",")
                    Next
                    sw.WriteLine(Format(amcon(il, 49999), "0.000e-00"))
                Next il
                sw.Close()
            End If
        End If
    End Sub
    Private Sub Button4_Click(ByVal sender As System.Object, ByVal e As System.EventArgs) Handles
Button4.Click
        Dim timx As Integer
        Dim wfac As Integer
        Dim d As Integer
        If Slide3.Value = 0 Then points = 99999
        If Slide3.Value = 1 Then points = 499999
        If Slide3.Value = 2 Then points = 999999
        If Slide3.Value = 3 Then points = 1999999
        If Slide3.Value = 4 Then points = 3999999
```

```
        rate = 200000
        If Slide5.Value = 0 Then winds = 10 'window step
        If Slide5.Value = 1 Then winds = 100
        If Slide5.Value = 2 Then winds = 1000
        xdiv = (points + 1) / winds
        ydiv = (winds / 2) - 1
        ReDim amcon(xdiv, ydiv)
        datal = points + 1
        lc = 0
        sampr = 1 / rate
        timx = 0
        For d = 1 To datal - (winds + 1) Step winds
            Dim fftdr(winds - 1) As Double
            For w = 0 To (winds - 1)
                fftdr(w) = hyd(w + d)
            Next
NationalInstruments.Analysis.SpectralMeasurements.Measurements.AmplitudePhaseSpectrum(fftdr,
unWrap:=False, dt:=sampr, amplitudeSpectrum:=amr, phaseSpectrum:=PV, df:=f)
            amcon(timx, 0) = 0.001
            amr(0) = 0.0001
            For il = 1 To ((winds / 2) - 1)
                amr(il) = (Math.Sqrt(2)) * (amr(il))
                amcon(timx, il) = amr(il)
            Next il
            ProgressBar2.Value = (d / datal) * 100
            timx = timx + 1
        Next d
        Form2.Visible = True
        Form2.IntensityGraph1.Plots(0).DefaultYIncrement = (200000.0 / winds)
        If Slide5.Value = 0 Then Form2.IntensityGraph1.Plots(0).DefaultXIncrement = 0.05
        If Slide5.Value = 1 Then Form2.IntensityGraph1.Plots(0).DefaultXIncrement = 0.5
        If Slide5.Value = 2 Then Form2.IntensityGraph1.Plots(0).DefaultXIncrement = 5
        Form2.IntensityGraph1.Plots(0).Plot(amcon, transposeZData:=False)
    End Sub
    Private Sub TextBox1_TextChanged(sender As System.Object, e As System.EventArgs) Handles
TextBox1.TextChanged
    End Sub
    Private Sub Label1_Click(sender As System.Object, e As System.EventArgs) Handles Label1.Click
    End Sub
    Private Sub Button2_Click_1(sender As System.Object, e As System.EventArgs) Handles Button2.Click
        temp = TextBox2.Text
        kappa = (0.0014429 * (temp ^ 2)) + (1.1009 * temp) + 27.4
        hemi = 8188.7147 / kappa
        TextBox3.Text = Format(kappa, "0.0")
        TextBox1.Text = Format(hemi, "0")
    End Sub
    Private Sub Button5_Click(sender As System.Object, e As System.EventArgs) Handles Button5.Click
        Rhem = TextBox1.Text
        poreh = TextBox4.Text
        porea = 0.002601
        ProgressBar3.Value = 0
        ReDim theta(ip - 1)
        ReDim alpha(ip - 1)
        For Me.ik = 0 To ip - 1
            theta(ik) = poreh / (porea * (Z(ik) - Rhem) * (kappa / 1000))
            alpha(ik) = (2 * (1 - theta(ik))) / (theta(ik) + 2)
            ProgressBar3.Value = (ik / (ip - 1)) * 100
        Next ik
        void_fraction.Visible = True
        void_fraction.WaveformGraph1.PlotY(alpha, 0, timeplot)
```

```
    End Sub
    Private Sub SaveVoidFractionToolStripMenuItem_Click(sender As System.Object, e As
System.EventArgs) Handles SaveVoidFractionToolStripMenuItem.Click
        ProgressBar1.Value = 0
        Dim saveFileDialog1 As New SaveFileDialog()
        saveFileDialog1.Filter = "txt files (*.txt)|*.txt|all files (*.*)|*.*"
        saveFileDialog1.FilterIndex = 1
        saveFileDialog1.RestoreDirectory = True
        If saveFileDialog1.ShowDialog() = DialogResult.OK Then
            Dim sw As StreamWriter = New StreamWriter(saveFileDialog1.OpenFile())
            If (sw IsNot Nothing) Then
                For Me.i = 0 To ip - 1
                    sw.WriteLine(Format(xscale(i), "0.00e-00") + "," + Format(alpha(i), "0.00e-00"))
                Next i
                sw.Close()
            End If
        End If
        void_fraction.WaveformGraph1.Caption = saveFileDialog1.FileName
    End Sub
    Private Sub Button6_Click(sender As System.Object, e As System.EventArgs) Handles Button6.Click
        ffacold = TextBox5.Text
        ffacnew = TextBox6.Text
        ProgressBar1.Value = 0
        ReDim Z(ip - 1)
        For Me.im = 0 To ip - 1
            Z(im) = (ru(im) * ffacold) / ffacnew
            ProgressBar1.Value = (im / (ip - 1)) * 100
        Next im
        Me.WaveformGraph1.PlotY(Z, 0, timeplot)
        If void_fraction.Visible = True Then
            Rhem = TextBox1.Text
            poreh = TextBox4.Text
            porea = 0.0025
            ProgressBar3.Value = 0
            ReDim theta(ip - 1)
            ReDim alpha(ip - 1)
            For Me.ik = 0 To ip - 1
                theta(ik) = poreh / (porea * (Z(ik) - Rhem) * (kappa / 1000))
                alpha(ik) = (2 * (1 - theta(ik))) / (theta(ik) + 2)
                ProgressBar3.Value = (ik / (ip - 1)) * 100
            Next ik
            void_fraction.Visible = True
            void_fraction.WaveformGraph1.PlotY(alpha, 0, timeplot)
        End If
    End Sub
    Private Sub SaveFFTToolStripMenuItem_Click(sender As System.Object, e As System.EventArgs)
Handles SaveFFTToolStripMenuItem.Click
        ProgressBar1.Value = 0
        Dim saveFileDialog1 As New SaveFileDialog()
        saveFileDialog1.Filter = "txt files (*.txt)|*.txt|all files (*.*)|*.*"
        saveFileDialog1.FilterIndex = 1
        saveFileDialog1.RestoreDirectory = True
        If saveFileDialog1.ShowDialog() = DialogResult.OK Then
            Dim sw As StreamWriter = New StreamWriter(saveFileDialog1.OpenFile())
            If (sw IsNot Nothing) Then
                For Me.i = 0 To ip - 1
                    sw.WriteLine(Format(xscale(i), "0.00e-00") + "," + Format(Z(i), "0.00e-00"))
                    ProgressBar1.Value = (i / ip) * 100
                Next i
                sw.Close()
```

```
            End If
            Me.WaveformGraph1.Caption = saveFileDialog1.FileName
        End If
    End Sub

    Private Sub Button7_Click(sender As System.Object, e As System.EventArgs) Handles Button7.Click
        ' Set initial state of peakDetector
        initialThreshold = NumericUpDown2.Value
        initialWidth = NumericUpDown1.Value
        peakDetector.Reset(initialThreshold, initialWidth, PeakPolarity.Peaks)
        endOfData = True
        peakDetector.Detect(ru, endOfData, amplitudes, locations, secondDerivatives)
        Dim locationtime(locations.Length - 1) As Double
        Dim pl As Integer
        For pl = 0 To locations.Length - 1
            locationtime(pl) = (locations(pl) * 0.00002)
        Next
        TextBox8.Text = amplitudes.Length
        peakplot.Visible = True
        peakplot.ScatterGraph1.Plots(0).PlotXY(locationtime, amplitudes)
        peakplot.ScatterGraph1.Plots(1).PlotXY(xscale, ru)
        Dim centerValues(9) As Double
        Dim histogramData() As Integer
        Dim histogramBase, histogramTop As Double
        Dim histogramIntervals As Integer
        histogramIntervals = NumericUpDown3.Value
        ' Get the minimum and maximum values in the array
        histogramBase = ArrayOperation.GetMin(amplitudes)
        histogramTop = ArrayOperation.GetMax(amplitudes)
        ' Calculate histogram
        histogramData = Statistics.Histogram(amplitudes, histogramBase, histogramTop, histogramIntervals,
centerValues)
        ReDim histint(histogramData.Length - 1)
        ReDim hisval(histogramData.Length - 1)
        Dim ph As Integer
        For ph = 0 To (histogramData.Length - 1)
            histint(ph) = (((histogramTop - histogramBase) / histogramIntervals) * ph) + histogramBase
            hisval(ph) = histogramData(ph)
        Next
        hisl = histogramData.Length - 1
        peakplot.ScatterGraph2.PlotXY(histint, hisval)
    End Sub
    Private Sub Button8_Click(sender As System.Object, e As System.EventArgs) Handles Button8.Click
        ReDim hyd(ip - 1)
        For Me.i = 0 To (ip - 1)
            hyd(i) = cap(i) / 0.02344
        Next i
        WaveformGraph1.Plots(1).PlotY(hyd, 0, timeplot)
        WaveformGraph1.YAxes(1).Caption = "Hydrophone/kPa"
        WaveformGraph1.YAxes(1).CaptionForeColor = Color.Red
        WaveformGraph1.Plots(1).LineColor = Color.Red
    End Sub
End Class
```

9.9.4 Stepper Motors

These two programs were used to control the stepper motors used to control the position of the aluminium/steel reflectors used in the cylindrical cell investigations (Chapter 3).

The form for the first of these programs is given in Figure 9.20.

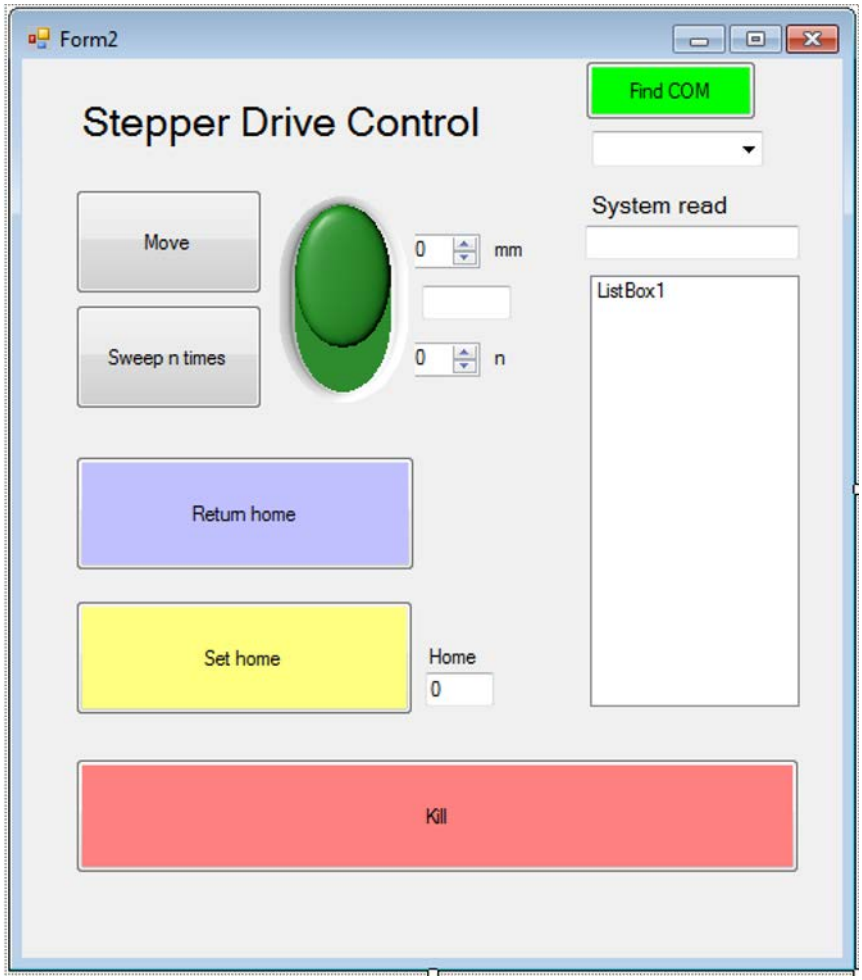

Figure 9.20 Form for stepper motor control program.

The code for this program is given below. This program was written in collaboration with Dr Peter Birkin.

```
Imports System.IO.Ports.SerialPort
Imports System.IO
Public Class Form2
    Dim timest As Single
    Dim comstr As String
    Dim startm, startwait, DISTANCE, towait As Single
    Dim wey As Integer
    Dim home As Single
    Dim clockp As Double
    Dim steps, Texts, moveup, movedown As String
    Private Sub Button1_Click(ByVal sender As System.Object, ByVal e As System.EventArgs) Handles
Button1.Click
        Dim start_time As DateTime
        Static stop_time As DateTime
```

```
        Dim elapsed_time As TimeSpan
        Button1.Visible = False
        comstr = ComboBox1.Text ' MSComm1.CommPort = TextBox2
        SerialPort1.PortName = comstr
        SerialPort1.BaudRate = 9600
        SerialPort1.DataBits = 8
        SerialPort1.StopBits = 1
        SerialPort1.Open()
        start_time = Now
        'MSComm1.Settings = "9600,N,8,1"
        'MSComm1.PortOpen = True
        SerialPort1.Write("1ON" & Chr(13))
        SerialPort1.Write("1LIMITS(3,0,0)" & Chr(13))
        DISTANCE = NumericUpDown1.Value
        If Switch1.Value = True Then
            home = home + NumericUpDown1.Value
        Else
            home = home - NumericUpDown1.Value
        End If
        If Switch1.Value = True Then DISTANCE = DISTANCE * -1
        steps = (DISTANCE / 0.0025) * 10 ' number of steps
        SerialPort1.Write("1V5" & Chr(13))
        SerialPort1.Write("1A5" & Chr(13))
        SerialPort1.Write("1D" + steps & Chr(13)) 'report distance
        SerialPort1.Write("1G" & Chr(13)) 'do the move
        SerialPort1.Write("1V" & Chr(13)) 'report current velocity
        Texts = SerialPort1.ReadLine()
        TextBox1.Text = Texts
        ListBox1.Items.Add(TextBox1.Text)
        SerialPort1.Write("1OFF" & Chr(13))
        Do
            towait = ((NumericUpDown1.Value * 2) / 5) * 1.1
            stop_time = Now
            elapsed_time = stop_time.Subtract(start_time)
            clockp = elapsed_time.TotalSeconds.ToString("0.00")
        Loop Until clockp > towait
        TextBox3.Text = home
        Button1.Visible = True
        SerialPort1.Close()
    End Sub
    Private Sub Switch1_StateChanged(ByVal sender As System.Object, ByVal e As
NationalInstruments.UI.ActionEventArgs) Handles Switch1.StateChanged
        If Switch1.Value = True Then
            TextBox2.Text = "Up"
        Else
            TextBox2.Text = "Down"
        End If
    End Sub
    Private Sub Button6_Click(ByVal sender As System.Object, ByVal e As System.EventArgs) Handles
Button6.Click
        Me.Visible = False
    End Sub
    Private Sub Button4_Click(ByVal sender As System.Object, ByVal e As System.EventArgs) Handles
Button4.Click
        comstr = ComboBox1.Text ' MSComm1.CommPort = TextBox2
        SerialPort1.PortName = comstr
        SerialPort1.BaudRate = 9600
        SerialPort1.DataBits = 8
        SerialPort1.StopBits = 1
        SerialPort1.Open()
```

```
        SerialPort1.Write("1ON" & Chr(13))
        SerialPort1.Write("1LIMITS(3,0,0)" & Chr(13))
        steps = (TextBox3.Text / 0.0025) * 10 ' number of steps
        TextBox3.Text = 0
        home = 0
        SerialPort1.Write("1V5" & Chr(13))
        SerialPort1.Write("1A5" & Chr(13))
        SerialPort1.Write("1D" + steps & Chr(13)) 'report distance
        SerialPort1.Write("1G" & Chr(13)) 'do the move
        SerialPort1.Write("1V" & Chr(13)) 'report current velocity
        Texts = SerialPort1.ReadLine()
        TextBox1.Text = Texts
        ListBox1.GetItemText(TextBox1)
        SerialPort1.Write("1OFF" & Chr(13))
        SerialPort1.Close()
    End Sub
    Private Sub Button5_Click(ByVal sender As System.Object, ByVal e As System.EventArgs) Handles
Button5.Click
        home = 0
        TextBox3.Text = home
    End Sub
    Private Sub Button2_Click(ByVal sender As System.Object, ByVal e As System.EventArgs) Handles
Button2.Click
        Dim DISTANCE As Single
        Dim x As Integer
        Dim start_time As DateTime
        Static stop_time As DateTime
        Dim elapsed_time As TimeSpan
        Button2.Visible = False
        comstr = ComboBox1.Text ' MSComm1.CommPort = TextBox2
        SerialPort1.PortName = comstr
        SerialPort1.BaudRate = 9600
        SerialPort1.DataBits = 8
        SerialPort1.StopBits = 1
        SerialPort1.Open()
        start_time = Now
        DISTANCE = NumericUpDown1.Value
        If Switch1.Value = True Then
            home = home + NumericUpDown1.Value
        Else
            home = home - NumericUpDown1.Value
        End If
        If Switch1.Value = True Then DISTANCE = DISTANCE * -1
        steps = (DISTANCE / 0.0025) * 10
        'For x = 0 To ComboBox1.SelectedValue - 1
        For x = 0 To NumericUpDown2.Value - 2
            SerialPort1.Write("1ON" & Chr(13))
            SerialPort1.Write("1LIMITS(3,0,0)" & Chr(13))
            SerialPort1.Write("1V15" & Chr(13))
            SerialPort1.Write("1A15" & Chr(13))
            SerialPort1.Write("1D" + steps & Chr(13)) 'report distance
            SerialPort1.Write("1G" & Chr(13)) 'do the move
            Texts = SerialPort1.ReadLine()
            TextBox1.Text = Texts
            ListBox1.Items.Add(TextBox1.Text)
            SerialPort1.Write("1OFF" & Chr(13))
            Do
                stop_time = Now
                elapsed_time = stop_time.Subtract(start_time)
                clockp = elapsed_time.TotalSeconds.ToString("0.00")
```

```
            Loop Until clockp > 5
            SerialPort1.Write("1ON" & Chr(13))
            SerialPort1.Write("1LIMITS(3,0,0)" & Chr(13))
            SerialPort1.Write("1V15" & Chr(13))
            SerialPort1.Write("1A15" & Chr(13))
            steps = (DISTANCE / 0.0025) * 10
            SerialPort1.Write("1D" + steps & Chr(13)) 'report distance
            SerialPort1.Write("1G" & Chr(13)) 'do the move
            start_time = Now
            Do
               stop_time = Now
               elapsed_time = stop_time.Subtract(start_time)
               clockp = elapsed_time.TotalSeconds.ToString("0.00")
            Loop Until clockp > 5
         Next x
         start_time = Now
         Do
            towait = ((NumericUpDown1.Value * 2 * NumericUpDown2.Value) / 5) * 1.1
            stop_time = Now
            elapsed_time = stop_time.Subtract(start_time)
         Loop Until clockp > towait
         TextBox3.Text = home * NumericUpDown2.Value
         Button2.Visible = True
         SerialPort1.Close()
      End Sub
      Private Sub Button3_Click(ByVal sender As System.Object, ByVal e As System.EventArgs) Handles
Button3.Click
         For Each sp As String In My.Computer.Ports.SerialPortNames
            ComboBox1.Items.Add(sp)
         Next
      End Sub
      Private Sub TextBox2_TextChanged(ByVal sender As System.Object, ByVal e As System.EventArgs)
Handles TextBox2.TextChanged
      End Sub
      Private Sub TextBox3_TextChanged(ByVal sender As System.Object, ByVal e As System.EventArgs)
Handles TextBox3.TextChanged
      End Sub
      Private Sub TextBox1_TextChanged(ByVal sender As System.Object, ByVal e As System.EventArgs)
Handles TextBox1.TextChanged
      End Sub
End Class
```

The form for the second stepper motor control program is given in Figure 9.21.

Figure 9.21 Form for stepper motor control program.

The code for this program is given below. This program was written in collaboration with Dr Peter Birkin.

```
Imports System.IO.Ports.SerialPort
Imports System.IO
Public Class Form1
    Dim comstr As String
    Dim ts As String
    Dim wey As Integer
    Dim err As String
    Dim Lendata As Integer
    Dim vscale1 As Double
    Dim vscale2 As Double
    Dim timescale As Double
    Dim V(499) As Double
    Dim V2(499) As Double
    Dim t(499) As Double
    Dim w As Integer
    Dim position As Double
    Dim offsetV1 As Double
    Dim offsetV2 As Double
    Dim triglevelV As Double
    Private Sub Button1_Click(ByVal sender As System.Object, ByVal e As System.EventArgs)
        For Each sp As String In My.Computer.Ports.SerialPortNames
            ComboBox1.Items.Add(sp)
        Next
    End Sub
    Private Sub Form1_Load(ByVal sender As System.Object, ByVal e As System.EventArgs) Handles
MyBase.Load
        For Each sp As String In My.Computer.Ports.SerialPortNames
            ComboBox1.Items.Add(sp)
        Next
    End Sub
    Private Sub Button3_Click(ByVal sender As System.Object, ByVal e As System.EventArgs) Handles
Button3.Click
```

```
        Button3.Visible = False
        Static start_time As DateTime
        Static stop_time As DateTime
        Dim time_elapsed As TimeSpan
        Dim ztime As Double
        position = position + 10
        TextBox1.Text = position
        ListBox3.Items.Clear()
        SerialPort1.Close()   'Connect to the serial port
        comstr = ComboBox1.Text
        SerialPort1.PortName = comstr
        SerialPort1.BaudRate = 9600 'The speed data used
        SerialPort1.DataBits = 8 'Width of the data used.  Note this is important 7 will work but has
problems!!!!
        SerialPort1.Parity = Ports.Parity.None
        SerialPort1.StopBits = 1 'number of stop bits used
        SerialPort1.Handshake = Ports.Handshake.None
        'SerialPort1.ReadTimeout = 2000
        SerialPort1.Open()   'Connect to the serial port
        wey = 0
        Try
            SerialPort1.WriteLine("6")
            'Do
            'ts = SerialPort1.ReadChar
            'ListBox3.Items.Add(ts)
            'Loop
        Catch ex As TimeoutException
        End Try
        SerialPort1.Close()   'Connect to the serial port
        start_time = Now
        Do
            stop_time = Now
            time_elapsed = stop_time.Subtract(start_time)
            ztime = time_elapsed.TotalSeconds.ToString(0.0)
            Application.DoEvents()
        Loop Until ztime > 4 Or wey = 1
        Button3.Visible = True
    End Sub
    Private Sub Button4_Click(ByVal sender As System.Object, ByVal e As System.EventArgs) Handles
Button4.Click
        Button4.Visible = False
        Static start_time As DateTime
        Static stop_time As DateTime
        Dim time_elapsed As TimeSpan
        Dim ztime As Double
        position = position - 10
        TextBox1.Text = position
        ListBox3.Items.Clear()
        SerialPort1.Close()   'Connect to the serial port
        comstr = ComboBox1.Text
        SerialPort1.PortName = comstr
        SerialPort1.BaudRate = 9600 'The speed data used
        SerialPort1.DataBits = 8 'Width of the data used.  Note this is important 7 will work but has
problems!!!!
        SerialPort1.Parity = Ports.Parity.None
        SerialPort1.StopBits = 1 'number of stop bits used
        SerialPort1.Handshake = Ports.Handshake.None
        SerialPort1.ReadTimeout = 100
        SerialPort1.Open()   'Connect to the serial port
        wey = 0
```

```
        Try
            SerialPort1.WriteLine("5")
            Do
                ts = SerialPort1.ReadLine
                ListBox3.Items.Add(ts)
            Loop
        Catch ex As TimeoutException
        End Try
        SerialPort1.Close()   'Connect to the serial port
        start_time = Now
        Do
            stop_time = Now
            time_elapsed = stop_time.Subtract(start_time)
            ztime = time_elapsed.TotalSeconds.ToString(0.0)
            Application.DoEvents()
        Loop Until ztime > 4 Or wey = 1
        Button4.Visible = True
    End Sub
    Private Sub Button5_Click(ByVal sender As System.Object, ByVal e As System.EventArgs) Handles
Button5.Click
        ListBox3.Items.Clear()
        SerialPort1.Close()
        comstr = ComboBox1.Text
        SerialPort1.PortName = comstr
        SerialPort1.BaudRate = 9600 'The speed data used
        SerialPort1.DataBits = 8 'Width of the data used.  Note this is important 7 will work but has
problems!!!!
        SerialPort1.Parity = Ports.Parity.None
        SerialPort1.StopBits = 1 'number of stop bits used
        SerialPort1.Handshake = Ports.Handshake.None
        SerialPort1.ReadTimeout = 200
        SerialPort1.Open()   'Connect to the serial port
        wey = 1
        Try
            SerialPort1.WriteLine("0")
            Do
                ts = SerialPort1.ReadLine
                ListBox3.Items.Add(ts)
            Loop
        Catch ex As TimeoutException
        End Try
        SerialPort1.Close()   'Connect to the serial port
    End Sub
    Private Sub ComboBox1_SelectedIndexChanged(ByVal sender As System.Object, ByVal e As
System.EventArgs) Handles ComboBox1.SelectedIndexChanged
        Button3.Visible = True
        Button2.Visible = True
        Button6.Visible = True
        Button7.Visible = True
        Button4.Visible = True
        Button5.Visible = True
        Button8.Visible = True
        Button9.Visible = True
        Button10.Visible = True
    End Sub
    Private Sub SaveToolStripMenuItem_Click(ByVal sender As System.Object, ByVal e As
System.EventArgs)
    End Sub
    Private Sub OpenToolStripMenuItem_Click(ByVal sender As System.Object, ByVal e As
System.EventArgs)
```

```
    End Sub
    Private Sub Button1_Click_1(ByVal sender As System.Object, ByVal e As System.EventArgs)
    End Sub
    Private Sub ScatterGraph1_PlotDataChanged(ByVal sender As System.Object, ByVal e As
NationalInstruments.UI.XYPlotDataChangedEventArgs)
    End Sub
    Private Sub CheckBox1_CheckedChanged(ByVal sender As System.Object, ByVal e As
System.EventArgs)
    End Sub
    Private Sub CheckBox2_CheckedChanged(ByVal sender As System.Object, ByVal e As
System.EventArgs)
    End Sub
    Private Sub CheckBox3_CheckedChanged(ByVal sender As System.Object, ByVal e As
System.EventArgs)
    End Sub
    Private Sub ProgressBar2_Click(ByVal sender As System.Object, ByVal e As System.EventArgs)
    End Sub
    Private Sub Button2_Click(ByVal sender As System.Object, ByVal e As System.EventArgs) Handles
Button2.Click
        Button2.Visible = False
        Static start_time As DateTime
        Static stop_time As DateTime
        Dim time_elapsed As TimeSpan
        Dim ztime As Double
        position = position + 100
        TextBox1.Text = position
        ListBox3.Items.Clear()
        SerialPort1.Close()   'Connect to the serial port
        comstr = ComboBox1.Text
        SerialPort1.PortName = comstr
        SerialPort1.BaudRate = 9600 'The speed data used
        SerialPort1.DataBits = 8 'Width of the data used.  Note this is important 7 will work but has
problems!!!!
        SerialPort1.Parity = Ports.Parity.None
        SerialPort1.StopBits = 1 'number of stop bits used
        SerialPort1.Handshake = Ports.Handshake.None
        SerialPort1.ReadTimeout = 200
        SerialPort1.Open()   'Connect to the serial port
        wey = 0
        Try
            SerialPort1.WriteLine("8")
            Do
                ts = SerialPort1.ReadLine
                ListBox3.Items.Add(ts)
            Loop
            SerialPort1.Close()   'Connect to the serial port
        Catch ex As TimeoutException
        End Try
        start_time = Now
        Do
            stop_time = Now
            time_elapsed = stop_time.Subtract(start_time)
            ztime = time_elapsed.TotalSeconds.ToString(0.0)
            Application.DoEvents()
        Loop Until ztime > 12 Or wey = 1
        Button2.Visible = True
    End Sub
    Private Sub Button6_Click(ByVal sender As System.Object, ByVal e As System.EventArgs) Handles
Button6.Click
        Button6.Visible = False
```

```
        Static start_time As DateTime
        Static stop_time As DateTime
        Dim time_elapsed As TimeSpan
        Dim ztime As Double
        position = position - 100
        TextBox1.Text = position
        ListBox3.Items.Clear()
        SerialPort1.Close()   'Connect to the serial port
        comstr = ComboBox1.Text
        SerialPort1.PortName = comstr
        SerialPort1.BaudRate = 9600 'The speed data used
        SerialPort1.DataBits = 8 'Width of the data used.  Note this is important 7 will work but has
problems!!!!
        SerialPort1.Parity = Ports.Parity.None
        SerialPort1.StopBits = 1 'number of stop bits used
        SerialPort1.Handshake = Ports.Handshake.None
        SerialPort1.ReadTimeout = 200
        SerialPort1.Open()   'Connect to the serial port
        wey = 0
        Try
            SerialPort1.WriteLine("7")
            Do
                ts = SerialPort1.ReadLine
                ListBox3.Items.Add(ts)
            Loop
            SerialPort1.Close()   'Connect to the serial port
        Catch ex As TimeoutException
        End Try
        start_time = Now
        Do
            stop_time = Now
            time_elapsed = stop_time.Subtract(start_time)
            ztime = time_elapsed.TotalSeconds.ToString(0.0)
            Application.DoEvents()
        Loop Until ztime > 12 Or wey = 1
        Button6.Visible = True
    End Sub
    Private Sub Button7_Click(ByVal sender As System.Object, ByVal e As System.EventArgs) Handles
Button7.Click
        Button7.Visible = False
        position = position + 1
        TextBox1.Text = position
        ListBox3.Items.Clear()
        SerialPort1.Close()   'Connect to the serial port
        comstr = ComboBox1.Text
        SerialPort1.PortName = comstr
        SerialPort1.BaudRate = 9600 'The speed data used
        SerialPort1.DataBits = 8 'Width of the data used.  Note this is important 7 will work but has
problems!!!!
        SerialPort1.Parity = Ports.Parity.None
        SerialPort1.StopBits = 1 'number of stop bits used
        SerialPort1.Handshake = Ports.Handshake.None
        SerialPort1.ReadTimeout = 200
        SerialPort1.Open()   'Connect to the serial port
        Try
            SerialPort1.WriteLine("4")
            Do
                ts = SerialPort1.ReadLine
                ListBox3.Items.Add(ts)
            Loop
```

```
        Catch ex As TimeoutException
        End Try
        SerialPort1.Close()   'Connect to the serial port
        Button7.Visible = True
    End Sub
    Private Sub Button8_Click(ByVal sender As System.Object, ByVal e As System.EventArgs) Handles
Button8.Click
        Button8.Visible = False
        position = position - 1
        TextBox1.Text = position
        ListBox3.Items.Clear()
        SerialPort1.Close()   'Connect to the serial port
        comstr = ComboBox1.Text
        SerialPort1.PortName = comstr
        SerialPort1.BaudRate = 9600 'The speed data used
        SerialPort1.DataBits = 8 'Width of the data used.  Note this is important 7 will work but has
problems!!!!
        SerialPort1.Parity = Ports.Parity.None
        SerialPort1.StopBits = 1 'number of stop bits used
        SerialPort1.Handshake = Ports.Handshake.None
        SerialPort1.ReadTimeout = 200
        SerialPort1.Open()   'Connect to the serial port
        Try
            SerialPort1.WriteLine("3")
            Do
                ts = SerialPort1.ReadLine
                ListBox3.Items.Add(ts)
            Loop
        Catch ex As TimeoutException
        End Try
        SerialPort1.Close()   'Connect to the serial port
        Button8.Visible = True
    End Sub
    Private Sub Button9_Click(ByVal sender As System.Object, ByVal e As System.EventArgs) Handles
Button9.Click
        Button9.Visible = False
        position = position + 0.1
        TextBox1.Text = position
        ListBox3.Items.Clear()
        SerialPort1.Close()   'Connect to the serial port
        comstr = ComboBox1.Text
        SerialPort1.PortName = comstr
        SerialPort1.BaudRate = 9600 'The speed data used
        SerialPort1.DataBits = 8 'Width of the data used.  Note this is important 7 will work but has
problems!!!!
        SerialPort1.Parity = Ports.Parity.None
        SerialPort1.StopBits = 1 'number of stop bits used
        SerialPort1.Handshake = Ports.Handshake.None
        SerialPort1.ReadTimeout = 200
        SerialPort1.Open()   'Connect to the serial port
        Try
            SerialPort1.WriteLine("2")
            Do
                ts = SerialPort1.ReadLine
                ListBox3.Items.Add(ts)
            Loop
        Catch ex As TimeoutException
        End Try
        SerialPort1.Close()   'Connect to the serial port
        Button9.Visible = True
```

```
    End Sub
    Private Sub Button10_Click(ByVal sender As System.Object, ByVal e As System.EventArgs) Handles
Button10.Click
        Button10.Visible = False
        position = position - 0.1
        TextBox1.Text = position
        ListBox3.Items.Clear()
        SerialPort1.Close()   'Connect to the serial port
        comstr = ComboBox1.Text
        SerialPort1.PortName = comstr
        SerialPort1.BaudRate = 9600 'The speed data used
        SerialPort1.DataBits = 8 'Width of the data used.  Note this is important 7 will work but has
problems!!!!
        SerialPort1.Parity = Ports.Parity.None
        SerialPort1.StopBits = 1 'number of stop bits used
        SerialPort1.Handshake = Ports.Handshake.None
        SerialPort1.ReadTimeout = 200
        SerialPort1.Open()   'Connect to the serial port
        Try
            SerialPort1.WriteLine("1")
            Do
                ts = SerialPort1.ReadLine
                ListBox3.Items.Add(ts)
            Loop
        Catch ex As TimeoutException
        End Try
        SerialPort1.Close()   'Connect to the serial port
        Button10.Visible = True
    End Sub
    Private Sub Button1_Click_2(sender As System.Object, e As System.EventArgs) Handles Button1.Click
        position = 0
        TextBox1.Text = 0
    End Sub
End Class
```

9.9.5 Ultrasonic pulsing

This program was designed to control turning the ultrasonic horn on and off in a sequence of pulses. The form for this program is displayed in Figure 9.22.

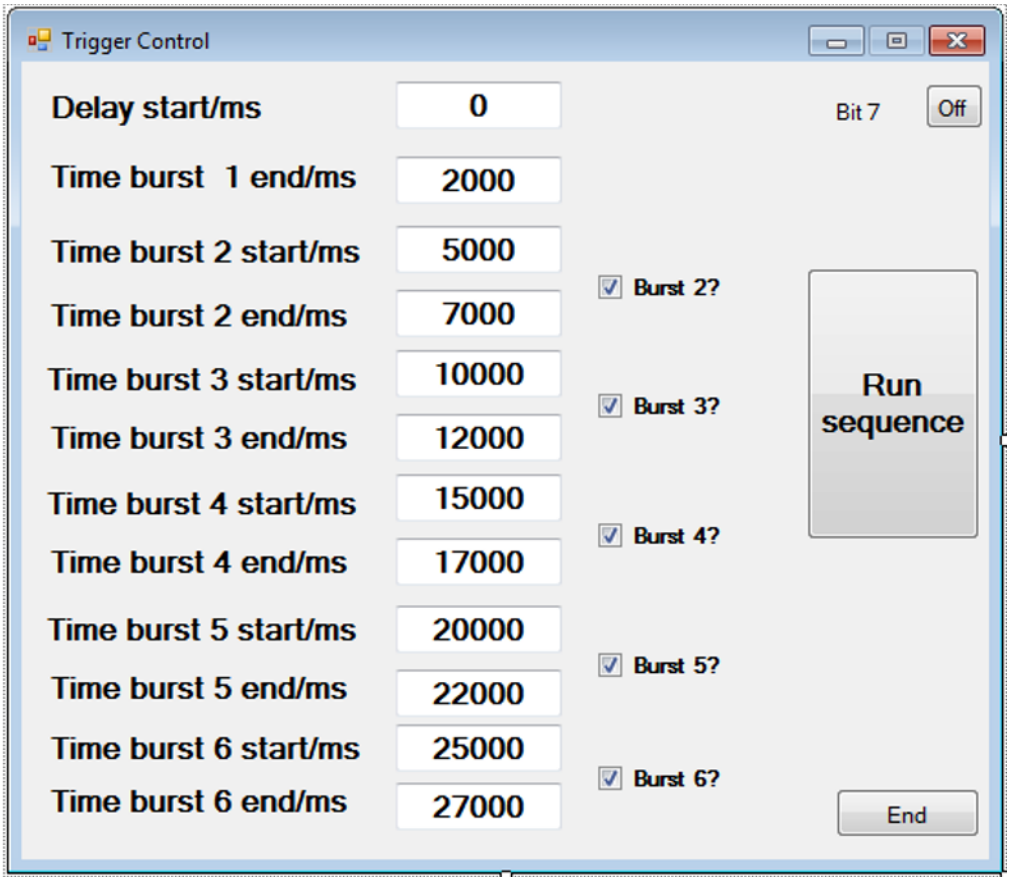

Figure 9.22 Form controlling pulse setup.

The code for this program is given below. This program was written in collaboration with Dr Peter Birkin.

```
Public Class Form1
    Public Daqboard As New MccDaq.MccBoard()
    Dim ulstat As MccDaq.ErrorInfo
    Dim Status As Boolean
    Private Sub Form1_Load(ByVal sender As System.Object, ByVal e As System.EventArgs) Handles
MyBase.Load
        'First Lets make sure there's a USB-200 Series plugged in:
        Dim BoardNum As Integer
        Dim Numboards As Integer = 99
        Dim Boardfound As Boolean = False
        For BoardNum = 0 To Numboards - 1
            Daqboard = New MccDaq.MccBoard(BoardNum)
            If Daqboard.BoardName.Contains("201") _
              Or Daqboard.BoardName.Contains("202") _
              Or Daqboard.BoardName.Contains("204") _
              Or Daqboard.BoardName.Contains("205") Then
                Boardfound = True
                Daqboard = New MccDaq.MccBoard(BoardNum)
                Daqboard.FlashLED()
```

```
            Exit For
          End If
        Next
        If Boardfound = False Then
          MsgBox("No USB-200 Series device found in system.  Please run InstaCal.", MsgBoxStyle.Critical,
"No Board detected")
          End
        End If
        Dim mystring As String = Daqboard.BoardName.Substring(0, Daqboard.BoardName.Trim.Length) + _
          " found as board number: " + Daqboard.BoardNum.ToString
        Me.Text = mystring
        'Configure the Port (all 8 bits) to output.
        ulstat = Daqboard.DConfigPort(MccDaq.DigitalPortType.AuxPort,
MccDaq.DigitalPortDirection.DigitalOut)
        If ulstat.Value <> 0 Then Call errhandler(ulstat)
    End Sub
    Public Sub errhandler(ByVal ulstat As MccDaq.ErrorInfo)
        'Generic UL error handler
        MessageBox.Show(ulstat.Message, "Universal Library Error ", MessageBoxButtons.OK,
MessageBoxIcon.Error)
    End Sub
    Private Sub Button6_Click(ByVal sender As System.Object, ByVal e As System.EventArgs) Handles
Button6.Click
        ulstat = Daqboard.DOut(MccDaq.DigitalPortType.AuxPort, 0) 'turn all bits back off.
        If ulstat.Value <> 0 Then Call errhandler(ulstat)
        End
    End Sub
    Public Sub SetBitVal(ByVal sender As System.Object)
        'So as not to repeat the same routine 8 times,  This subroutine is called each time the user clicks on a
        'specific bit's related checkbox event.  This way there is only one place to look for and modify the
DBitOut method
        'First, extract the last character of the objects name which is the bit number.
        'Use the bitnum to find out if the objects text is "Off" or "On".  Change the label of the object from Off
to On or
        'On to Off, and change the state of the related bit appropriately.
        Dim bitname, bitnumber As String
        Dim bitlength, returnstring As Int16
        With sender 'sender is the checkbox that is used to change the state of the bit.
          bitname = .name
          bitlength = bitname.Length
          If bitlength = 7 Then returnstring = 1 Else returnstring = 2
          bitnumber = bitname.Substring(bitlength - returnstring, returnstring).Trim
          Dim bitnum As Integer
          bitnum = Val(bitnumber)
          If .text = "Off" Then
            .text = "On"
            ulstat = Daqboard.DBitOut(MccDaq.DigitalPortType.AuxPort, bitnum,
MccDaq.DigitalLogicState.High)
          Else
            .text = "Off"
            ulstat = Daqboard.DBitOut(MccDaq.DigitalPortType.AuxPort, bitnum,
MccDaq.DigitalLogicState.Low)
          End If
        End With
        If ulstat.Value <> 0 Then Call errhandler(ulstat)
    End Sub
    Private Sub chkBit7_CheckedChanged(ByVal sender As Object, ByVal e As System.EventArgs) Handles
chkBit7.CheckedChanged
        SetBitVal(chkBit7)
    End Sub
```

```
    Private Sub Button1_Click(ByVal sender As System.Object, ByVal e As System.EventArgs) Handles
Button1.Click
        Dim start_time As DateTime
        Static stop_time As DateTime
        Dim elapsed_time As TimeSpan
        Dim timegot As Double
        'First pulse on here
        start_time = Now
        Do
            stop_time = Now
            elapsed_time = stop_time.Subtract(start_time)
            timegot = elapsed_time.TotalSeconds.ToString("00.000")
        Loop Until timegot > (TextBox1.Text / 1000)
        ulstat = Daqboard.DBitOut(MccDaq.DigitalPortType.AuxPort, 7, MccDaq.DigitalLogicState.High)
        'First pulse off here
        Do
            stop_time = Now
            elapsed_time = stop_time.Subtract(start_time)
            timegot = elapsed_time.TotalSeconds.ToString("00.000")
        Loop Until timegot > (TextBox2.Text / 1000)
        ulstat = Daqboard.DBitOut(MccDaq.DigitalPortType.AuxPort, 7, MccDaq.DigitalLogicState.Low)
        If CheckBox1.Checked = False Then GoTo Skippy Else
        'Second pulse on here
        Do
            stop_time = Now
            elapsed_time = stop_time.Subtract(start_time)
            timegot = elapsed_time.TotalSeconds.ToString("00.000")
        Loop Until timegot > (TextBox3.Text / 1000)
        ulstat = Daqboard.DBitOut(MccDaq.DigitalPortType.AuxPort, 7, MccDaq.DigitalLogicState.High)
        'Second pulse off here
        Do
            stop_time = Now
            elapsed_time = stop_time.Subtract(start_time)
            timegot = elapsed_time.TotalSeconds.ToString("00.000")
        Loop Until timegot > (TextBox4.Text / 1000)
        ulstat = Daqboard.DBitOut(MccDaq.DigitalPortType.AuxPort, 7, MccDaq.DigitalLogicState.Low)
        If CheckBox2.Checked = False Then GoTo Skippy Else
        'Third pulse on here
        Do
            stop_time = Now
            elapsed_time = stop_time.Subtract(start_time)
            timegot = elapsed_time.TotalSeconds.ToString("00.000")
        Loop Until timegot > (TextBox5.Text / 1000)
        ulstat = Daqboard.DBitOut(MccDaq.DigitalPortType.AuxPort, 7, MccDaq.DigitalLogicState.High)
        'Third pulse off here
        Do
            stop_time = Now
            elapsed_time = stop_time.Subtract(start_time)
            timegot = elapsed_time.TotalSeconds.ToString("00.000")
        Loop Until timegot > (TextBox6.Text / 1000)
        ulstat = Daqboard.DBitOut(MccDaq.DigitalPortType.AuxPort, 7, MccDaq.DigitalLogicState.Low)
        If CheckBox3.Checked = False Then GoTo Skippy Else
        'Fourth pulse on here
        Do
            stop_time = Now
            elapsed_time = stop_time.Subtract(start_time)
            timegot = elapsed_time.TotalSeconds.ToString("00.000")
        Loop Until timegot > (TextBox7.Text / 1000)
        ulstat = Daqboard.DBitOut(MccDaq.DigitalPortType.AuxPort, 7, MccDaq.DigitalLogicState.High)
        'Fourth pulse off here
```

```
        Do
            stop_time = Now
            elapsed_time = stop_time.Subtract(start_time)
            timegot = elapsed_time.TotalSeconds.ToString("00.000")
        Loop Until timegot > (TextBox8.Text / 1000)
        ulstat = Daqboard.DBitOut(MccDaq.DigitalPortType.AuxPort, 7, MccDaq.DigitalLogicState.Low)
        If CheckBox4.Checked = False Then GoTo Skippy Else
        'Fifth pulse on here
        Do
            stop_time = Now
            elapsed_time = stop_time.Subtract(start_time)
            timegot = elapsed_time.TotalSeconds.ToString("00.000")
        Loop Until timegot > (TextBox9.Text / 1000)
        ulstat = Daqboard.DBitOut(MccDaq.DigitalPortType.AuxPort, 7, MccDaq.DigitalLogicState.High)
        'Fifth pulse off here
        Do
            stop_time = Now
            elapsed_time = stop_time.Subtract(start_time)
            timegot = elapsed_time.TotalSeconds.ToString("00.000")
        Loop Until timegot > (TextBox10.Text / 1000)
        ulstat = Daqboard.DBitOut(MccDaq.DigitalPortType.AuxPort, 7, MccDaq.DigitalLogicState.Low)
        If CheckBox5.Checked = False Then GoTo Skippy Else
        'Sixth pulse on here
        Do
            stop_time = Now
            elapsed_time = stop_time.Subtract(start_time)
            timegot = elapsed_time.TotalSeconds.ToString("00.000")
        Loop Until timegot > (TextBox11.Text / 1000)
        ulstat = Daqboard.DBitOut(MccDaq.DigitalPortType.AuxPort, 7, MccDaq.DigitalLogicState.High)
        'Sixth pulse off here
        Do
            stop_time = Now
            elapsed_time = stop_time.Subtract(start_time)
            timegot = elapsed_time.TotalSeconds.ToString("00.000")
        Loop Until timegot > (TextBox12.Text / 1000)
        ulstat = Daqboard.DBitOut(MccDaq.DigitalPortType.AuxPort, 7, MccDaq.DigitalLogicState.Low)
Skippy:
    End Sub
End Class
```